



UNIVERSITY OF THE
WITWATERSRAND,
JOHANNESBURG

**EFFICIENCY AND OPTO-ELECTRICAL
STUDIES OF SOLUTION PROCESSED
BULK HETEROJUNCTION ORGANIC
PHOTOVOLTAIC DEVICES**

Lesias Morake Kotane

**A thesis submitted to the Faculty of Science, University of the
Witwatersrand, Johannesburg, in fulfilment of the requirements
for the degree of Doctor of Philosophy**

Johannesburg, 2019

Declaration

I declare that this thesis is my own, unaided work. It is being submitted for the Degree of Doctor of Philosophy, in the Faculty of Sciences, at the University of the Witwatersrand, Johannesburg. It has not been submitted before for any degree or examination at any other University.



(Signature of candidate)

On this 29th day of November 2019

Abstract

Endeavours to provide safe, clean and renewable energy have sustained considerable interest in photovoltaic (PV) technologies. The potential to harvest and harness solar energy, with an abundance of available materials, has spurred on the research in the fabrication and characterisation of organic photovoltaic (OPV) devices. Given their solution processability, OPV devices bear the promise of a large scale cost effective production process. Furthermore, the potential of producing lightweight and flexible energy sources broadens the range of applications of these devices.

However, many challenges still remain in as far as the envisaged widespread usage of OPVs is concerned. Performance related inadequacies based on poor power conversion efficiencies (PCEs) and environmental stability, have thus far prevented the full commercialisation of organic solar cells. This scenario has necessitated the collation of a clearer understanding of the physics underpinning the fabrication and the operation of these devices.

In this work, molecular engineering mechanisms of organic photoactive layers where different parameters including the choice of materials and their mass ratios were investigated. The working principles of fabricated polymer:fullerene bulk heterojunction (BHJ) devices were studied to deepen our understanding of the physics of organic solar cells. Three different approaches were selected for this purpose viz. the fabrication and opto-electrical characterisation of (i) P3HT:PC₇₁BM devices, (ii) ternary devices based on the donor:acceptor1:acceptor2 configuration i.e. P3HT:PC₆₁BM:PC₇₁BM and (iii) P3HT:PC₆₁BM devices with nitrogen-doped multi walled carbon nanotubes (N-MWCNTs) added in the photoactive layer. These photoactive blends completed a working OPV device by being sandwiched between a transparent conducting oxide (ITO) – the anode and aluminium (Al) –the cathode.

The optimisation of device fabrication processes, was key to the efficient operation of devices. Optical absorption and current-voltage measurements provided the

bedrock on which this work was carried out. PCEs, with their dependence on the morphology and charge carrier transport dynamics of devices, were not only extracted from the $J - V$ experimental data but were also compared to establish best performing devices. This was done by establishing current limiting mechanisms in devices where interface potential barriers were compared using the Fowler-Nordheim (FN) and the Richardson-Schottky (RS) emission models and with bulk transport properties estimated from space charge limited current (SCLC) models. Noting that recombination processes are a major contributor to the reduction in generated photocurrents leading to lower PCEs, the physics of charge carrier recombination was studied by focussing on the dependencies of the FF , V_{oc} and J_{sc} on incident light intensity.

The study on P3HT:PC₇₁BM devices focussed on the identification of the optimum mass ratio between the electron donor material (P3HT) and the electron acceptor material (PC₇₁BM). Additionally, kinetic and energetic properties of the optimised blend were probed. The best PCE was measured for the 1:0.8 blend and kinetically and energetically, for the device annealed at 50 °C for 10 minutes. The ternary blend that gave the highest PCE was of the form P3HT:PC₆₁BM:PC₇₁BM \equiv 1:0.4:0.6.

The study on the inclusion of N-MWCNTs in to the photoactive layer of P3HT:PC₆₁BM did not yield the expected increase in the PCE. Instead, it highlighted the importance of a thorough, appropriate and effective preparation of CNTs for their inclusion in OPV devices.

L ERATO
EBOGANG
ESEDI

Acknowledgements

I would like to express my deepest gratitude to my supervisor, Prof. Daniel Wamwangi, for his guidance, support, motivation and exceptional knowledge that he availed in abundance during my Ph.D. studies. Noting the challenges associated with part-time studies, his patience and encouragement deserve a special mention.

I also wish to acknowledge the role played by Dr Ziyayi Chiguvare in stimulating my interest in the field of organic solar cells and for helping to set my research project in motion.

I would also like to express my great appreciation to the following for hours spent in the labs and for very stimulating discussions: Kamalannan Ranganathan, Francis Otieno Otieno, Ibrahim Bala Usman and Lordwell Jhamba. On many occasions we shook our heads, we scratched our heads, we went through highs and lows, however, our quest to unravel some complexities we encountered in our projects made the journey exciting and fulfilling. Thanks gents!

I am also grateful to the School of Physics for facilitating and supporting my studies. My gratitude also goes to all the staff in the School of Physics Workshop for their technical assistance that solved many a problem in our laboratories. Assistance provided by Dr. Rudolph Erasmus in all the spectroscopic measurements is greatly appreciated.

Finally, I would like to acknowledge my family for being with me throughout this journey. I would like to express the greatest appreciation to my beloved wife, Lerato, who was always by my side throughout this journey. Thank you Mlavisto! Furthermore, I would like to thank my children, Lebogang and Lesedi. Your questions and words of encouragement will remain priceless!

Contents

DECLARATION	i
ABSTRACT	ii
DEDICATION	iv
ACKNOWLEDGEMENTS	v
LIST OF FIGURES	xii
LIST OF TABLES	xxi
LIST OF SYMBOLS AND ABBREVIATIONS	xxiii
PUBLICATIONS AND PRESENTATIONS	183

CHAPTER 1 INTRODUCTION

1.1	Energy overview.....	1
1.2	Development of photovoltaic devices.....	3
1.2.1	First Generation.....	3
1.2.2	Second Generation.....	4
1.2.3	Third Generation.....	4
1.2.4	Fourth Generation.....	5
1.3	Motivation for Organic Photovoltaic (OPV) research.....	5
1.4	Aim and objectives.....	8
1.4.1	Aim.....	8
1.4.2	Objectives.....	8
1.5	Thesis outline.....	9
1.6	References.....	11

CHAPTER 2 THEORETICAL ASPECTS

2.1	Overview of organic semiconductors.....	14
2.2	The bulk heterojunction (BHJ) OPV concept.....	17
2.3	Physics of organic photovoltaic devices.....	20
2.3.1	Light absorption and exciton creation.....	20
2.3.2	Exciton diffusion.....	22
2.3.3	Charge separation.....	23
2.3.4	Charge transfer and collection.....	25
2.4	Photovoltaic characteristics of an OPV device.....	26
2.4.1	The $J - V$ plot and the characteristic performance figures of merit...26	
2.4.2	Equivalent circuit diagram (ECD).....	29
2.5	Charge carrier dynamics in OPV devices.....	34
2.5.1	Charge injection and bulk transport in OPV devices.....	35
2.5.1.1	Richardson – Schottky (RS) thermionic emission model...36	
2.5.1.2	Fowler – Nordheim (FN) field emission model.....38	
2.5.1.3	Bulk charge transport.....	41
2.5.2	Charge recombination in OPV devices.....	46
2.6	References.....	51

CHAPTER 3 EXPERIMENTAL METHODS AND MATERIALS

3.1	Materials.....	57
3.1.1	Indium Tin Oxide (ITO).....	57
3.1.2	Poly(3,4-ethylenedioxythiophene)-polysyrenesulphonate (PEDOT:PSS).....	57
3.1.3	Poly (3-hexylthiophene 2,5 diyl) (P3HT).....	58
3.1.4	[6,6]-phenyl-C61 butyric acid methyl ester/[6,6]-phenyl-C71 butyric acid methyl ester (PC ₆₁ BM/ PC ₇₁ BM).....	59

3.2	Device fabrication set ups: Spin coating and metallization.....	60
3.2.1	Spin Coater.....	60
3.2.2	Thermal evaporator.....	60
3.2.3	Furnace.....	62
3.2.4	Cary 500 UV–visible spectrometer.....	63
3.2.5	I– V set up.....	64
3.3	Device fabrication methods.....	64
3.3.1	Layer and device characterization studies/procedures.....	66
3.4	Summary.....	67
3.5	References.....	68

CHAPTER 4 OPTICAL AND ELECTRICAL MASS RATIO STUDIES OF P3HT:PC₇₁BM BHI OPV DEVICES

4.1	Introduction.....	69
4.2	Experimental methods.....	71
4.2.1	Mass ratios solutions preparations.....	71
4.2.2	Samples preparation for energetics and kinetics measurements....	72
4.2.3	Fabrication of devices.....	72
4.3	Results and discussion.....	73
4.3.1	P3HT:PC ₇₁ BM mass ratio optimisation.....	73
4.3.1.1	Optical characteristics.....	73
4.3.1.2	Current – Voltage OPV performance characteristics of mass ratio optimisation.....	74
4.3.1.3	Charge transport properties as a function of mass ratio.....	77
4.3.1.3.1	Injection limited contribution.....	77
4.3.1.3.2	Bulk limited contribution.....	79
4.3.1.4	Light intensity behaviour as a function of mass ratio.....	81
4.3.2	Energetics of optimised blend ratio.....	87
4.3.2.1	Spectroscopic characteristics.....	87

4.3.2.2	Current – voltage energetics of optimised blend ratio.....	91
4.3.2.3	Charge transport properties of P3HT:PC ₇₁ BM as a function of annealing temperature.....	94
4.3.2.3.1	P3HT:PC ₇₁ BM (1:0.8) injection limited transport properties.....	94
4.3.2.3.2	P3HT:PC ₇₁ BM (1:0.8) bulk limited transport properties.....	99
4.3.2.4	P3HT:PC ₇₁ BM (1:0.8) OPV behaviour as a function of light intensity at different annealing temperatures.....	100
4.3.3	Kinetics of optimised blend ratio.....	103
4.3.3.1	Spectroscopic characteristics.....	103
4.3.3.2	Current – voltage kinetics of optimised blend ratio.....	105
4.3.3.3	Charge transport properties of P3HT:PC ₇₁ BM as a function of annealing time.....	107
4.3.3.3.1	P3HT:PC ₇₁ BM (1:0.8) injection limited transport properties.....	107
4.3.3.3.2	P3HT:PC ₇₁ BM (1:0.8) bulk limited transport properties.....	109
4.3.3.4	P3HT:PC ₇₁ BM (1:0.8) OPV behaviour as a function of light intensity.....	112
4.4	Conclusion.....	116
4.5	References.....	117

**CHAPTER 5 PERFORMANCE ASSESSMENT OF
DONOR:ACCEPTOR1:ACCEPTOR2 TERNARY BLEND
BHJ OPV DEVICES**

5.1	Introduction.....	123
5.2	Experimental details.....	125
5.3	Results and discussion.....	127

5.3.1	Spectroscopic characteristics; UV-Vis details.....	127
5.3.1.1	Structural studies of ternary blend by Raman spectroscopy.....	128
5.3.2	Current-Voltage characteristics.....	130
5.3.3	Charge transport properties of fabricated ternary devices.....	133
5.3.3.1	Emission contributions.....	133
5.3.3.2	Bulk limited transport.....	135
5.3.4	Variations of OPV parameters with incident light intensity.....	137
5.4	Conclusion.....	142
5.5	References.....	143

CHAPTER 6 PHOTOVOLTAIC INVESTIGATION OF N-MWCNT INCORPORATED BHJ OPV DEVICES

6.1	Introduction.....	146
6.2	Experimental details.....	148
6.2.1	Synthesis and functionalisation of N-MWCNTs.....	148
6.2.2	Preparation of P3HT:PC ₆₁ BM:N-MWCNT active layer solutions.....	149
6.2.3	Fabrication of BHJ OPV devices.....	150
6.3	Results and discussion.....	150
6.3.1	Spectroscopic characteristics.....	150
6.3.1.1	Optical absorption.....	150
6.3.1.2	Raman spectra characterisations.....	151
6.3.2	Electrical characteristics.....	152
6.3.3	Charge transport properties.....	155
6.3.3.1	Injection limited behaviour.....	155
6.3.3.2	Bulk limited behaviour.....	157

6.3.4	Key parameter variations with light intensity.....	159
6.4	P3HT:N-MWCNT.....	164
6.4.1	Fabrication of OPV devices.....	164
6.4.2	Spectroscopic characteristics.....	165
6.4.2.1	UV-Vis characterisation.....	165
6.4.2.2	Raman characteristics.....	166
6.4.3	$J - V$ characteristics.....	167
6.4.4	Charge transport properties.....	170
6.4.4.1	Injection limited.....	170
6.4.4.2	Bulk limited.....	172
6.4.5	Variations of OPV parameters with light intensity.....	173
6.5	Conclusion.....	176
6.6	References.....	177
 CHAPTER 7 CONCLUSIONS AND OUTLOOK		
7.1	Conclusions.....	180
7.2	Outlook.....	181

List of figures

1.1	World energy consumption – 2017.....	1
1.2	South Africa - 2017 energy consumption.....	1
1.3	Global PV power potential.....	2
1.4	Brabec triangle with OPVs in blue and inorganic PVs in green. IPV's are seen to be dominating efficiency and stability concerns whereas OPVs dominate concerns related to production costs.....	6
1.5	Overview of highest efficiencies in different PV technologies.....	7
2.1	A segment of polyacetylene showing conjugation.....	15
2.2	Ethene Lewis structure including the sp^2 hybridized orbital structure. (a) Double bonded carbon atoms with overlapping σ – orbitals and interacting π – orbitals. (b) Delocalised π – electrons. (c) Overview of complete orbital structure of ethane.....	16
2.3	A schematic of a single layer OPV device.....	18
2.4	Typical donor:acceptor OPV heterojunction structures showing (a) the planar bilayer heterojunction OPV structure and (b) the bulk heterojunction structure.....	19
2.5	Comparison of absorption spectra of the components of the photoactive layer with the AM1.5 solar spectrum.....	21
2.6	An illustration of the Frenkel and Wannier excitons, with an electron in black and a hole in red, showing different spacings.....	22

2.7	Misalignment of the donor and acceptor HOMO – LUMO energy levels for charge separation.....	25
2.8	Typical $J - V$ curves under dark and illumination conditions. Under illumination, the maximum power density generated by the cell is $P_{\max} = J_{\max} \times V_{\max}$. The FF is defined as the ratio of the area of the green rectangle with respect to the area of the rectangle spanned by the black sides. With this ratio less than unity, P_{\max} which is also given by $J_{sc} \times V_{oc} \times FF$, means that it is always smaller than $J_{sc} \times V_{oc}$	27
2.9	Ideal diode circuit with no series resistance and an infinite shunt resistance.....	30
2.10	Non-ideal diode circuit diagram showing parasitic resistances, R_s and R_{sh} ..	31
2.11	Charge injection models at metal/polymer interfaces.....	39
2.12	Illustration of trap and transport levels, DTL, STL represent the deep and shallow trap energy levels, respectively.....	45
2.13	A schematic of recombination processes in organic BHJ OPVs and their relative time scales.....	50
3.1	Chemical structure of the hole transport layer PEDOT:PSS.....	58
3.2	Chemical structure of P3HT.....	59
3.3	Chemical structures of PC ₆₁ BM and PC ₇₁ BM.....	59
3.4	A photograph of the 2-stage CHEMAT precision spin coater.....	60
3.5	A schematic diagram of a thermal evaporation system.....	61

3.6	A photograph of thermal evaporation setup showing the following: (1) Penning gauges, (2) vacuum chamber, (3) diffusion pump, (4) variac, (5) power supply and (6) rotary pump.....	62
3.7	A photograph of the Carbolite® high temperature tube furnace.....	63
3.8	A photograph of the Cary 500 UV - Vis NIR spectrophotometer.....	63
3.9	A photograph of the current - voltage (I – V) setup integrated with the optical unit for PV characterisation.....	64
3.10	Device fabrication process flow chart.....	66
4.1	UV - Vis absorption spectra of P3HT:PC ₇₁ BM with varying mass ratios.....	74
4.2	(a) Dark current $J - V$ plots for different mass ratios and (b) Semi-log dark current $J - V$ plots of different mass ratios.....	76
4.3	(a) $J - V$ characteristics of P3HT:PC ₇₁ BM mass ratios under AM1.5 illumination at 100 mW/cm ² (b) Semi-log plots of the same curves.....	76
4.4	FN plots compared for different P3HT:PC ₇₁ BM active layer mass ratios in the dark under forward bias with the relative slope guides indicated.....	78
4.5	RS plots compared for different P3HT:PC ₇₁ BM active layer mass ratios in the dark under forward and reverse bias showing the changes in the respective slopes.....	79
4.6	Dark current log-log plots of $J - V$ characteristics under forward bias for different P3HT:PC ₇₁ BM active layer mass ratio blends. Region I has slope = 1, indicating Ohmic conduction, region II has slope > 2, corresponding to SCLC characterised by trap filling and region III has a slope ≈ 2 and is described by Trap Free SCLC.....	80

4.7	Mott-Gurney linear fits for P3HT:PC ₇₁ BM active layer mass ratio blends with thicknesses of about 140 nm. The J vs V^2 plots are for regions of high applied voltage form the current – voltage characteristics.....	81
4.8	Variations of (a) Open circuit voltage (b) short circuit current density (c) fill factor (d) power conversion efficiency as a function of light intensity.....	82
4.9	The variation of the photocurrent density (J_{ph}) as a function of the effective voltage (V_{eff}) under 100 mW/cm ² illumination for devices with different P3HT:PC ₇₁ BM mass ratios of the active layer solar and an active layer with a thickness of 140 nm.....	87
4.10	Optical absorption spectra of P3HT:PC ₇₁ BM (1:0.8) at different annealing temperatures for the same annealing time of 10 mins.....	88
4.11	Raman spectra of P3HT:PC ₇₁ BM (1:0.8) at different annealing temperatures for the same annealing time of 10 min. The inset shows the 6 cm ⁻¹ shift of the C=C mode.....	90
4.12	A plot of the FWHM as a function of temperature.....	91
4.13	Dark current – voltage characteristics of P3HT:PC ₇₁ BM (1:0.8) at different annealing temperatures for the same annealing time. (a) linear plot (b) semi-log plot.....	92
4.14	(a) J - V characteristics of P3HT:PC ₇₁ BM (1:0.8 mass ratio) under AM1.5 illumination at 100 mW/cm ² for different annealing temperatures, (b) related dark current semi-log J - V characteristics.....	93
4.15	Fowler - Nordheim plots for ITO/PEDOT:PSS/P3HT:PC ₇₁ BM/Al devices for post fabrication thermal annealing temperature range 50 °C – 110 °C...	96

4.16	A comparison of Richardson - Schottky thermionic emission plots under forward and reverse bias for ITO/PEDOT:PSS/P3HT:PC ₇₁ BM/Al devices in the 50 °C – 110 °C post fabrication thermal annealing temperature range.....	97
4.17	Linear fits of RS (FP) plots at different post fabrication annealing temperatures showing the variation of the Schottky barrier height with temperature.....	98
4.18	Linear fits of current density against V^2 graphs for different post fabrication annealing temperatures modelled on the Mott-Gurney law with an assumption of trap filled and trap free SCLC.....	99
4.19	P3HT:PC ₇₁ BM (1:0.8) energetic variations of (a) Open circuit voltage (b) short circuit current density (c) fill factor (d) power conversion efficiency as a function of light intensity for different post fabrication thermal annealing temperatures.....	101
4.20	The variation of the photocurrent density (J_{ph}) as a function of the effective voltage (V_{eff}) under 100 mW/cm ² illumination for devices with the P3HT:PC ₇₁ BM (1:0.8) mass ratio of the photoactive layer. The variation of the generated photocurrent as a function of effective voltage for different annealing temperatures shows saturation of the photocurrent at 1.6 V for devices annealed the 50 °C and 80 °C.....	103
4.21	UV - Vis spectra for the photoactive layer P3HT:PC ₇₁ BM (1:0.8) with varying anneal times at the optimum 50 °C post fabrication annealing temperature. The GLASS/ITO/PEDOT:PSS/P3HT:PC ₇₁ BM/Al devices had an average photoactive layer of 140 nm.....	104
4.22	Raman traces of the P3HT:PC ₇₁ BM photoactive layers as a function of annealing times at 50 °C post fabrication annealing temperature. The inset shows the post annealing 6 cm ⁻¹ shift of the most intense peaks and the decrease in FWHM.....	105

4.23	Dark current – voltage characteristics of P3HT:PC ₇₁ BM (1:0.8) at different annealing times for the same annealing temperature. (a) linear plot (b) semi-log plot.....	106
4.24	(a) $J - V$ characteristics of P3HT:PC ₇₁ BM (1:0.8 mass ratio) under AM1.5 illumination at 100 mW/cm ² for different annealing times (b) related dark current semi-log $J - V$ characteristics.....	107
4.25	FN plots of GLASS/ITO/PEDOT:PSS/P3HT:PC ₇₁ BM/Al devices for varying post fabrication annealing times.....	108
4.26	RS plots of GLASS/ITO/PEDOT:PSS/P3HT:PC ₇₁ BM/Al devices for varying post fabrication annealing times.....	109
4.27	Dark current log-log plots of $J - V$ characteristics under forward bias for P3HT:PC ₇₁ BM active layer blends annealed at 50 °C for 10, 25 and 40 minutes. Region I has slope = 1, indicating Ohmic conduction, region II has slope > 2, corresponding to SCLC characterised by trap filling and region III has a slope ≈ 2 and is described by Trap Free SCLC.....	111
4.28	Mott-Gurney linear fits of J_{sc} against V^2 graphs for different post fabrication anneal times modelled on the Mott-Gurney law with an assumption of negligible deep localised states for a photoactive layer with a thickness of 140 nm.....	112
4.29	P3HT:PC ₇₁ BM (1:0.8) kinetic variations of (a) Open circuit voltage (b) short circuit current density (c) fill factor (d) power conversion efficiency as a function of light intensity.....	114
4.30	Variation of the photocurrent with effective voltage for different annealing times.....	115
5.1	Energy level diagram representation of the proposed P3HT:PC ₆₁ BM:PC ₇₁ BM ternary alloy device.....	124

5.2	A schematic of the GLASS/ITO/PEDOT:PSS/P3HT:PC ₆₁ BM:PC ₇₁ BM/Al ternary device showing different layers of ternary alloy device.....	126
5.3	UV - Vis absorption spectra of ternary blend devices with varying fullerene (C60) derative ratios.....	128
5.4	Raman spectra of ternary BHJ devices with varying acceptor1:acceptor2 mixtures acquired via an excitation with an Ar ion laser (514.5 nm) at 4 mW laser power.....	129
5.5	The variation of the FWHM of the most intense peak with the PC ₆₁ BM:PC ₇₁ BM mass ratio of the photoactive layer.....	130
5.6	Dark <i>J</i> - <i>V</i> characteristics of ternary devices in (a) linear and (b) semi-log scale.....	132
5.7	<i>J</i> - <i>V</i> characteristics of ternary devices at 100 mW/cm ² illumination (AM1.5G) in (a) linear and (b) semi-log scale.....	133
5.8	FN plots for ternary blends under forward bias in the dark outlining FN field emission and thermionic contributions to the measured current.....	134
5.9	RS plots for ternary blends stacked for better illustration. The PC ₇₁ BM component of the photoactive blend increases relative to the PC ₆₁ BM component from the top graph to the bottom one.....	135
5.10	<i>J</i> - <i>V</i> characteristics in the dark in log-log scale for varying donor:acceptor1:acceptor2 ratios in the photoactive layer of ITO/PEDOT:PSS/P3HT:PC ₆₁ BM:PC ₇₁ BM/Al devices.....	136
5.11	Linear fits of <i>J</i> _{sc} vs <i>V</i> ² based on the Mott-Gurney law for charge mobility extraction.....	137

5.12	Ternary blend variations of (a) open circuit voltage (b) short circuit current density (c) fill factor (d) power conversion efficiency as a function of light intensity (P_{light}).....	139
5.13	J_{ph} vs V_{eff} for ternary blends showing the attainment of saturation currents at high effective voltages.....	141
6.1	UV - Vis spectra comparing N-MWCNTs mass loadings in the P3HT:PC ₆₁ BM active layer.....	151
6.2	Raman spectra of P3HT:PC ₆₁ BM devices with varying N-MWCNT mass loadings.....	152
6.3	Dark (left) and 100 mW.cm ⁻² (AM1.5) illumination (right) plots.....	153
6.4	Dark and illuminated semi-log plots of J - V characteristics.....	154
6.5	FN plots for increased N-MWCNT loadings into P3HT:PC ₆₁ BM photoactive blends.....	156
6.6	RS plots under reverse and forward bias for devices with an increasing content of N-MWCNT.....	157
6.7	Dark current J - V characteristics in double log scale under forward bias..	158
6.8	Linear fit curves of the Mott-Gurney law for the determination of charge carrier mobilities as a function of N-MWCNT loading on the photoactive blend.....	159
6.9	N-MWCNT based variations of (a) open circuit voltage (b) short circuit current density (c) fill factor (d) power conversion efficiency as a function of light intensity.....	161
6.10	The graph of $(1+R_s/R_{sh})$ for different N-MWCNT mass loadings indicating the degree of the diminishing of the current density.....	162

6.11	J_{ph} vs V_{eff} curves for different N-MWCNT loadings in the 130 nm thick photoactive layer showing the degree of current saturation with respect to the effective field.....	163
6.12	Optical absorption spectra of devices with P3HT:N- MWCNT photoactive layer materials.....	166
6.13	Raman spectra of P3HT:N-MWCNT photoactive layers showing unchanged profiles for varying mass content of N-MWCNTs.....	167
6.14	Dark current $J - V$ plots (a) P3HT only (b) P3HT:N-MWCNT linear scale (c) P3HT:N-MWCNT linear scale semi-log scale.....	168
6.15	$J - V$ characteristics of P3HT:N-MWCNTs at 100 mW/cm ² (AM1.5) in (a) linear and (b) semi-log scale.....	169
6.16	FN plots for P3HT:N-MWCNTs as the photoactive layer in fabricated devices showing the prominence of thermionic emission.....	171
6.17	RS plots for P3HT:N-MWCNTs showing characteristic thermionic emission profiles.....	171
6.18	Log-log plots of $J - V$ characteristics of P3HT:N-MWCNTs indicating a higher Ohmic to SCLC threshold voltage for the 0.50 mg N-MWCNT.....	172
6.19	Linear fit of J_{sc} vs V^2 for P3HT:N-MWCNTs based on the Mott-Gurney law.....	173
6.20	Variation of (a) V_{oc} and (b) J_{sc} with light intensity to determine recombination parameters.....	174

6.21 Optical images of (a) P3HT:PC₆₁BM (b) P3HT:PC₆₁BM:N-MWCNT(0.13 mg) (c) P3HT:PC₆₁BM:N-MWCNT(0.25 mg) (d) P3HT:PC₆₁BM:N-MWCNT(0.50 mg).....175

List of tables

4.1	Prepared mass ratio samples showing individual P3HT and PC ₇₁ BM masses that make up the P3HT:PC ₇₁ BM active layer blend together with the volume of chlorobenzene (C ₆ H ₅ Cl) they were dissolved in.....	71
4.2	Rectification ratios for varying P3HT:PC ₇₁ BM mass ratios.....	75
4.3	A summary of the performance of the OPV devices with varying P3HT:PC ₇₁ BM mass ratios.....	77
4.4	A comparison of recombination (n and α) parameters and mobility (μ) values for different P3HT:PC ₇₁ BM active layer mass ratio blends.....	83
4.5	Comparison of mass ratio based maximum exciton generation rates and saturation current densities.....	86
4.6	Assignment of spectral features of the P3HT:PC ₇₁ BM Raman spectra.....	89
4.7	Performance parameters of the P3HT:PC ₇₁ BM OPV devices at different annealing temperatures.....	94
4.8	A comparison of light ideality factors (n), charge carrier mobility (μ) values and recombination types (α) at short circuit conditions for different annealing temperatures.....	101
4.9	Performance parameters of the P3HT:PC ₇₁ BM OPV devices at different annealing times for the GLASS/ITO/PEDOT:PSS/P3HT:PC ₇₁ BM/Al devices.....	107
4.10	A comparison charge carrier mobilities and recombination parameters for GLASS/ITO/PEDOT:PSS/P3HT:PC ₇₁ BM/Al devices annealed at 50 °C for varying anneal times.....	115

5.1	Rectification ratios of fabricated ternary devices.....	131
5.2	Performance parameters of OPV devices with different ratios of fullerene (C60) derivatives in the active layer.....	133
5.3	Average values for charge carrier mobilities and recombination parameters of ternary blends.....	140
5.4	Saturation current densities and maximum exciton generation rates for ternary blends.....	141
6.1	Rectification ratios for N-MWCNT loadings in P3HT:PC ₆₁ BM.....	153
6.2	Summary of the performance of fabricated OPV devices with varying N-MWCNT concentrations with the masses, in mg, of loaded N-MWCNTs shown next to the device label.....	154
6.3	Recombination parameters at open circuit voltage and short circuit current conditions with a charge mobility trend.....	160
6.4	Rectification ratios for P3HT:N-MWCNT devices.....	167
6.5	Summary of <i>J</i> - <i>V</i> performance characteristics of P3HT:N-MWCNT devices.....	169
6.6	Recombination parameters for light intensity measurements together with mobilities.....	174

List of symbols and abbreviations

Al	Aluminium
BHJ	Bulk heterojunction
FF	Fill factor
FN	Fowler-Nordheim
HOMO	Highest occupied molecular orbital
IPV	Inorganic photovoltaic
ITO	Indium tin oxide
J_{sc}	Short circuit current density
LUMO	Lowest unoccupied molecular orbital
OPV	Organic photovoltaic
OSC	Organic solar cell
P3HT	Poly (3-hexylthiophene 2,5 diyl)
PC ₆₁ BM	[6,6]-phenyl-C61 butyric acid methyl ester
PC ₇₁ BM	[6,6]-phenyl-C71 butyric acid methyl ester
PCE	Power conversion efficiency
PEDOT:PSS	Poly(3,4-ethylenedioxythiophene)-polysyrenesulphonate
PF	Poole-Frenkel
PV	Photovoltaic
R_s	Series resistance
R_{sh}	Shunt resistance
RS	Richardson-Schottky
SCLC	Space charge limited current
TFSCLC	Trap free space charge limited current
V_{oc}	Open circuit voltage
ϵ_r	Dielectric constant
ϕ_B	Potential barrier

Chapter 1

Introduction

1.1 Energy overview

The ever increasing global energy demand continues to place tremendous strain on the predominant primary sources of energy i.e. the dwindling fossil fuel based energy sources. The International Energy Agency's World Energy Outlook 2019 report has shown, amongst other things, that the burning of fossil fuels such as coal, gas and oil accounted for about 81% of the world energy supply in 2018 [1]. It is this burning of fossil fuels that is primarily responsible for the release of harmful and toxic gases which contribute to the degradation of the environment through climate change effects. Furthermore, it is of concern that, in 2018, about 860 million people were still without access to electricity [2], thereby placing an additional burden on the already threatened world flora as a result of cutting down of trees to provide wood for energy needs. The twin effects of decreasing fossil fuel reserves and negative environmental effects, make alternative renewable energy sources desirable if not necessary. However, locally the situation replicates the global scenario. Evidence adduced from Figures 1.1 and 1.2 illustrates that renewable energy systems have not gained sufficient traction to effectively address the concerns raised by the usage of fossil fuels as primary energy sources.

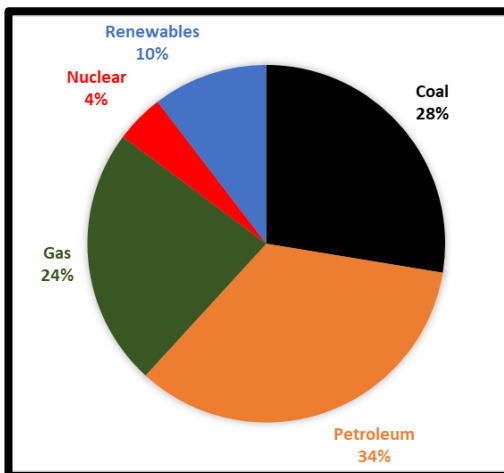


Figure 1.1: World energy consumption – 2017 [3]

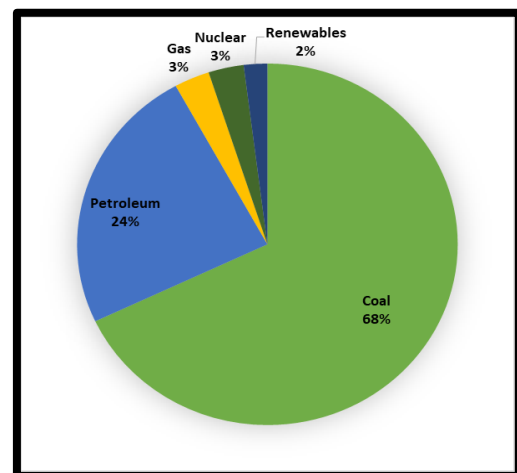


Figure 1.2: South Africa - 2017 energy consumption [4]

Renewable energy sources include solar, wind, hydro, geothermal and biomass/biogas based energies. Among these alternatives, solar energy stands out as the suitable candidate due to its high potential and sustainable availability (limitless). The average annual solar energy input on Earth by far exceeds the world's average annual energy consumption [5]. With regards to solar energy, the sun's energy can be tapped in either a passive or active manner. The difference being the usage of the sun's heat energy or its radiation (irradiance) that is then converted to electricity. Active solar technologies are those that are based on thermal collectors and photovoltaic (PV) devices.

The technology of employing photovoltaic (PV) materials in the harnessing of sunlight for conversion into electrical energy gained prominence in the mid-1950s when it was discovered that silicon created an electric charge when exposed to sunlight [6]. The widespread usage of photovoltaic systems has not been adequately realised in that commercial photovoltaic systems, which are made of inorganic materials, primarily silicon, have high manufacturing costs. The challenge therefore remains to develop technologies that make the photoconversion processes of sunlight into electricity easy to carry out, highly efficient and exceedingly cost effective. The global PV power potential shown in Figure 1.3 places South Africa at an advantage with respect to solar insolation endowment and this should provide the necessary impetus for the research and development of PV technological systems.

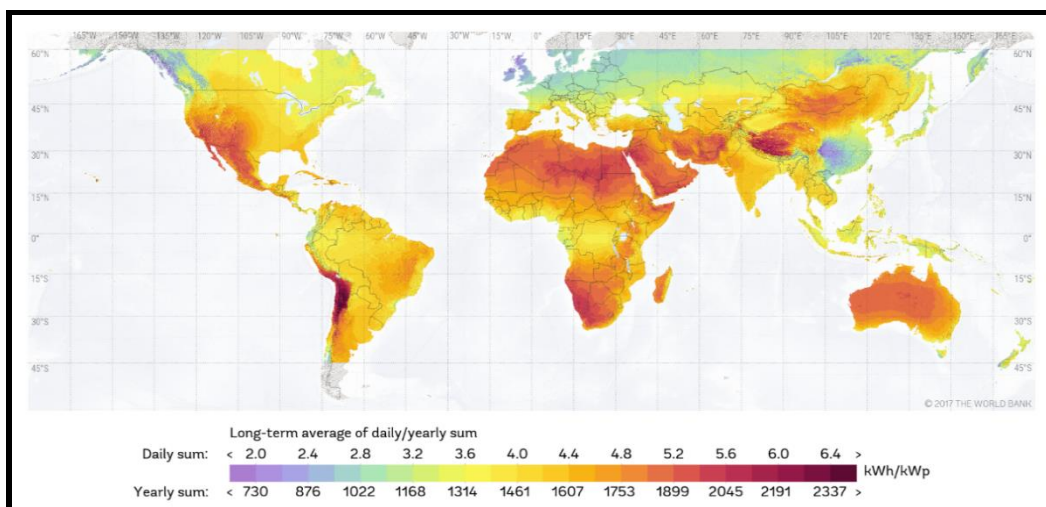


Figure 1.3: Global PV power potential [7].

1.2 Development of photovoltaics devices

Conventionally, photovoltaics devices (solar cells) have been categorised into three, time or sequence dependent, generations indicating the order of which a particular generation became prominent [8]. Lately, a fourth generation has been suggested, the details of which will be explained after a brief discussion on the conventional three generations. It should be noted though that in many instances the descriptions that are classified as fourth generation are still referred to as third generation in many texts. All these generations, briefly summarised below, have their own pros and cons.

1.2.1 First Generation

First generation (1G) solar cells are single junction, large-scale solar cells based on silicon technology. These solar cells were manufactured using monocrystalline (mono c-Si), polycrystalline (poly c-Si) or amorphous silicon. These types of solar cell account for about 80% of the photovoltaics market [9]. They have high power conversion efficiencies that are approaching the theoretical, Shockley–Queisser based, limit of 33%. State of the art devices are exhibiting efficiencies of about 26% [10]. The high manufacturing costs that used to be associated with the processing of silicon have seen a dramatic reduction. However, further cost reductions are held back by the challenge to reduce the thickness of c-Si but retaining crystallinity at the same time [11].

1.2.2 Second Generation

With the cost factors identified in relation to the 1G solar cells identified as obstacles to optimal photovoltaic commercialisation, research and development efforts were then directed at different technologies to find a remedy. This resulted in the development of second generation (2G) solar cells that were based on the thin film technology. These 2G solar cells had light absorbing layers in the order of about 1 μm as opposed to the 1G solar cells which had light absorbing layers of up to 350 μm [12]. The manufacturing of 2G solar cells could also be done quickly and

easily at temperatures lower than those associated with 1G solar cells. The requirement of thinner films meant that less material was required for fabrication thereby reducing costs even further. Prevalent amongst the 2G solar cells have been cadmium telluride (CdTe) and copper indium gallium selenide (CIGS) with power conversion efficiencies of about 21% and amorphous silicon clocking in at about 10% [10]. These thin film solar cells have lower production costs coupled with good efficiencies. However, they have some drawbacks. Chief amongst these are the scarcity and high cost of indium and the toxicity associated with cadmium [9]. The accumulation of cadmium (heavy metal) in human bodies, animals and plants portends adverse effects, making it undesirable for widespread usage [13 – 14].

1.2.3 Third Generation

The inadequacy of the 2G solar cells in addressing the shortcomings of the 1G type meant that there was further room for innovation and development. The driving force in this development has been further reduction in manufacturing and commercialisation costs, the realisation of higher power conversion efficiencies and a wider spread of photovoltaic applications.

Third generation (3G) solar cells are different from the other two generations as they do not rely on the p-n junction design for the separation of photogenerated charge carriers. This 3G approach is a thin film solar cell technology that uses conductive polymers, small molecules and organic materials for light absorption, charge separation and charge transport. Varieties of solar cells that are included in this category are:- nanocrystalline solar cells, photo-electrochemical (PEC) cells such as Grätzel Cells or dye-sensitized solar cells (DSSCs), hybrid solar cells, organic or polymer solar cells (planar heterojunction, bulk heterojunction and ternary), Perovskite solar cells and multi-junction cells. These solar cells are, in general, solution processable, thin film based and offer an excellent potential for large-scale electricity generation. Environmental or operational stability and power conversion efficiencies of 3G vary according to solar cell type. For example, dye-sensitized solar cells and organic solar cells have reported PCEs of above 11% whereas perovskites have surpassed the 20% mark [10]. With regards to organic

solar cells, low material and processing costs can be seen as a counter to unfavourable PCEs [15].

1.2.4 Fourth Generation

The fourth generation (4G) photovoltaic technology has been developed with the aim of improving opto-electrical properties of low cost thin film photovoltaics. The enhancement of charge transport [16] and an improvement in the optical coupling [17] are to be achieved through the inexpensive solution based fabrication process. The fabrication in this 4G approach is geared towards producing hybrid organic-inorganic photovoltaic devices by incorporating inorganic nanostructures into organic device architectures. These inorganic components have the potential to improve the harvesting of solar energy, the dissociation of charges and the transportation of charge carriers within the photovoltaic device. Given the challenges associated with lifetimes of some of the 3G solar cells, it has also been found that the incorporation of some inorganic nanostructures contributes to their stability and lifetime [18].

1.3 Motivation for Organic Photovoltaic (OPV) research

In section 1.1 a general overview on the world energy status was given and therein the drive towards the search for low cost, high efficiency PV devices with reasonable life expectancy was highlighted in an effort to mitigate growing energy challenges. We pay particular attention to the research in solar energy as an integral part of the renewable and clean energy initiatives. Our focus is specifically on the research and development of organic photovoltaics as an energy source.

Organic materials, unlimited in their availability, hold the promise towards the development of an economically viable, large-scale energy source that is safe for the environment. The OPV technology is based on the physics of organic semiconductors. Organic semiconductors afford a less expensive alternative to inorganic semiconductor technology. They offer band gap tunability and have very high optical absorption coefficients making them ideal for thin film solar cells, thereby requiring small amounts of materials for fabricating devices. They are

processable over large areas at low temperatures, and they provide possibilities of fabricating light and flexible devices through processes such as vacuum deposition, stamping, solution casting and ink-jet printing. Well established printing techniques based on the roll-to roll process can be employed in fabricating devices at a very high throughput [19 – 20].

Thus far, the major factor that drives research in organic photovoltaics (OPVs) is the favourable production cost of versatile organic active layers, particularly when compared to inorganic semiconductor based photovoltaic devices. However, the attractiveness of any PV device for commercialisation purposes is reviewed against the backdrop of three factors viz. cost, efficiency and lifetime [21]. The relationship between these factors and the organic PV *versus* inorganic PV (IPV) is elucidated in the so-called Brabec triangle shown in Figure 1.4. It is instructive to note that indicated thereon is the fact that organic photovoltaics have lower power conversion efficiencies and shorter lifetimes as compared to inorganic photovoltaics making them suitable for consumer electronics.

The power conversion efficiency is the ratio of the output power to the input power (more detail in Chapter 2). The comparison of solar cell efficiencies in Figure 1.5 clearly indicates the status of OPVs in as far as their efficiency roadmap is concerned. The upward trend in the curve relays a promising message that further development can be and should be maintained.

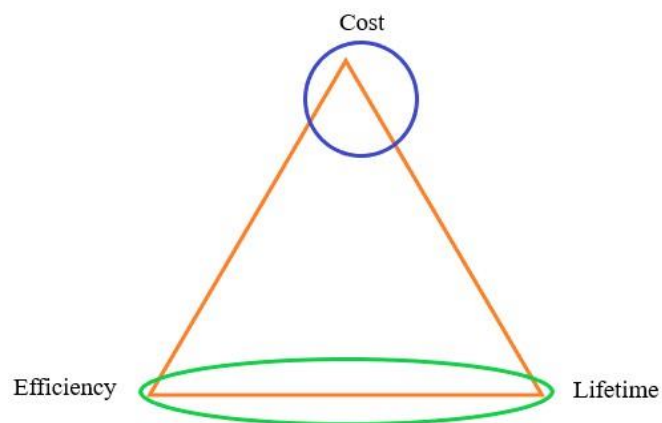


Figure 1.4: Brabec triangle with OPVs in blue and inorganic PVs in green. IPVs are seen to be dominating efficiency and stability concerns whereas OPVs dominate concerns related to production costs [22].

With regards to lifetimes of OPVs, the process to accurately determine their lifetime improvements is still a major challenge. Coordinated efforts through platforms such as the **International Summit on Stability of Organic and Perovskite Solar Cells (ISOS)** continue to shape baselines, benchmarks and standards in as far as gauging the stability and lifetime of OPVs is concerned.

It is a commonly held view that operational stability of up to 5 years is a reasonable basis for lifetime determination of organic solar cells, especially for domestic based electronic appliances and consumer electronics [23, 24]. However, it should be noted that, on a comparative scale, OPVs have relatively poor lifetimes especially when held up against silicon-based inorganic PVs. For example, on a T80 standard, where manufacturers offer a 25 year warranty for crystalline silicon solar cells, it means that the power output should not be less than 80% of rated power after 25 years of operation. On the other hand, large scale OPV modules operating outdoors have been reported to be having lifetimes of about 2 years [24]. This highlights one of the obstacles towards widespread outdoor usage that OPVs have encountered, given that at current power conversion efficiencies, lifetimes of about 5 years are needed to successfully bring OPVs into the market as competitive photovoltaic products [25].

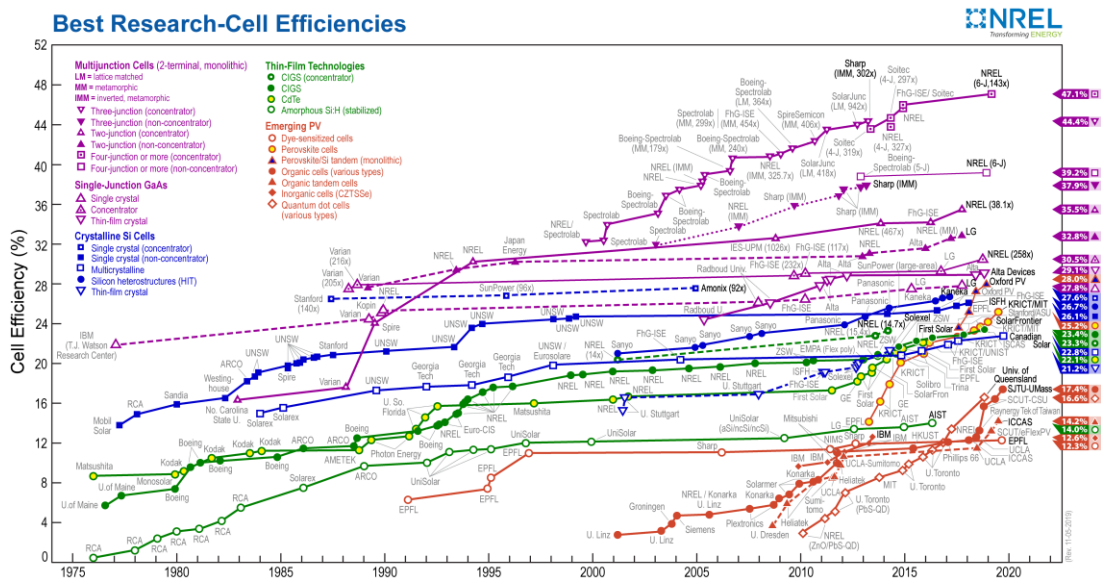


Figure 1.5: Overview of highest efficiencies in different PV technologies [26]

In relation to the three factors, as indicated in the Brabec triangle, that are pivotal in the development of OPV technologies, this project will focus on the power conversion efficiencies of OPV devices and this will be done by studying the fabrication and performance of a variety of solution processed polymer:fullerene solar cells.

1.4 Aim and objectives

1.4.1 Aim

The aim of this project is to gain a deeper understanding and to add to the knowledge base of the fabrication regimes of solution processed polymer:fullerene bulk heterojunction photovoltaic devices under ambient conditions with a particular focus on related power conversion efficiencies. Electrical and optical behaviour of fabricated devices is systematically characterised to establish whether materials that make up the devices and their configuration, enhance or degrade their performance.

1.4.2 Objectives

- To benchmark and streamline the solution-based fabrication processes of polymer:fullerene bulk heterojunction photovoltaic devices under ambient conditions.
- To fabricate P3HT:PC₇₁BM bulk heterojunction photovoltaic devices and to establish the effect of the variation of the fullerene derivative mass ratio on their optical and electrical characteristics.
- To gauge the power conversion efficiencies of fabricated ternary bulk heterojunction organic photovoltaic devices based on the donor:acceptor1:acceptor2 active layer configuration through the determination of the optimum relative ‘acceptor’ ratios for a constant donor content and to characterise related electro-optical absorption properties.
- To investigate the feasibility and effectiveness of incorporating varying concentrations of nitrogen-doped multi-walled carbon nanotubes (N-MWCNTs) in the active layers of fabricated polymer:fullerene devices and

to describe resultant photovoltaic performances of these devices by determining the effects of such concentrations on key figures of merit.

1.5 Thesis outline

Chapter 1 provides a general view on the global energy scenario. The chapter also outlines the motivation, aims and objectives of this thesis.

Chapter 2 presents the theoretical framework of this research work. The chapter reviews the semiconductor theory by focussing on the physics of organic semiconductors. The electronic band structure also forms the basis of the elucidation on the working mechanism of an OPV device. Key performance parameters of OPV devices and charge carrier dynamics are explained by summarising related $J - V$ characteristics.

Chapter 3 discusses the materials used and the method followed in the fabrication of a typical BHJ OPV device. Any unique additive to this generic device will be dealt with in the chapter concerned.

Chapters 4 – 6: These chapters are based on the fabrication of different architectures of BHJ OPV devices. The chapters give an account of the study of what is considered the most important figure of merit in describing the performance of solar cells i.e. the power conversion efficiency (PCE). The PCE of these devices is studied against the backdrop of extensive optical and electrical characterisation. Device dependent $J - V$ characteristics are established and linked to performance determining parameters such as the short-circuit current density (J_{sc}), the open-circuit voltage (V_{oc}) and the fill factor (FF). Furthermore, $J - V$ measurements, in the dark and under illumination are discussed in the description of charge carrier dynamics. Light intensity analysis is carried out to describe dominant recombination mechanisms under short

and open circuit conditions. Fowler-Nordheim (FN) field emission, Richardson-Schottky thermionic emission and space charge limited current (SCLC) models are made use of in the description of charge injection and bulk charge transport in different BHJ OPV devices.

- Chapter 4** describes the search for the optimum mass ratio of the BHJ P3HT:PC₇₁BM photovoltaic devices by varying the mass of PC₇₁BM.
- Chapter 5** reports on the fabrication of ternary BHJ OPV devices using P3HT:PC₆₁BM:PC₇₁BM as the active layer blend. The best performing device is identified by varying the PC₆₁BM:PC₇₁BM ratio.
- Chapter 6** gives an account of the photovoltaic performance with different mass loadings of N-MWCNTs in the P3HT:PC₆₁BM based BHJ OPV devices.
- Chapter 7** gives a general summary and concludes the thesis. Possible recommendations emanating of this work are also given.

1.6 References

- [1] IEA (2019). *World Energy Outlook 2019*, (OECD Publishing), Paris.
- [2] www.iea.org/sdg/electricity/ [accessed 28/11/2019].
- [3] Elavarasan, R.M. (2019). *European Journal of Sustainable Development Research* 3 (1), em0076.
- [4] British Petroleum Company (2018). *BP statistical review of world energy*, (British Petroleum Co.) London.
- [5] Wohrle, D. and Meissner, D. (1991). *Advanced Materials* 3 (3), 129.
- [6] Chapin, D.M., Fuller, C.S. and Pearson, G.L. (1954). *Journal of Applied Physics* 25 (5), 676.
- [7] https://www.worldenergy.org/wpcontent/uploads/2013/10/WER_2013_8_Solar_revised.pdf [accessed 30/12/2017].
- [8] Bagnall, D.M. and Boreland, M. (2008). *Energy Policy* 36 (12), 4390.
- [9] Ranabhat, K, Patrikeev, L., Revina, A.A., Adrianov, K. and Sofronova, E. (2016). *Journal of Applied Engineering Science* 14 (4), 405, 481.
- [10] Green, M.A., Dunlop, E.D., Levi, D.H., Hohl-Ebinger, J., Yoshita, M. and Ho-Baillie, A.W.Y. (2019). *Progress in Photovoltaics: Research and Applications* 27 (7), 565.
- [11] Hasegawa, K., Takazawa, C., Fujita, M., Noda, S. and Ihara, M. (2018). *CrystEngComm* 20 (13), 1774.
- [12] Chopra, K.L., Paulson, P.D. and Dutta, V. (2004). *Progress in Photovoltaics: Research and Applications* 12 (2 - 3), 69.

- [13] Luque, A. and Hegedus, S. (2003). *Handbook of Photovoltaic Science and Engineering 2nd Edition*, John Wiley & Sons, Ltd., Hoboken.
- [14] Elsabawy, K.M., El-Hawary, W.F. and Refat, M.S. (2012). *International Journal of Chemical Sciences* **10** (4), 1869.
- [15] Krebs, F.C. (2008). *Polymer Photovoltaics: A Practical Approach*. SPIE Press, Bellingham, Washington.
- [16] Nismy, N.A., Adikaari, A.A.D.T. and Silva, S.R.P. (2010). *Applied Physics Letters* **97** (3), 033105.
- [17] Gilot, J., Barbu, I., Wienk, M.M. and Janssen, R.A.J. (2007). *Applied Physics Letters* **91** (11), 113520.
- [18] Sun, Y.M., Takacs, C.J., Cowan, S.R., Seo, J.H., Gong, X., Roy, A. and Heeger, A.J. (2011). *Advanced Materials* **23** (19), 2226.
- [19] Shaheen, S.E., Radspinner, R., Peyghambarian, N. and Jabbour, G.E. (2001). *Applied Physics Letters* **79** (18), 2996.
- [20] Gustafsson, G., Cao, Y., Treacy, G.M., Klavetter, F., Colaneri, N. and Heeger, A.J. (1992). *Nature* **357** (6378), 477.
- [21] Brabec, C.J. (2004). *Solar Energy Materials and Solar Cells* **83** (2–3), 273.
- [22] Brabec, C.J., Sariciftci, N.S. and Hummelen, J.C. (2001). *Advanced Functional Materials* **11** (1), 15.
- [23] Azzopardi, B., Emmott, C.J.M., Urbina, A., Krebs, F.C., Mutale, J. and Nelson, J. (2011). *Energy and Environmental Science* **4** (10), 3741.

- [24] Jørgensen, M., Carlé, J.E., Søndergaard, R.R., Lauritzen, M., Dagnæs-Hansen, N.A., Byskov, S.L., Andersen, T.R., Larsen-Olsen, T.T., Böttiger, A.P.L., Andreasen, B., Fu, L., Zuo, L., Liu, Y., Bundgaard, E., Zhan, X., Chen, H., Krebs, F.C. (2013). *Solar Energy Materials and Solar Cells* **119**, 84.
- [25] Roth, B., dos Reis Benatto, G.A., Corazza, M., Søndergaard, R.R., Gevorgyan, S.A., Jørgensen, M., Krebs, F.C. (2015). *Advanced Energy Materials* **5** (9), 1401912.
- [26] <https://www.nrel.gov/pv/> [accessed 25/11/2019].

Chapter 2

Theoretical aspects

2.1 Overview of organic semiconductors

The ability to conduct electricity is the basis upon which materials are classified as conductors, semiconductors or insulators. Typical insulators have high electrical resistivity values that are in the order of $1 \times 10^{13} \text{ } \Omega \cdot \text{m}$ and conductors have very low electrical resistivities of about $1 \times 10^{-6} \text{ } \Omega \cdot \text{m}$. Semiconductors, which are neither good insulators nor good conductors have intermediate resistivity values. However, with doping strategies, the resistivity can be tuned for electronic applications.

Semiconductors can thus be classified broadly into two, namely inorganic and organic semiconductors. A difference between these types of semiconductors that can be highlighted is in electron transport, for which organic semiconductors, more often than not, exhibit localised charge transport or phonon assisted variable range hopping (VRH). Organic semiconductors are organic materials that exhibit semiconducting properties with strongly bound excitons (Frenkel) due to their low dielectric constant. These materials are generally categorised into two major classes, i.e. polymers and small molecules [1]. Polymers, sometimes referred to as macromolecules, are molecules that are made up of monomers or repeating structural units and are usually very large in size. A typical, often referred to example of a polymer is **Polyacetylene**, the simplest linear synthetic polymer (Figure 2.1). A characteristic feature of organic semiconductors is the presence of conjugation in their structures. Conjugation refers to the alternating single and double bonds between adjacent carbon atoms as can be seen in Figure 2.1.

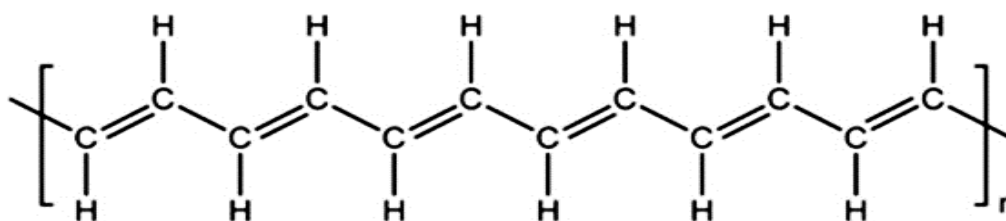


Figure 2.1: A segment of polyacetylene showing conjugation [2].

The configuration of electrons of atomic carbon in the ground state is represented as $\{1s^2 2s^2 2p^2\}$, meaning that four electrons occupy the 2s and 2p valence orbitals whereupon these can accommodate a maximum of 8 electrons or octet stability. The mechanism of hybridization in the carbon atom leads to the following three possible scenarios:

- sp hybridization: in this case only the 2s and one of the 2p orbitals hybridize to form two sp orbitals that form an angle of 180° with each other. The remaining 2p orbitals are oriented in a plane that is orthogonal to these hybridized orbitals. The formation of a triple bond can then be realised through the sp orbital forming a σ – bond with the remaining two 2p orbitals forming π – bonds.
- sp^2 hybridization: consider each carbon, one 2s orbital and two 2p orbitals hybridize to form three sp^2 orbitals that are aligned in a trigonal planar structure having an angle of 120° between the three orbitals with the remaining 2p in an orthogonal plane. The carbon atoms exhibit a double bond when they bond in this manner. The sp^2 orbitals form σ – bonds while the remaining 2p orbitals overlap and lead to the creation of weaker π – bonds. This type of hybridization is demonstrated much clearer by using ethene as an example in Figure 2.2.
- sp^3 hybridization: the 2s and the three 2p orbitals form sp^3 hybrid orbitals with four σ – bonds around each carbon atom configured at angles of 109.5° which can be seen as pointing at vertices of a regular tetrahedron.

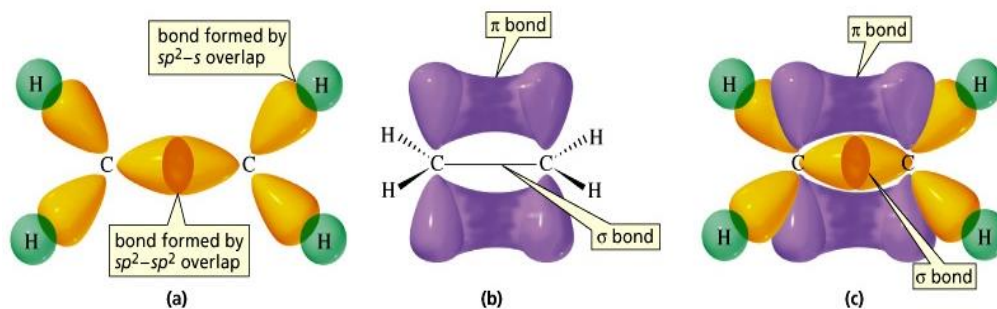


Figure 2.2: Ethene Lewis structure including the sp^2 hybridized orbital structure. (a) Double bonded carbon atoms with overlapping σ – orbitals and interacting π – orbitals. (b) Delocalised π – electrons. (c) Overview of complete orbital structure of ethane [3].

All organic semiconductors owe their electrical properties to conjugated π – electrons. The closeness of π – bonds in conjugated systems means that their wave functions overlap and π - electrons can hop along the conjugation path. This overlapping of π - orbitals is analogous to the band structure of inorganic semiconductors that is characterised by two energy levels that are separated by a region of forbidden energies, namely the conduction and the valence band. When it comes to conjugated systems, Peierls instability leads to the formation of two delocalised energy bands, the bonding (π) and the antibonding (π^*) orbitals, which are also known as the highest occupied molecular orbital (HOMO) and the lowest unoccupied molecular orbital (LUMO) respectively [4]. These energy bands are separated by a gap of about one to three electron volts, right in the range of semiconductors with all their related properties. These include, light absorption or luminescence in the visible, near infrared or near ultraviolet range of the electromagnetic spectrum [5]. The properties of these materials have made them attractive for applications in optoelectronic devices such as field effect transistors (FETs) [6, 7], light emitting diodes (LEDs) [8, 9] and solar cells [10, 11].

2.2 The bulk heterojunction (BHJ) OPV concept

The description of the BHJ concept, which will be given in this section, will be preceded by a brief overview of the photovoltaic phenomenon. In order to provide a basis to the discussion in the results chapters, we shall focus our discussion on the working principles of organic solar cells.

In semiconductors, incident light absorption by charge carriers i.e. electrons and holes leads to the generation of photocurrent. As a general description, a photovoltaic cell is a semiconductor diode that is designed to separate and collect charge carriers and ultimately conduct the generated photocurrent in a specific direction (in an asymmetric manner) [12].

An organic photovoltaic (OPV) cell consists of a photoactive region that is sandwiched between two electrodes with different workfunctions i.e. electrodes with dissimilar energy differences between their respective Fermi levels and vacuum levels. One of the electrodes has to be transparent to allow incoming light to reach the photoactive region. Charge carriers, such as electrons and holes, generated initially as Coulombically bound electron-hole pairs (excitons) in the photoactive region under the influence of incident light, are separated and collected at both electrodes. In this way, photons are converted into electricity.

Whereas p – n heterostructures are characteristic of inorganic semiconductor electronic and optoelectronic devices, the physics governing the operation of OPV devices is based on the utilisation of electronically dissimilar materials in the photoactive region. The photoactive region in OPV devices generally contains two components or materials with different electronic levels i.e. different lowest unoccupied molecular orbit (LUMO) and highest occupied molecular orbit (HOMO) levels. One is an electron-donating material (the donor with active electronic transitions in the LUMO) and the other one an electron-accepting material (the acceptor, hole transitions in the HOMO). Conjugated polymers, due to their strong photo-absorption qualities, have been prominent materials of choice to act as electron donors in OPV devices. Whilst on the other hand, fullerenes or fullerene derivatives, with their high electron affinities, are commonly used as electron acceptors.

When photons strike the absorber material, commonly the donor material, it excites electrons into its LUMO, thereby creating strongly bound electron-hole pairs called Frenkel excitons. These strongly bound excitons have to overcome their binding energies (typically 0.5 – 1.0 eV) to dissociate into free charge carriers, failure to which recombination will take place resulting in loss of photocurrent.

To harness this solar energy, a model was reported in 1959, where anthracene, an organic material was sandwiched between two electrodes of different workfunctions, as illustrated in Figure 2.3, to create a single layer OPV device [13]. This single junction device exhibited very high charge recombination since the exciton creation and dissociation were taking place in the same material. As a result very low, much less than 1%, power conversion efficiencies were realised.

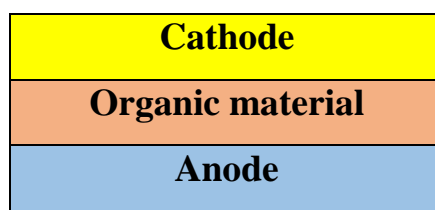


Figure 2.3: A schematic of a single layer OPV device.

Our consideration of organic solar cells that began to breach the 1% PCE mark makes it necessary, at this point, that we distinguish two main types of organic heterojunctions i.e. the planar bilayer heterojunctions and the three dimensional bulk heterojunctions (Figure 2.4) that were introduced sequentially, in order to address the shortcomings of the single layer device.

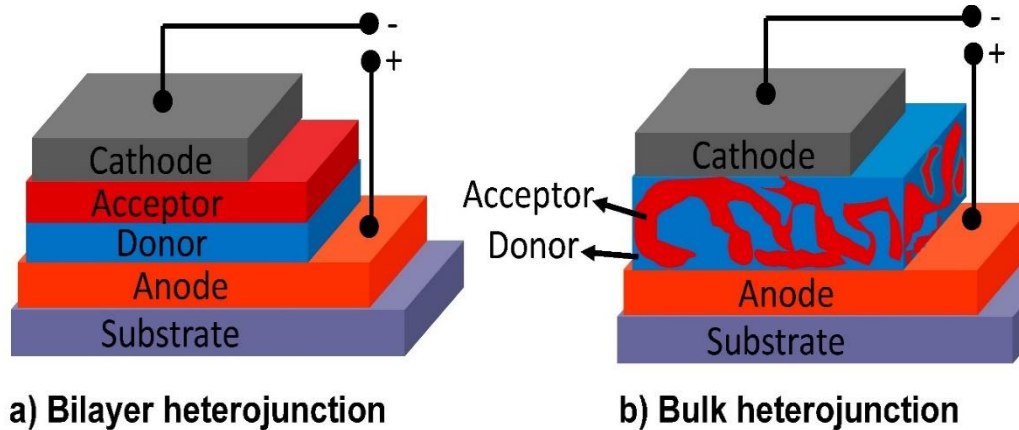


Figure 2.4: Typical donor:acceptor OPV heterojunction structures showing a) the planar bilayer heterojunction OPV structure and b) the bulk heterojunction structure [14].

Noting that once excitons are generated, the electron – hole pair needs to be separated before recombination, C.W. Tang [15] fabricated the first OPV devices based on a bilayer heterojunction structure. Two electronically different organic semiconductors namely copper phthalocyanine and perylene derivative (CuPc:PV) were sandwiched between two dissimilar electrodes. This new device configuration surpassed the 1% PCE mark. The creation of the donor:acceptor photoactive region meant that two materials with different electron affinities created an energy offset at their interface. This offset provided the driving force for excitons to dissociate into free charge carriers. The dissociation into free carriers at the donor:acceptor interface requires the diffusion of the excitons to the donor:acceptor interface. However, the diffusion of excitons is governed by finite lifetimes (usually in the picosecond time scales) and finite diffusion lengths (10 nm) [16, 17]. So, excitons that fail to reach the interface will decay and there will be no free charges to create an electrical current. With the requirement of a sufficiently thick photoactive region, of about 100 nm, to absorb light efficiently, the diffusion of excitons in the bilayer configuration becomes an impediment as a comparatively small fraction of excitons tends to be generated within the 10 nm distance from the donor:acceptor interface.

The absorption *versus* exciton diffusion conundrum in bilayer OPV devices was addressed by the introduction of the bulk heterojunction (BHJ) approach in OPV device fabrication. Aided by the property of organic semiconductors that sees them being soluble in readily available organic solvents, an intimate mixture of the donor and the acceptor materials was formulated as a way of maximising the interface and minimising the distance the exciton must travel to reach an interface. Furthermore, the blending of donor and acceptor materials into a single photoactive layer demonstrated the attractiveness of solution processing of OPV devices. Solution processing meant that OPV devices could be fabricated much more easily, with higher throughputs. Reports emerged in 1995 of the first solution processed OPV device. The photoactive layer of the OPV device was fabricated by blending polymers MEH-PPV and cyano-PPV (CN-PPV) as donor and acceptor materials and reached external quantum efficiencies up to 6% [18, 19]. This improvement in spectral response still produced devices with a power conversion efficiency (PCE) of less than 1 %. Lately, the blending of a polymer such as poly (3-hexylthiophene) (P3HT) and a small molecule [6,6]-phenyl C61 butyric acid methyl ester (PCBM) or some other C₆₀ derivative, have found common usage as donor and acceptor materials respectively.

2.3 Physics of organic photovoltaic devices

In this section, a background on the key processes that govern the working of organic solar cells shall be presented. The polymer:fullerene BHJ structure will largely form the basis of the descriptions provided.

2.3.1 Light absorption and exciton creation

As seen in previous sections, organic semiconductors have high absorption coefficients thereby requiring far less material to absorb light (~100 nm thickness). Generally, in polymer:fullerene i.e. (donor:acceptor) OPV devices, most of the incident light is absorbed by the donor polymer. Thickness dependent absorption coefficients in the order of 10^5 cm^{-1} readily characterise light absorption properties of these materials. However, most semiconducting polymers have bandgaps too

high, more than 2.0 eV (600nm), limiting the possible absorption to about 30%. For example, with the Air Mass 1.5 (AM1.5) standard solar spectrum as a reference, the electron donor, P3HT, has a coverage of 30% [20]. The optimum bandgap for a PV device based on a single light absorbing medium is 1.1 eV.

The relative absorbances of the donor and acceptor materials, individually and in a blend, are compared to the AM1.5 solar spectrum in Figure 2.5. Noting that the AM1.5 standard solar spectrum provides the intensity of solar radiation in W/m^2 for each wavelength.

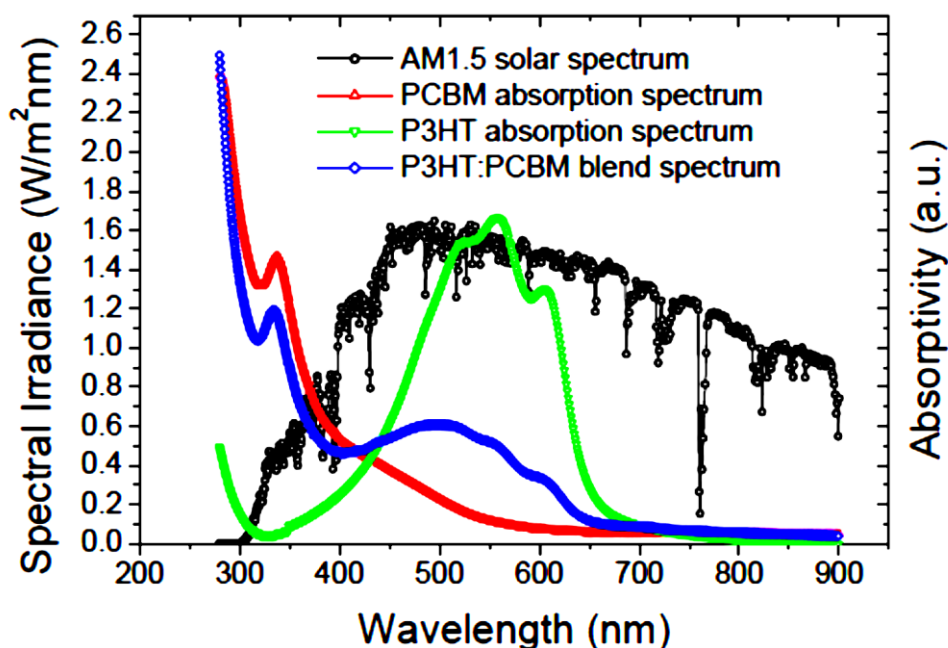


Figure 2.5: Comparison of absorption spectra of the components of the photoactive layer with the AM1.5 solar spectrum [21].

The absorption of incident light of sufficient energy by an organic semiconducting material results in an electron being promoted into the LUMO level thus leaving behind a hole in the HOMO level. As previously stated, one of the most pronounced differences between inorganic and organic materials is their response to photoexcitation. Photoexcitation in organic materials does not automatically lead to the generation of free charge carriers, instead it leads to Coulombically bound electron-hole pairs known as excitons. This comes about as a result of low dielectric constants ($\epsilon_r \approx 3-4$) compared to most inorganic semiconductors ($\epsilon_r > 10$).

Whereas Mott–Wannier excitons are generated in inorganic semiconductors with binding energies of around 25 meV (300 K), Frenkel excitons with binding energies in the 500 meV range are predominantly generated in organic semiconductors. In comparison to the latter excitons, the former have larger electron – hole spacings that extend over many molecules (delocalized) as shown in Figure 2.6.

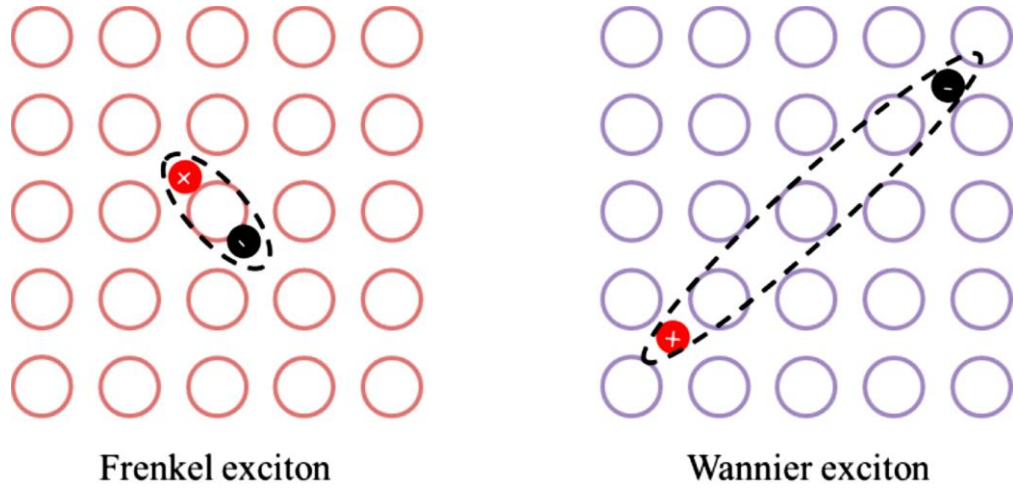


Figure 2.6: An illustration of the Frenkel and Wannier excitons, with an electron in black and a hole in red, showing different spacings [22].

2.3.2 Exciton diffusion

That which is desirable is that the excitons should reach a dissociation interface during their lifetime. Ideally, the diffusion length of the exciton should be equal to the thickness of the photoactive layer. These diffusion lengths are typically in the order of about 10 nm to preclude recombination [23]. However, for sufficient absorption to occur, photoactive layers of about 100 nm are required. To this end, the BHJ structure of OPVs aids immensely in the increase of interfacial donor:acceptor sites thus minimising the diffusion distances of generated excitons.

The exciton diffusion length L_{exct} ,

$$L_{exct} = \sqrt{\tau_{exct} D_{exct}} \quad (2.1)$$

depends on the exciton lifetime τ_{excit} which is in the picosecond range and the diffusion coefficient D_{excit} as shown in Equation (2.1).

It is instructive to reemphasise the desirability of the BHJ structure in the fabrication of an organic photovoltaic device as this trades-off the exciton diffusion lengths, exciton lifetimes and thicknesses of photoactive layers.

2.3.3 Charge separation

Photogenerated excitons that reach the donor:acceptor interface or defects sites can dissociate into free charge carriers i.e. electrons and holes if germinate recombination does not take place. In inorganic semiconductors, weakly bound Wannier (Mott-Wannier) excitons which exhibit binding energies below $k_B T$ (≈ 25 meV at room temperature) are easily separated into free charge carriers upon illumination. Their typical dielectric constants ($\epsilon_r > 10$) lead to a screened Coulomb potential. On the other hand, electrostatically bound electron-hole pairs known as Frenkel excitons are photogenerated in organic photovoltaics. It has already been mentioned that strongly bound Frenkel excitons have comparatively low dielectric constants ($\epsilon_r \approx 3-4$) causing strong Coulomb attraction between respective holes and electrons [24, 25]. To separate excitons with these high binding energies requires fairly large separation between holes and electron. The Coulombic radius r_c defines the equalisation between the binding and separation energies. This is given as,

$$r_c = \frac{e^2}{4\pi\epsilon_r\epsilon_0 k_B T} \quad (2.2)$$

where e is the charge of the free carrier, ϵ_0 is the permittivity of free space, ϵ_r is the dielectric constant of a material, k_B is the Boltzmann constant and T the temperature. Typical r_c values are in the region of about 20 nm.

The other consideration is the Van der Waals interaction. This weak interaction between molecules that results in a small Bohr radius r_B of the relevant charge

carrier. For example, in semiconductors with hydrogen-like wave functions, the Bohr radius of the lowest electronic state is [26]

$$r_B = r_0 \epsilon \frac{m_e}{m_{eff}} \quad (2.3)$$

where the first Bohr radius of an electron of the hydrogen is $r_0 = 0.53 \text{ \AA}$, m_e is the rest mass of the electron and m_{eff} is the effective mass of the electron in a semiconductor. Looking at Equation (2.3), the Bohr radius will be smaller for a lower value of the dielectric constant ϵ_r and a larger effective mass of an electron. A comparison of the two radii, Coulomb and Bohr, can give an indication whether excitons of free charge carriers will be formed upon light absorption. That is, if $r_C > r_B$, then excitons will be formed.

In as far as an assessment of energy levels between the donor and the acceptor is concerned, charge separation at the donor:acceptor interface can occur if the LUMO and HOMO levels of the acceptor (A) and the donor (D), respectively, are misaligned (Figure 2.7) such that the charge transfer from the donor to the acceptor becomes energetically favourable [27]. Therefore, the probability of effective charge separation increases if the energy offset between the LUMOs of the donor and acceptor is greater than 0.3 eV. In short, LUMO – LUMO energy offset between the donor and the acceptor has to be large enough to facilitate electron (e^-) transfer from the donor to the acceptor upon photoexcitation of the donor – acceptor blend and similarly, the HOMO – HOMO energy offset between the donor and the acceptor has to be large enough to facilitate hole (h^+) transfer from the acceptor to the donor.

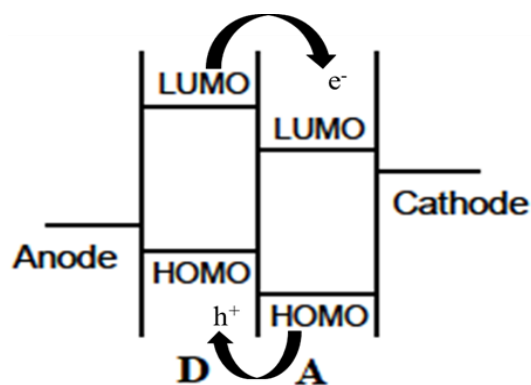


Figure 2.7: Misalignment of the donor and acceptor HOMO – LUMO energy levels for charge separation.

2.3.4 Charge transfer and collection

Separated electrons and holes that reside in the acceptor and donor materials, respectively, are driven through the photoactive layer by a built-in field, a drift via the external electric field and diffusion based on their concentration. However, after separation, the electron and the hole, though residing in two separate materials, are still Coulombically bound due to the weak screening of the electric field in organic semiconductors. This stage, the intermediate state between the initial exciton and the free charge carriers is known as the charge transfer state (CT). The ‘charge transfer state exciton’ is made up of the so called polaron hole and polaron electron. This is a field and temperature dependent state towards the generation of a photocurrent which also influences the fill factor and the short circuit current [28].

The workfunction mismatch of the anode and cathode materials assures the collection of free charge carriers. Furthermore, the workfunctions of the collecting electrodes must, ideally, form Ohmic contacts with the HOMO and LUMO levels of the photoactive materials. The hole collecting electrode must form an Ohmic contact with the HOMO of the donor material whilst the electron collecting electrode must form an Ohmic contact with the LUMO of the acceptor material. The potential barrier at the electrode/active layer interface should be minimised so as not to limit charge collection. A choice of electrodes should therefore take these factors into account.

2.4 Photovoltaic characteristics of an OPV device

An understanding of the performance of organic photovoltaics necessitates a description of the main properties that characterise their photovoltaic properties. This will enable an informed experimental and analytical process that can be geared towards possible changes and improvements.

2.4.1 The current density - voltage ($J - V$) plot and the characteristic performance figures of merit

An analysis of the performance of an OPV device, or a solar cell in general, requires an understanding of its current (I) – voltage (V) characteristics which are determined by the measurement of the current density and voltage parameters, both in the dark and under illumination. The outcome of the measurement is presented by plotting $I - V$ curves or $J - V$ curves as in Figure 2.8 {with $J = I/A$, the current density for performance comparability amongst different devices with A being the active area of the device}, where the device's current or current density, $J(V)$ is measured as a function of applied voltage. The measurement, in the dark and under illumination, of the diode characteristics of the solar cell enables parameters such as the open circuit voltage (V_{oc}), the short circuit current density (J_{sc}), the power conversion efficiency (PCE), the fill factor (FF), series resistance (R_s), shunt resistance (R_{sh}), ideality factors (n), rectification ratios (RR) and charge carrier mobilities (μ) amongst many others, to be extracted directly or derived, for performance analysis. The analysis of the performance of an organic photovoltaic device usually culminates in the main performance evaluation indicator of a solar cell which is described by its power conversion efficiency (PCE). The performance of an OPV device can be expressed through the measurement of:

- The open circuit voltage (V_{oc}),
- The short circuit current density (J_{sc}),
- The fill factor (FF).

These parameters are however dependent on the types of materials used in the fabrication process. This variability means that there is a strong reliance of the microstructure of the donor-acceptor components and the general processing conditions.

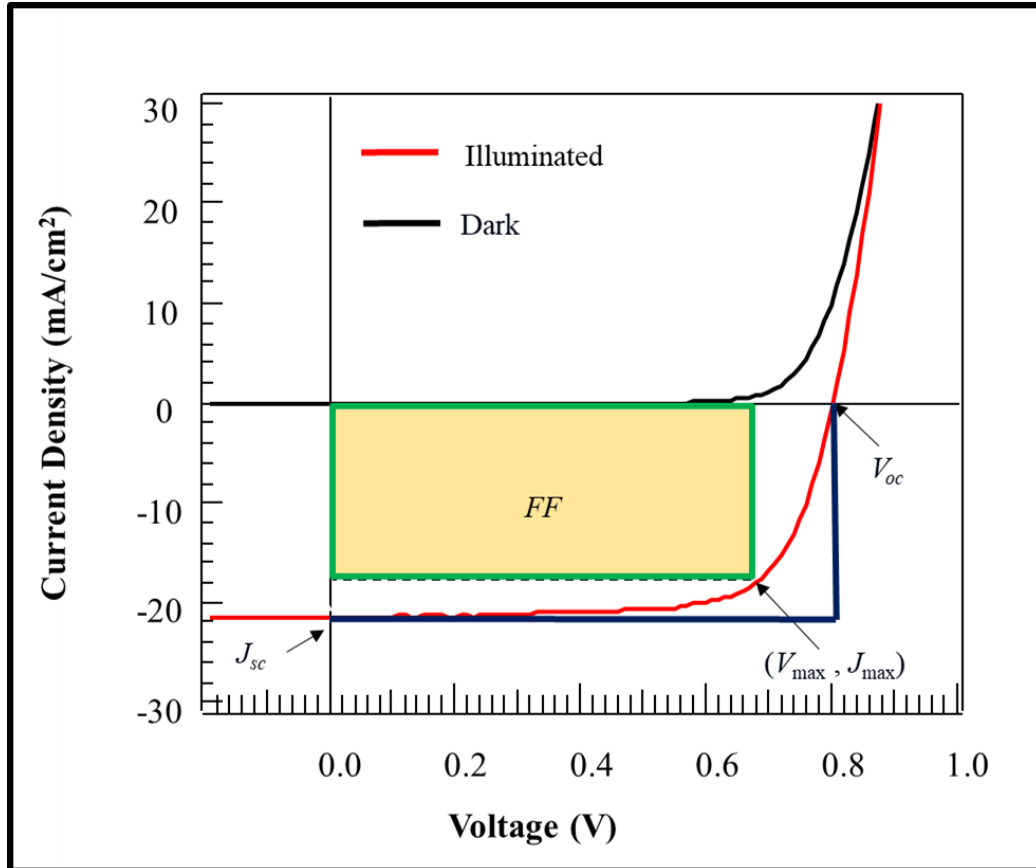


Figure 2.8: Typical $J - V$ curves under dark and illumination conditions. Under illumination, the maximum power density generated by the cell is $P_{\max} = J_{\max} \times V_{\max}$. The FF is defined as the ratio of the area of the green rectangle with respect to the area of the rectangle spanned by the black sides. With this ratio less than unity, P_{\max} also given by $J_{sc} \times V_{oc} \times FF$. means that it is always smaller than $J_{sc} \times V_{oc}$.

- The incident light dependent photovoltaic effect leads to the generation and eventual collection of charge carriers thereby setting up a photocurrent in an organic solar cell. With the current showing a dependence on the illuminated area of the solar cell, it is often practical to consider and make

use of the current density J instead of just the current I in order to remove this dependence in describing the current generated by the solar cell. Readily identified on the $J - V$ curve is the short-circuit current density, J_{sc} . This is the current density when the applied voltage V , is $V = 0$ presenting conditions same as the two electrodes of the cell are being short-circuited. At this point, no power produced by the device but this point marks the onset of power generation. In devices that are free of current limiting factors i.e. ideal devices, the J_{sc} is the same as the photocurrent density J_{ph} .

- Another point of note on the $J - V$ curve is the point where current density $J = 0$. This marks the open-circuit voltage, V_{oc} . The power being the product of current and voltage, is zero at this point but the V_{oc} also marks the boundary for voltages at which devices can produce power. In BHJ OPV devices, the V_{oc} strongly depends on the energy difference between the HOMO of the donor and the LUMO acceptor material. This specifies the energy level offset at the D/A interface of the cell as opposed to the HOMO - LUMO energy gap of the donor material. It has been found experimentally that the V_{oc} values can differ from those determined from the HOMO - LUMO difference. The difference in values can, amongst other factors, depend on the D/A blend morphology and on the material characteristics of electrodes [29].
- The rectangle labelled FF is used to extract the fill factor value of the device. The fill factor gives a relative measure of how much power is produced by an OPV device. That is, it relates the maximum obtainable power given by V_{max} and J_{max} to the ideal power given by J_{sc} and V_{oc} . In other words, it defines the working region (operating point) of the solar cell. Ideally, the FF should equals to unity but parasitic resistances and effects of unfavourable fabrication processes combine to lower its value. The consequence of this is that the fill factor can be viewed as a measure of the quality of the current - voltage characteristic of the solar cell. The fill factor of a solar cell can be determined using the equation:

$$FF = \frac{J_{\max} V_{\max}}{J_{sc} V_{oc}} \quad (2.4)$$

- The power conversion efficiency (PCE) is the most prominent of the characteristic performances figure of merit. The PCE relates the power output P_{OUT} of the device to the power of incident light P_L in the following manner:

$$PCE = \frac{P_{OUT}}{P_L} = \frac{J_{\max} V_{\max}}{P_L} \quad (2.5)$$

with P_L being the incident light power per unit area. From Equation (2.1) the PCE can also be written as

$$PCE = \frac{J_{sc} V_{oc} FF}{P_L} \quad (2.6)$$

2.4.2 Equivalent circuit diagram (ECD)

A solar cell, considered to be a diode, leads to the model that is based on the equivalent circuit diagram in the extraction of its PV characteristics. Let us first consider the case of a solar cell based on an ideal diode (Figure 2.9) behaviour in order to gain a better perspective of the models involved. In this case, the series resistance (R_s) = 0 and the shunt resistance (R_{sh}) = ∞ [30]. These are parasitic resistances in a solar cell that dissipate power leading to a decrease in the efficiency of a solar cell. An exponential relation based on the Shockley ideal diode equation, approximates the dark current I_D as

$$I_D = I_o \left[\exp\left(\frac{qV}{nkT}\right) - 1 \right], \quad (2.7)$$

with $1 < n < 2$. I_o is the reverse dark saturation current, q is the elementary charge, V is the applied voltage, n is the ideality factor, k is Boltzmann's constant and T is the temperature. An ideality factor with values approaching 2 ($n \rightarrow 2$), can be readily seen at low voltages and these correspond to space charge regions exhibiting

behaviour that is dominated by recombination. With higher voltages, ($n \rightarrow 1$) correlated with recombination that is dominated by diffusion in the quasi-neutral regions [31]. Ideality factors with values greater than 2, at low bias voltages, have been reported for organic and inorganic solar cells. Typical reasons for these observations range from leaks along surface channels, tunnelling effects, breakdown by micro-plasmas, etc.

There has also been a suggestion by Hall [32] that the ideality factor could be less than 1 where junctions have saturation currents that are determined by Auger recombination.

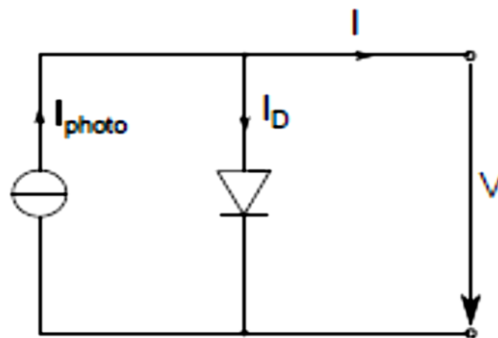


Figure 2.9: Ideal diode circuit [28] with no series resistance and an infinite shunt resistance.

A solar cell under illumination can be supplied with a variable voltage leading to the measurements of the current through and the voltage across the cell. The current through the illuminated cell varies between 0 and I_{sc} , the short circuit current. The I_{sc} being the current that is drawn in the cell if the load is zero.

This current that flows when the illuminated solar cell is connected to a load is a result of a linear combination [33] of two opposing components of the internal current. These being,

- The incident induced photogenerated current, I_L , due to the generation of charge carriers.
- The diode, or dark current, I_D , stemming from the recombination of charge carriers, that is external voltage driven. The voltage being the photogenerated voltage that is necessary to deliver power to the load.

The components of the internal current lead to the measurement of the external current I as shown in the expression

$$I = I_L - I_D \quad (2.8)$$

The current – voltage characteristics of a solar cell under illumination thus become

$$I = I_L - I_o \left[\exp\left(\frac{qV}{nkT}\right) - 1 \right] \quad (2.9)$$

At short circuit conditions i.e. at $V = 0$, the external current reduces to $I = I_L = I_{SC}$ i.e. the short circuit current.

Under open – circuit conditions i.e. when the external current $I = 0$, the photogenerated current is wholly cancelled by the bias current in the dark meaning $I_L = I_D$. The related voltage across the positive and negative terminals, the open – circuit voltage (V_{oc}) can be determined from Equation (2.9) as,

$$V_{oc} = \frac{nk_B T}{q} \ln\left(\frac{I_L}{I_o} - 1\right) \quad (2.10)$$

The usage of equivalent circuit diagrams in modelling solar cell dynamics cannot be solely based on idealised situations. In Figure 2.10 an equivalent circuit diagram that includes parasitic resistances is presented in furthering the description of the electrical behaviour of organic photovoltaic devices.

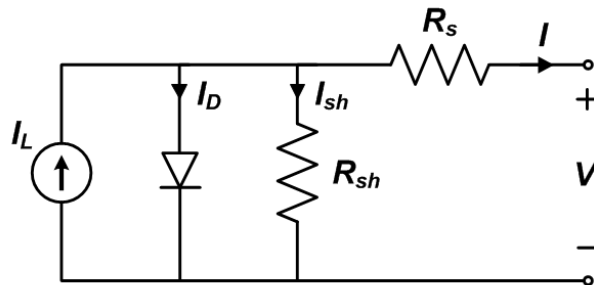


Figure 2.10: Non-ideal diode circuit diagram showing parasitic resistances, R_s and R_{sh} [34].

The dissipation of power in real devices normally occurs through resistances at the contacts, through interfaces in the device or through leakage currents within the device. This power dissipation is generally ascribed to two parasitic resistances namely, the series resistance (R_s) and the shunt (parallel) resistance (R_{sh})

The shunt resistance is generally identified with the degree of the leakage of the current through the device. This can also take the form of a recombination of charge carriers in and around dissociation sites such as the donor:acceptor interface. R_{sh} has also been linked to imperfections during the device fabrication processes resulting in the loss of charge carriers through surface defects, charge carrier traps, recombination of excitons at the donor:acceptor interface and pinholes in the films. The shunt resistance can be obtained from the $I - V$ (or $J - V$) curve by taking the inverse of the slope in the neighbourhood of 0 V. That is,

$$R_{sh} = \left(\frac{dI}{dV} \right)_{V \rightarrow 0}^{-1} \quad (2.11)$$

or

$$R_{sh} = \left(\frac{dI}{dV} \right)_{I=I_{sc}}^{-1} \quad (2.12)$$

On the other hand, the series resistance is associated with the bulk conductivity of a transport medium as well as the contact resistance between respective device layers and at the interface of the active layers and electrodes. The conductivity or put slightly differently, the mobility of charge carriers, can be affected by space charges, traps or barriers. The thickness of the transport medium has also been found to have an impact on the magnitude of the series resistance i.e. the thicker the transport layer the greater the series resistance. The R_s can also be determined from, the $I - V$ (or $J - V$) curve. This is done by taking the inverse of the slope around $I = 0$ as in

$$R_s = \left(\frac{dI}{dV} \right)_{I=0}^{-1} \quad (2.13)$$

or

$$R_s = \left(\frac{dI}{dV} \right)_{V=V_{oc}}^{-1} \quad (2.14)$$

Electrical characteristics of a solar cell that are inclusive of power dissipating resistances are derived by making use of the non-ideal equivalent circuit diagram in conjunction with Kirchhoff's current and voltage laws. These junction and loop rules with reference to Figure 2.10, result in the external current in the circuit being simplified as

$$I = I_L - I_o \left[\exp \left(\frac{q(V - IR_s)}{nkT} \right) - 1 \right] - \frac{V + IR_s}{R_{sh}} \quad (2.15)$$

Furthermore, Kirchhoff's current junction and the voltage loop rules, based on the circuit in Figure 2.9, can lead to the following relations:

$$I_L - I_D - I = I_{sh} \quad (2.16)$$

$$(I_L - I_D - I)R_{sh} = V + IR_s \quad (2.17)$$

Equation (2.17) can be re-written as

$$I(R_{sh} + R_s) = I_L R_{sh} - I_D R_{sh} - V \quad (2.18)$$

Dividing equation (2.18) by R_{sh} gives

$$I \left(1 + \frac{R_s}{R_{sh}} \right) = I_L - I_D - \frac{V}{R_{sh}} \quad (2.19)$$

Equation (2.7), the Shockley ideal diode equation can be substituted for the second term on the right hand side of the above equation. However, in the interest of clarity, we focus on the factor $\left(1 + \frac{R_s}{R_{sh}} \right)$, on the left hand side of Equation (2.19). As opposed to inorganic solar cells where R_{sh} can be about 3 orders of magnitude or

greater than R_s [35], resulting in $\left(1 + \frac{R_s}{R_{sh}}\right)$ being essentially 1, the situation is very different in organic solar cells. Organic solar cells very often exhibit high series resistances with relatively smaller shunt resistances. This means that $\left(1 + \frac{R_s}{R_{sh}}\right)$ yields values greater than 1. We propose that the term $\left(1 + \frac{R_s}{R_{sh}}\right)$, with its direct influence on the measured current in the external circuit, indicates the degree of recombination in an organic photovoltaic device.

2.5 Charge carrier dynamics in OPV devices

A better characterisation of the performance of organic photovoltaic devices, requires a deeper understanding of how electrical charges travel through a device and how they are affected by parameters such as applied voltages. A much more detailed analysis should include other factors such as morphological effects, however these fall beyond the scope of this thesis.

Organic materials, characterised by structural disorder at a nanoscale level where adjacent molecules couple to each other via weak Van der Waals forces, display a low transfer of charge carriers between molecules as a result of little orbital overlap. The π – electron delocalisation along the carbon - carbon bonds leads to a charge transport in which an electron hops from one π – system to the next [36], in ‘band transport-like’ conduction along the polymer backbone or tunnelling between conducting materials [37]. This form of transport can be phonon assisted through enhancement of the degree of overlap of the pi electron wave functions.

A number of approaches have been followed over time, to determine the mobility of charge carriers in organic materials. It has been found that experimental methods and conditions have a direct impact on the results since mobility depends on a variety of parameters. With this understanding, it can be concluded that different measurement methods will present advantages and disadvantages depending on the mobility measurement conditions.

To demonstrate the extent of different charge mobility measurement approaches in terms of scope and historical background, we provide a representative list, without delving into any of the details as follows: Charge extraction by linearly increasing voltage (CELIV) [38], space-charge-limited-current (SCLC) [39], Hall effect measurement [40], conductivity/concentration method [41], Admittance spectroscopy [42], transient space-charge-limited-current [39], Time-of-flight (TOF) [43] and transient electroluminescence [44].

In the sections that follow immediately hereon, we present a discussion that will be focussing on charge injection, charge mobility and recombination dynamics.

2.5.1 Charge injection and bulk transport in OPV devices

The conduction of electrical current in OPV devices involves the flow of both electrons and holes. Since we are dealing with metal/polymer/metal systems, a description of processes related to charge injection at metal/polymer interfaces and charge transport in the bulk material are key in the understanding of performances of fabricated devices. The pre-eminence of one process over the other is dependent on the experimental conditions and device configurations i.e. electrode workfunction, external bias, temperature, transport and trapping levels of the polymer, trap density, etc. [21]. With the two processes contributing to the current flow in the device, the one with lower rate is deemed the limiting one as it controls the characteristics of the current in the device. Thus the current is deemed injection limited if the injection at an interface is of a lower rate or bulk transport limited if the transportation through the polymer is lower [45]. Temperature and voltage bias determine the transition between injection limited and bulk transport limited. The potential barrier height, ϕ at the metal/polymer interface given by the difference between the workfunction of the electrode and the corresponding energy level of the polymer and the externally applied electric field are two parameters that determine whether the current is injection limited or bulk transport limited [46]. It is now understood that current is exclusively bulk transport limited for $\phi < 0.2$ eV since charge injection is favourable. The range 0.2 eV to 0.5 eV specifies barrier

heights transition. Injection limited current is associated with barrier heights that are greater than 0.5 eV with a moderate externally applied bias voltage [47].

Having introduced injection and bulk transport limited concepts, a summary of the models describing charge injection and transport in single and double carrier devices namely, the Richardson Schottky thermionic emission, Fowler-Nordheim field emission, and space charge limited currents (SCLC) will be presented.

2.5.1.1 Richardson – Schottky (RS) thermionic emission model

Thermionic emission theory proposes that electrons having energy larger than the height of the Schottky barrier will cross it and contribute to current if they are at the metal/semiconductor interface. So, an electron from the metal can be injected into the polymer if it has acquired sufficient thermal energy to go over the maximum potential barrier that is formed by a combination of a potential formed by the applied bias and the image charge potential [48, 49]. The RS model is valid for lower applied electric fields and higher temperatures ($e\phi_{TF} \ll k_B T$). The image force lowering i.e. the lowering of the Schottky barrier height at higher fields leads to the reduction of the metal workfunction for thermionic emission. Therefore, the RS model is given by [45], [48] and [50],

$$J = A^* T^2 \exp\left(\frac{-\phi_B}{k_B T}\right) \exp\left[\left(\frac{q^3 V}{4\pi\epsilon_o\epsilon_r d}\right)^{\frac{1}{2}} / k_B T\right] \quad (2.20)$$

where T is the temperature, ϕ_B is the interface potential barrier height, d is the thickness of the active film, ϵ_o and ϵ_r are the permittivity of free space and the relative permittivity respectively, k_B is Boltzmann's constant, V is the applied voltage – which is positive for forward bias and negative for reverse bias, q the elementary electronic charge and A^* is the Richardson – Schottky constant. The constant is given by $A^* = 4\pi q m^* k_B^2 / h^3 = 120 \text{ A/cm}^2 \text{ K}$ for free electrons with h being the Planck's constant. The effective mass m^* is taken as equal to that of the

rest mass of electrons, alternatively it depends on the anisotropy of the material [49].

Considering the variation of current density with temperature in the (RS) model given by Equation (2.20), thermionic emission can still be investigated for conditions of constant temperature. In such cases, an investigation can be carried out by varying the bias voltage. Therefore, Equation (2.20) can be re-arranged in the form:

$$\ln J = \ln A^* + 2 \ln T - \frac{\phi_B}{k_B T} + \left[\frac{1}{k_B T} \left(\frac{q^3}{4\pi\epsilon_o\epsilon_r d} \right)^{\frac{1}{2}} \right] \sqrt{V} \quad (2.21)$$

From the current – voltage characteristics of an OPV device, the positive slope in (RS) plot of $\ln J$ vs \sqrt{V} indicates charge injection by thermionic emission through the metal/polymer interface.

This slope is given by,

$$\frac{d(\ln J)}{d(\sqrt{V})} = \frac{1}{k_B T} \left(\frac{q^3}{4\pi\epsilon_o\epsilon_r d} \right)^{\frac{1}{2}} \quad (2.22)$$

With the intercept, c as,

$$c = \ln A^* + 2 \ln T - \frac{\phi_B}{k_B T} \quad (2.23)$$

The potential barrier at constant temperature corresponding to injection by thermionic emission at the metal/polymer interface is then,

$$\phi_B = (\ln A^* + 2 \ln T - c) k_B T \quad (2.24)$$

Equation (2.20) can also be rewritten by taking natural logs with a variation in temperature. Such that at high temperatures, the RS model is given as,

$$\ln\left(\frac{J}{T^2}\right) = \left[\frac{1}{k_B} \left(-\phi_B + \sqrt{\frac{q^3 V}{4\pi\epsilon_o\epsilon_r d}} \right) \right] \frac{1}{T} + \ln A^* \quad (2.25)$$

From Equation (2.25) a plot of $\ln\left(\frac{J}{T^2}\right)$ vs $\frac{1000}{T}$ at a given potential (V) is a straight line, with all other parameters constant. The slope of Equation (2.25) is called the activation energy and the effective barrier height (between the electrode and the film) is determined from the slope as,

$$\phi_B = -\text{slope} \cdot k_B + \sqrt{\frac{q^3 V}{4\pi\epsilon_o\epsilon_r d}} \quad (2.26)$$

2.5.1.2 Fowler – Nordheim (FN) field emission model

In classical physics, when electrons encounter a potential barrier with an energy less than that of the potential barrier, they will be reflected. However, quantum mechanics predicts that there is a finite probability of an electron tunnelling through the potential barrier. In this instance, the electron wave function will extend through the potential barrier especially for potential barriers that are $< 100 \text{ \AA}$ thick [51].

The tunnelling of charge carriers under an intense electric field through a potential barrier from a metal to a semiconductor or a dielectric material, is described by the field emission theory. Effectively, due to the large applied electric field, the potential barrier is lowered and the charge carriers “see” a triangular barrier. This is the basis of Fowler - Nordheim tunnelling. A visual conceptualisation of different charge injection models is illustrated in Figure 2.11.

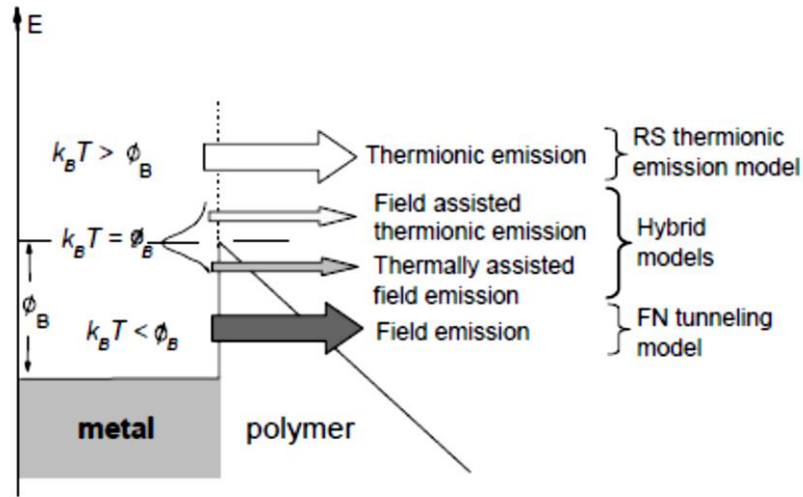


Figure 2.11: Charge injection models at metal/polymer interfaces [21].

The Fowler – Nordheim field emission model describing the tunnelling of charge carriers through a potential barrier, considers a one-dimensional time independent Schrödinger equation for the wave function of an electron. That is,

$$-\frac{\hbar^2}{2m} \frac{d^2\psi}{dx^2} + V(x)\psi = E\psi \quad (2.27)$$

Assuming a slow varying potential $V(x)$ with distance x , the solution of Equation (2.27) is approximated as

$$\psi = \psi_o \exp \left[\pm i \frac{\sqrt{2m}}{\hbar} \sqrt{E - V(x)} \right] \quad (2.28)$$

It can then be established that the ratio of the probability density $|\psi|^2$, i.e. the transmission coefficient ψ_T , at the exit from the barrier to the value it had at the entrance gives the penetration probability into the barrier.

For a triangular-shaped potential barrier, with an applied field F , the WKB (Wentzel, Kramers, Brillouin) approximation suffices and the tunnelling probability (which is proportional to the tunnelling current) is thus given in the form,

$$P(E) = \exp\left[-\frac{4}{3} \frac{\sqrt{2qm}}{\hbar} \frac{\phi_B^{3/2}}{F}\right] \quad (2.29)$$

From Equation (2.29) it should be noted that the width of the barrier is approximately ϕ_B/F with the maximum barrier height being ϕ_B .

Expressing ϕ_B in eV and F in V/cm and noting that the value for ϕ_B generally ranges between 2 and 5 eV, an electric field of the order 10^7 V/cm will be required for appreciable numbers of electrons to be emitted into the vacuum.

To link the FN field emission model with the characterisation of OPV devices, we note that the current flow at a metal/semiconductor interface may be treated in the same way as that at a metal/vacuum boundary. In the limit of field emission domination, the FN model can be used to obtain the tunnelling injection current density. This is done by ignoring all possible Schottky barrier lowering effects and assuming quantum tunnelling from a metal through a triangular potential barrier into unbound continuum states [21]. The resulting current density is then

$$J = AF^2 \exp\left[\frac{8\pi\sqrt{2m^*}\phi_B^{3/2}}{3hqF}\right] \quad (2.30)$$

where m^* is the effective charge carrier mass, ϕ_B the potential barrier height, q the elementary electronic charge, F the applied electric field and A (given in A/V^2) is a rate coefficient that contains a tunnelling pre-factor and rate of current back-flow[52]. The expression for A has been deduced as [45]

$$A = \frac{q^3}{8\pi h \phi_B} \quad (2.31)$$

For easier visualisation, Equation (2.30) can be rewritten as

$$J = AF^2 \exp\left[\frac{-K}{F}\right] \quad (2.32)$$

with the constant,
$$K = \frac{8\pi\sqrt{2m^*}\phi_B^{3/2}}{3hq} \quad (2.33)$$

Knowing the value of K enables the determination of the barrier height between the electrode and the film from Equation (2.32) as

$$\phi_B = \left(\frac{3hqK}{8\pi\sqrt{2m^*}} \right)^{\frac{2}{3}} \quad (2.34)$$

For practicality, we now consider an OPV device having an active layer d under an applied bias V , meaning that it is in an applied electric field, $F = V/d$. This means that Equation (2.32) can be rewritten as

$$\frac{J}{V^2} \cdot d^2 = A \exp \left[-Kd \frac{1}{V} \right] \quad (2.35)$$

Taking natural logs leads to

$$\ln \left(\frac{J}{V^2} \right) = \ln A - \ln d^2 - Kd \left(\frac{1}{V} \right) \quad (2.36)$$

Plotting a graph of $\ln \left(\frac{J}{V^2} \right)$ vs $\left(\frac{1}{V} \right)$ will give a straight line with a negative slope equal to $-Kd$. The potential barrier can be obtained from this FN plot as

$$\phi_B = \left(-\frac{3hq(\text{slope})}{8\pi d\sqrt{2m^*}} \right)^{\frac{2}{3}} \quad (2.37)$$

2.5.1.3 Bulk charge transport

A description of bulk charge transport mechanisms in organic materials is generally covered by the following processes: Ohmic conduction, Hopping conduction (Variable Range Hopping), Poole-Frenkel emission mechanism, Space Charge Limited Conduction, Ionic conduction and Grain-boundary-limited conduction [53].

Organic semiconductors have been described as being characterised by delocalisation over single molecules. Additionally, the weak coupling of adjacent molecules, with negligible orbital overlap, due to Van der Waals interactions means that the likelihood of a transfer of charge carriers between them is somewhat diminished resulting in low mobilities. This then means that in these organic systems, that are characterised by disorder [54], charge carriers are in general transported via a hopping mechanism from one molecular site to the other. This temperature dependent hopping mechanism [54] means that thermal activation is required for overlap of molecular orbitals corresponding to energy differences between different molecular sites.

Though acknowledging that the exact details of charge transport mechanisms in organic semiconductors are still under debate, Zhou and Facchetti [54] have highlighted a model for hopping transport that shows the relationship between carrier mobility and temperature.

To provide a clearer theoretical framework for the bulk of the experiments done in this project, a brief description of bulk charge transport mechanisms related to the Ohmic conduction and the Space Charge Limited Conduction (Current) is provided. From the outset it has to be said that, discussions on the bulk charge transport mechanisms will invariably have descriptions of charge mobility featuring very prominently. Charge carrier mobility is a key parameter that characterises bulk charge transport. Studies on charge transport of organic materials have tended to focus on improving the conductivity, σ , of these materials while correlating or making direct comparisons with the conductivity of inorganic materials [55]. Over time, the focus has shifted more to charge carrier mobility, μ [55]. Unlike conductivity, which can be measured quite easily with a two-point or a four-point probe by measuring the reciprocal of resistance between electrodes, charge carrier mobility brings in the complexity of determining carrier concentration when determined through similar conductivity and Hall-effect type measurements. See Equation (2.38).

$$\sigma = ne\mu \text{ and } \mu = vE \quad (2.38)$$

where n is the charge carrier concentration, e is the electron charge, v is the charge carrier velocity and E the electric field.

The discussion that follows will have charge carrier mobility featuring prominently in the descriptions of bulk charge transport mechanisms.

We now revisit the concept of limiting currents that was dealt with earlier in section 2.5.1. It was seen that when current is bulk transport limited, the charge transport, after injection into the bulk is slower than the injection rate. The difference in the injection and sweeping away rates builds-up space charge in the device which creates an opposing field that prevents further injection of charges into the bulk. The current obtained is limited by the rate at which carriers are transported through the bulk and it is referred to as Space Charge Limited Current (SCLC). The implication thereof is that the charge density in and around the contact is much greater than in the bulk, effectively creating a reservoir of charge carriers – an Ohmic contact. Considering the bulk material (a thin semiconducting film in OPVs), Ohmic contacts can be maintained by selecting a low workfunction metal (compared to the semiconductor) for electron injection and another metal with a high work-function for hole injection. With a uniform bias applied across the film relatively larger than the electric field due to injected charge carriers, a linear current-voltage relation is established at low biases. The current-voltage behaviour in this range is described by Ohm's law with the slope of the log-log plot between current density J and voltage V at low bias equal to 1 [56]. The current density is then related to the voltage as

$$J = qn\mu \frac{V}{d} \quad (2.39)$$

with q being the electronic charge, n the charge carrier density, μ the charge carrier mobility, V the applied voltage and d the thickness of the active layer.

Thus far a condition where the applied voltage dominates the bias created by space charge has been described. The question of what happens at the contacts when injected charge carriers create a field that is greater than the applied bias requires

consideration. When this happens i.e. with the current flow that is not injection limited but limited by the space charge formed within the semiconducting film, the current flow can be represented by the Mott-Gurney law provided there are no active traps in the semiconductor. This trap free space charge limited current (TFSCCLC) is given by

$$J = \frac{9}{8} \varepsilon_o \varepsilon_r \mu \frac{V^2}{d^3} \quad (2.40)$$

where ε_o is the permittivity of free space, ε_r the relative permittivity, μ the charge carrier mobility, V the applied voltage and d the thickness of the photoactive layer. It can be seen that the nature of the current shows a quadratic dependence on the voltage, meaning that the slope of a $\log J$ versus $\log V$ plot will be equal to 2. It has to be noted that the description ‘trap free’ does not solely mean that there are not traps in the material, rather that all traps are filled [57].

A relaxation of the ‘trap free’ condition, that yielded a current density given by Equation (2.40), requires a focus on real, practical cases where material properties are affected by the presence of traps. Charge traps can emanate from chemical or structural defects in charge transport layers. With organic semiconductors and their related structural disorder amongst many other attributes, charge carrier trapping is unavoidable. This is prevalent in OPV devices whereby impurities such as oxygen act as traps to migrating excitons leading to poor photovoltaic performances.

In general, charge traps can be classified as shallow (largely structural) or deep (generally chemical) traps depending on the energy levels of the traps [45]. An illustration of this classification was shown by Oskar *et al.* [58] as in Figure 2.12, when they investigated the dielectric response of solar cell devices based on oxygen-doped P3HT:PC₆₁BM blends as a function of temperature between 133 K and 303 K.

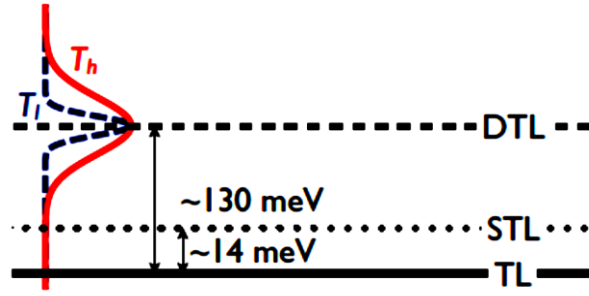


Figure 2.12: Illustration of trap and transport levels, DTL, STL represent the deep and shallow trap energy levels, respectively.

To account for the contributions due to shallow traps, Equation (2.40) is adjusted by including a parameter, θ that gives the ratio of free to trapped charges, in the form,

$$J = \varepsilon_o \varepsilon_r \mu \theta \frac{V^2}{d^3} \quad (2.41)$$

When we have trap free conditions $\theta = 1$. Otherwise,

$$\theta = \frac{N_C}{N_{ST}} \exp\left(-\frac{E_T}{k_B T}\right) \quad (2.42)$$

where N_C is the effective density of states in the conduction band edge, N_{ST} the shallow trap concentration at the discrete energy level, E_T the energy gap between trap level and conduction band, k_B the Boltzmann's constant and T the absolute temperature, with θ always less than unity.

Looking at Ohmic conduction and SCLC, a transition from the former to the latter conductivity is identified as taking place when injected carrier concentration exceeds thermally generated carrier concentration. From the current – voltage characteristics, a transition voltage V_t can be determined through equating Equations (2.39) and (2.40). The transition voltage is,

$$V_t = \frac{8qnd^2}{9\theta\epsilon_r\epsilon_o} \quad (2.43)$$

With the presence of traps in organic semiconducting materials, a common assumption is that traps are exponential distribution in energy such that the $J - V$ is of the form

$$J = q^{1-l} \mu N_v \left(\frac{2l+1}{l+1} \right)^{\frac{1}{l}} \left(\frac{l}{l+1} \frac{\epsilon\epsilon_o}{N_{\text{total}}} \right)^l \frac{V^{l+1}}{d^{2l+1}} \quad (2.44)$$

with q the electronic charge, μ the charge carrier mobility, N_v the density of states in the valence band, N_{total} the total density of traps, ϵ the dielectric constant, ϵ_o the permittivity of free space, d is the sample thickness and l is defined in terms of a characteristic constant of the trap distribution and it is greater than 1 [m slope]. With $m = l + 1$, the power law $J \propto V^m$ is obtained where $m = 1$ is the Ohmic region and $m \geq 2$ is the SCLC region.

2.5.2 Charge recombination in OPV devices

A recombination of charge carriers results in the annihilation of an electron and a hole and it is more pronounced in disordered organic semiconductors. Recombination is a loss mechanism with a negative effect on the performance of OPV devices because it reduces the generation rate of free charge carriers. This loss mechanism affects the performance of OPV devices with an impact right through from light harvesting to transportation of generated free charge carriers [59]. Understanding its dynamics is key as its minimisation will lead to the optimisation of the PCE of OPV devices. Recombination in OPV devices, as shown in Figure 2.13, can generally be summarised as:

- Exciton recombination

As previously described, in BHJ OPVs the absorption of incident light by the photoactive layer leads to the formation of excitons. These need to

migrate/diffuse to a donor/acceptor interface for dissociation. However, Coulombic force driven recombination can occur if the exciton does not reach the donor/acceptor interface timeously.

- Germinate recombination (GR)

Photon absorption leads to a strongly bound electron-hole quasi-particle, the exciton. This Coulombically bound exciton needs to undergo dissociation into a free electron and hole via the charge transfer (CT) state. However, an electron and a hole (polarons) can recombine and decay to a ground state before dissociation can take place. This type of recombination seen as a first order recombination, where the electron and the hole originate from the same exciton, is referred to as geminate recombination or monomolecular recombination in some cases. It is a first order recombination in that the recombination rate is proportional to the charge carrier density to the power 1 i.e. $R \propto n^1$. Geminate recombination exhibits a significant field dependence and has been used to provide a contextual basis for experiment work related to BHJ cells [60-62]. Furthermore, a model based on the Onsager and/or the Braun-Onsager theory of geminate charge recombination has been utilised to describe experimentally observed field and temperature dependence of generated photocurrents in polymer-fullerene blends [63, 64]. Geminate recombination is an ultrafast process with typical time scales that are in the order of fs to ps. It can be tracked through experimental techniques such as transient absorption spectroscopy (TAS).

With every absorbed photon creating an electron-hole pair, it can be said that geminate recombination shows a linear dependence with light intensity. Geminate recombination rate, R_{gem} , is then given by

$$R_{gem} = \frac{PP}{\tau_{pp}} \quad (2.45)$$

where PP is the polaron pair density and τ_{pp} is the finite lifetime of the polaron pair.

- Non-germinate recombination (NGR)

An effective extraction of freed charge carriers, following exciton dissociation, needs to take place at the electrodes. However, free charge carriers may recombine through a process called non-geminate or bimolecular recombination before they are extracted. A consequence of this is bimolecular recombination is generally associated with bulk transport properties. NGR is a dominant recombination mechanism in trap free OPV devices. In the presence of traps, a trap assisted recombination process defined by the Shockley-Read-Hall (SRH) process is defined. Conclusions to the effect that in many organic semiconductors, the electron currents are strongly trap limited have been made [65]. Describing bimolecular recombination in terms of recombination order, it is described as a second order recombination in that the recombination rate scales quadratically with the charge carrier density, $R \propto n^2$.

Bimolecular recombination has also been referred to a Langevin type recombination [66] since the recombination rate is subject to a probability that an electron – hole pair will encounter each other in a mutually set Coulombic potential whose upper limit is set by the Langevin type recombination. The rate at which bimolecular recombination occurs is given by

$$R = \gamma_L (np - n_i p_i) \quad (2.46)$$

where n and p are the free electron and hole densities, $n_i p_i = N_{CV} \exp\left(\frac{-E_{gap}}{kT}\right) = n_i^2$, $n_i p_i$ denote intrinsic electron and hole densities in the material, E_{gap} the energy gap, N_{CV} the effective density of states and γ_L is the Langevin recombination constant. The Langevin recombination constant for pristine materials is given by

$$\gamma_L = \frac{q}{\epsilon} (\mu_e + \mu_h) \quad (2.47)$$

where q is the elementary charge, ε is the dielectric constant and $\mu_{e(h)}$ is the electron (hole) mobility.

It has been suggested that in blends, as opposed to pristine materials, a spatial average value for electron and hole mobilities should be used as a way of compensating for the differences in their mobilities. Therefore in blends such as BHJ OPVs, bimolecular recombination is limited by the slower charge carrier [66] leading to the modification of the Langevin recombination constant as

$$\gamma_L = \frac{q}{\varepsilon} \min(\mu_e, \mu_h) \quad (2.48)$$

The presence of impurities and defects in the organic semiconducting material can cause traps [67]. These traps can for example, be located within the band gap creating one or more localised energy levels where an exchange of charge carrier can take place between these localised energy levels and the valence or conduction bands [Petty traps]. Here we note that, Kirchartz *et al.* [69] in their study of recombination via tail states in polythiophene-fullerene solar cells, stated that even in completely defect-free organic solar cells, their inherent disorder and molecular environment lead to sub-band gap states that could contribute to charge carrier recombination.

Localised energy levels are referred to as recombination centres where a trapped electron or hole attracts a respective opposite charge to recombine. This process is defined as trap-assisted recombination. The Shockley-Read-Hall (SRH) model, though developed for inorganic semiconductors has been used to study trap-assisted recombination processes in organic semiconductors [70, 71]. The trap-assisted recombination rate based on the SRH model can be given by the following relation assuming thermal equilibrium for electron emission and electron capture processes:

$$R_{SRH} = B_{SRH} (np - n_i p_i) \quad (2.49)$$

with
$$B_{SRH} = \frac{C_n C_p N_t}{[C_n (n + n_i) + C_p (p + p_i)]} \quad (2.50)$$

where C_n is the probability per unit time that an electron in the conduction band will be captured by a neutral centre, C_p is the probability per unit time that a hole will be captured by a trapped electron and N_t is the density of electron traps.

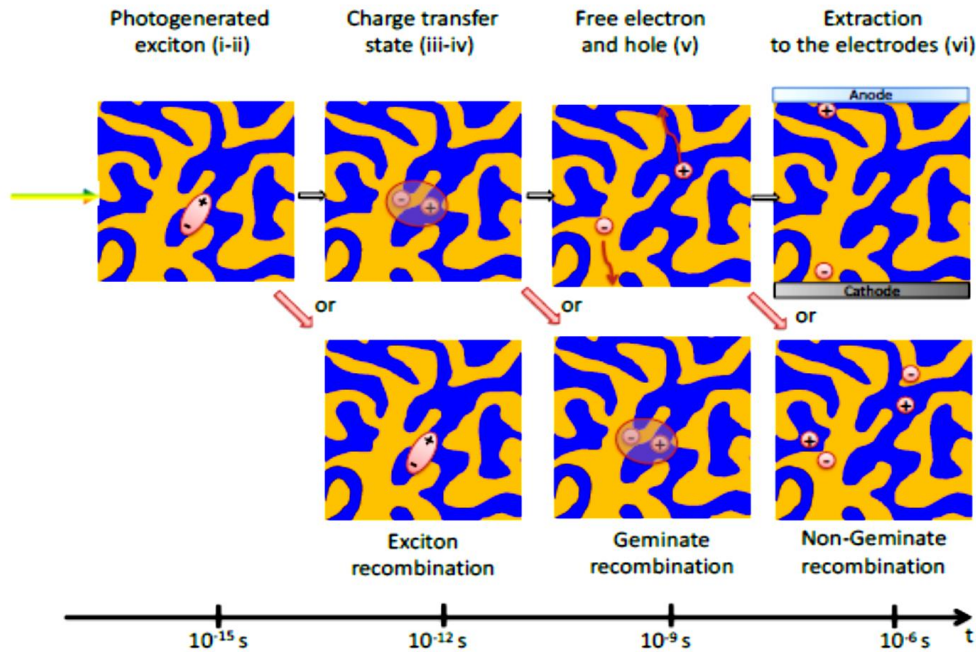


Figure 2.13: A schematic of recombination processes in organic BHJ OPVs and their relative time scales [59].

Recombination processes have been studied within the framework of understanding, studying and characterising power conversion efficiencies of fabricated OPV devices. Current – voltage ($J - V$) characteristics have been studied where the behaviour of current and voltage were tracked as a function of incident light intensity. To do this, information from the intensity dependence of J_{sc} and V_{oc} was used to describe recombination processes involved.

2.6 References

- [1] Chiang, C.K., Fincher, C.R., Park, Y.W., Heeger, A.J., Shirakawa, H., Louis, E.J., Gau, S.C. and MacDiarmid, A.G. (1977). *Physical Review Letters* **39** (17), 1098.
- [2] <https://howlingpixel.com/i-en/Polyacetylene> [accessed 10/03/2019]
- [3] Moiz, S.A., Khan, I.A., Younis, W.A. and Karimov, K.S. (2016). Chapter 5, in *Conducting Polymers: Space Charge-Limited Current Model for Polymers*, edited by Faris Yilmaz (Intech).
- [4] Deibel, C. and Dyakonov, V. (2010). *Reports on Progress in Physics* **73** (9), 096401.
- [5] Brütting, W., Bronner, M., Götzenbruggen, M. and Opitz, A. (2008). *Macromolecular Symposia* **268** (1), 38.
- [6] Garnier, F., Hajlaoui, R., Yassar, A. and Srivastava, P. (1994). *Science* **265** (5179), 1684.
- [7] Braga, D. and Horowitz, G. (2009). *Advanced Materials* **21**(14-15), 1473.
- [8] Reineke, S., Lindner, F., Schwartz, G., Seidler, N., Walzer, K., Lussem, B. and Leo, K. (2009). *Nature* **459** (7244), 234.
- [9] Wu, J., Agrawal, M., Becerril, H.A., Bao, Z., Liu, Z., Chen, Y. and Peumans, P. (2010). *ACS Nano* **4** (1), 43.
- [10] Peumans, P., Yakimov, A. and Forrest, S.R. (2003). *Journal of Applied Physics* **93** (7), 3693.
- [11] Hadipour, A., de Boer, B. and Blom, P.W.M. (2008). *Advanced Functional Materials* **18** (2), 169.

- [12] Gray, J.L. (2011). Chapter 3, in *Handbook of Photovoltaic Science and Engineering: The physics of the solar cell*, edited by Antonio Luque and Steven Hegedus (John Wiley & Sons, Ltd.).
- [13] Kallmann, H., and Pope, M. (1959). *Journal of Chemical Physics* **30** (2) 585.
- [14] Kumaresan, P., Vegiraju, S., Ezhumalai, Y., Yau, S.L., Kim, C., Lee, W.-S. and Chen, M.-C. (2014). *Polymers* **6** (10), 2645.
- [15] Tang, C.W. (1986). *Applied Physics Letters* **48** (2), 183.
- [16] Mikhnenko, O.V., Azimi, H., Scharber, M., Morana, M., Blom, P.W.M. and Loi, M.A. (2012). *Energy & Environmental Science* **5** (5), 6960.
- [17] Dimitrov, S.D., Nielsen, C.B., Shoaee, S., Tuladhar, P.S., Du, J., McCulloch, I. and Durrant, J.R. (2012). *Journal of Physical Chemistry Letters* **3** (1), 140.
- [18] Halls, J.J.M., Walsh, C.A., Greenham, N.C., Marseglia, E.A., Friend, R.H., Moratti, S.C., and Holmes, A.B. (1995). *Nature* **376** (6540), 498.
- [19] Yu, G. and Heeger, A.J. (1995). *Journal of Applied Physics*, **78** (7), 4510-4515.
- [20] Kroon, R., Lenes, M., Hummelen, J.C., Blom, P.W.M. and de Boer, B. (2008). *Polymer Reviews* **48** (3), 531.
- [21] Chiguvare, Z. (2005). *Electrical and Optical Characterization of Bulk Heterojunction Polymer- Fullerene Solar Cells*. PhD thesis, Oldenburg University, Germany.
- [22] Yu, S. (2015). *Performance Enhancement of Organic Photovoltaic Cells through Nanostructuring and Molecular Doping*. PhD thesis, Humboldt University of Berlin, Germany.

- [23] Vacar, D., Maniloff, E.S., McBranch, D.W. and Heeger, A.J. (1997). *Physical Review B* **56** (8), 4573.
- [24] Hill, I.G., Kahn, A., Soos, Z.G. and Pascal, R.A. (2000). *Chemical Physics Letters* **327** (3-4), 181.
- [25] Deibel, C., Mack, D., Gorenflot, J., Schöll, A., Krause, S., Reinert, F., Rauh, D. and Dyakonov, V. (2010). *Physical Review B* **81** (8-15), 085202.
- [26] Gregg, B.A., Chen, S.-G. and Cormier, R.A. (2004). *Chemistry of Materials* **16** (23), 4586.
- [27] Brabec, C.J. (2004). *Solar Energy Materials & Solar Cells* **83** (2), 273.
- [28] Lackner, G. (2012). *Carbon Nanotubes In Organic Solar Cells*. PhD thesis, University of Duisberg-Essen, Germany.
- [29] Blakesley, J.C. and Neher, D. (2011). *Physical Review B* **84** (7), 075210.
- [30] Boden, N., Bissell, R., Clements, J. and Movaghar, B. (1996). *Liquid Crystals Today* **6** (1), 1.
- [31] Lorentzo, E. (1994). *Solar Electricity: Engineering of Photovoltaic Systems*, Progensa (Earthscan Publications Ltd.) Madrid, Spain.
- [32] Hall, R.N. (1981). *Solid-State Electronics* **24** (7) (1981) 595.
- [33] Lorenzo, E. (1994). *Solar Electricity: Engineering of Photovoltaic Systems*, (James and James Limited), London, UK.
- [34] Wolf, M. and Rauschenbach, H. (1963). *Advance Energy Conversion* **3** (2), 455.
- [35] Boden, N., Bushby, R.J., Clements, J. and Luo, R. (1995). *Journal of Materials Chemistry* **5** (10), 1741.
- [36] Brabec, C.J., Dyakonov, V., Parisi, J. and Sariciftci, N.S. (2003). *Organic Photovoltaics: concepts and realization*, (Springer) Berlin.

- [37] Jaiswal, M. and Menon, R. (2006). *Polymer International* **55** (12), 1371.
- [38] Juška, G., Arlauskas, K., Viliūnas, M. and Kočka, J. (2000). *Physical Review Letters* **84** (21), 4946.
- [39] Abkowitz, M. and Pai, D. M. (1986). *Philosophical Magazine B* **53** (3), 193.
- [40] Charles Jr., H.K., King, R.J. and Ariotedjo, A.P. (1980). *Solar Cells* **1** (3), 327.
- [41] Nguyen, P.H., Paasch, G., Brütting, W. and Riess, W. (1994). *Physical Review B* **49** (8), 5172.
- [42] Tsang, S.W., So, S.K. and Xu, J.B. (2006). *Journal of Applied Physics* **99** (1), 013706.
- [43] Hosokawa, C., Tokailin, H., Higashi, H. and Kusumoto, T. (1992). *Applied Physics Letters* **60** (10), 1220.
- [44] Spear, W.E. (1969). *Journal of Non-Crystalline Solids* **1** (3), 197.
- [45] Kao, K.C. and Hwang, W. (1981). *Electrical Transport in Solids, with particular reference to organic semiconductors*, volume 14 of *International Series in the Science of the solid State*, (Pergamon Press), Oxford.
- [46] Blom, P.W.M. and Vissenberg, M.C.J.M. (2000). *Material Science and Engineering* **27** (3-4), 53.
- [47] Feller, F., Rothe, M., Tammer, M., Geshke, D. and Monkman, A.P. (2002). *Journal of Applied Physics* **91** (11), 9225.
- [48] Das, R.R., Battacharya, P., Perez, W., Katiyar, R.S. and Bhalla, A.S. (2002). *Applied Physics Letters* **81** (5), 880.
- [49] Henisch, H.K. (1984). *Semiconductor Contacts, An approach to ideas and models*. International Series of Monographs on Physics No.70. (Clarendon Press), Oxford.

- [50] Braun, D. (2003). *Journal of Polymer Science B* **41** (21), 2622.
- [51] Chien, F.-C. (2014). *Advances in Materials Science and Engineering* **2014** (7), 1.
- [52] Davids, P.S., Campbell, I.H. and Smith, D.L. (1997). *Journal of Applied Physics* **82** (12), 6319.
- [53] Simmons, J.G. (1971). *Journal of Physics D: Applied Physics* **4** (5), 613.
- [54] Zhou, N. and Facchetti, A. (2014). Chapter 2, in *Organic and Hybrid Solar Cells. Charge Transport and Recombination in Organic Solar Cells (OSCs)*, edited by H. Huang and J. Huang 2014 (Springer), Berlin.
- [55] Heeger, A. (2001). *Journal of Physical Chemistry B* **105** (36), 8475.
- [56] Lampert, M.A. and Mark, P. (1970). *Current Injection in Solids* (Academic Press), New York.
- [57] Abkowitz, M., Facci, J.S. and Rehm, J. (1998). *Journal of Applied Physics* **83** (5):2670.
- [58] Armbruster, O., Lungenschmied, C. and Siegfried Bauer, S. (2012). *Physical Review B* **86** (23), 235201.
- [59] Gasparini, N. (2017). *Controlling charge recombination in ternary organic solar cells*. PhD thesis, Friedrich-Alexander University Erlangen-Nurnberg, Germany.
- [60] Marsh, R.A., Hodgkiss, J.M. and Friend, R.H. (2010). *Advanced Materials* **22** (23), 3672.
- [61] Albrecht, S., Schindler, W., Kurpiers, J., Kniepert, J., Blakesley, J.C., Dumsch, I., Allard, S., Fostiropoulos, K., Scherf, U. and Neher, D. (2012). *Journal of Physical Chemistry Letters* **3** (5), 640.

- [62] Veldman, D., Ipek, O., Meskers, S.C.J., Sweelssen, J., Koetse, M.M., Veenstra, S.C., Kroon, J.M., van Bavel, S.S., Loos, J. and Janssen, R.A.J. (2008). *Journal of the American Chemical Society* **130** (24), 7721.
- [63] Onsager, L. (1938). *Physical Review* **54** (8), 554.
- [64] Goodman, A.M. and Rose, A. (1971). *Journal of Applied Physics* **42** (7), 2823.
- [65] Blom, P.W.M. M., de Jong, J.M. and Vleggaar, J.J.M. (1996). *Applied Physics Letters* **68** (23), 3308.
- [66] Pivrikas, A., Sariciftci, N.S., Juška, G. and Österbacka, R. (2007). *Progress in Photovoltaics* **15** (8), 677.
- [67] Sze, S.M. (1985). *Semiconductor Devices Physics and Technology* (Wiley), New York.
- [68] Petty, M.C. (2007). *Molecular Electronics: From Principles to Practice* (Wiley), Chichester.
- [69] Kirchartz, T., Pieters, B.E., Kirkpatrick, J., Rau, U. and Nelson, J. (2011). *Physical Review B* **83** (11), 115209.
- [70] Cowan, S.R., Roy, A. and Heeger, A.J. (2010). *Physical Review B*, **82** (24), 245207.
- [71] Kuik, M., Koster, L.J.A., Wetzelaer, G.A.H. and Blom, P.W.M. (2011). *Physical Review Letters*, **107** (25), 256805.

Chapter 3

Experimental methods and materials

In this chapter we introduce the materials used in this study, provide an overview of key equipment used and highlight general OPV device fabrication methods.

A typical OPV device structure that was fabricated in this work was based on the following geometry: Substrate/anode (TCO)/hole transport layer/active layer (BHJ)/cathode (metal) for which the components used in each layer are given below:

Substrate	Anode	Hole transport layer	Active layer	Cathode
Glass	ITO	PEDOT:PSS	P3HT:PCBM	Aluminium

3.1 Materials

3.1.1 Indium Tin Oxide (ITO)

Indium Tin Oxide (ITO) is a transparent conductive oxide (TCO) that is widely used as an anode material in organic photovoltaics. Properties that make it attractive in organic solar cell applications include its high transparency in the visible range (400 – 800 nm), high electrical conductivity ($30 - 2.3 \Omega^{-1}\text{cm}^{-1}$) and superior substrate adherence [1].

ITO is made up of a mixture of In_2O_3 (90%) and SnO_2 (10%). It has a bandgap of 3.7 eV and a workfunction of about 4.7 eV.

The ITO coated glass substrates used in this study had a surface resistivity of 30 – 60 Ω/sq and were purchased in batches of 2.5 cm^2 pieces from Sigma Aldrich.

3.1.2 Poly(3,4-ethylenedioxythiophene)-polystyrenesulphonate (PEDOT:PSS)

PEDOT:PSS as represented in Figure 3.1, results from taking a conducting polymer poly(3,4-ethylenedioxythiophene) and doping it with poly(styrene sulfonate)

anions. PEDOT:PSS (1.3 wt % dispersion in H₂O) was purchased from Sigma Aldrich and appears dark blue in colour to the human eye.

PEDOT:PSS performs several functions in an OPV device. Firstly, it smoothens the “rough” ITO surface thus preventing short circuits. Secondly, it acts as a buffer between ITO and the active layer thereby preventing possible diffusion of oxygen from the ITO into the active layer. Thirdly, it acts as hole transport layer (HTL) as a result of having a workfunction higher than that of ITO [2, 3].

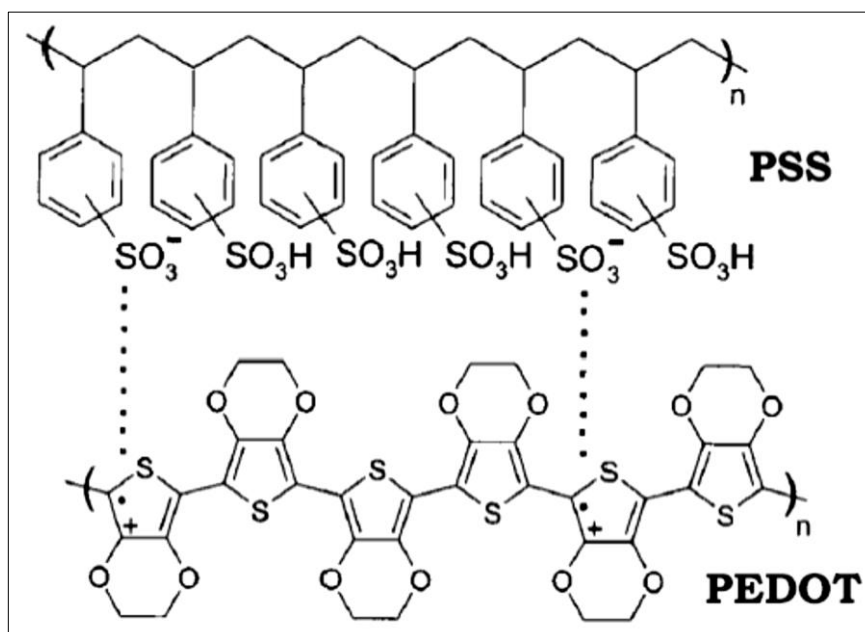


Figure 3.1: Chemical structure of the hole transport layer PEDOT:PSS.

3.1.3 Poly (3-hexylthiophene 2,5 diyl) (P3HT)

The P3HT (purity: 99.995%) used in this study was purchased from Sigma Aldrich. P3HT, as seen in Figure 3.2, is a conjugated polymer which exhibits a high degree of regioregularity (rr). Regioregularity has a direct effect on the degree of crystallinity and subsequently, on the charge transport.

P3HT is an electron donor material having an electrical conductivity that results from the delocalization of electrons along its polymer backbone. Its LUMO level is 3.2 eV and the HOMO level is at 5.1 eV [4].

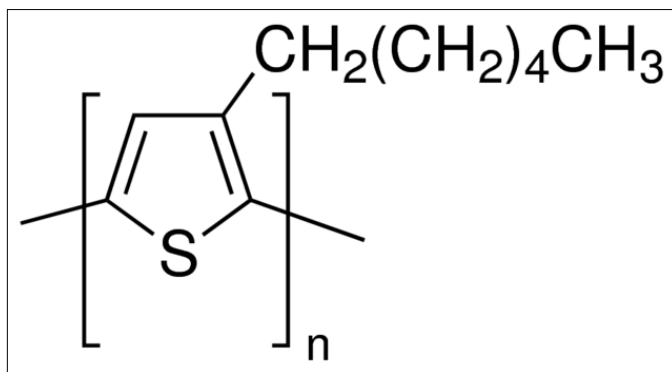


Figure 3.2: Chemical structure of P3HT.

3.1.4 [6,6]-phenyl-C₆₁ butyric acid methyl ester / [6,6]-phenyl-C₇₁ butyric acid methyl ester (PC₆₁BM/PC₇₁BM)

Two fullerene derivatives, [6,6]-phenyl-C₆₁ butyric acid methyl ester (PC₆₁BM) and [6,6]-phenyl-C₇₁ butyric acid methyl ester (PC₇₁BM) were used as electron acceptor materials in this study. These PCBM (purity: 99.5%) materials, Figure 3.3, were purchased from Sigma Aldrich as well. These fullerene derivatives are highly soluble in common organic solvents such as chlorobenzene (C₆H₅Cl) and chloroform (CHCl₃). The HOMO and LUMO levels for both fullerenes have been found to be about 6 eV and 4 eV respectively [5 - 7].

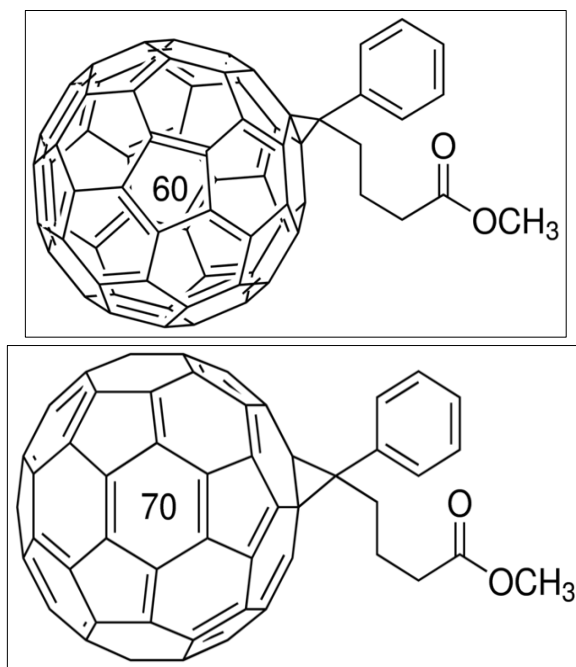


Figure 3.3: Chemical structures of PC₆₁BM and PC₇₁BM.

3.2 Device fabrication set ups: Spin coating and metallization

3.2.1 Spin Coater

A 2-stage CHEMAT precision spin coater (Figure 3.4), was used in this study for the attainment of precise and uniform deposition of thin films and coatings. The added advantage of being a 2-stage spin coater is that it allows for variation in rotation speeds, a feature that is vital in obtaining coatings that are uniform.

The ability to consistently deposit uniform thin films was critical in this study. A variety of organic materials were deposited on the transparent conducting oxide (TCO) as part of the fabrication process of OPV devices. Spin coating is a cost effective, reliable method of coating TCOs with thin films. Spin coating uniform thin films of organic materials on TCOs enables the variation of film thicknesses, by varying spin rates (rpm). Spin coating provides an added advantage of enabling a quick and easy way of producing uniform films that can have thicknesses ranging from a few nanometres to a few microns [8].



Figure 3.4: A photograph of the 2-stage CHEMAT precision spin coater.

3.2.2 Thermal evaporator

Thermal Evaporation, as one of the simplest of the Physical Vapor Deposition (PVD) techniques, continues to be employed in many thin film coating applications. In this study, thermal evaporation was used as a primary technique of forming the

Al cathode in the fabrication of OPV devices. Thermal evaporation is a vacuum based technique that involves three basic processes:

- evaporation (or sublimation) of the source material,
- mass transport of the evaporant (flux)
- condensation of the evaporant on the substrate (Figure 3.5).

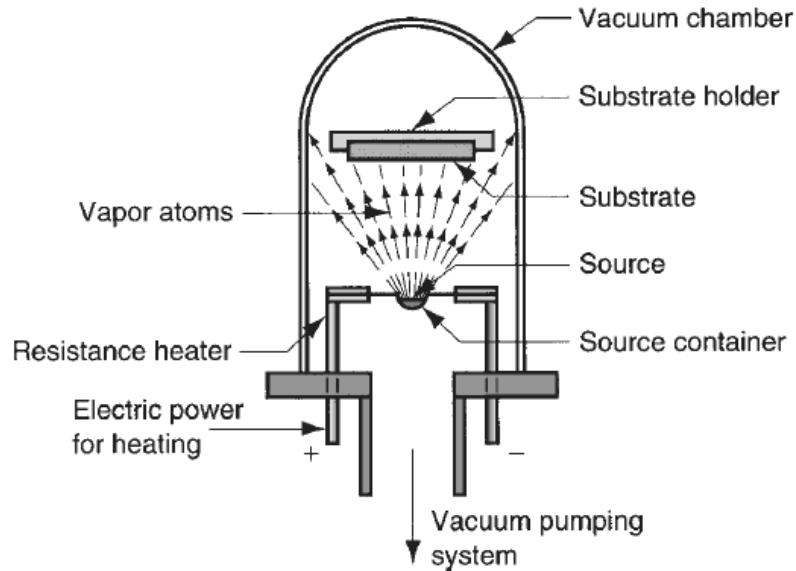


Figure 3.5: A schematic diagram of a thermal evaporation system [9].

Besides simplicity, other advantages of employing a vacuum thermal evaporation technique are that solid materials melt at lower temperatures in a vacuum and there is a reduced chance of oxide formation thereby limiting impurities to the barest minimum. Furthermore, the technique ensures homogeneity of deposited films at relatively high deposition speeds. The film thicknesses and deposition rates can be readily monitored, during the deposition process, by a quartz crystal monitor.

The metallisation of the aluminium electrode through a specially machined mask was realised by first pumping the vacuum chamber to sufficiently high vacuum ($<2 \times 10^{-5}$ mbar). With the aluminium placed on a helix-shaped tungsten wire ($T_M = 3422^\circ\text{C}$) or on a helix-shaped molybdenum wire ($T_M = 2623^\circ\text{C}$), a current was passed through to melt and thereby vaporise aluminium. The vapour atoms condense on the substrate, placed appropriately above the source, forming a thin aluminium film

of about 100 nm. The thermal evaporator that was used in the metallisation of aluminium electrodes is shown in Figure 3.6.



Figure 3.6: A photograph of thermal evaporation setup showing the following: (1) Penning gauges, (2) vacuum chamber, (3) diffusion pump, (4) variac, (5) power supply and (6) rotary pump.

3.2.3 Furnace

Annealing of fabricated OPV devices was done in a Carbolite® high temperature tube furnace, operated with a Eurotherm temperature controller as seen in Figure 3.7. The tube was modified to allow for annealing under various gas (O, Ar, Ar:H) environments. In our case, all OPV devices were in an argon environment in the ramping and hold up cycles. The argon flow was monitored using a purpose built gas bubbler system.

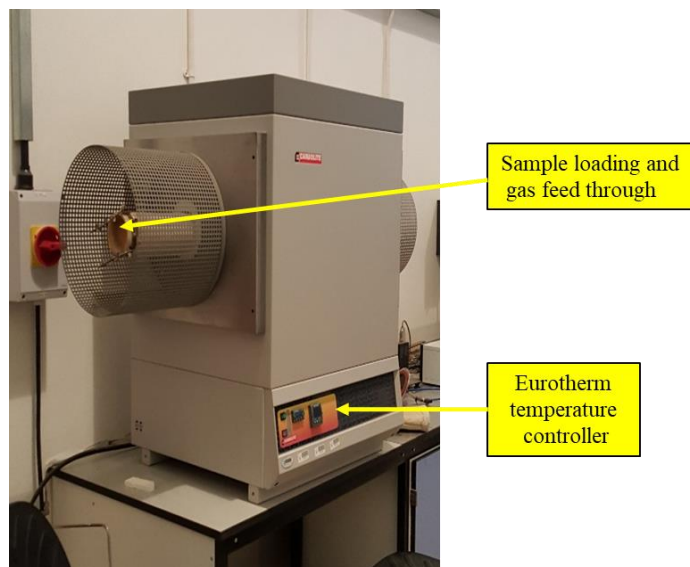


Figure 3.7: A photograph of the Carbolite® high temperature tube furnace.

3.2.4 Cary 500 UV–visible spectrometer

The Cary 500 Scan UV-Vis NIR Spectrometer (UV = 200 - 400 nm, visible = 400 - 800 nm) (Figure 3.8), probes the electronic transitions of molecules as they absorb light in the UV and visible regions of the electromagnetic spectrum and can also be used to investigate free carrier excitations in the NIR region. In this study, the instrument was used to characterise the optical properties i.e. the absorption characteristics of fabricated OPV devices.

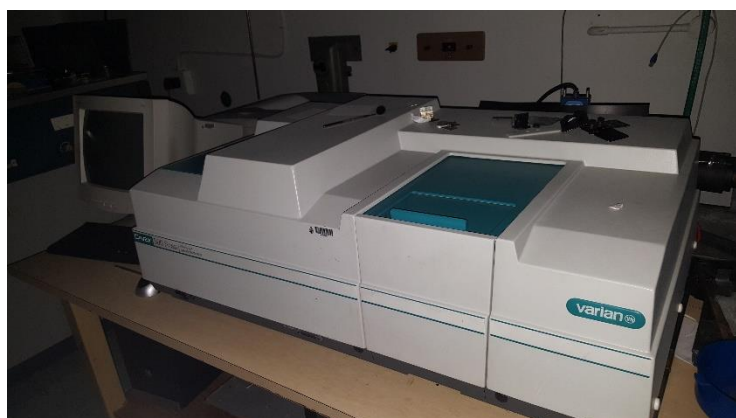


Figure 3.8: A photograph of the Cary 500 UV–vis NIR spectrophotometer.

3.2.5 I – V set up

Our home built I – V measurement setup is shown in Figure 3.9. An assembly of a Newport xenon lamp solar simulator, coupled to a source/Measure unit (HP 4141B DC), together with 1.5 air mass filters (AM 1.5), provided the required platform to carry out current–voltage (I–V) measurements on fabricated OPV devices under dark or illumination conditions. A PC with LabVIEW software was integrated into I – V measurement setup to give an output of measured current – voltage characteristics. Furthermore, measured I – V data was analysed using a specially coded Python based program.

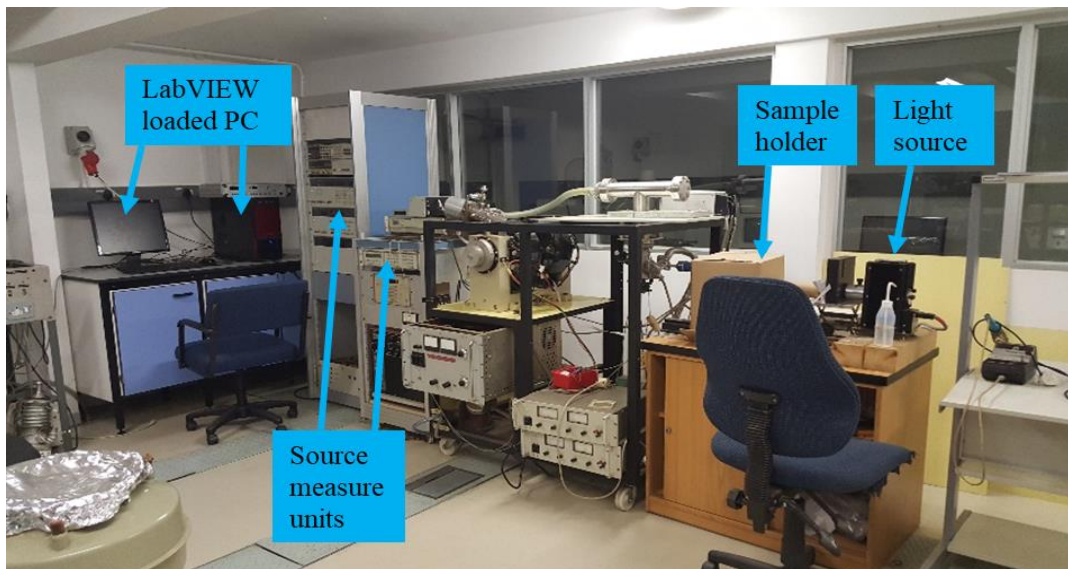


Figure 3.9: A photograph of the current - voltage (I – V) setup integrated with the optical unit for PV characterisation.

3.3 Device fabrication methods

The overview of the device fabrication methodology is shown in Figure 3.9. This description covers the basic fabrication process of an OPV device, any deviations that relate to specific devices will be mentioned in their respective chapters.

The fabrication process commences with the preparation of active layer solutions in the following manner:

10 mg of P3HT and PCBM each were dissolved separately in 0.5 ml of chlorobenzene by stirring the solutions for three hours in ambient conditions. The two solutions were then mixed and again magnetically stirred, in ambient, for two hours to form a 20 mg/ml solution i.e. a 1:1 wt % solution.

The preparation of the ITO coated glass substrates was done whilst the solutions were being stirred for the cumulative five hour period.

The ITO coated glass substrates bought as 2.5 cm² pieces were cut into 1.25 cm × 1.25 cm slices using a diamond tipped scribe. These smaller squares were then etched via a wet chemistry method using zinc powder and 2M hydrochloric acid. Patterning of the ITO substrates is carried out to ensure complete isolation of the anode and the cathode such that the devices do not short circuit during I - V measurements.

The cleaning of the substrates was commenced with a thorough wash with a liquid soap detergent and a subsequent rinse with deionized (DI) water. Further cleaning included an ultrasonic bathing of the substrates with DI, acetone and ethanol for 5 minutes each in a sequential manner, to remove organic stains and surface contaminants. The substrates were dried with nitrogen prior to the sequential spin coating of the device layers. The hole transport layer, PEDOT:PSS was subsequently spin coated onto the patterned ITO substrates at 2000 rpm for 60 seconds and later annealed at 100 °C on a hot plate in ambient for 15 min to remove any residual water [10].

Using a pipette to deliver a volume that covered the patterned 1.25 cm² slices, the polymer:fullerene, P3HT:PCBM, blend was then spin coated at 2000 rpm for 60 seconds onto the ITO/PEDOT:PSS layer to yield a homogeneous film. The hot plate annealing and the spin coating were done in a fume cupboard under ambient conditions.

Aluminium, the metal top electrode was deposited by thermal evaporation, in a vacuum of about 2×10^{-6} mbar, through a mask with a cross-sectional area of about 16 mm² from which a device active area of about 7 mm² was determined due to patterning. Devices with structures GLASS/ITO/PEDOT:PSS/P3HT+PCBM/Al were then annealed in argon before characterisation of optical structural and electronic properties. The temperatures at which devices were annealed and the

durations for which they were annealed depended on the specific details of the study at hand. The specific details are mentioned in the results chapters.

3.3.1 Layer and device characterization studies/procedures

The current–voltage (I–V) measurements were done using the solar simulator (150 W Xe lamp) with 1.5 air mass filters and a source/Measure unit (HP 4141B DC) unit under 100 mW/cm^2 illumination. Optical absorption measurements of fabricated devices were made using the Cary 500 UV – VIS - NIR spectrometer. The Raman bands and the structural order of all the films were examined using a Jobin Yvon T64000 Raman spectrometer which was fitted with an Olympus BX41 microscope not only to focus incident light and to collect backscattered light, but also to take optical micrographs of samples if needed. Additionally, it was equipped with an Ar ion laser (514.5 nm) which was normally tuned at 4 mW laser power due to radiation damage considerations.

For clarity and emphasis we re-state the fact that in this work, fabrication and characterisation processes were carried out in ambient.

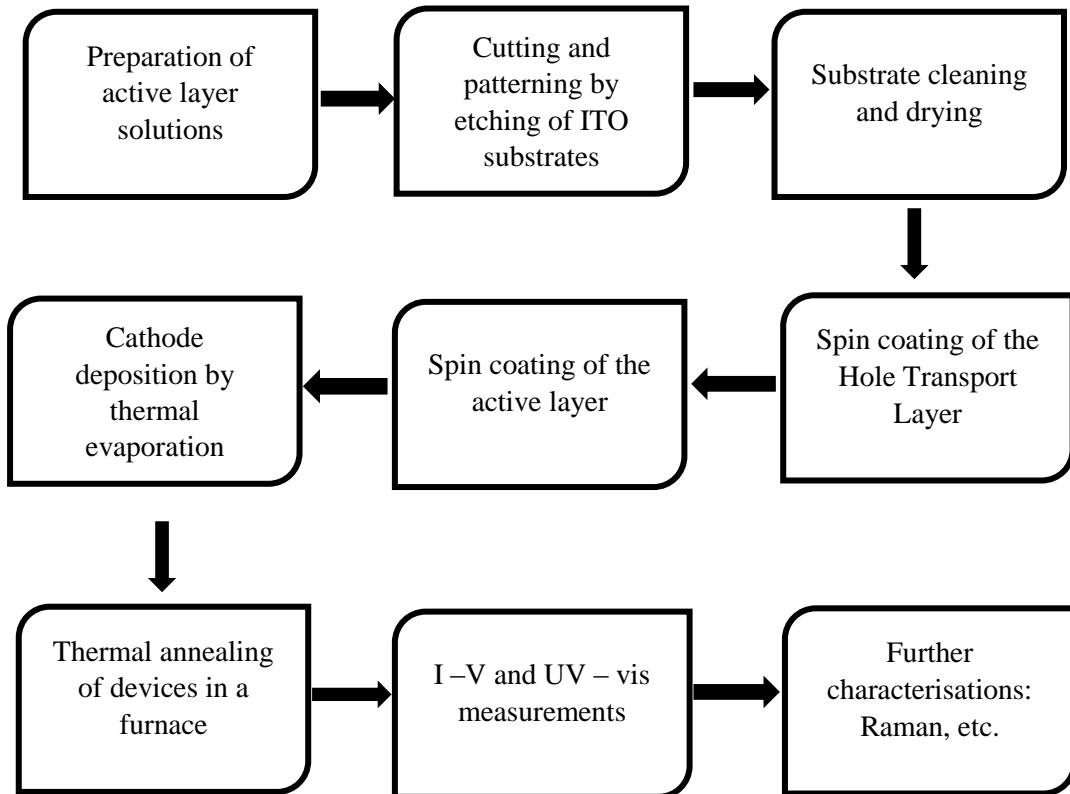


Figure 3.10: Device fabrication process flow chart.

3.4 Summary

This chapter details device fabrication materials and their basic properties. Additionally, an introduction to key equipment used in the fabrication of OPV devices is made and an overview of the fabrication and characterisation of a typical OPV is given.

3.5 References

- [1] Chiguvare, Z. (2005). *Electrical and Optical Characterization of Bulk Heterojunction Polymer- Fullerene Solar Cells*. PhD thesis, Oldenburg University, Germany.
- [2] Huang, J., Miller, P.F., Wilson, J.S., de Mello, A.J., de Mello, J.C. and Bradley, D.D.C. (2005). *Advanced Functional Materials* **15** (2), 290.
- [3] Koch, N., Vollmer, A. and Elschner, A. (2007). *Applied Physics Letters* **90** (4), 043512.
- [4] Veldman, D., Meskers, S. and Janssen, R. (2009). *Advanced Functional Materials* **19** (12), 1939.
- [5] Mihailetschi, V.D., van Duren, J.K., Blom, P.W.M., Hummelen, J.C., Janssen, R.A.J., Kroon, J.M., Rispen, M.T., Verhees, W.J.H. and Wienk. M.M. (2003). *Advanced Functional Materials* **13** (1), 43.
- [6] Thompson, B.C., Kim, Y. and Reynolds, J.R. (2005). *Macromolecules* **38** (13), 5359.
- [7] Zhou, H., Yang, L., Stoneking, S. and You, W. (2010). *ACS Applied Materials & Interfaces* **2** (5), 1377.
- [8] <https://www.ossila.com/pages/spin-coating> [accessed 16/03/2014].
- [9] <http://www.mechscience.com/physical-vapor-deposition/> [accessed 10/01/2017]
- [10] Otieno, F., Airo, M., Ranganathan, K. and Wamwangi, D. (2016). *Thin Solid Films* **598**, 177.

Chapter 4

Optical and electrical mass ratio studies of P3HT:PC₇₁BM BHJ OPV devices

4.1 Introduction

Organic photovoltaics based on the polymer:fullerene bulk heterojunction (BHJ) architectures continue to attract intensive research in the quest for lower production and manufacturing costs and the attainment of higher power conversion efficiencies. As stated in Chapter 2, a BHJ is a three-dimensional heterostructure made up by at least two materials:

one primarily absorbs light and is an electron donor and the other one is an electron acceptor. Research on these devices has seen numerous studies on the employment of P3HT as an electron donor and the fullerene [6,6] phenyl-C60-butyric acid methyl ester (PC₆₀BM) or its derivative (PC₆₁BM) as an acceptor material in organic solar cells. These studies have covered a range of investigations that include: efficiency and stability [1 - 4], effect of thermal annealing [5 - 7], morphology and nanostructure [8 - 10] and the inclusion of additives in fabricated devices [11 - 16]; all as part of the endeavour to not only improve the photovoltaic performance but also to better understand the working principle of OPV devices.

The fullerene derivative [6,6]-phenyl-C71butyric acid methyl ester (PC₇₁BM) is a higher fullerene analogue of (PC₆₁BM). As compared to (PC₆₁BM), (PC₇₁BM) has better optical absorption in the visible region [17, 18]. Furthermore, it has been reported that given the same testing conditions, the substitution of (PC₆₁BM) with (PC₇₁BM) in the fabrication of polymer solar cells has led to a 50% increase in photocurrent [19]. However, a prevalent method of incorporating (PC₇₁BM) as an electron acceptor into an OPV device tends to be done in conjunction with low band gap polymers such as PTB7, PCDTBT or PBDTT-DPP [20 - 22].

Reports are not that widespread where the well-studied and characterised polymer, P3HT, has been used solely (i.e. without additives) with (PC₇₁BM) in the

fabrication of OPV devices. Recently, Singh .et .al [23] carried out a study where P3HT:PC₇₁BM OPV devices were fabricated albeit with an inclusion of different cathode buffer layers such as Lithium Fluoride (LiF), Bathocuproine (BCP) and Bathophenanthroline (BPhen). In their study, devices with varying P3HT:PC₇₁BM mass ratios (1:0.6; 1:0.8; 1:1.0; and 1:1.2) and under varying annealing temperatures (100 °C, 125 °C, 150 °C and 175 °C) were investigated. Their studies concluded that the best performing device was the one with the 1:0.8 mass ratio annealed at a temperature of 150 °C. This, in part, they ascribed to better phase separation of the active layer blend due to the improvement of the crystallinity of the P3HT donor material. As a result of their usage of buffer layers, they also pointed out the better hole blocking capacity of BCP/Al cathode as another reason for the improvement in performance.

The photovoltaic performance of fabricated OPV devices depends on a number of factors such as deposition techniques (spin coating, doctor blading, drop casting, etc.), solvent choice, solvent annealing, active layer blend composition and post fabrication thermal annealing of devices. Though we did not set out to make a direct comparative study between P3HT:PC₆₁BM and P3HT:PC₇₁BM OPV devices, given stated advantages that PC₇₁BM has over PC₆₁BM, we set out to study the BHJ P3HT:PC₇₁BM OPV system in order to better understand its current - voltage characteristics and how these influence its PCE at optimised mass ratios of the BHJ P3HT:PC₇₁BM OPV device. Additionally, the effect of thermal treatment regime on the current – voltage characteristics and the eventual PCE of fabricated devices was investigated for systemic understanding of the charge transport and recombination dynamics that influenced the measured power conversion efficiencies.

Numerous reports on thermal annealing of polymer:fullerene OPV devices point to the beneficial effects of thermal annealing towards the photovoltaic performance of fabricated devices. However, the reported annealing temperatures and annealing times point to the need for more concerted efforts in the understanding of the underlying physics that underpins the observations. Key amongst the identified observations that are beneficial to PV performance as a result of thermal annealing,

is the resulting phase segregation of the active layer materials coupled with improved crystallinity within each phase, an effect that is more pronounced in the P3HT donor material. The effect thereof is the improvement in charge transport by the creation of continuous pathways to respective electrodes [24 - 34].

4.2 Experimental methods

4.2.1 Mass ratios solutions preparations

The polymer:fullerene, P3HT:PC₇₁BM, blend solutions were prepared by firstly weighing three 10 mg samples of the P3HT polymer and three samples of the PC₇₁BM fullerene with masses 10 mg, 8 mg and 6 mg. The 6 samples were individually dissolved in 0.5 ml (each) of chlorobenzene, as in Table 4.1, by stirring them with magnetic stirrers for 3 hours in the fume cupboard under ambient conditions. Thereafter, P3HT:PC₇₁BM blend solutions with mass ratios 1:1; 1:0.8 and 1:0.6 resulting in the following composition solutions in chlorobenzene: 20 mg/ml; 18 mg/ml and 16 mg/ml, were stirred under the same conditions for 2 more hours to obtain a thoroughly mixed donor:acceptor solution. This means that in each experimental run, three carefully marked substrates were prepared for this leg of the device fabrication process that was meant to identify the optimum P3HT:PC₇₁BM mass ratio for active layer. The mass ratio that gave the best power conversion efficiency was deemed the optimum ratio and was then selected for further analysis. To this effect, the 1:0.8, P3HT:PC₇₁BM, active layer blend was the one identified and selected for further study.

Table 4.1: Prepared mass ratio samples showing individual P3HT and PC₇₁BM masses that make up the P3HT:PC₇₁BM active layer blend together with the volume of chlorobenzene (C₆H₅Cl) they were dissolved in.

Mass ratio	P3HT		PC ₇₁ BM	
	Mass (mg)	Volume (ml)	Mass (mg)	Volume (ml)
1:1	10	0.5	10	0.5
1:0.8	10	0.5	8	0.5
1:0.6	10	0.5	6	0.5

4.2.2 Samples preparation for energetics and kinetics measurements

A P3HT:PC₇₁BM blend in the ratio 1:0.8 was prepared resulting in an 18 mg/ml solution in chlorobenzene. Numerous patterned ITO coated glass substrates were prepared for fabricating devices for ‘energetics and kinetics’ measurements. In summary, three devices were fabricated and then annealed in argon at 50 °C, 80 °C and 110 °C all for 10 minutes. Furthermore, three devices were then fabricated and annealed in argon at 50 °C for 10, 25, 40 minutes.

4.2.3 Fabrication of devices

The general OPV device fabrication method outlined in Chapter 3 was followed however, adaptations were made specific to the study covered in this chapter. The mixing of solutions, the cleaning of the ITO patterned glass substrates and the annealing of the PEDOT:PSS layer on the hot plate were done in a fume cupboard with the extractor running at all times. Apart from annealing of completed devices, the rest of the steps in the fabrication process and all device characterisations were carried out at ambient conditions. Stemming from the results obtained from the measurements on P3HT:PC₆₁BM bulk heterojunction devices in our lab under similar conditions [35], the starting temperature for the annealing of the devices after the metallisation of the cathode by thermal evaporation, was 50 °C for 10 minutes in an argon-filled furnace. The ITO patterning and the cathode deposition resulted in devices having an active area of about 7.0 mm². The current – voltage (*I* - *V*) characteristics of the devices were obtained for different light intensities with the aid of a solar simulator (150W Xe lamp) using AM 1.5 filters and a source measure unit (HP 4141B DC). Optical absorption measurements of the devices were made using a Cary 500 UV–visible spectrophotometer. The structural properties of all the films were examined using a Jobin Yvon T64000 Raman spectrometer equipped with an Ar ion laser (514.5 nm) at 4 mW laser power.

4.3 Results and discussion

Part I

4.3.1 P3HT:PC₇₁BM mass ratio optimisation

4.3.1.1 Optical characteristics

Figure 4.1 shows the absorption spectra of fabricated devices having the structure GLASS/ITO/PEDOT:PSS/P3HT:PC₇₁BM/Al with the variations in the active layer blend as indicated. Measurements were taken on the on the P3HT:PC₇₁BM active layer thin films. The most prominent feature in the spectra is the broad optical absorption peak in the visible range at about 500 nm most commonly associated with the P3HT $\pi-\pi^*$ band transitions [36]. This is accompanied by vibronic shoulders at 559 nm and 608 nm, the dotted red and green lines respectively. The 559 nm vibronic shoulder is associated with increased conjugation as a result of ordered stacking of the P3HT backbone. The one at 608 nm is related to the interchain $\pi-\pi$ interaction via electronic hopping. A less distinguishable, weaker PCBM optical absorption peak can be seen at 378 nm, marked by the solid yellow line.

As the amount of PCBM is decreased from the 1:1 ratio to 1:0.6 there is a red shift of the peak absorption wavelength from 486 nm to 510 nm. The red shift is greater for the 1:0.08 mass ratio. The observed enhancement in absorption could be due to increased inter-chain interaction in the P3HT which is highly likely at decreased PCBM ratio in the P3HT:PCBM blend [37 – 38].

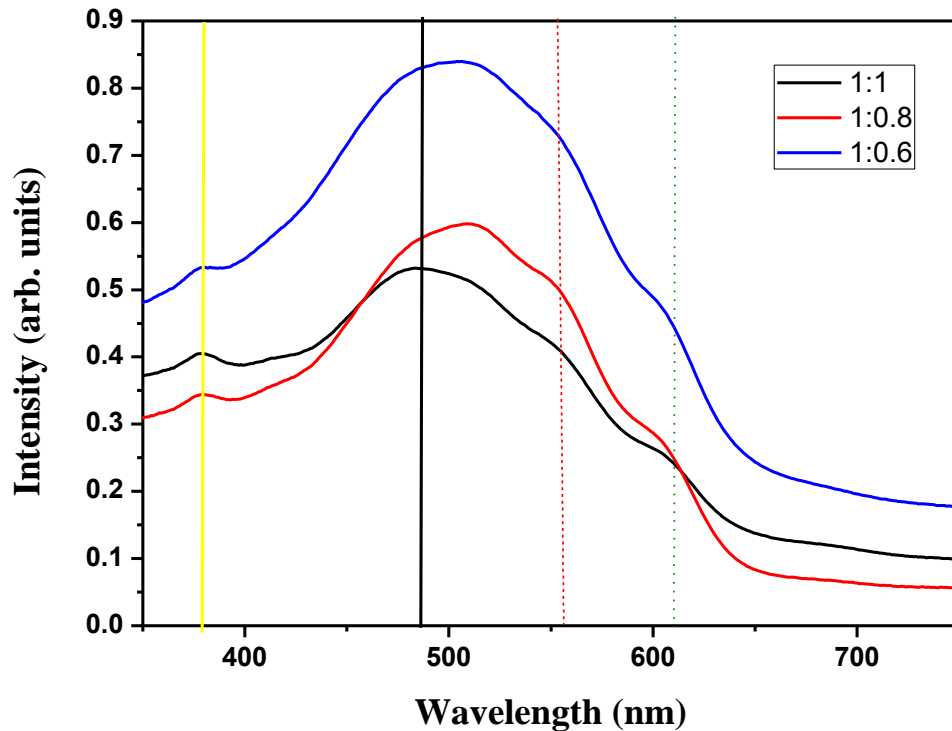


Figure 4.1: UV - Vis absorption spectra of P3HT:PC₇₁BM with varying mass ratios.

4.3.1.2 Current – Voltage OPV performance characteristics of mass ratio optimisation

The dark current plots, in both linear and semi-log scale, of fabricated devices are given in Figure 4.2. It is evident that the asymmetric nature of the $J - V$ curve indicates rectification in the fabricated devices. In electronic processes rectification occurs in diodes and can be quantified from current – voltage characteristics. Briefly, an ideal rectifier only allows current to flow in one direction and this manifests itself as an exponential $J - V$ plot in the analysis of current – voltage characteristics. As stated in Section 2.2, a photovoltaic cell can be described as a diode, meaning that the rectification ratio can be regarded as a figure of merit for comparing the effectiveness of rectification in fabricated devices [39]. Device rectification, determined by calculating the rectification ratio (factor) RR or RF using:

$$RR = \left| \frac{I(V)}{I(-V)} \right| \quad (4.1)$$

That is, from current-voltage characteristics (or curve), RR is the absolute value of the ratio of the current at two equal but opposite voltages. Put differently, it is the absolute value of the ratio of the forward bias current to the reverse bias current at a specific voltage. The following RR values were obtained at 1.0 V:

Table 4.2: Rectification ratios for varying P3HT:PC₇₁BM mass ratios.

Sample	Mass Ratio	RR
R1	1:1	2046
R2	1:0.8	2562
T3	1:0.6	1666

The decrease in rectifying behaviour observed in sample T3, is indicative of the decrease in R_{sh} as will be seen later in Table 4.3. It is generally attributed to a degradation of potential barriers or charge carrier barriers at the metal/organic semiconductor interfaces. At metal-semiconductor interfaces in ITO/PEDOT:PSS/P3HT:PCBM/Al OPV devices, large potential barriers can be found under reverse bias conditions. This tends to lead to high RR values commonly found in organic diodes [40 – 42].

Noted from Figures 4.2 (a) and (b) is that there is a variation in the generated photocurrent as a result of changing the P3HT:PC₇₁BM mass ratios. The decrease in the PC₇₁BM content in the P3HT:PC₇₁BM blend from 1:1 to 1:0.6 resulted in almost a 1.5 times increase in the current density i.e. from 7.20 mA/cm² to 10.5 mA/cm². In a study of P3HT:PC₇₁BM blend ratios as a function of storage time, Kwon [43] found that comparing ratios 4:1, 1:0.6, 1:0.8 and 1:4, the 1:0.6 blend gave the highest current density albeit by a small amount as compared to the 1:0.8 blend. The key focus of this study revolved around the monitoring of solar cell parameters for devices as a function of storage time. It should be noted though that the devices fabricated in this study followed a somewhat different fabrication process and included TiO_x and LiF as buffer layers between the active layer blend

and the cathode. Furthermore, we have already seen that Singh *et al.* [23] established a mass ratio of 1:0.8 as the optimal ratio for best device performance. Considering the key performance figure of merit, the PCE, The P3HT:PC₇₁BM blend ratio of 1:0.8 gave the best value of 2.86% as can be seen in Table 4.2.

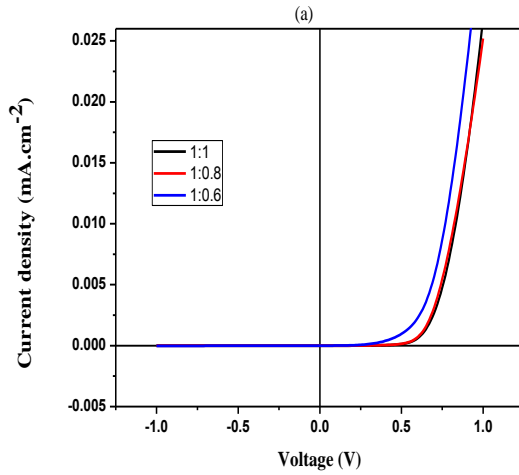


Figure 4.2: (a) Dark current $J - V$ plots for different mass ratios.

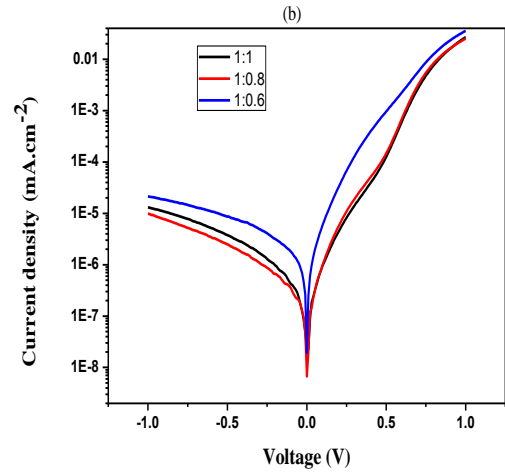


Figure 4.2: (b) Semi-log dark current $J - V$ plots of different mass ratios.

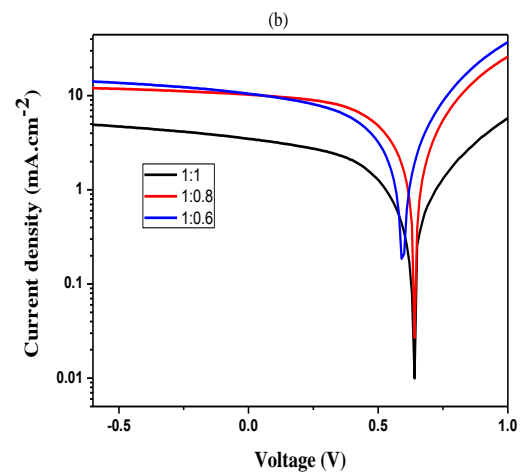
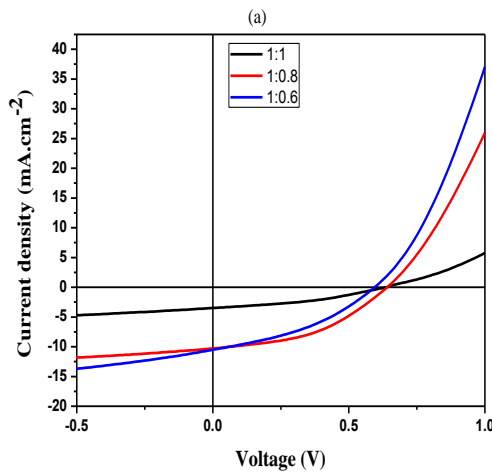


Figure 4.3: (a) $J - V$ characteristics of P3HT:PC₇₁BM mass ratios under AM1.5 illumination at 100 mW/cm² (b) Semi-log plots of the same curves.

Table 4.3: A summary of the performance of the OPV devices with varying P3HT:PC₇₁BM mass ratios.

Sample	Mass Ratio	V_{oc} (V)	J_{sc} (mA/cm ²)	FF (%)	PCE (%)	R_{sh} (Ω cm ²)	R_s (Ω cm ²)
R1	1:1	0.63	7.20	43.5	1.97	250.0	31.5
R2	1:0.8	0.63	10.3	43.4	2.86	250.0	24.7
T3	1:0.6	0.60	10.5	37.6	2.35	126.9	25.9

4.3.1.3 Charge transport properties as a function of mass ratio

We investigated charge carrier injection dynamics by employing Fowler-Nordheim and Richardson-Schottky models and with regards to bulk transport properties, we applied the Mott-Gurney law to calculate charge carrier mobilities of fabricated devices.

4.3.1.3.1 Injection limited contribution

In Chapter 2 we saw that the contribution towards the total generated current in an OPV device can be explained in terms of emission models at metal – polymer interfaces and bulk transport dynamics. The Richardson-Schottky (RS) thermionic emission model and the Fowler-Nordheim (FN) field emission model were applied to study contributions coming from injection limited currents. Figures 4.4 and 4.5 show the FN plots and the RS plots as functions of different P3HT:PC₇₁BM mass ratios. The nature and shapes of the plots give confirmation of the existence of interfacial charge injection. Each plot in Figure 4.4 is based on the $\ln(J/V^2)$ vs $(1/V)$ relation due to FN theory of charge injection at metal – polymer interfaces.

The FN plots in Figure 4.4 show the characteristic trends exhibiting negative slopes at high fields (3.6×10^6 V/m) indicating quantum mechanical tunnelling of charge carriers through a potential barrier. A transition electrical field, denoting a cross-over from field emission to thermionic emission, can be ascertained from the minimum of the curve. Thermionic emission being the low electric field region specified from the $(1/V)$ region. From these FN plots, individual slopes of the curves lead to the determination of magnitudes of potential barriers. With the

steepness of the slope directly proportional to the barrier height, fitted values can be obtained where the greater the slope, the higher is the associated potential barrier, ϕ_B . A dependence of the steepness of the slope on the P3HT:PC₇₁BM mass ratios was observed with slope 1:1 > slope 1:0.8 > slope 1:0.6. Thus establishing a mass ratio based pattern of the degree of difficulty in injecting charge carriers through a metal – active layer junction.

In Figure 4.5 we observe the expected plots based on the RS thermionic emission model at lower electric fields. That is, at lower fields, plots of $\ln J$ vs \sqrt{V} show a positive slope of a straight line fit and this is indicative of charge injection by thermionic emission through the metal - polymer interface. Once again, potential barriers at constant temperature, corresponding to injection by thermionic emission can be found from Equation (2.24) i.e. $\phi_B = (\ln A^* + 2 \ln T - c)k_B T$. The greater the negative intercept, c , leads to the greater potential barrier. In this case, the intercept pattern was found to be 1:1 > 1:0.8 > 1:0.6.

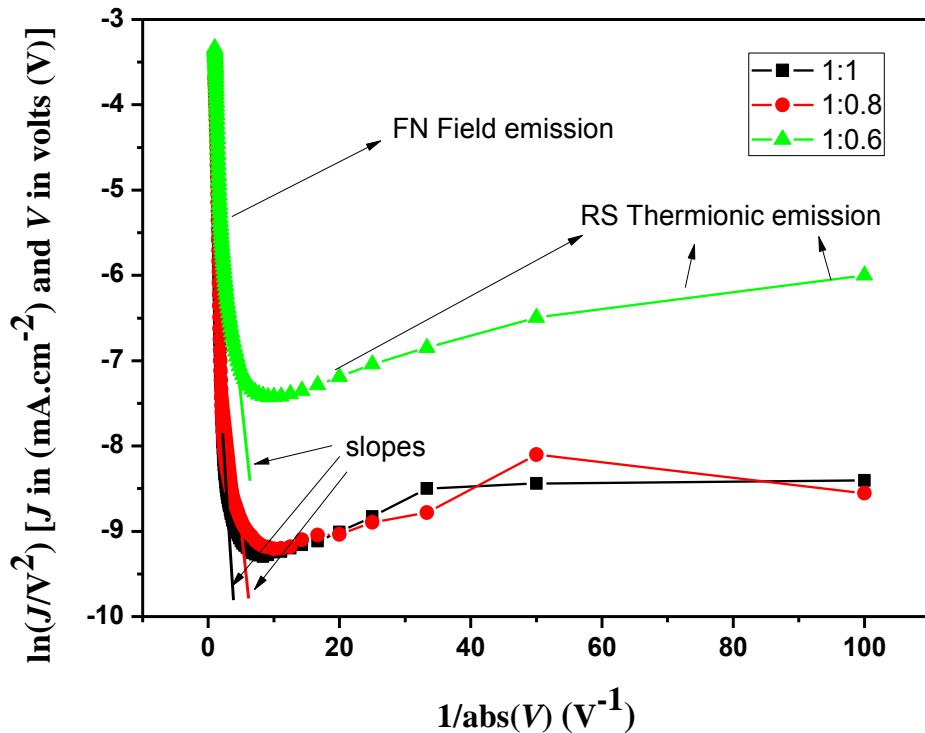


Figure 4.4: FN plots compared for different P3HT:PC₇₁BM active layer mass ratios in the dark under forward bias with the relative slope guides indicated.

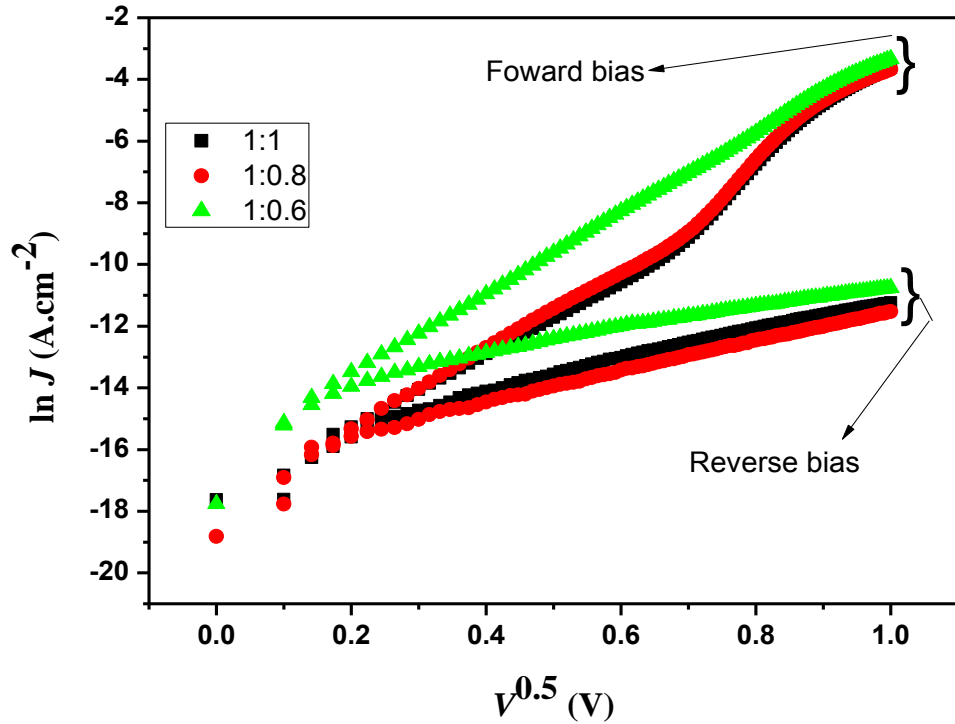


Figure 4.5: RS plots compared for different P3HT:PC₇₁BM active layer mass ratios in the dark under forward and reverse bias showing the changes in the respective slopes.

4.3.1.3.2 Bulk limited contribution

Figure 4.6 shows the $\log J$ vs $\log V$ plots for different mass ratios. The longbow-like or better still recurve-like shape can be divided into three parts depending on the general slope of the curves in each region. Region I exhibits a linear relation between J and V such that bulk charge carrier transport follows Ohmic behaviour i.e. $J \propto V$. In regions II and III, the slopes of the log-log plots take on values 2 and greater, these are the non-linear regions. With slopes ≥ 2 charge transport in the bulk is attributed to SCLC. Slopes ≈ 2 are associated with trap-free SCLC (TFSCLC). However, it should be noted that for slopes > 2 it does not necessarily imply that there are no traps, rather that traps are filled. The $J - V$ dependence in these regions is based on the Mott-Gurney law as in Equation (4.2) [44].

$$J = \frac{9}{8} \varepsilon_o \varepsilon_r \mu \frac{V^2}{d^3} \quad (4.2)$$

The linear fits of the Mott-Gurney law for different mass ratios are shown in Figure 4.7. The plot of J as a function of V^2 yields a straight line with a slope that enables the calculation of the charge carrier mobility, μ , where the measured thicknesses of the active layers were about 140 nm. This means that graphically, the greater the slope the higher the charge carrier mobility. So, from the graphs, it can be seen that $\mu_{1:0.6} > \mu_{1:0.8} > \mu_{1:1}$.

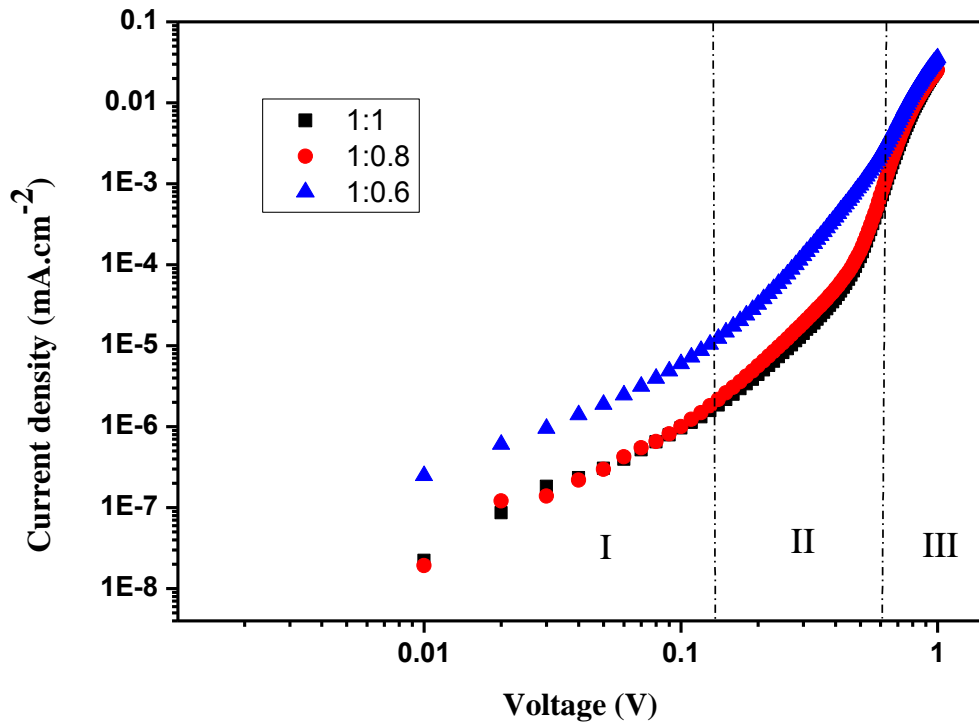


Figure 4.6: Dark current log-log plots of $J - V$ characteristics under forward bias for different P3HT:PC₇₁BM active layer mass ratio blends. Region I has slope = 1, indicating Ohmic conduction, region II has slope > 2, corresponding to SCLC characterised by trap filling and region III has a slope ≈ 2 and is described by Trap Free SCLC.

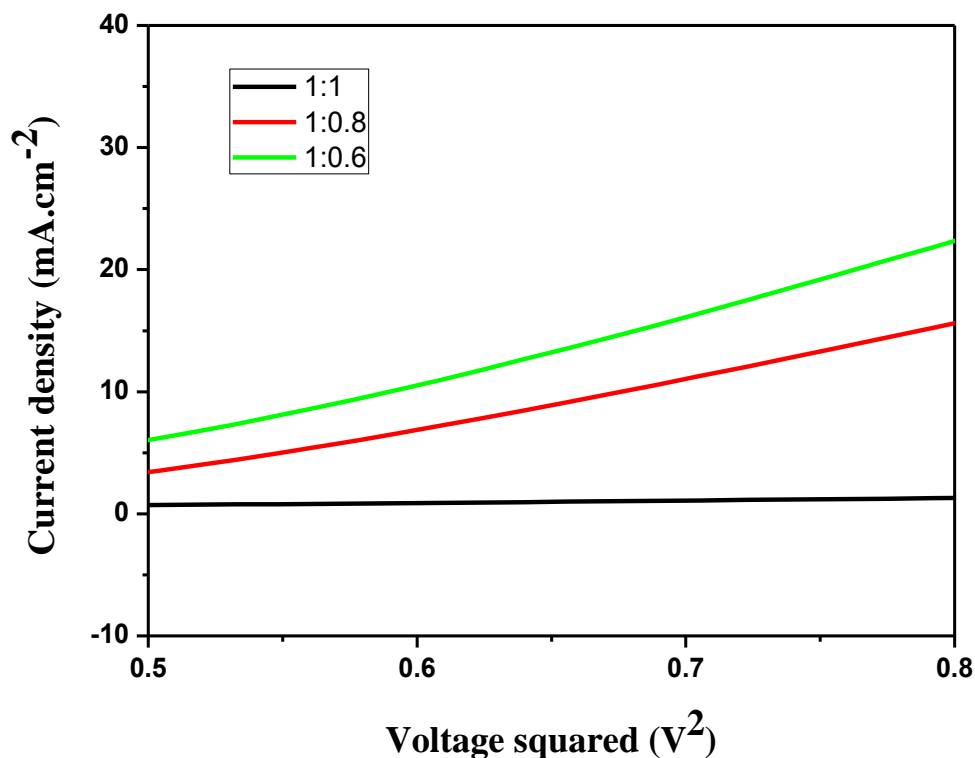


Figure 4.7: Mott-Gurney linear fits for P3HT:PC₇₁BM active layer mass ratio blends with thicknesses of about 140 nm. The J vs V^2 plots are for regions of high applied voltage form the current – voltage characteristics.

4.3.1.4 Light intensity behaviour as a function of mass ratio

To get a deeper insight into the photovoltaic performance and the charge transport mechanisms of fabricated devices, we measured parameters that are key in performance characterisation as a function of light intensity. An understanding of recombination dynamics at play for different mass ratios was found from the slopes of the plots of V_{oc} and J_{sc} as functions of light intensity. In short, recombination behaviour was probed via light intensity dependent measurements. Furthermore, a decreasing fill factor has been reported to have series resistance and bimolecular recombination based origins [45].

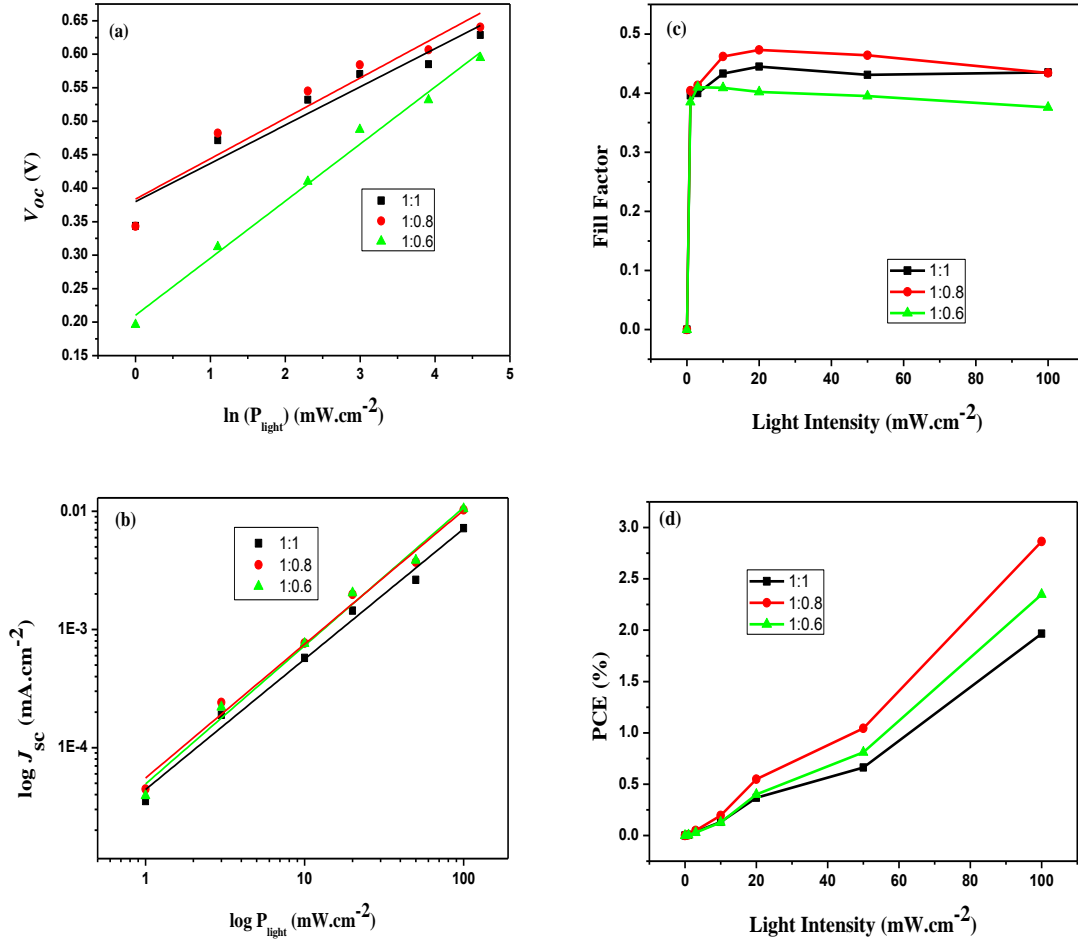


Figure 4.8: Variations of (a) Open circuit voltage (b) short circuit current density (c) fill factor (d) power conversion efficiency as a function of light intensity.

Figure 4.8 (a) is a semi-log plot of V_{oc} as a function of light intensity (P_{light}). Immediately, it can be observed that V_{oc} increases linearly as a function of the natural log of light intensity and that increase rates are different for P3HT:PC71BM mass ratios. Kirchatz et. al. [46], showed that experimentally, ideality factors can be determined from dark current $J - V$ plots or from light intensity *versus* V_{oc} plots. Therein, the authors elaborate on details related to each method (dark current or light intensity) are discussed. The ideality factor from the dark $J - V$ plot is defined as

$$n = \left(\frac{q}{k_B T} \right) \left(\frac{dV}{d(\ln(J))} \right) \quad (4.1)$$

with symbols taking on their usual meanings. On the other hand the ideality factor using $J - V$ plots under illumination is

$$n = \left(\frac{q}{k_B T} \right) \left(\frac{dV_{oc}}{d \ln(P_{light})} \right) \quad (4.2)$$

We used Equation (4.2) in the determination of ideality factors and hence the recombination type at open circuit voltage. Under open circuit conditions, charge generation = charge recombination hence the current is zero. That is, all photogenerated carriers recombine within the cell. This means that recombination dynamics near open circuit are particularly tuned to the details of the prevailing recombination mechanism. Thus providing direct motivation to characterise such recombination behaviour. As shown in Table 4.4, there is a mass ratio dependence of ideality factors with the mass ratio 1:1 showing the least and the mass ratio 1:0.6 the highest. Strong bimolecular recombination is indicated by ideality factors = 1, whilst an ideality factor of 2 (or more) is interpreted as trap-assisted type recombination. In this study ideality factors were found to be above 2 and even more than 3 in the case of the 1:0.6 mass ratio which is indicative of trap-assisted recombination as already mentioned. Such high ideality factors have been determined from P3HT:PCBM systems and were found to be resulting from an increase in induced density of deep states as a result of prolonged exposure to light [47, 48].

Table 4.4: A comparison of recombination (n and α) parameters and mobility (μ) values for different P3HT:PC₇₁BM active layer mass ratio blends.

Sample	Mass Ratio	n ± 0.26	μ $\pm 0.004 \times 10^{-6}$ (cm ² /Vs)	α ± 0.06
R1	1:1	2.22	2.568	1.10
R2	1:0.8	2.35	3.327	1.13
T3	1:0.6	3.32	4.663	1.17

For organic semiconductors, a power-law dependence of J_{sc} on illumination intensity (P_{light}) is followed. This means

$$J_{sc} = (P_{light})^{\alpha} \quad (4.3)$$

where α is a power law-scaling exponent. The values for α , for different active layer blends, are shown in Table 4.4.

Equation (4.3) is briefly explained as follows: its log-log plot yields a straight line with slope α . Values of $\alpha = 1$ are interpreted as weak bimolecular recombination i.e. strong monomolecular recombination is at play at short-circuit conditions. On the other hand, any deviation from $\alpha = 1$ points towards charge transport limited behaviour due to bimolecular recombination. With bimolecular recombination generally associated with bulk transport properties, it has been reported that the asymmetric nature of charge carrier mobility of holes and(or) electrons leads to the formation of space charge regions and this can be seen in deviations from $\alpha = 1$ [49].

In Figure 4.8 (c) we see the dependence of the fill factor on light intensity. For all 3 devices, the fill factor can be observed peaking between incident light intensities of 10 and 20 mW/cm². It then tapers off as the incident light intensity reaches 100 mW/cm². The 1:0.6 P3HT:PC₇₁BM mass ratio shows a bigger decrease and comparative values at 100 mW/cm² are listed in Table 4.4. This device shows comparatively higher bimolecular recombination at both open and short circuit conditions. This could explain its comparatively lower *FF*. However, with this observed, it was puzzling to see the device producing the highest photocurrent. This warranted further investigations that are beyond the scope of this study. The PCEs of the devices, calculated using Equation (2.6), are plotted as a function of light intensity in Figure 4.8 (d). These show an upward trend with increasing light intensity. The steepest increases can be witnessed when the incident light intensity is increased from 50 mW/cm² to 100 mW/cm².

To gain more insight into the effect of varying the mass ratio of the P3HT:PC₇₁BM active layer on the photovoltaic performance of fabricated devices we determined

the saturation current density J_{sat} and the maximum exciton generation rate (G_{max}). This was achieved by measuring the photocurrent density (J_{ph}) as a function of effective voltage (V_{eff}), as shown in Figure 4.9. Additionally, the exciton dissociation probabilities (P(E,T)) of each configuration can be determined for further analysis if needed.

J_{ph} is found as $J_{ph} = J_L - J_D$, where J_L is the current density under illumination by one sun and J_D is the current density in the dark. V_{eff} is determined as $V_{eff} = V_0 - V_a$, where V_0 is the voltage at which $J_{ph} = 0$ and V_a is the applied bias voltage [50, 51]. It is generally assumed that all photogenerated excitons are dissociated into free charge carriers and the saturation current density J_{sat} is only limited by the maximum exciton generation rate G_{max} . Such that,

$$J_{sat} = qG_{max}L \quad (4.4)$$

where q is the elementary charge and L is the thickness of the active layer [52]. It has to be highlighted that since not all electron-hole pairs dissociate into free charge carriers, G_{max} represents the field and temperature dependent maximum possible generation rate of excitons and hence the contribution towards the generated photocurrent J_{ph} . This means that the generation rate of free charge carriers $G(T,E)$ can be described as

$$G(T,E) = G_{max}P(T,E) \quad (4.5)$$

where $P(T,E)$ is the dissociation probability at the donor - acceptor interface.

The dissociation probability $P(E,T)$ is determined from the ratio of J_{ph}/J_{sat} and this can, for example, be determined at key device operational conditions such as short circuit conditions or at maximum power point. In the ideal case, J_{sc} is equal to J_{ph} . An increase in electric field under reverse bias will lead to a more effective separation of excitons and the generated photocurrent will increase until a saturated level is reached.

Figure 4.9 further shows a linearly increasing photocurrent at lower effective voltages, which is a sign that diffusion of photogenerated charge carriers is playing a key role in the generated photocurrent. At higher effective voltages, the drift

contribution towards the generated photocurrent is dominant as the current reaches saturation. At high internal fields, saturation current densities are only dependent on light absorption as high fields prohibit monomolecular and bimolecular recombination losses [53, 54]. Using Equation (4.4) and the fitting of the curves in Figure 4.9, Table 4.4 was populated as shown with the dependence of the fullerene content in the P3HT:PC₇₁BM active layer on the noted parameters clearly indicated.

Table 4.5: Comparison of mass ratio based maximum exciton generation rates and saturation current densities.

Sample	Mass Ratio	G_{max} ($\times 10^{27}$) ($m^{-3}s^{-1}$)	J_{sat} ($mA.cm^{-2}$)
R1	1:1	4.26	8.87
R2	1:0.8	5.93	12.35
T3	1:0.6	7.06	14.70

Though all devices were measured under 100 mW/cm² illumination and relatively large reverse bias voltages, the 1:0.6 mass ratios displays a photocurrent that saturates at even higher applied biases. This means that the device requires a much larger field to completely dissociate and sweep out charge carriers implying a greater sensitivity of J_{ph} to the internal electric field [55]. The expectation that the enhancement of G_{max} should be consistent with improved J_{sc} values extracted under 100 mW/cm² illumination is borne out by the direct correlation between the J_{sc} values in Table 4.3 and the G_{max} values in Table 4.5.

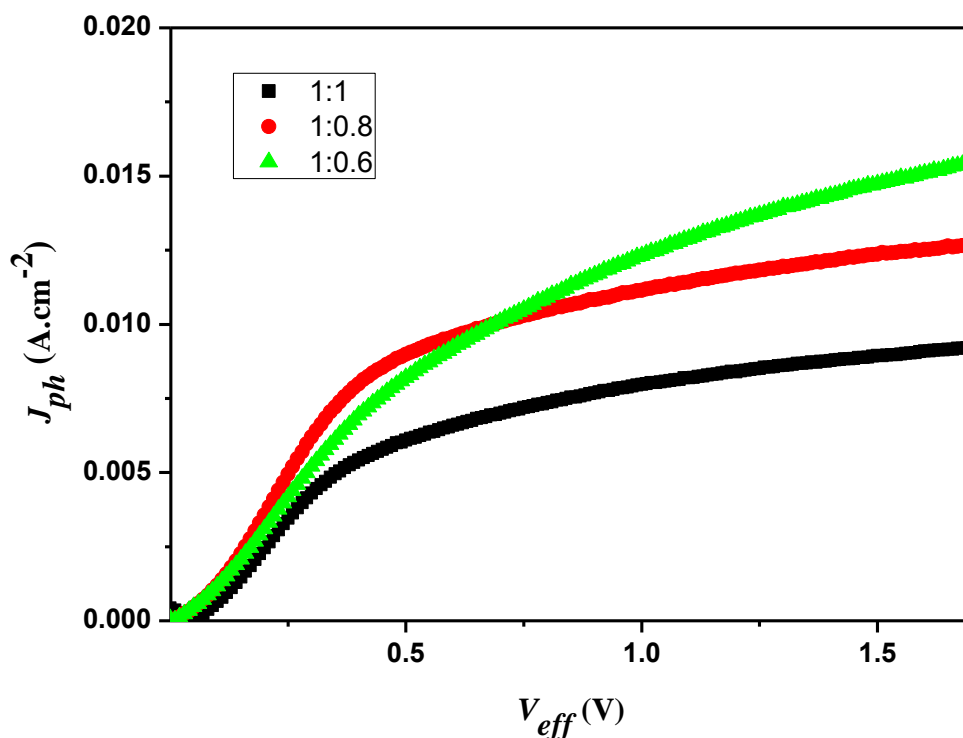


Figure 4.9: The variation of the photocurrent density (J_{ph}) as a function of the effective voltage (V_{eff}) under 100 mW/cm^2 illumination for devices with different P3HT:PC₇₁BM mass ratios of the active layer solar and an active layer with a thickness of 140 nm.

PART II Energetics and kinetics of the optimised blend ratio

In this section, we present the results of thermal annealing experiments of the optimised P3HT:PC₇₁BM mass ratio. Fabricated devices with the optimised mass ratio P3HT:PC₇₁BM (1:0.8) were annealed as explained in section 4.2.2.

4.3.2 Energetics of optimised blend ratio

4.3.2.1 Spectroscopic characteristics

In Figure 4.10 we observe an increase in optical absorbance with an increase in annealing temperature for fabricated devices with thicknesses of 140 nm. The variation in absorption profiles that could arise from thickness dependencies was

eliminated by the maintenance of constant active layer thicknesses, by using the same spin coater spin rate, for fabricated devices. With the annealing temperature increasing from room temperature to 110 °C, it is believed that there is greater crystallinity of P3HT leading to more $\pi - \pi^*$ absorption [56 – 58]. Also observable with an increase in temperature are the characteristic P3HT absorption shoulders at 560 nm and 610 nm. These are associated with conjugation due to ordered stacking of the P3HT backbone, restricting rotational motion and inter-chain $\pi - \pi$ interaction via electronic hopping, respectively. Furthermore, upon thermal annealing, the main absorption peak of the blend undergoes a red-shift of about 20 nm caused by the change of the average conjugation length in the polymer. Also noticeable is an improvement in the spectral overlap with the solar spectrum as a result of thermal annealing.

The absorption peak at 381 nm (green dotted line) is due to the PC₇₁BM content of the active layer and it showed no spectral shift with changes in annealing temperature.

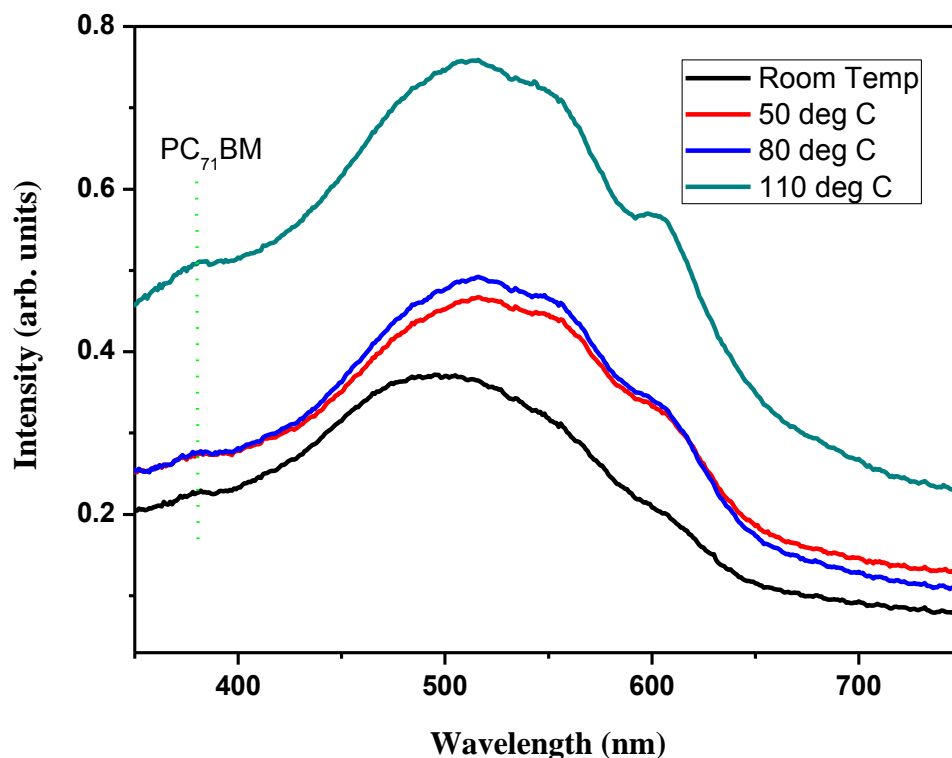


Figure 4.10: Optical absorption spectra of P3HT:PC₇₁BM (1:0.8) at different annealing temperatures for the same annealing time of 10 mins.

The Raman spectroscopy of the P3HT:PC₇₁BM at different annealing temperatures is shown in Figure 4.11. The vibration modes in the Raman spectra are attributed to those of P3HT as no features attributable to PC₇₁BM could be resolved. The spectra are presented with a background subtraction to enable an easier visualisation and comparison of features. The peak assignments are as follows [59, 60]:

Table 4.6: Assignment of spectral features of the P3HT:PC₇₁BM Raman spectra.

rr-P3HT wavenumber (cm ⁻¹)	Assignment
725	C – S – C ring deformation
1000	C _β - C _{alkyl} stretching mode
1090	C - H bending mode
1167	C _α - C _α symmetric stretching mode
1202	Combination of C _α - C _α stretching and the C _β - H stretching mode
1376	C – C intraring stretching
1456	C = C stretching mode
1516	C _α = C _β antisymmetric stretching mode

The advantageous effect that thermal annealing has on fabricated polymer:fullerene devices has been alluded to earlier. Tsoi *et al.* [61, 62] highlighted the influence that post-deposition annealing of P3HT:PCBM samples has on the Raman spectra in the following way:

- The C = C stretching mode in P3HT will undergo a shift to lower Raman modes
- There will be a decrease in the FWHM of the C = C stretching mode in P3HT
- There will be an increase in the ratio of the C - C intraring mode relative to the C = C stretching mode

These observations are said to be indicative of a more ordered structure in the morphology of the P3HT:PCBM samples. In Figure 4.11 we see the strongest peak centred at about 1456 cm⁻¹ which has been identified as a symmetric stretch of the C = C along the backbone of the conjugated polymer, P3HT [62]. Furthermore, it

can be mentioned that strong Raman modes have their genesis in the vibration of the conjugated backbone of the polymer which is the optically active part. Focussing on the most intense peak, we observe a shift of about 6 cm^{-1} of this peak to a lower mode i.e. $1456\text{ cm}^{-1} \rightarrow 1450\text{ cm}^{-1}$ (as shown in the inset of Figure 4.11). The peak positions of the devices annealed at $50\text{ }^{\circ}\text{C}$, $80\text{ }^{\circ}\text{C}$ and $110\text{ }^{\circ}\text{C}$ remained relatively unchanged at about 1450 cm^{-1} subsequent to the shift when compared to the room ‘temperature device’. The change in morphology as a result of post-deposition annealing manifested as an enhancement in the crystallisation of the active layer of the P3HT:PC₇₁BM devices. This effect was also observed in the optical absorption spectra in Figure 4.10. A decrease in the full width at half maximum (FWHM) of the most intense peak was observed with an increase in annealing temperature. Starting at a FWHM value of $51.68 \pm 0.04\text{ cm}^{-1}$ for the room temperature (Room Temp) device it decreased as follows: $41.55 \pm 0.03\text{ cm}^{-1}$ for $50\text{ }^{\circ}\text{C}$, $40.59 \pm 0.04\text{ cm}^{-1}$ for $80\text{ }^{\circ}\text{C}$ and $39.71 \pm 0.08\text{ cm}^{-1}$ for $110\text{ }^{\circ}\text{C}$. The variation of the measured FWHM on temperature is shown in Figure 4.12.

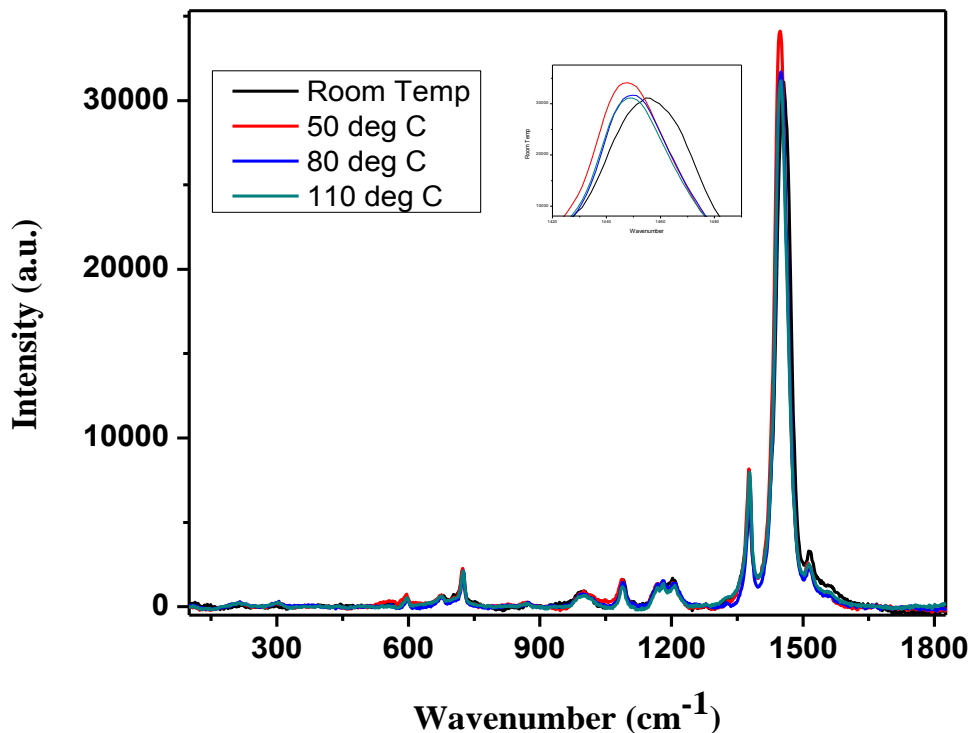


Figure 4.11: Raman spectra of P3HT:PC₇₁BM (1:0.8) at different annealing temperatures for the same annealing time of 10 min. The inset shows the 6 cm^{-1} shift of the C=C mode.

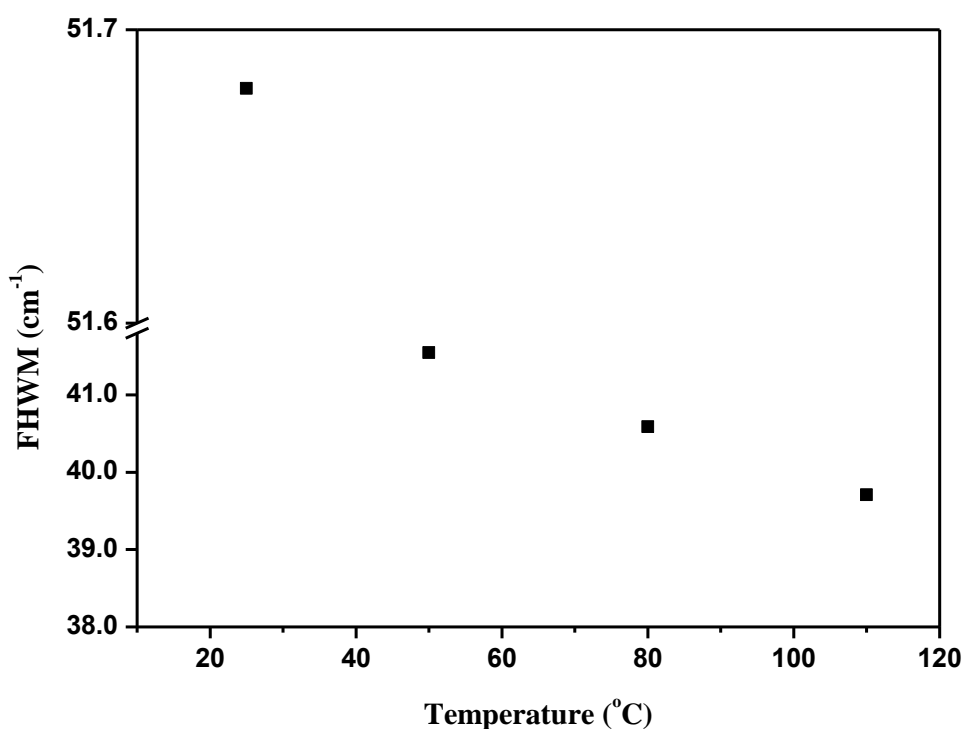


Figure 4.12: A plot of the FWHM as a function of temperature.

4.3.2.2 Current – voltage energetics of optimised blend ratio

The current – voltage measurements carried out in this section were based on the 50 °C annealing temperature as a reference. The thinking behind this was based on the observation that unannealed devices exhibited very little photovoltaic behaviour. The key for us was to identify a annealing temperature that was going to lead to optimised photovoltaic behaviour. Figure 4.13 shows the variation in dark current densities as a function of annealing temperature for GLASS/ITO/PEDOT:PSS/P3HT:PC₇₁BM/Al device architecture. Figure 4.13 (a) is the linear plot while the corresponding semi-logarithmic plot is given in Figure 4.13 (b). The dark current rectification ratios (RR) were obtained at 1.0 V using Equation (4.1) and these showed a decrease with an increase in annealing temperature as follows:

- 50 °C ; $RR = 472.3 \pm 0.4$
- 80 °C : $RR = 543.7 \pm 1.2$
- 110 °C : $RR = 82.5 \pm 0.3$

In Figures 4.14 (a) and (b) we see the $J - V$ curves for the same devices at 100 mW/cm^2 (AM1.5). The current density for devices annealed at $80 \text{ }^\circ\text{C}$ and $110 \text{ }^\circ\text{C}$ are lower than the one annealed at $50 \text{ }^\circ\text{C}$. The reduction in current after each annealing step could be as a result of de-doping the polymer of impurities such as oxygen, water and any possible remnant solvent [63]. Comparing the reductions, it can be concluded that the de-doping increases as the annealing temperature increases and it is prominent in the $110 \text{ }^\circ\text{C}$ annealed device as compared to the $80 \text{ }^\circ\text{C}$ case. Of interest was the emergence of the so-called S - shaped $J - V$ curve for the device annealed at $110 \text{ }^\circ\text{C}$. Though interesting, we did not explore the causes of this behaviour in detail, however it is likely that the increased annealing temperature leads to the segregation of P3HT and PCBM into separate domains that make recombination favourable and also possible reduction in the mobility of the charge carriers. As can be seen in Figure 4.14 (a), an S-shaped $J - V$ curve ruins the resulting calculated value of the device's FF considerably with the device showing poor photovoltaic performance. Despite numerous studies on the appearance of these S - shaped curves in organic solar cell research, their origin has been ascribed to different reasons such as poor charge carrier transport in any one of the OPV device layers or the formation of interfaces that hinder charge extraction [64 – 66].

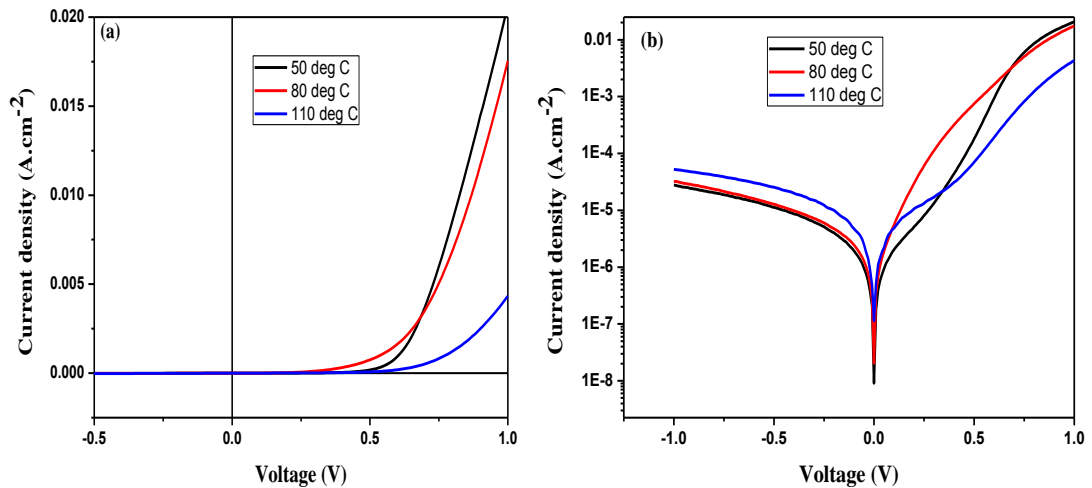


Figure 4.13: Dark current – voltage characteristics of P3HT:PC₇₁BM (1:0.8) at different annealing temperatures for the same annealing time. (a) linear plot (b) semi-log plot.

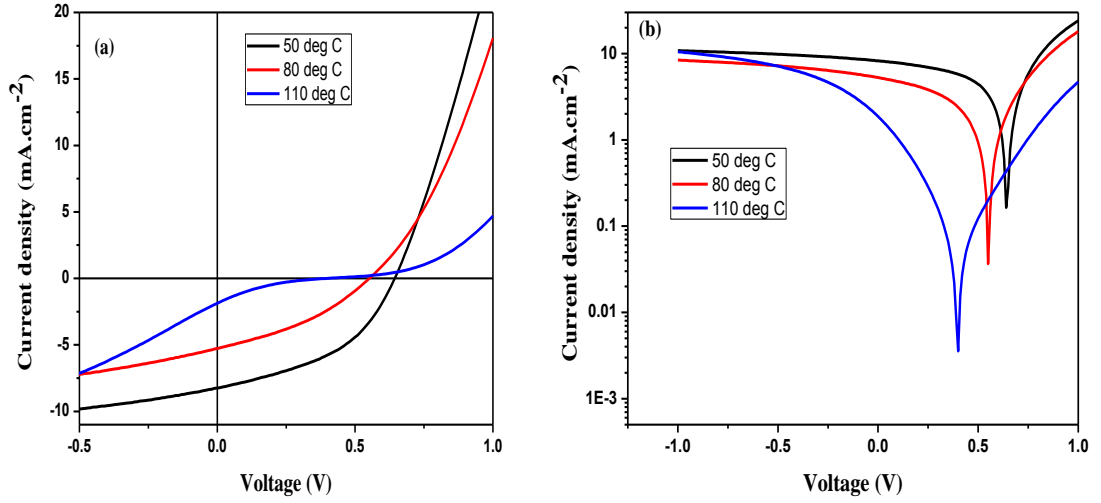


Figure 4.14: (a) J - V characteristics of P3HT:PC₇₁BM (1:0.8 mass ratio) under AM1.5 illumination at 100 mW/cm² for different annealing temperatures, (b) related dark current semi-log J - V characteristics.

The performance parameters of P3HT:PC₇₁BM devices as a function of annealing temperature are shown in Table 4.6. A deterioration in performance is evident, having had a peak device power conversion efficiency of 2.35% at 50 °C annealing.

The impact of the factor $\left(1 + \frac{R_s}{R_{sh}}\right)$ on the measured current density, as seen in

Equation (2.19), can be seen in Table 4.7. The decrease in the shunt resistance accompanied by an increase in the series resistance leads to values greater than 1. The increase in this factor correlates very well with the decrease in current density values obtained. For the realisation of a better PV performance it is always desirable to have a very low series resistance and a very high shunt resistance. It can be seen in this case that an increase in annealing temperature induces the opposite of that which is desired.

Table 4.7: Performance parameters of the P3HT:PC₇₁BM OPV devices at different annealing temperatures.

Temp	V_{oc} (V)	J_{sc} (mA/cm ²)	FF (%)	PCE (%)	R_{sh} (Ω cm ²)	R_s (Ω cm ²)	$1+R_s/R_{sh}$
50 °C	0.64	8.24	44.2	2.35	350.0	22.5	1+0.064
80 °C	0.55	5.27	35.7	1.04	233.3	52.8	1+0.226
110 °C	0.40	1.87	14.4	0.11	100.0	811.0	1+8.110

4.3.2.3 Charge transport properties of P3HT:PC₇₁BM as a function of annealing temperature

4.3.2.3.1 P3HT:PC₇₁BM (1:0.8) injection limited transport properties

The FN plots in Figure 4.15 confirm the contribution by emission currents towards the total currents measured in devices. Noting that the field is given by $F = V/d$, negative slopes were measured on the straight lines towards x intercept. However, these are high field regions since the horizontal scale is expressed as V^{-1} . So, it can be concluded that charge carriers are penetrating the potential barriers at the metal-active layer interfaces of the device by FN quantum tunnelling i.e. by the field emission mechanism. The plots show quantum mechanical tunnelling of charge carriers at high fields and thermionic emission contributions towards the current at low electric fields. The field dependent transition point from thermionic emission to field emission shows the device annealed at 80 °C with the lowest value and the highest electric field being required by the 110 °C annealed device.

In Figure 4.16 we see a combination of straight line and nonlinear sections in the RS plots. These indicate that the flow charge carriers through the interface is driven by thermionic emission, however the charge injection is predominantly due to FN tunnelling.

The contribution of thermally assisted charge transport due to the effects stemming from changes to potential barrier heights can be explained by Poole-Frenkel (PF) or Richardson-Schottky (RS) models. Additionally, it has been established that an increased electric field leads to greater barrier lowering due to image charge. The

RS model, where we have charge transport represented by a transition over a potential barrier under the effect of an electric field [67], can be mirrored by the PF model where charge transport is underpinned by thermal emission of charge carriers from randomly distributed traps to the conduction band stemming from the lowering of the potential barrier by the external electric field effect [68]. Consequently, Equation (2.25) depicting the RS model at high temperatures holds for the FP model as well. The relation between the PF parameter and the RS parameter is shown clearly in by M.A. Gaffar *et al.* [67]. This then means that the potential barrier in the PF model is a measure of the depth of a potential well, as oppose to the height in the RS model (essentially the same thing depending on perspective). A conventional Richardson-Schottky plot is shown in Figure 4.17 where the plot of $\ln(J/T^2)$ vs $1000/T$ is found to be linear with a negative slope in the annealing temperature ranging from 50 °C – 110 °C. The straight line plots with negative slopes indicate the presence of thermionic emission. In this case we see thermionic emission scaling with an increase in annealing temperature. This shows that a higher injection barrier exists at the interface due to the fact that a greater amount of thermal energy is needed by charge carriers to overcome the barrier. This effect can also be seen in Figure 4.15 where thermionic emission dominates at lower electric fields and scaling with temperature as well.

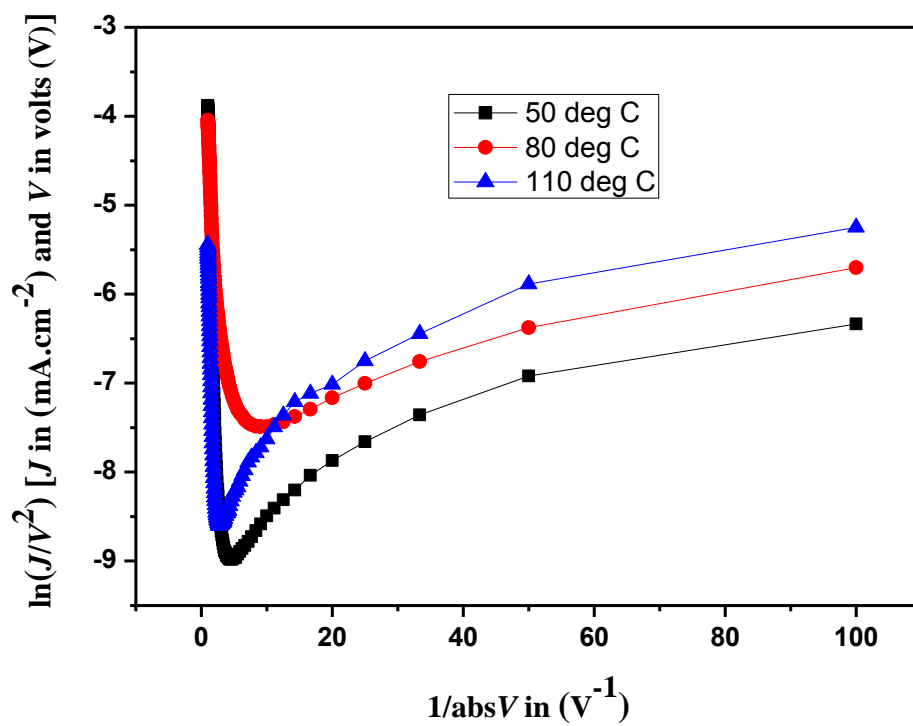


Figure 4.15: Fowler - Nordheim plots for ITO/PEDOT:PSS/P3HT:PC₇₁BM/Al devices for the post fabrication thermal annealing temperature range 50 °C – 110 °C.

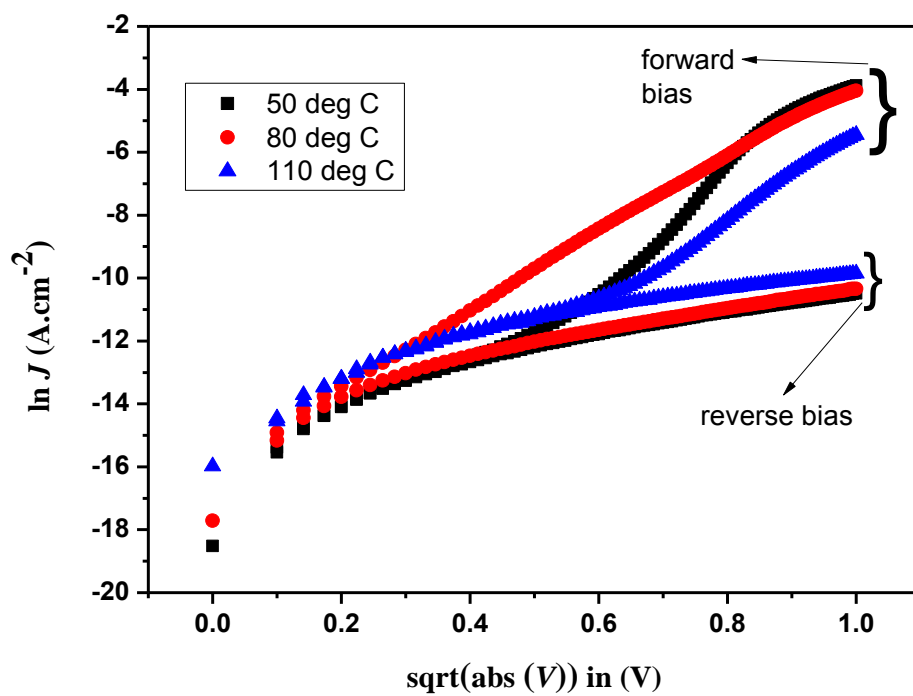


Figure 4.16: A comparison of Richardson - Schottky thermionic emission plots under forward and reverse bias for devices with a structure ITO/PEDOT:PSS/P3HT:PC₇₁BM/Al in the post fabrication thermal annealing temperature range 50 °C – 110 °C.

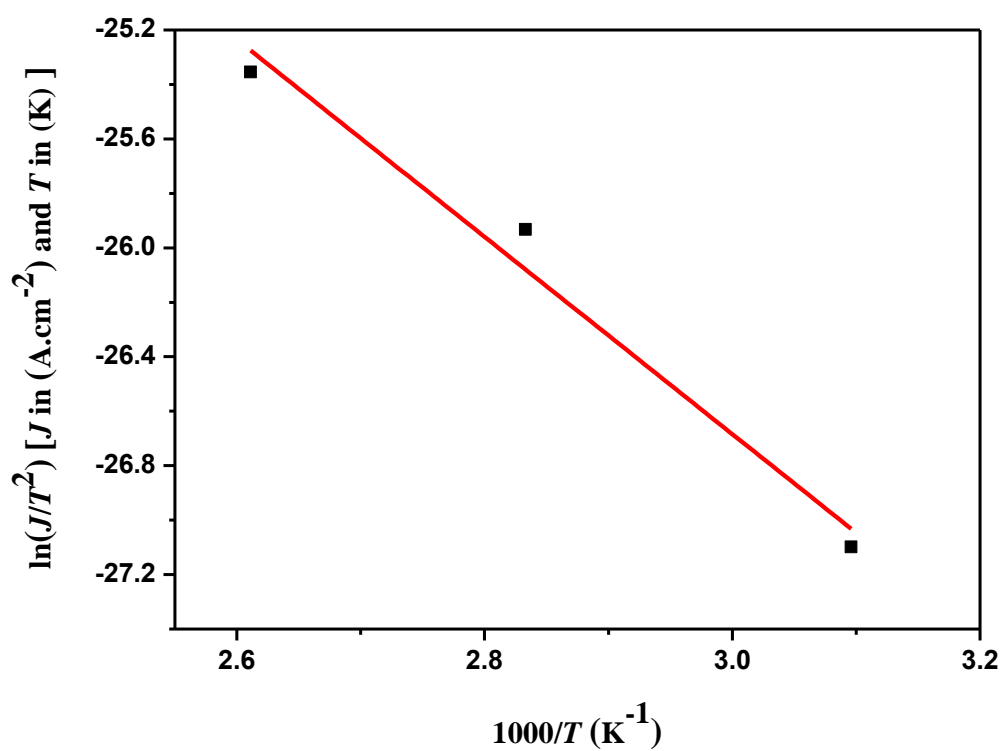


Figure 4.17: Richardson - Schottky plots of $\ln(J/T^2)$ vs $1000/T$ of devices with P3HT:PC₇₁BM blends in their photoactive layers at the post fabrication thermal annealing temperature range 50 °C – 110 °C.

4.3.2.3.2 P3HT:PC₇₁BM (1:0.8) bulk limited transport properties

Figure 4.18 shows the dependence of charge carrier mobility on annealing temperature. The linear fit of the graphs was modelled on the Mott-Gurney law (Equation (2.40)) as seen in Chapter 2. This is based on the assumption that there is an existence of negligible deep localised states and that the mobility is field independent.

An analysis of the graph indicates that the steeper the slope the greater the hole mobility. Therefore, in this case it can be seen that the device annealed at 50 °C has the greatest charge carrier mobility and the mobility decreases with an increase in annealing temperature. Here we note that the potential of a formation of domains with an extended separation that is larger than the exciton diffusion length, could be a contributing factor to the observed temperature correlated decrease in charge carrier mobility.

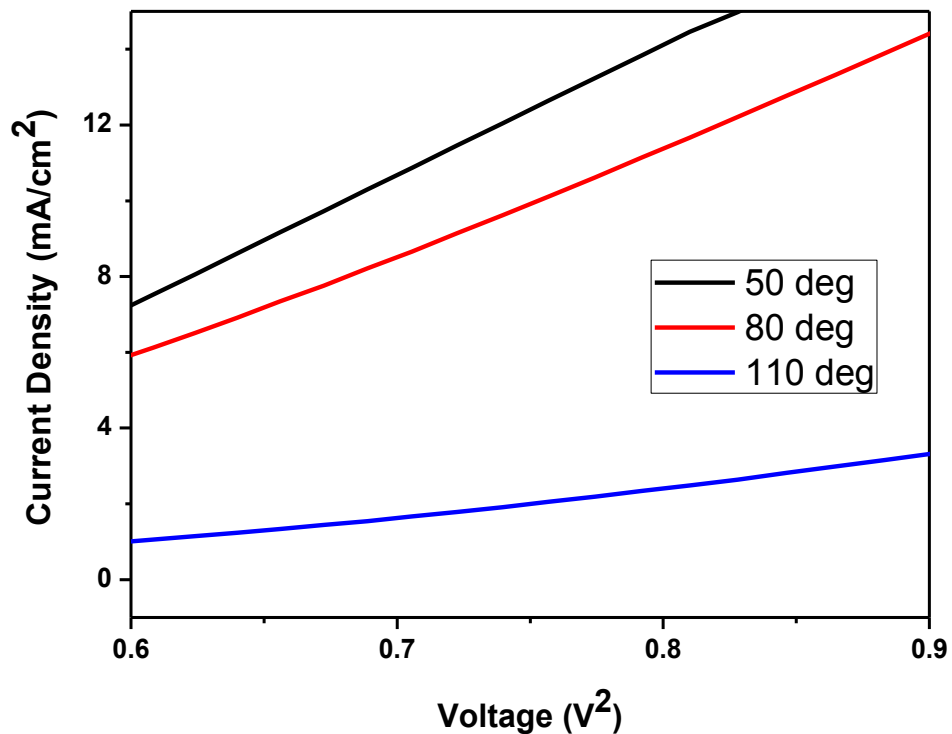


Figure 4.18: Linear fits of current density against V^2 graphs for different post fabrication annealing temperatures modelled on the Mott-Gurney law with an assumption of trap filled and trap free SCLC.

Nakazono *et al.* have suggested that the density of charge carriers induced by the structural defects and by the oxygen or moisture may decrease upon heat treatment, leading to a reduction in conductivity [69]. Traps are a particular problem in fabricating organic semiconductor devices. For example, exposure to oxygen during the device fabrication process can easily lead to oxygen being reduced to act as an electron trap [70]. It has been established that oxygen can capture and retain electrons. This then increases the number of holes in the HOMO of P3HT that can contribute to the current. The observed reduction in mobility may therefore be interpreted as the reduction in electron trapping centres that leads to a reduction in trap induced hole density [71]. Other causes of the reduction in charge carrier mobility that could be stemming from more morphological contributions such as the deterioration of P3HT crystallites as a result of higher annealing temperatures, were not probed in this study as this would require a more thorough study of the nanoscale morphology of fabricated devices.

4.3.2.4 P3HT:PC₇₁BM (1:0.8) OPV behaviour as a function of light intensity at different annealing temperatures

The knowledge of whether an OPV device exhibits Langevin type bimolecular (non-geminate) recombination or Shockley Reed Hall (SRH) type monomolecular (geminate) recombination is key to understanding of its output characteristics. Two key areas are probed for this purpose i.e. short circuit and open circuit conditions. Figures 4.19 (a) and (b) map the dependence of V_{oc} and J_{sc} on light intensity, respectively. The recombination types are summarised in Table 4.8. We should recall that, with regards to the variation of J_{sc} with light intensity, α values that are equal to 1 indicate strong monomolecular recombination. The device annealed at 110 °C shows the weakest bimolecular recombination in comparison to the other two. Furthermore, since we do not have an ideality factor equal to 1 for any of the devices, we can conclude that we do not have any sign of exclusive bimolecular recombination at open circuit conditions. With obtained ideality factors that are greater than 2, we conclude that a high degree of trap assisted recombination, particularly for the device annealed at 80 °C, is dominant.

Table 4.8: A comparison of light ideality factors (n), charge carrier mobility (μ) values and recombination types (α) at short circuit conditions for different annealing temperatures.

Sample	Temperature (°C)	n ± 0.43	μ $\pm 0.003 \times 10^{-6}$ (cm^2/Vs)	α ± 0.07
AK1	50	4.34	5.287	1.21
AK2	80	6.24	4.196	1.19
AK4	110	2.71	1.058	1.00

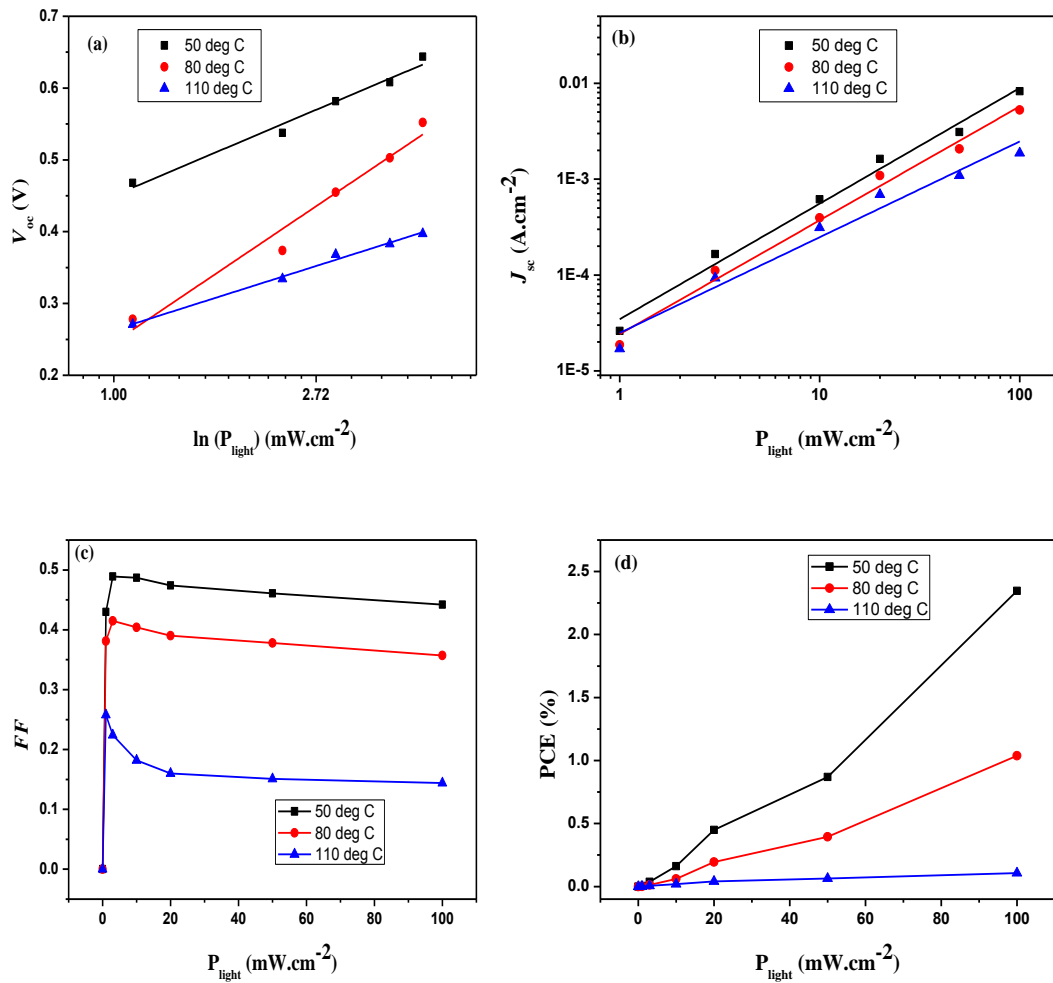


Figure 4.19: P3HT:PC₇₁BM (1:0.8) energetic variations of (a) Open circuit voltage (b) short circuit current density (c) fill factor (d) power conversion efficiency as a function of light intensity for different post fabrication thermal annealing temperatures.

The fill factor and the PCE show a dependence on annealing temperature as shown in Figures 4.19 (c) and 4.19 (d). An increase in annealing temperature is accompanied by a decrease in the fill factor signifying a temperature linked degradation. The fill factor of all devices peaks at lower light intensities before decreasing towards 100 mW.cm^{-2} . The deterioration of devices, more specifically a deterioration in PV performance can be seen in the increase in series resistance together with a decrease in shunt resistance as the annealing temperature is increased. At all annealing temperatures, the PCE appears to be increasing with the increase in light intensity although the effect is less noticeable for the $110 \text{ }^\circ\text{C}$ annealing temperature.

The device annealed at $50 \text{ }^\circ\text{C}$ shows a consistently higher PCE at different light intensities as compared to devices annealed at $80 \text{ }^\circ\text{C}$ and $110 \text{ }^\circ\text{C}$.

In Figure 4.20 we see an almost negligible influence of diffusion on the generated photocurrent for the device annealed at $110 \text{ }^\circ\text{C}$. The other two devices show an expected linear increase in photocurrent at lower effective fields. Saturated current densities, at high electric field of $1.23 \times 10^7 \text{ V/m}$ (1.6 V) for the devices annealed at $50 \text{ }^\circ\text{C}$ and $80 \text{ }^\circ\text{C}$ are 10.49 mA and 8.03 mA respectively. Their respective maximum exciton generation rates can be calculated using Equation (4.4). These are $G_{\text{max}} = 5.04 \times 10^{27} \text{ m}^{-3}\text{s}^{-1}$ and $G_{\text{max}} = 3.86 \times 10^{27} \text{ m}^{-3}\text{s}^{-1}$. The higher exciton generation rate can lead to a higher J_{sc} if for example, holes and electrons that dissociate at the P3HT:PC₇₁BM interface are collected at the electrodes with minimal recombination. The α values that are greater than 1 as seen in the plot of J_{sc} vs light intensity, suggest that a greater number of charge carriers are swept out by the internal field and there is a small loss of charge carriers due to bimolecular recombination.

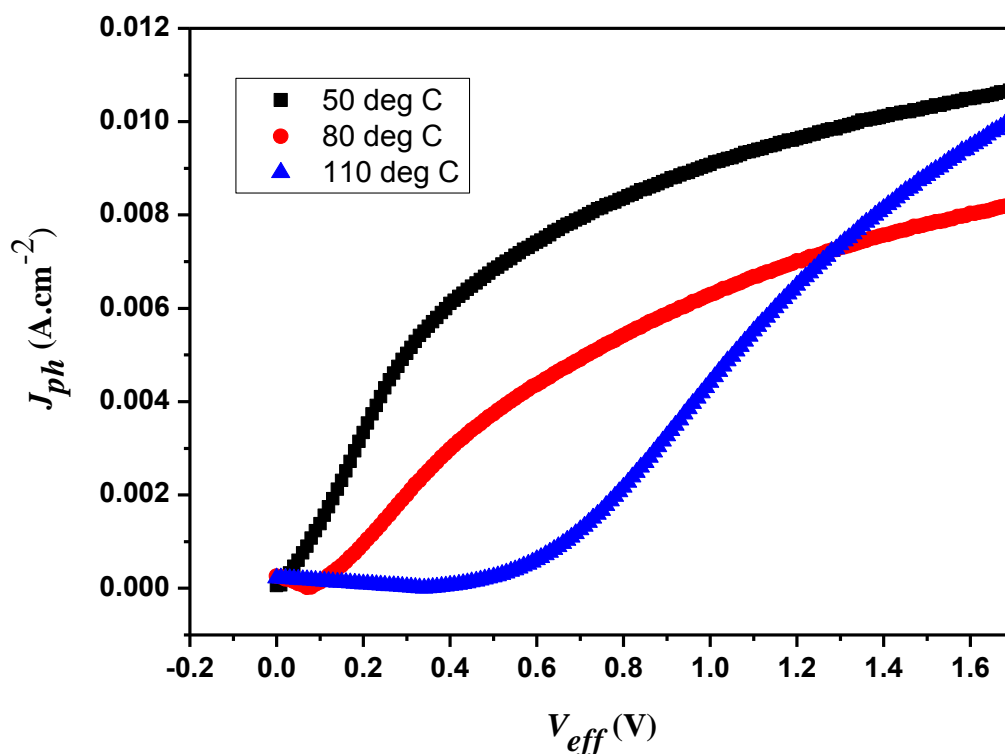


Figure 4.20: The variation of the photocurrent density (J_{ph}) as a function of the effective voltage (V_{eff}) under 100 mW/cm^2 illumination for devices with the P3HT:PC₇₁BM (1:0.8) mass ratio of the photoactive layer. The variation of the generated photocurrent as a function of effective voltage for different annealing temperatures shows saturation of the photocurrent at 1.6 V for devices annealed the 50 °C and 80 °C.

4.3.3 Kinetics of optimised blend ratio

4.3.3.1 Spectroscopic characteristics

Having identified the 50 °C as the optimum post fabrication annealing temperature, we set out to conduct further studies at this annealing temperature with a view of optimising the anneal time. In Figure 4.21 we see a somewhat varied optical response to different thermal annealing times at a constant annealing temperature of 50 °C. There is no outright pattern that can be identified with regards to an absorption profile and the annealing times. However, the absorption pattern is still

dominated by the P3HT absorption profile whilst the less prominent PC₇₁BM absorption peak is still observable at about 380 nm. The major difference between this section of the work and the earlier energetics study, is that the maximum absorption peak does not show any noticeable shift with the increase in anneal times.

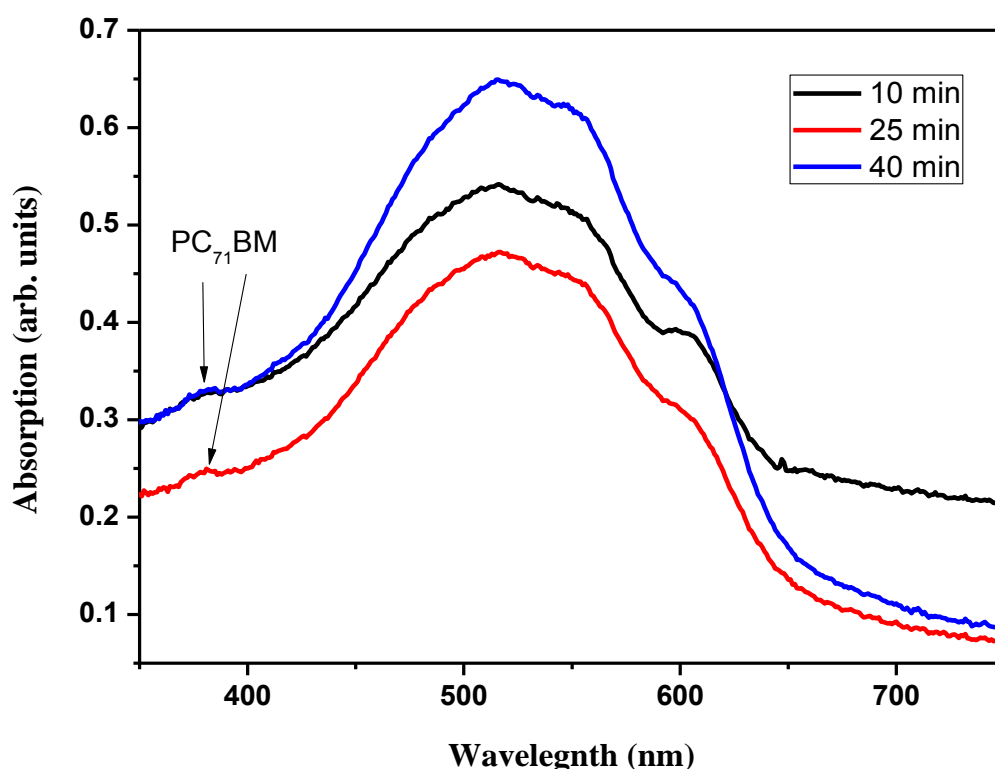


Figure 4.21: UV-Vis spectra for the photoactive layer P3HT:PC₇₁BM (1:0.8) with varying anneal times at the optimum 50 °C post fabrication annealing temperature. The average thickness of the photoactive layer of fabricated GLASS/ITO/PEDOT:PSS/P3HT:PC₇₁BM/Al devices was about 140 nm.

The Raman spectra for the different anneal times also show no effect on the structural order of the active layer materials. The expected red shift, of the most intense peak, from room temperature devices to 50 °C annealing temperature was observed. Once again we observed a shift of 6 cm⁻¹ from 1456 cm⁻¹ to 1450 cm⁻¹ with reasons for this the same as those given in section 4.3.2.1. In this case, the

FWHM started at the previously stated value of $51.68 \pm 0.04 \text{ cm}^{-1}$ and stayed fairly constant at $40.75 \pm 0.90 \text{ cm}^{-1}$ with the increase in annealing time. This is shown in the inset of Figure 4.22.

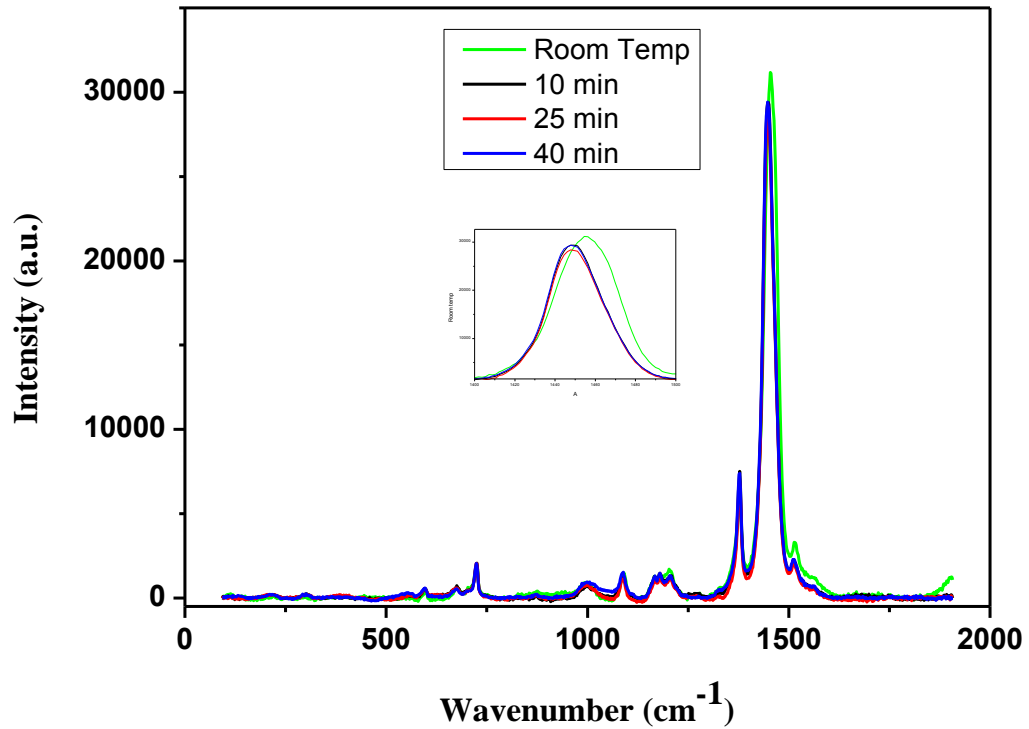


Figure 4.22: Raman traces of the P3HT:PC₇₁BM photoactive layers as a function of anneal times at 50 °C post fabrication annealing temperature. The inset shows the post annealing 6 cm^{-1} shift of the most intense peaks and the decrease in FWHM.

4.3.3.2 Current –voltage kinetics of optimised blend ratio

The dark and illuminated current – voltage characteristics are shown in Figures 4.23 and 4.24 respectively. In the dark, a Schottky barrier to prevent back electron transfer at the P3HT/Al interface can be assessed from the rectification behaviour. To this effect rectification ratios can be determined in order to determine whether fabricated OPV devices are good rectifying devices or not. We used Equation (4.1) to calculate rectification ratios at 1.0 V for the three devices and obtained the following values: 10 min anneal time, $RR = 4.72 \times 10^2$; 25 min anneal time,

$RR=3.14\times 10^2$ and 40 min anneal time, $RR=2.19\times 10^2$. A decrease of the RR with anneal time indicates the increasing probability of having leakage currents.

Table 4.9 contains OPV performance parameters that were largely obtained from Figure 4.24. The open circuit voltage drops by about 7.5% from 10 minutes to 25 minutes annealing time and does not change when the annealing time is increased to 40 minutes. The FF shows a slight decrease when the anneal time is changed from 10 minutes to 25 minutes. However, there is almost a 10% decrease in the FF when the anneal time is increased to 40 minutes. The series and shunt resistances deteriorate with increasing anneal time. Previously introduced as an indication or measure of the degree of recombination, the factor $\left(1 + \frac{R_s}{R_{sh}}\right)$, as can be seen in Table 4.9, increases with an increase in anneal time. The effect thereof can be seen in the decrease in the J_{sc} values as the anneal time increased. The overall performance of devices, as shown by the PCE in Table 4.9, decreased with anneal times.

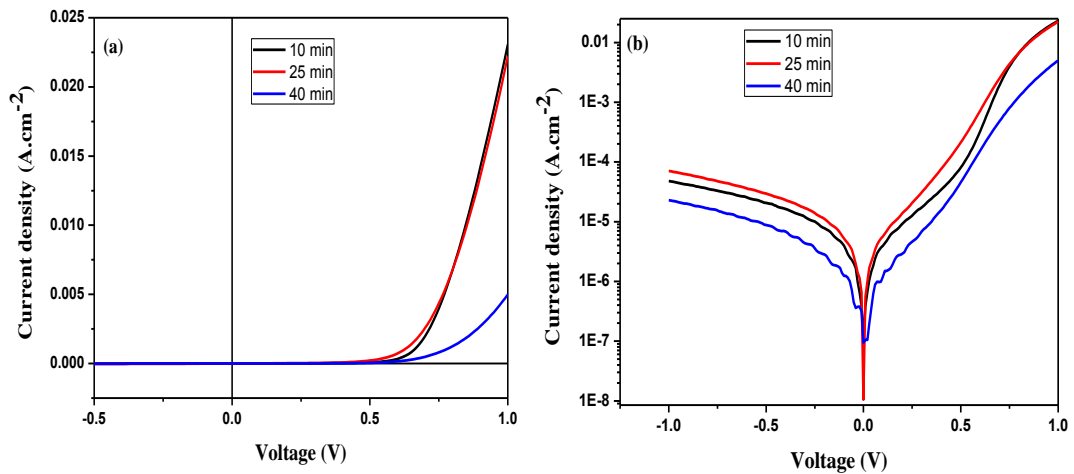


Figure 4.23: Dark current – voltage characteristics of P3HT:PC71BM (1:0.8) at different annealing times for the same annealing temperature. (a) linear plot (b) semi-log plot.

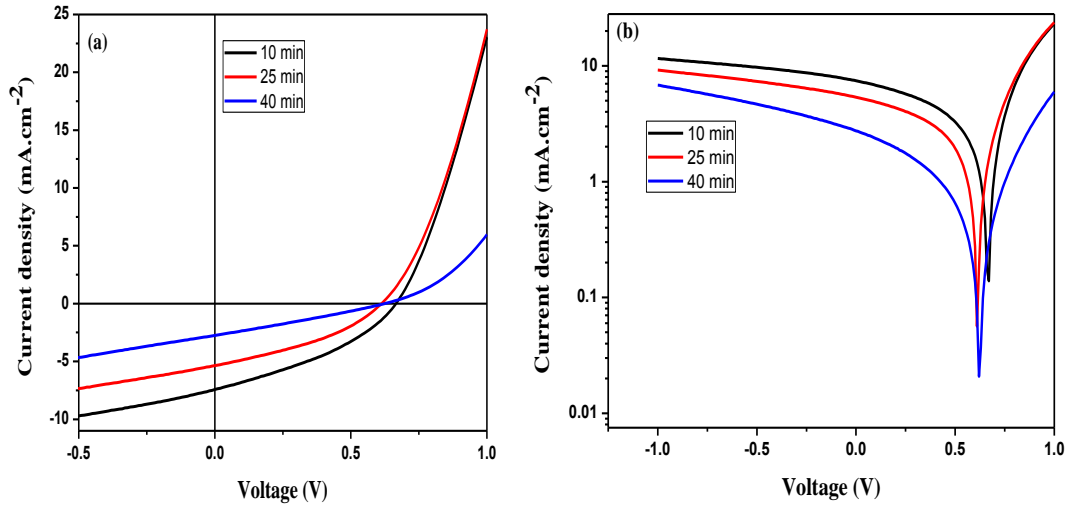


Figure 4.24: (a) J - V characteristics of P3HT:PC₇₁BM (1:0.8 mass ratio) under AM1.5 illumination at 100 mW/cm² for different anneal times (b) related dark current semi-log J - V characteristics.

Table 4.9: Performance parameters of the P3HT:PC₇₁BM OPV devices with a GLASS/ITO/PEDOT:PSS/P3HT:PC₇₁BM/Al structure at different annealing times.

Sample	Temp	V_{oc} (V)	J_{sc} (mA/cm ²)	FF (%)	PCE (%)	R_{sh} (Ω cm ²)	R_s (Ω cm ²)	$1+R_s/R_{sh}$
N1	10 min	0.67	7.49	35.5	1.78	171.4	29.8	1+0.174
N2	25 min	0.62	5.36	36.5	1.20	233.3	44.0	1+0.189
N3	40 min	0.62	2.74	27.3	0.47	276.3	170.8	1+0.618

4.3.3.3 Charge transport properties of P3HT:PC₇₁BM as a function of annealing time

4.3.3.3.1 P3HT:PC₇₁BM (1:0.8) injection limited transport properties

We once again observed quantum mechanical tunnelling and thermionic emission contributions towards the measured current densities in the fabricated devices. The FN plots and the RS plots of Figures 4.25 and 4.26, respectively, show tunnelling behaviour at high electric fields and thermionic emission at lower electric field. The

FN plots show annealing time dependent slopes in that there is decrease in magnitude of the slope with increasing annealing time from 10 to 25 minutes. However, the FN slope for the 25 minutes is almost equal to the one for the 40 minutes annealing time. Furthermore, for the device annealed for 40 minutes, we see an emergence of a second negative slope (marked by a green dashed line). This second slope could be indicative of the recombination of charge carriers in the bulk. The slopes that are associated with tunnelling effects are obtained from linear fits of the curves as follows: 10 min = - 4.93; 25 min = - 3.32 and 40 min = 3.35. The electric fields at which transition from thermionic emission to tunnelling emission take place were found to be:- 10 min, $F = 2.42 \times 10^6$ V/m; 25 min, $F = 1.67 \times 10^6$ V/m and 40 min, $F = 1.63 \times 10^6$ V/m.

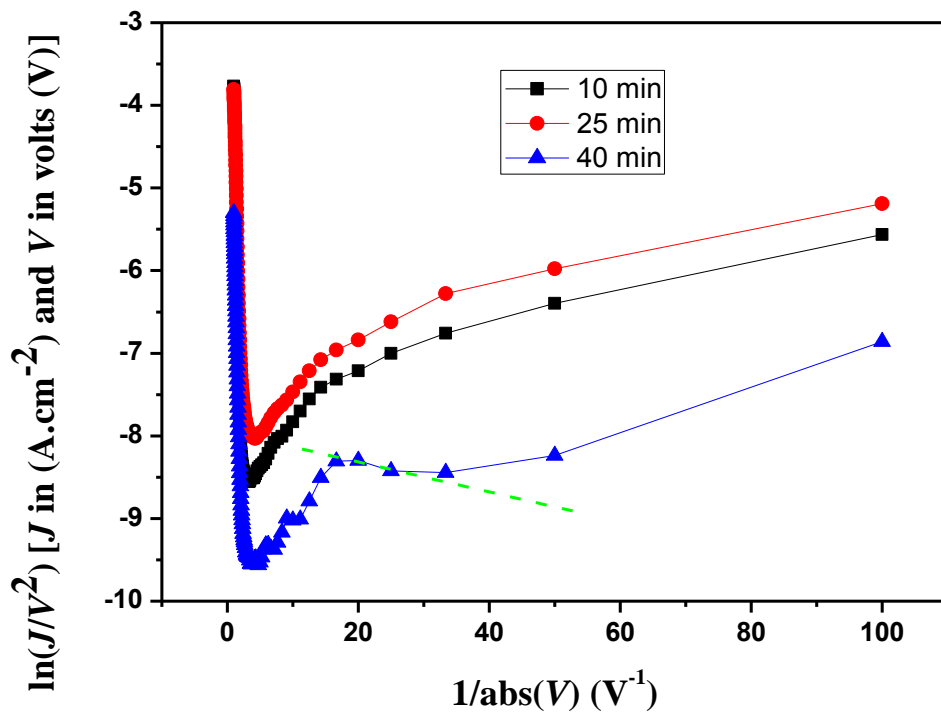


Figure 4.25: FN plots of GLASS/ITO/PEDOT:PSS/P3HT:PC₇₁BM/Al devices for varying post fabrication annealing times.

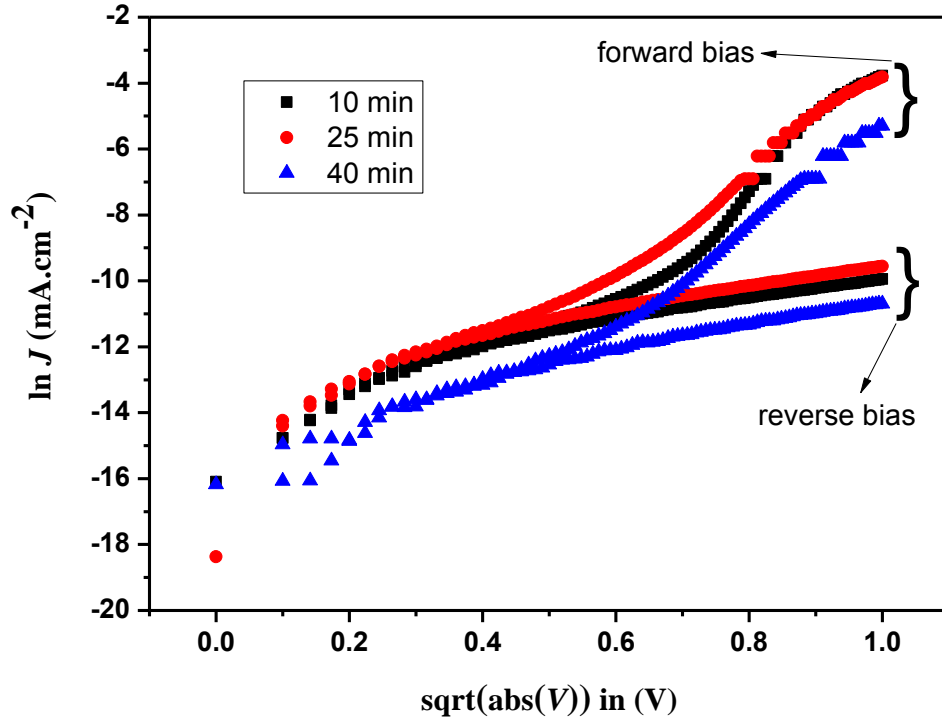


Figure 4.26: RS plots of GLASS/ITO/PEDOT:PSS/P3HT:PC₇₁BM/Al devices for varying post fabrication annealing times

4.3.3.3.2 P3HT:PC₇₁BM (1:0.8) bulk limited transport properties

Three regions of interest are identified in Figure 4.27. This current density vs voltage log-log plot indicates Ohm's law dominated charge carrier transport mechanism in region I. This is dominant at low applied voltages up to 0.1 V. This direct proportionality between current density and applied voltage breaks down when the injected charge carrier density becomes large such that the field created by the charge carriers themselves dominates over the external bias. The charge transport behaviour becomes space charge limited and the trap free space charge limited current (TFSCLC) takes the form of the Mott-Gurney law, Equation (2.40).

$$\text{Rewritten here for easy reference, } J = \frac{9}{8} \epsilon_o \epsilon_r \mu \frac{V^2}{d^3}.$$

Once more it has to be highlighted that region II in Figure 4.27 is associated more with trap filling hence the application of the TFSCLC approach does not suggest an absence of traps but that traps are filled. A plot of J vs V^2 yields a slope that contains charge carrier mobility μ . Therefore the slope is,

$$\text{slope} = \frac{9}{8d^3} \epsilon_o \epsilon_r \mu \quad (4.6)$$

The charge carrier mobility can then be determined as

$$\mu = \text{slope} \times \frac{8d^3}{9\epsilon_o \epsilon_r} \quad (4.7)$$

Form Figure 4.28 it can be seen that, with the charge carrier mobility directly proportional to the slope, the magnitudes of charge carrier mobilities decrease with an increase in annealing temperature. Once again, as can be seen in Table 4.10, we observe low charge carrier mobilities that are normally associated with disordered materials.

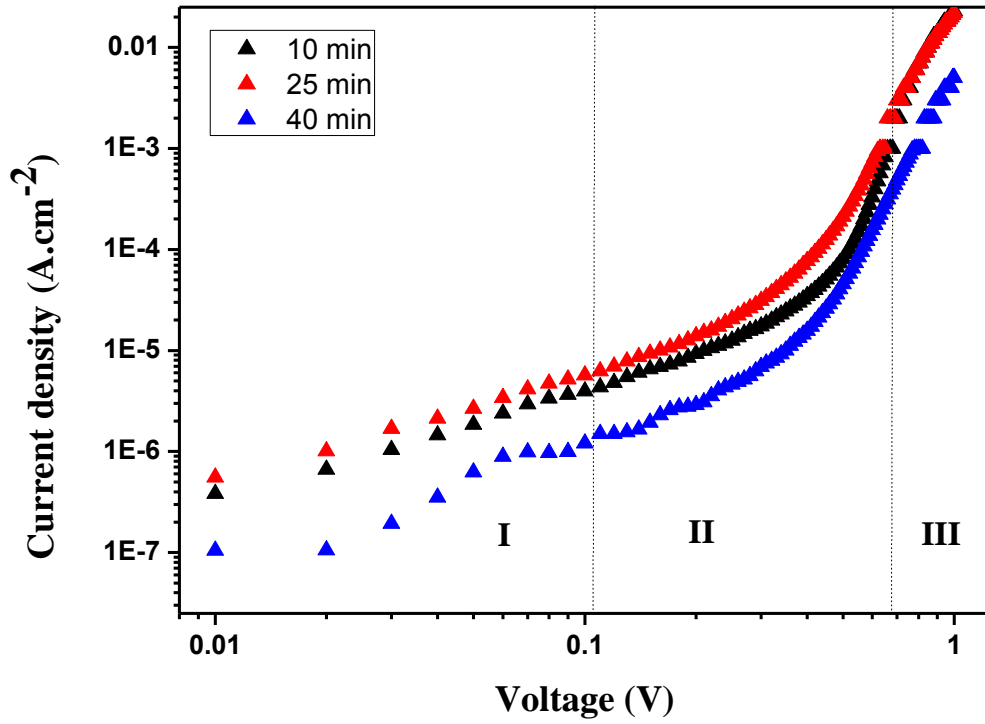


Figure 4.27: Dark current log-log plots of $J - V$ characteristics under forward bias for P3HT:PC₇₁BM active layer blends annealed at 50 °C for 10, 25 and 40 minutes. Region I has slope = 1, indicating Ohmic conduction, region II has slope > 2, corresponding to SCLC characterised by trap filling and region III has a slope ≈ 2 and is described by Trap Free SCLC

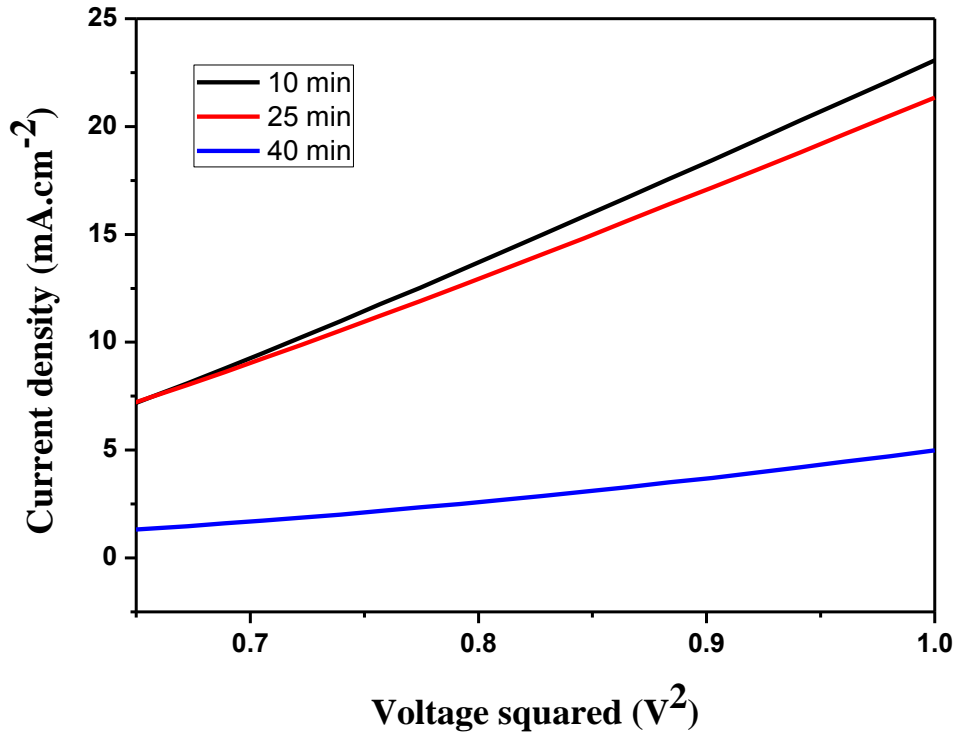


Figure 4.28: Mott-Gurney linear fit linear fits of J_{sc} against V^2 graphs for different post fabrication annealing times modelled on the Mott-Gurney law with an assumption of negligible deep localised states for a photoactive layer with a thickness of 140 nm

4.3.3.4 P3HT:PC₇₁BM (1:0.8) OPV behaviour as a function of light intensity

Further characterisation of anneal time based PV performance is made by incident light intensity analysis of key characteristic parameters of merit. A focus on open circuit conditions leads to a plot of V_{oc} vs $\ln P_{light}$ as shown in Figure 4.29 (a). From the linear fits of the curves we extract the slopes that give us information on ideality factors and hence the recombination mechanisms. We can rewrite Equation (4.2) such that the slope of the curve is

$$\text{slope} = \frac{dV_{oc}}{d(\ln(P_{light}))} = \frac{nk_B T}{q} \quad (4.8)$$

The slope of the V_{oc} vs natural logarithm of the light intensity gives $k_B T/q$ for bimolecular recombination [72, 73]. The slopes in this case give the following behaviours: 10 min anneal time, slope = $2.55k_B T/q$; 25 min anneal time, slope = $1.96k_B T/q$ and 40 min anneal time, slope = $2.67k_B T/q$. With all the slopes greater than $k_B T/q$, it can be concluded that a combination of both monomolecular (SRH-type) and bimolecular (Langevin-type) recombination processes are present at open circuit conditions.

The log-log plot, in Figure 4.29 (b), of the current density *versus* incident light intensity (P_{light}) shows that there is domination of monomolecular recombination at short circuit conditions, especially for the devices annealed for 25 and 40 minutes. The α values for the 25 min and 40 min anneal time devices shown in Table 4.10 are the closest 1. The differences in FF , though minor between the 10 and 25 minutes annealing times, can be seen to be increasing with increasing input light intensity (Figure 4.29 (c)). The dependence of the PCE on anneal times is shown in Figure 4.29 (d), where the increase in input light intensity leads to an increase in PCE albeit at different rates and with different values at 100 mW.cm^{-2} (AM1.5).

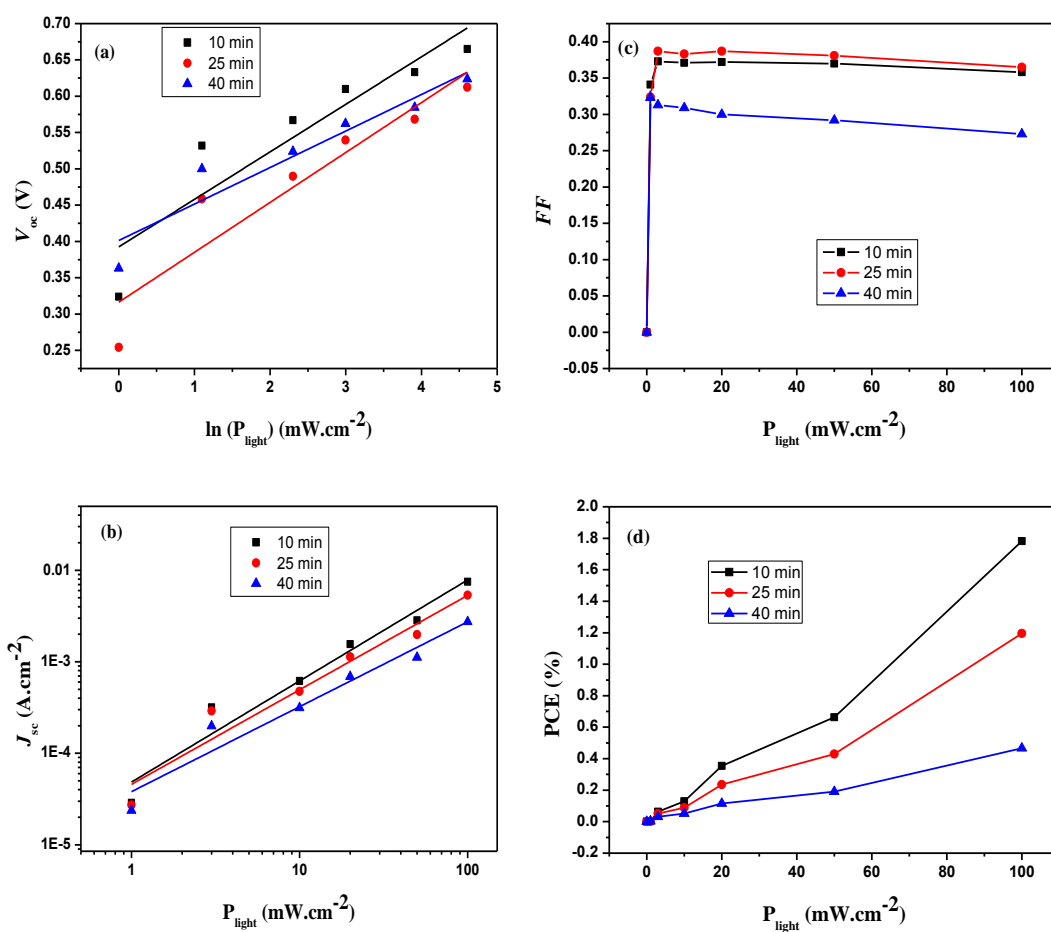


Figure 4.29: P3HT:PC₇₁BM (1:0.8) kinetic variations of (a) Open circuit voltage (b) short circuit current density (c) fill factor (d) power conversion efficiency as a function of light intensity.

Table 4.10: A comparison charge carrier mobilities and recombination parameters for GLASS/ITO/PEDOT:PSS/P3HT:PC₇₁BM/Al devices annealed at 50 °C for varying annealing times.

Sample	Temperature (°C)	n ± 0.47	μ $\pm 0.005 \times 10^{-6}$ (cm ² /Vs)	α ± 0.11
N1	10 min	2.55	6.326	1.10
N2	25 min	1.96	5.672	1.03
N3	40 min	2.67	1.234	0.93

Observed in Figure 4.30, is that the device annealed for 40 minutes does not show the linear dependence of the photocurrent with effective voltage at low bias voltages. These devices do not show saturation of current densities within given effective voltage scales. This could mean that larger electric fields are required to sweep out dissociated charge carriers.

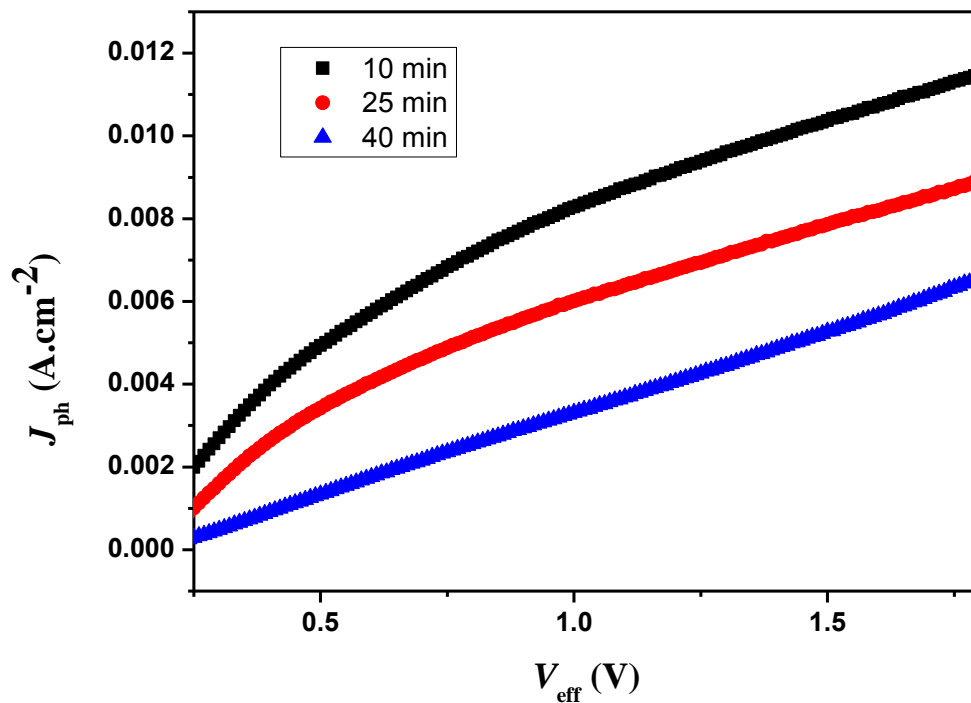


Figure 4.30: Variation of the photocurrent with effective voltage for different annealing times.

4.4 Conclusion

In this chapter, it was shown that the optimum mass ratio for the P3HT:PC₇₁BM polymer:fullerene blend in the fabrication of organic photovoltaic devices with this active layer blend, is 1:0.8. The performance of the optimised blend ratio was found to deteriorate with an increase in both annealing temperature at a constant annealing time and with an increase in annealing time at a constant annealing temperature. As far as recombination behaviours are concerned, fabricated BHJ OPV devices tended to indicate an existence of a combination of recombination mechanisms. Several factors could be at play in the determination of effective recombination mechanisms. These could include, the types and nature of materials used and conditions under which devices are fabricated and characterised.

4.5 References

- [1] Dang, M.T., Hirsch, L., Wantz, G. (2011). *Advanced Materials* **23** (31), 3597.
- [2] Reyes-Reyes, M., Kim, K. and Carroll, D.L. (2005). *Applied Physics* **87** (8), 83506.
- [3] Li, G., Shrotriya, V., Huang, J., Yao, Y., Moriarty, T., Emery, K. and Yang, Y. (2005). *Nature Materials* **4** (11), 864.
- [4] Hauch, J.A., Schilinsky, P., Choulis, S.A., Childers, R., Biele, M. and Brabec, C.J. (2008). *Solar Energy Materials and Solar Cells* **92** (7), 727.
- [5] Kim, Y., Choulis, S.A., Nelson, J. and Bradley, D.D.C. (2005). *Applied Physics Letters* **86** (6), 063502.
- [6] Ma, W., Yang, C., Gong, X., Lee, K. and Heeger, A.J. (2005). *Advanced Functional Materials* **15** (10), 1617.
- [7] Oklobia, O. and Shafai, T.S. (2013). *Solar Energy Materials and Solar Cells* **117**, 1.
- [8] DeLongchamp, D.M., Kline, R.J. and Herzing, A. (2012) *Energy & Environmental Science* **5** (3), 5980.
- [9] Chen, W., Nikiforov, M.P. and Darling, S.B. (2012). *Energy & Environmental Science* **5** (8), 8045.
- [10] Huang, Y., Kramer, E.J., Heeger, A.J. and Bazan, G.C. (2007). *Chemical Reviews* **114** (14), 7006.
- [11] Peet, J., Kim, J.Y., Coates, N.E., Ma, W.L., Moses, D., Heeger, A.J. and Bazan, G.C. (2007). *Nature Materials* **6** (7), 497.
- [12] Moule', A.J. and Meerholz, K. (2008). *Advanced Materials* **20** (2), 240.

- [13] Lee, J.K., Ma, W.L., Brabec, C.J., Yeun, J., Moon, J.S., Kim, J.Y., Lee, K., Bazan, G.C. and Heeger, A.J. (2008). *Journal of the American Chemical Society* **130** (11), 3619.
- [14] Liao, H-C., Ho, C-C., Chang, C-Y., Jao, M-H., Darling, S.B. and Su, W.F. (2013). *Materials Today* **16** (9), 326.
- [15] Perez, L.A., Rogers, J.T., Brady, M.A., Sun, Y., Welch, G.C., Schmidt, K., Toney, M.F., Jinnai, H., Heeger, A.J., Chabinyc, M.L., Bazan, G.C. and Kramer, E.J. (2014). *Chemistry of Materials* **26** (22), 6531.
- [16] Sharma, S.S., Sharma, G.D. and Mikroyannidis, J.A. (2011). *Solar Energy Materials and Solar Cells* **95** (4), 1219.
- [17] Wienk, M.M., Kroon, J.M, Verhees, W.J.H., Knol, J., Hummelen, J.C., van Hal, P.A. and Janssen, R.A.J. (2003). *Angewandte Chemie* **42** (29), 3371.
- [18] Liu, Z., Xue, F., Su, Y. and Varshney, K. (2006). *IEEE Electron Device Letters* **27** (3), 151.
- [19] Jiang, Y., Yu, D., Lu, L., Zhan, C., Wu, D., You, W., Xie, Z. and Xiao, S. (2013). *Journal of Materials Chemistry A* **1** (28), 8270.
- [20] Srinivasan, M.V., Tsuda, N., Shin, P.-K. and Ochiai, S. (2015). *Royal Society of Chemistry Advances* **5** (69), 56262.
- [21] Chen, Y., Elshobaki, M., Ye, Z., Park, J-M., Noack, M.A., Ho, K-M. and Chaudhary, S. (2013). *Physical Chemistry Chemical Physics* **15** (12), 4297.
- [22] Chang, S.-Y., Cheng, P., Li, G. and Yang, Y. (2018). *Joule* **2** (6), 1039.
- [23] Singh, A., Dey, A. and Iyer, P.K. (2017). *Organic Electronics* **51**, 428.
- [24] Etxebarria, I., Ajuria, J. and Pacios, R. (2015). *Organic Electronics* **19**, 34.
- [25] Dimitrov, S.D., Schroeder, B.C., Nielsen, C.B., Bronstein, H., Fei, Z., McCulloch, I., Heeney, M. and Durrant, J.R. (2016). *Polymers* **8** (1), 14.

- [26] Kim, Y., Stelios, A.C., Nelson, J., Cook, D.D.C.B.S. and Durrant, J.R. (2005). *Applied Physics Letters* **86** (6) 063502.
- [27] Chiguvare, Z., Parisi, J. and Dyakonov, V. (2007). *Z Naturforsch* **62a**, 609.
- [28] Kadem, B.Y., Al-hashimi, M.K. and Hassan, A.K. (2014). *Energy Procedia* **50** 237.
- [29] Ma, W., Yang, C., Gong, X., Lee, K., Heeger, A. J. (2005). *Advanced Functional Materials* **15** (10), 1617.
- [30] Li, G., Yao, Y., Yang, H., Shrotriya, V., Yang, G. and Yang, Y. (2007). *Advanced Functional Materials* **17** (10), 1636.
- [31] Huang, Y.-C., Liao, Y.-C., Li, S.-S., Wu, M.-C., Chen, C.-W. and Su, W.-F. (2009). *Solar Energy Materials and Solar Cells* **93** (6 – 7), 888.
- [32] Jo, J., Kim, S.-S., Na, S.-I., Yu, B.-K. and Kim, D.-Y. (2009). *Advanced Functional Materials* **19** (6), 866.
- [33] Thompson, B.C. and Fréchet, J.M.J. (2008). *Angewandte Chemie International Edition* **47** (1), 58.
- [34] Chu, C.-W., Yang, H., Hou, W.-J., Huang, J., Li, G. and Yang, Y. (2008). *Applied Physics Letters* **92** (10), 103306.
- [35] Otieno, F.O. (2015). *Enhancement of photo-conversion efficiency of organic solar cells by plasmon resonance effect*, MSc dissertation, University of the Witwatersrand, Johannesburg.
- [36] Chen, T.-A., Wu, X. and Rieke, R.D. (1995). *Journal of the American Chemical Society* **117** (1), 233.
- [37] Li, G., Shrotriya, V., Yao, Y. and Yang, Y. (2005). *Journal of Applied Physics* **98** (4), 043704.

- [38] Yang, X., Loos, J., Veenstra, S.C., Verhees, W.J.H., Wienk, M.M., Kroon, J.M., Michels, M.A.J. and Janssen, R.A.J. (2005). *Nano Letters* **5** (4), 579.
- [39] Lee, Y.-S. and Chow, M.H.L. (2018). Chapter 7 in *Power Electronics Handbook (4th ed.): Diode Rectifiers*, edited by M.H. Rashid (Butterworth-Heinemann), Oxford, UK.
- [40] Hwang, J.D. and Lee, K.S. (2008). *Journal of The Electrochemical Society* **155** (4), H259.
- [41] Mahapatro, A.K. and Ghosh, S. (2001). *IEEE Transactions on electron devices* **48** (9), 1911.
- [42] Ahmad, Z., Sayyad, M.H., Saleem, M., Kamirov, K.S. and Shah, M. (2008). *Physica E* **41** (1), 18.
- [43] Kwon, M.H. (2012). *Transactions on electrical and electronic materials* **13** (2), 98.
- [44] Lampert, M.A. and P. Mark, P. (1970). *Current Injection in Solids*, (Academic Press), New York.
- [45] Liu, Z., Niu, S. and Wang, N. (2017). *Solar Energy* **155**, 1044.
- [46] Kirchatz, T., Deledalle, F., Tuladhar, P.S., Durrant, J.R. and Nelson, J. (2013). *Journal of Physical Chemistry Letters* **4** (14), 2371.
- [47] Street, R.A., Krakaris, A. and Cowan, S.R. (2012). *Advanced Functional Materials* **22** (21), 4608.
- [48] Street, R.A., Northrup, J.E. and B. S. Krusor, B.S. (2012). *Physical Review B* **85** (20), 205211.
- [49] Kyaw, A.K.K., Wang, D.H., Gupta, V., Leong, W.L., Ke, L., Bazan, G.C. and Heeger, A.J. (2013). *ACS Nano* **7** (5), 4569.
- [50] Lu, L., Luo, Z., Xu, T. and Yu, L. (2012). *Nano Letters* **13** (1), 59.

- [51] Wu, J.-L., Chen, F.-C., Hsiao, Y.-S., Chien, F.-C., Chen, P., Kuo, C.-H., Huang, M.H. and Hsu, C.-S. (2011). *ACS Nano* **5** (2), 959.
- [52] Mihailetchi, V.D., Xie, H.X., de Boer, B., Koster, L.J.A. and Blom, P.W.M. (2006). *Advanced Functional Materials* **16** (5), 699.
- [53] Mihailetchi, V.D., Koster, L.J.A., Hummelen, J.C. and Blom, P.W.M. (2004). *Physical Review Letters* **93** (21), 216601.
- [54] Deibel, C., Strobel, T. and Dyakonov, V. (2010). *Advanced Materials* **22** (37), 4097.
- [55] Zhang, Y., Dang, X.-D., Kim, C. and Nguyen, T.-Q. (2011). *Advanced Energy Materials* **1** (4), 610.
- [56] Vanlaeke P., Swinnen, A., Haeldermans, I., Vanhoyland, G., Aernouts, T., Cheyns, D., Deibel, C., D'Haen, J., Heremans, P., Poortmans, J. and Manca, J.V. (2006). *Solar Energy Materials and Solar Cells* **90** (14), 2150.
- [57] Verploegen, E., Mondal, R., Bettinger, C.J., Sok, S., Toney, M.F. and Bao, Z. (2010). *Advanced Functional Materials* **20** (20), 3519.
- [58] Cui, J., Martínez-Tong, D.E., Sanz, A., Ezquerra, T.A., Rebollar, E. and Nogales, A. (2016). *Macromolecules* **49** (7), 2709.
- [59] Falke, S., Eravuchira, P., Materny, A. and Lienau, C. (2011). *Journal of Raman Spectroscopy* **42** (10), 1897.
- [60] Motaung, D.E., Malgas, G.F., Arendse, C.J., Mavundla, S.E. and Knoesen, D. (2009). *Materials Chemistry and Physics* **116** (1), 279.
- [61] Tsoi, W.C., Spencer, S.J., Yang, L., Ballantyne, A.M., Nicholson, P.G., Turnbull, A., Shard, A.G., Murphy, C.E., Bradley, D.D.C., Nelson, J. and Kim, J.-S. (2011). *Macromolecules* **44** (8), 2944.

- [62] Tsoi, W.C., James, D.T., Kim, J.S., Nicholson, P.G., Murphy, C.E., Bradley, D.D.C., Nelson, J. and Kim, J.-S. (2011). *Journal of the American Chemical Society* **133** (25), 9834.
- [63] Mattis, B.A., Chang, P.C. and V. Subramanian, V. (2003). *Materials Research Society Symposium Proceedings* **771**, L10.35.1.
- [64] Krebs, F.C. and Norrman, K. (2007). *Progress in Photovoltaics: Research and Applications* **15** (8), 697.
- [65] Lilliedal, M.R., Medford, A.J., Madsen, M.V., Norrman, K. and Krebs, F.C. (2010). *Solar Energy Materials and Solar Cells* **94** (12), 2018.
- [66] Alstrup, J., Jørgensen, M., Medford, A.J. and Krebs, F.C. (2010). *ACS Applied Materials and Interfaces* **2** (10), 2819.
- [67] Gaffar, M.A., Abu El-Fadl, A. and Bin Anooz, S. (2004). *Solid State Communications* **129** (12), 797.
- [68] El-Samanoudy, M.M. (2003). *Applied Surface Science* **207** (1 – 4):219.
- [69] Nakazono, M., Kawai, T. and Yoshino, K. (1994). *Chemistry of Materials* **6** (6), 864.
- [70] Horowitz, G. (1998). *Advanced Materials* **10** (5), 365.
- [71] Chiguvare, Z. (2005). *Electrical and Optical Characterization of Bulk Heterojunction Polymer- Fullerene Solar Cells*. PhD thesis, Oldenburg University, Germany.
- [72] Cowan, S.R., Roy, A. and Heeger, A.J. (2010). *Physical Review B*, **82** (24), 245207.
- [73] Wetzelaer, G.A.H., Kuik, M., Lenes, M. and Blom, P.W.M. (2011). *Applied Physics Letters* **99** (15), 153506.

Chapter 5

Performance assessment of donor:acceptor1:acceptor2 ternary blend BHJ OPV devices

5.1 Introduction

OPVs have not made a prominent mark in as far as commercialisation is concerned due to their low efficiencies and inferior lifetime stabilities when compared to readily available inorganic solar cells [1]. These deficiencies have meant that further research is needed in the quest for the realisation of enhanced power conversion efficiencies and improved lifetimes.

As seen in Chapter 2, the power conversion efficiency (PCE) of a solar cell depends on the short-circuit current density J_{sc} , the open-circuit voltage V_{oc} and the fill factor FF . Equation (2.6) can also be written as,

$$\text{PCE} = \frac{J_{sc} \times V_{oc} \times FF}{P_L} \times 100\% \quad (5.1)$$

with P_L being the power of the incident light (mW/cm^2). Any fabrication of OPV devices has to take into account that any PCE improvement depends on the related enhancements of the V_{oc} , the J_{sc} and the FF . The J_{sc} is primarily governed by the optical absorption properties of the active layer, the band gap overlap with the maximum photon flux in the solar emission spectrum and the nano-scale morphology of the BHJ. The photocurrent can thus be increased by the absorption of light into the near infrared region. In binary polymer:fullerene systems, improvements in blend morphologies and testing of a variety of polymers and fullerene C(60) derivatives are among a few initiatives to this effect over and above the usage of low bandgap donor materials [2].

The use of a ternary blend in OPVs is continuing to gain traction as a strategy towards achieving cost effective, simple and efficient approach towards the fabrication of higher power conversion efficiency devices. In general, ternary OPVs contain three materials in their active layers i.e. in addition to the conventional binary polymer:fullerene, a third component is added to enhance the performance of the device. The choice of this component can be drawn from small molecules, dyes, nanoparticles [3 – 8], quantum dots [9] or polymers [10 - 11]. Ternary blend OPVs are generally grouped into three categories namely,

- one-donor:two-acceptors (D:A1:A2),
- two-donors:one-acceptor (D1:D1:A)
- one-donor:one non-volatile additive:one-acceptor.

The work by Thompson *et al.* highlighted a ternary model named the “alloy model” [12 – 16]. The alloy model proposed a mechanism where two electronically similar ternary active layer components (either two donors or two acceptors), combine to form an electronic alloy instead of having each material forming an independent parallel-linkage mechanism with respective acceptor or donor materials. The alloy then forms common HOMO and LUMO energy levels depending on the average composition of the two materials. To this effect, the energy diagram of the fabricated ternary system is shown in Figure 5.1.

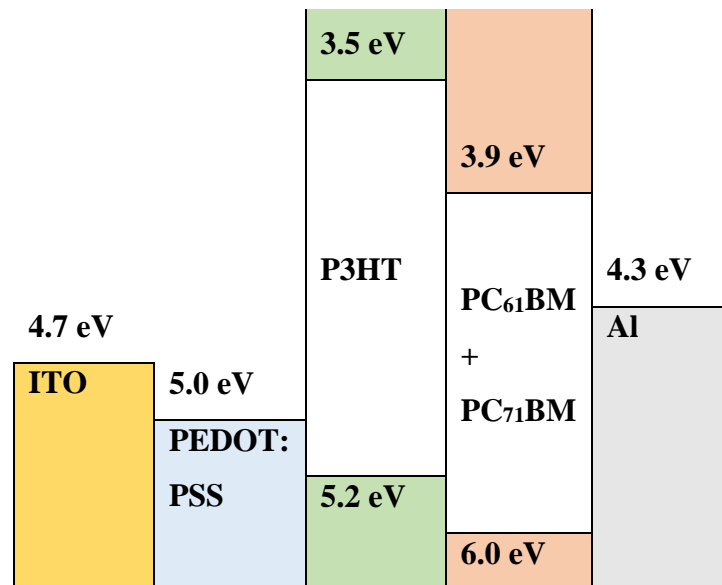


Figure 5.1: Energy level diagram of the proposed P3HT:PC₆₁BM:PC₇₁BM ternary alloy device.

In this study, we fabricated and characterised donor:acceptor1:acceptor2 BHJ OPV devices. PC₆₁BM and PC₇₁BM are fullerene derivatives that have been studied extensively in varied BHJ polymer:fullerene OPV systems. The fullerene (C60) derivatives have an almost identical structure and subsequently similar electronic properties (the HOMO and LUMO levels are very similar). Despite these fullerene derivatives featuring prominently in BHJ OPV research, a mixture of the two in a ternary blend device has hardly been studied. In the Ko *et al.* study, the mixture of PC₆₁BM and PC₇₁BM fullerene derivatives as acceptor materials was combined with a low bandgap polymer, namely; the poly(5,6-bis(octyloxy)-4-(thiophen-2yl)benzo[c][1,2,5]thiadiazole) (PTBT) as a donor material [17]. In our case, we used P3HT as a donor material. Here we sought to harness the excellent optical absorption of PC₇₁BM and the relatively good electron affinity of PC₆₁BM as acceptor materials. Additionally, the miscibility of PCBM and P3HT has meant that BHJ devices can readily be fabricated with minimal complexity. In their study on annealing temperature dependence of morphological stability, Santo *et al.* reported on mixing PC₆₁BM and PC₇₁BM with P3HT in the fabrication and characterisation of inverted OPV devices [18]. The study also mentioned the cost benefit of using a mixture of these fullerene C(60) derivatives as this negated the necessity of purifying PC₆₁BM and PC₇₁BM, a necessary process if either fullerene was to be used on its own.

Optical and electrical characteristics of the P3HT: PC₆₁BM: PC₇₁BM BHJ ternary blend were analysed by fabricating devices with varied mass ratios of PC₆₁BM: PC₇₁BM as acceptor materials in the active layer blend. The optimum blend mixture exhibited a superior J_{sc} and an improved PCE when compared to binary mixtures of P3HT: PC₆₁BM and P3HT: PC₇₁BM.

5.2 Experimental details

In this study, both PCBM derivatives (purity: 99.5%), ITO coated glasses (surface resistivity: 30-60 Ω /sq), P3HT (purity: 99.995%) and PEDOT:PSS (1.3 wt% dispersion in H₂O) were purchased from Sigma Aldrich. In general, the experimental procedure outlined in Chapter 3 was followed, aspects particular to this section of the work will be highlighted.

The active layer mixture was prepared by dissolving 10 mg of P3HT and 10 mg of PC₆₁BM: PC₇₁BM in the ratios (1:0, 0.8:0.2, 0.6:0.4, 0.4:0.6, 0.2:0.8 and 0:1) separately in 0.5 ml of chlorobenzene by stirring the solutions for three hours. The separate solutions were then mixed and again stirred for two more hours to form a 20mg/ml solution of P3HT: PC₆₁BM: PC₇₁BM with ratios 1:1:0, 1:0.8:0.2, 1:0.6:0.4, 1:0.4:0.6, 1:0.2:0.8 and 1:0:1. Patterned ITO coated glass substrates were prepared by etching the ITO via a wet chemistry method using zinc powder and hydrochloric acid. Substrates were then cleaned to remove organic stains and any possible surface contaminants. The hole transport layer, PEDOT:PSS, was then spin coated onto the patterned ITO substrates at 2000 rpm for 60 seconds and subsequently annealed at 100 °C on a hot plate in air for 15 min to remove any residual water. The active layer blend was then spin coated at 2000 rpm for 60 seconds to yield a homogeneous film. Aluminium, the metal top electrode was deposited by thermal evaporation, through a mask, in a vacuum of about 2×10^{-6} mbar. Devices, as in Figure 5.2, with the following structures:

- GLASS/ITO/PEDOT:PSS/P3HT:PC₆₁BM:PC₇₁BM/Al
- GLASS/ITO/PEDOT:PSS/P3HT: PC₆₁BM/Al
- GLASS/ITO/PEDOT:PSS/P3HT:PC₇₁BM/Al

were then annealed in argon at 50°C for 10 minutes before proceeding with any characterisation.

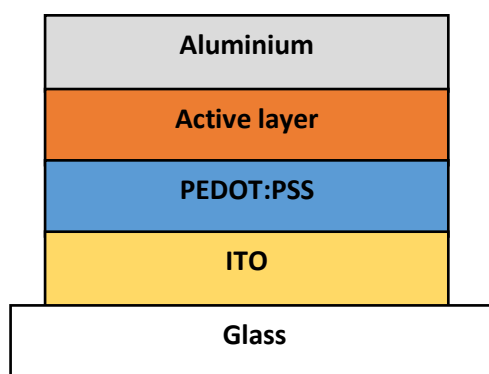


Figure 5.2: GLASS/ITO/PEDOT:PSS/P3HT:PC₆₁BM:PC₇₁BM/Al schematic of the ternary device showing different layers of ternary alloy.

The current–voltage (I–V) measurements were done using the solar simulator (150 W Xe lamp) equipped with 1.5 air mass filters and a source/Measure unit (HP 4141B DC) unit under 100 mW/cm² illumination. Optical absorption measurements of fabricated devices were made using the Cary 500 UV – VIS - NIR spectrophotometer. The Raman bands and the structural order of all the films were examined using a Jobin Yvon T64000 Raman spectrometer equipped with an Ar ion laser (514.5 nm) at 4 mW laser power. All fabrication and characterisation processes were carried out in air at room temperature.

5.3 Results and discussion

5.3.1 Spectroscopic characteristics; UV-Vis details

Optical absorption spectra were collected for different mixtures of the P3HT:PC₆₁BM:PC₇₁BM active layer blends in order to determine their optical properties. Figure 5.3 shows the dependence of optical absorption on the mass ratios of the fullerene C(60) derivatives in the active layer blend. The binary blends of each fullerene derivative have been excluded in our study on the ternary systems to establish the joint optoelectronic effects due to the miscibility of these two derivatives. It can be seen that the absorption is enhanced with an increase in the PC₇₁BM content for a given PC₆₁BM decrease. Also observable is the emergence of the characteristic PC₇₁BM absorption peak at 378 nm as its blend concentration is increased. This is accompanied by a diminishing PC₆₁BM absorption peak at 335 nm. The peak positions emanating from PC₆₁BM and PC₇₁BM absorption remain at the same position, they just change in intensity relative to the PC₆₁BM:PC₇₁BM mass ratio in the active layer blend. The most prominent absorption peak associated with P3HT, was observed at 507 nm due to $\pi - \pi^*$ transitions and two vibronic shoulder absorption peaks at 559 nm and 608 nm. A detailed description of the optical absorption spectrum of P3HT was given in Chapter 4.

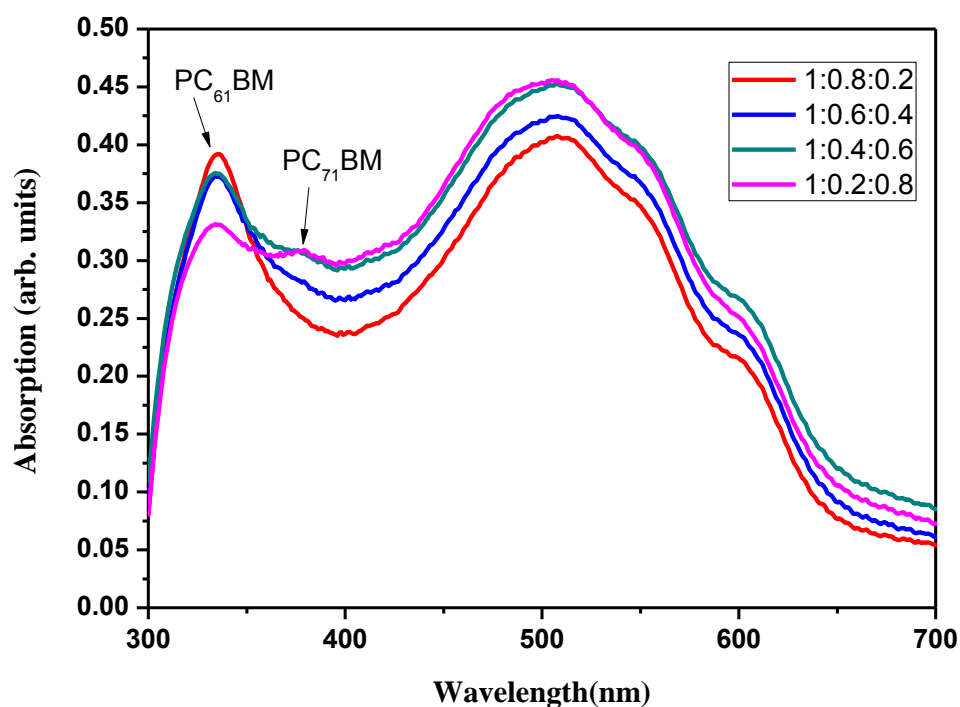


Figure 5.3: UV-Vis absorption spectra of ternary blend devices with varying fullerene C(60) derivatives ratios.

5.3.1.1 Structural studies of ternary blend by Raman spectroscopy

In the Raman spectra (Figure 5.4) characteristic bands associated with symmetric C=C stretching mode (1450 cm^{-1}), inter-ring C-C stretch mode (1380 cm^{-1}) {sensitive to π – electron delocalisation} and C-S-C deformation mode (728 cm^{-1}) identified in P3HT:PCBM blends did not show any change. However, it was thought that PC₇₁BM being a slightly bigger molecule, might disrupt the intermolecular ordering and the π – π^* stacking as its concentration increases. The Raman spectrum of the ternary blends is also dominated by the P3HT component just like in binary P3HT:PC₇₁BM systems we encountered in Chapter 4. A more detailed description of the P3HT Raman spectrum was given in Table 4.6. The most intense peak at 1452 cm^{-1} virtually remains unchanged (does not undergo any shift) as the relative mass ratio of the fullerenes is changed. The FWHM values of this peak show a slight decrease as the PC₇₁BM to PC₆₁BM ratio increases: P3HT:PC₆₁BM:PC₇₁BM (1:0.8:0.2) = $40.40 \pm 0.04\text{ cm}^{-1}$; P3HT:PC₆₁BM:PC₇₁BM

(1:0.6:0.4) = $39.73 \pm 0.03 \text{ cm}^{-1}$; P3HT:PC₆₁BM:PC₇₁BM (1:0.4:0.6) = $39.45 \pm 0.04 \text{ cm}^{-1}$ and P3HT:PC₆₁BM:PC₇₁BM (1:0.2:0.8) = $39.44 \pm 0.01 \text{ cm}^{-1}$. These variations in the FWHM values are shown in Figure 5.5. The variation of the relative C60 fullerene ratio in the photoactive layer for fabricated ternary devices does not seem to affect the structural order of the ternary blend.

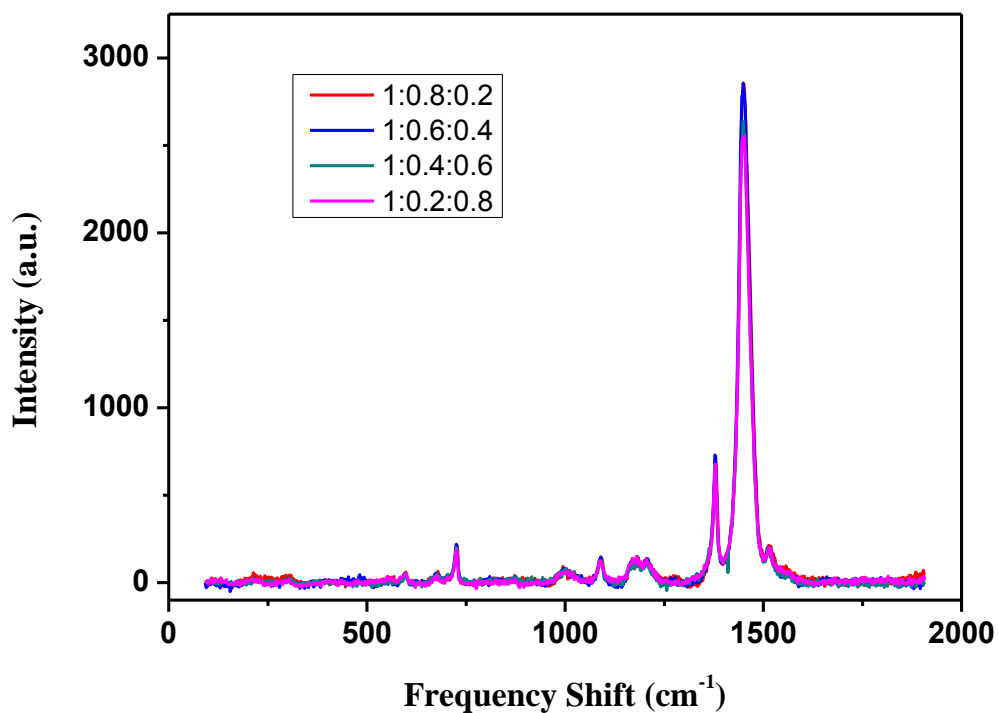


Figure 5.4: Raman spectra of ternary BHJ devices with varying acceptor1:acceptor2 mixtures acquired via an excitation with an Ar ion laser (514.5 nm) at 4 mW laser power.

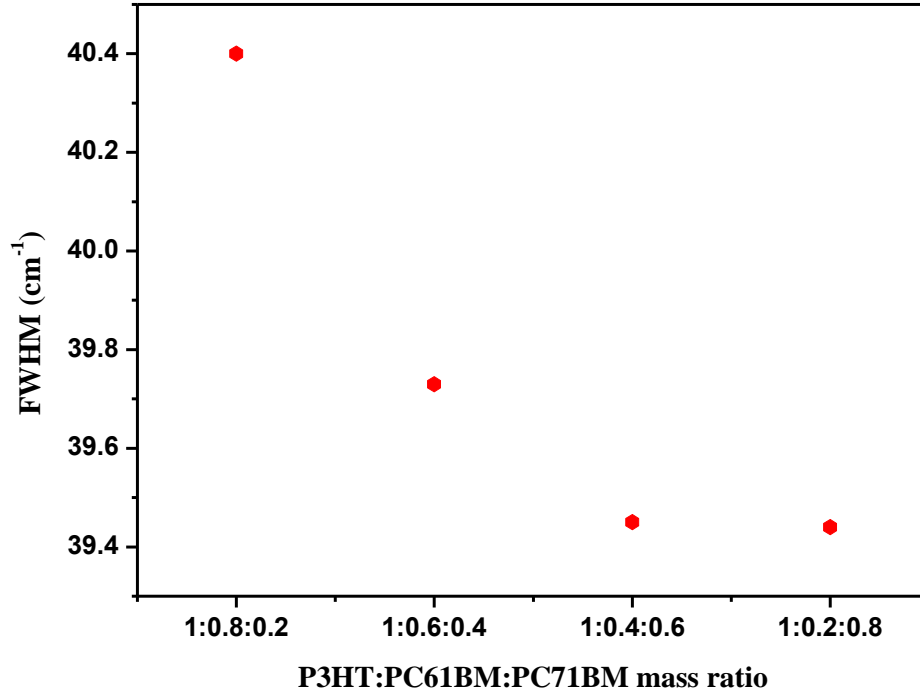


Figure 5.5: The variation of the FWHM of the most intense peak with the PC₆₁BM:PC₇₁BM mass ratio of the photoactive layer.

5.3.2 Current-Voltage characteristics

Figures 5.6 (a) and (b) show the $J - V$ behaviour of the fabricated devices in the dark in linear and semi-log scales respectively. It is important to understand whether junctions (especially metal/active layer junctions) that form in these devices will be rectifying (Schottky) or Ohmic. Since it is known that PV devices must show rectification, we monitored their rectification behaviour by analysing measured current – voltage characteristics. This was done with the knowledge that an assessment of rectification behaviour can be established with a calculation of a rectification ratio (RR). The rectification ratios for the devices were calculated using Equation (5.2) as follows:

$$|RR|_V = \left| \frac{J_F}{J_R} \right|_V \quad (5.2)$$

That is, the absolute value of the ratio of the forward bias current or current density to the reverse bias current or current density at the same applied bias V . The rectification in the devices can be seen in exponential nature of the curves in Figure 5.6 with their actual values given in Table 5.1.

Table 5.1: Rectification ratios of fabricated ternary devices.

Device	<i>RR</i>
1:1:0	32.00
1:0.8:0.2	1160.85
1:0.6:0.4	1256.69
1:0.4:0.6	992.88
1:0.2:0.8	1228.55
1:0:1	1073.03

Though all devices show rectification, we can see from Table 5.1 that rectification ratios do not follow any pattern in as far as the ratios or the fullerene derivatives in the active layer are concerned. The P3HT:PC₆₁BM device, exhibited an anomalous behaviour, with a rectification factor that is much lower than the rest. This could be an indication of poor device quality.

Current – voltage measurements done under 100 mW.cm⁻² illumination using an AM 1.5 filter are shown in Figure 5.7. Clearly observable is the dependence of the short circuit current density on the active layer blend mixture of PC₆₁BM:PC₇₁BM. Given the superior optical absorption properties of PC₆₁BM is comparison to PC₇₁BM, it was anticipated that increasing its concentration in the active layer blend was going to lead to an increase the generated photocurrent. Established from the current – voltage measurements, was that the J_{sc} increased from 7.73 to 11.5 mA/cm² when the PC₆₁BM:PC₇₁BM mass ratio in the active layer was altered from PC₆₁BM rich to PC₇₁BM rich. This increase could be due to the increase seen in the optical absorption spectra as the thicknesses of the photoactive layers of the devices were kept fairly constant at 130 nm. Also observed in Figure 5.6 (a) is that the ternary blend 1:1:0 showed the highest leakage current. This is in good agreement

with the rectification ratios in Table 5.1. This particular blend had the lowest RR value.

The V_{oc} is largely limited by the energy levels of the HOMO of the donor and LUMO of the acceptor. It has been suggested by Street *et al.* [14] that V_{oc} can be tuned in a ternary alloy OPV depending on the materials used. In this case, given the closeness of the HOMO and LUMO levels of PC₆₁BM and PC₇₁BM, changes are negligible with the average value found to be 0.59 ± 0.03 V.

The PCE for different active layer mixtures peaks at 2.69% for the blend ratio P3HT:PC₆₁BM:PC₇₁BM of 1:0.4:0.6. In the PTBT:PC₆₁BM:PC₇₁BM study [17], they found an optimum blend ratio to be 1:0.8:1.2. i.e. they had used double the mass of the fullerene derivatives as compared to our case. The OPV performance parameters are summarised in Table 5.2. The sample 1:0.2:0.8 showed an anomalous stunting of the shunt resistance which could be due to fabrication defects.

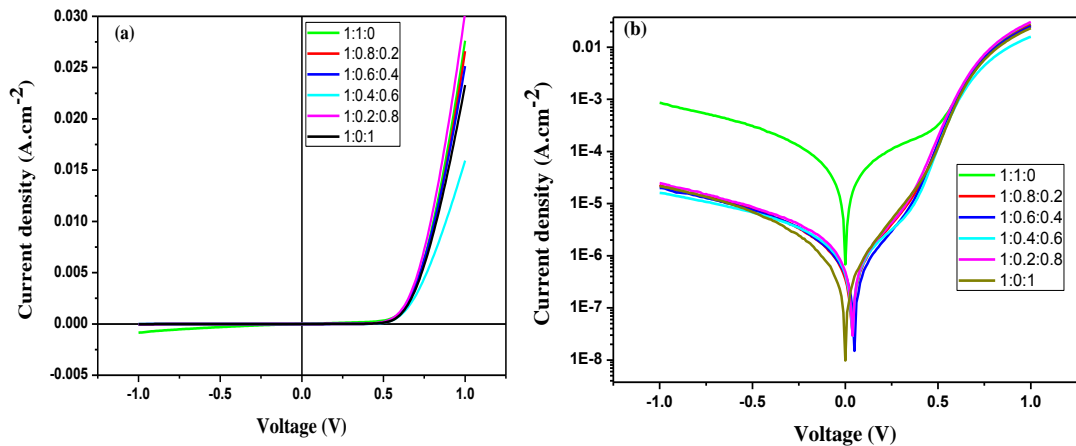


Figure 5.6: Dark $J - V$ characteristics of ternary devices in (a) linear and (b) semi-log scale.

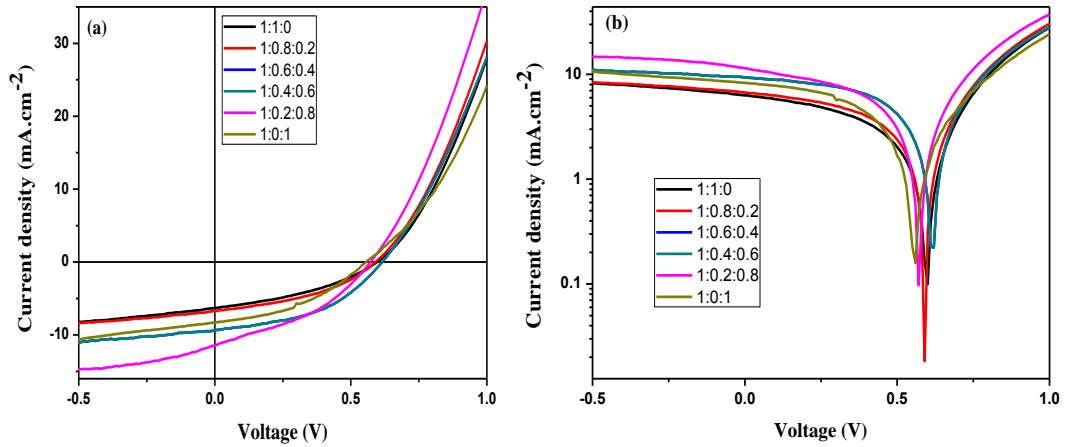


Figure 5.7: $J - V$ characteristics of ternary devices at 100 mW/cm^2 illumination (AM1.5G) in (a) linear and (b) semi-log scale.

Table 5.2: Performance parameters of OPV devices with different ratios of fullerene (60) derivatives in the active layer.

Device P3HT:PC ₆₁ BM:PC ₇₁ BM	V_{oc} (V)	J_{sc} (mA/cm ²)	FF (%)	PCE (%)	R_{sh} (Ω cm ²)	R_s (Ω cm ²)
1:1:0	0.61	6.00	39.6	1.44	300.0	34.7
1:0.8:0.2	0.59	7.73	40.6	1.61	203.2	30.2
1:0.6:0.4	0.62	9.36	44.6	2.57	140.0	22.3
1:0.4:0.6	0.62	10.71	40.2	2.69	210.0	29.3
1:0.2:0.8	0.57	11.49	37.8	2.49	79.2	21.2
1:0:1	0.56	8.29	39.8	1.83	233.3	32.3

5.3.3 Charge transport properties of fabricated ternary devices

The details that are related to current that is expected from emission and bulk transport mechanisms are discussed in sections 5.3.3.1 and 5.3.3.2.

5.3.3.1 Emission contributions

FN plots for ternary devices are shown in Figure 5.8. At low $1/|absV|$ values, representing high electric fields limited to within 2 V^{-1} ($\approx 3.85 \times 10^6 \text{ V/m}$), straight lines with negative slopes can be fitted to the FN curves. Current injection by

quantum mechanical tunnelling is seen to be dependent on the mass ratio of the ternary blend given the variations in the slopes of the fitted FN curves. These variations in the Schottky barrier are indicated by a decrease in the slope as the relative content of PC₇₁BM to PC₆₁BM in the photoactive layer increases. This could also be the reason for the increase in the J_{sc} together with the optical effects that were observed. It was established in Chapter 2 that the slope is directly proportional to the potential barrier and determination of the barrier was given by Equation (2.37). Of interest in this case was the observed trend in the variation of the slope rather than an involved quantitative analysis.

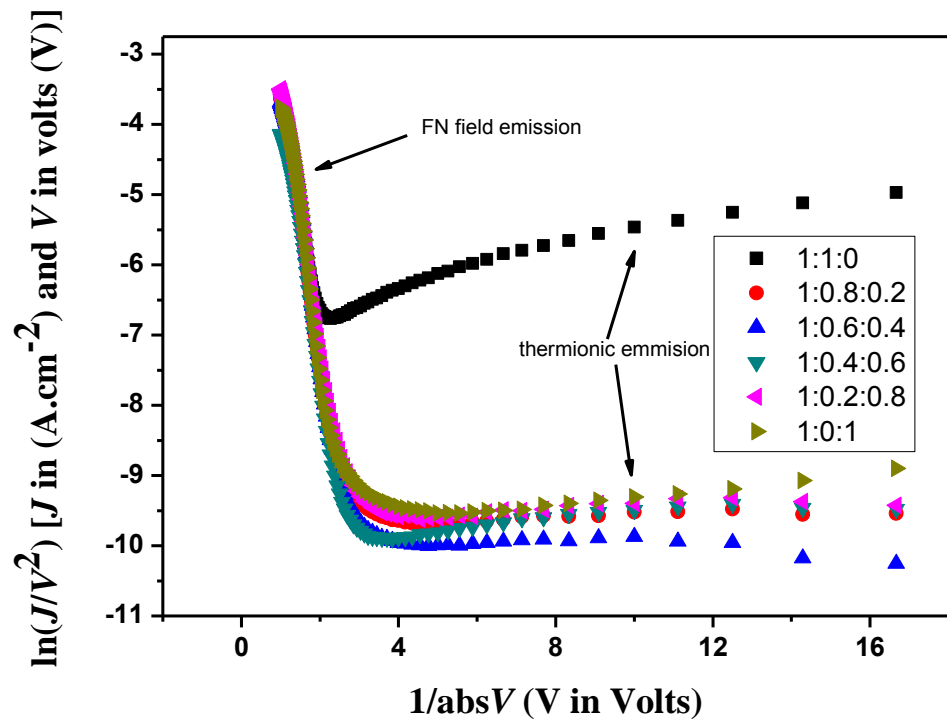


Figure 5.8: FN plots for ternary blends under forward bias in the dark outlining FN field emission and thermionic contributions to the measured current.

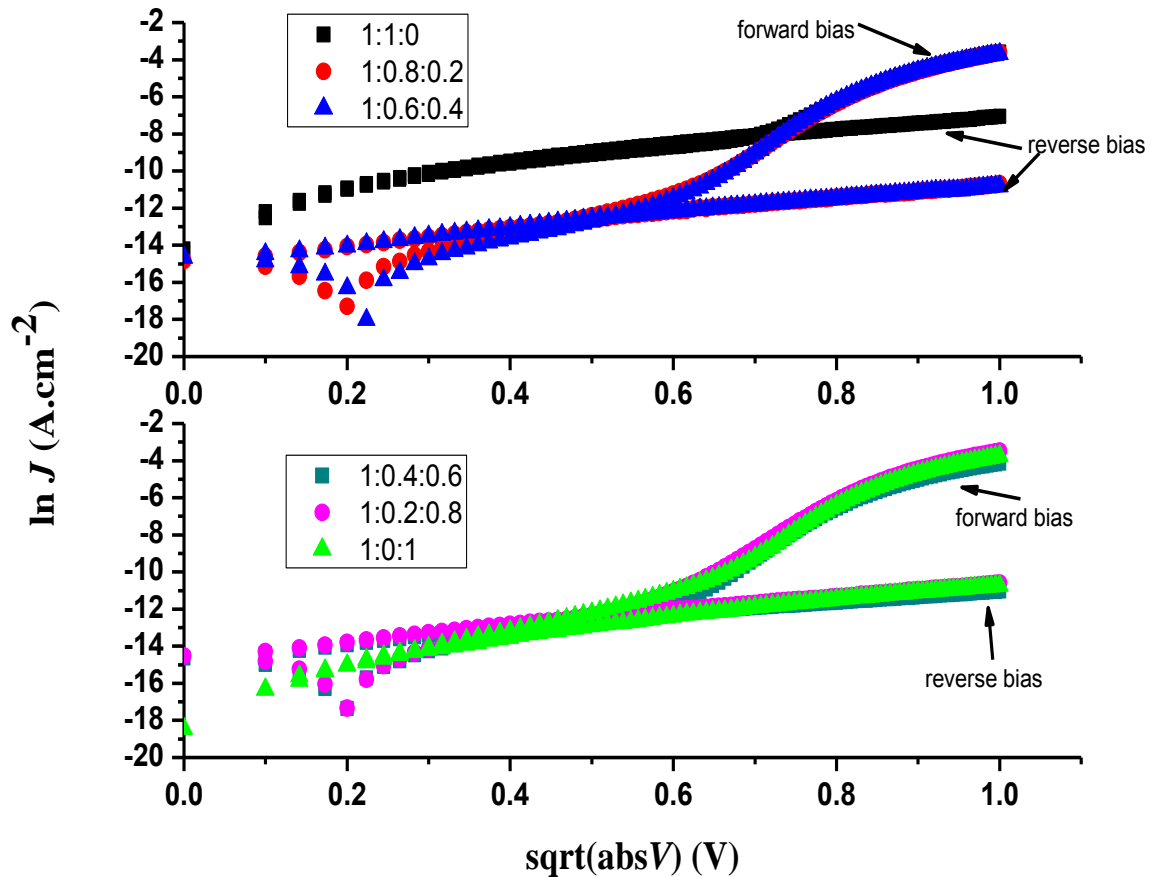


Figure 5.9: RS plots for ternary blends stacked for better illustration. The PC₇₁BM component of the photoactive blend increases relative to the PC₆₁BM component from the top graph to the bottom one.

It can be observed from both Figures 5.8 and 5.9 that thermionic emission is evident at low applied fields. The device 1:1:0 makes the greatest contribution towards the current via thermionic emission.

5.3.3.2 Bulk limited transport

The log-log plot of J as a function of V in Figure 5.10 shows an Ohmic conduction for the 1:1:0 device well into higher bias voltages at about 0.5 V. This is in contrast to the ternary as well as the 1:0:1 devices, that show the onset of SCLC at voltages of about 0.2 V, indicated as region I. However, the onset voltage is higher than

$k_B T/q \approx 0.026$ V. Beyond region I the current density under forward bias for all the devices, bar the 1:1:0 device, obeyed the power law of the form $J \propto V^m$ with $m > 2$ described by space charge limited current in the presence of exponentially distributed traps within the band gap [19]. It has been shown that the SCLC model in the presence of exponentially distributed traps gives the same qualitative results as the trap free SCLC [20].

Having made this consideration we then determined charge carrier mobilities by applying the Mott-Gurney law to the $J - V$ characteristics of ternary devices. The linear fits are displayed in Figure 5.11. With $\epsilon_0 = 8.85 \times 10^{-12}$ F.m⁻¹, $\epsilon_r = 3.5$ and $d = 130$ nm, charge carrier mobilities for the bends can be determined as shown in Table 5.3.

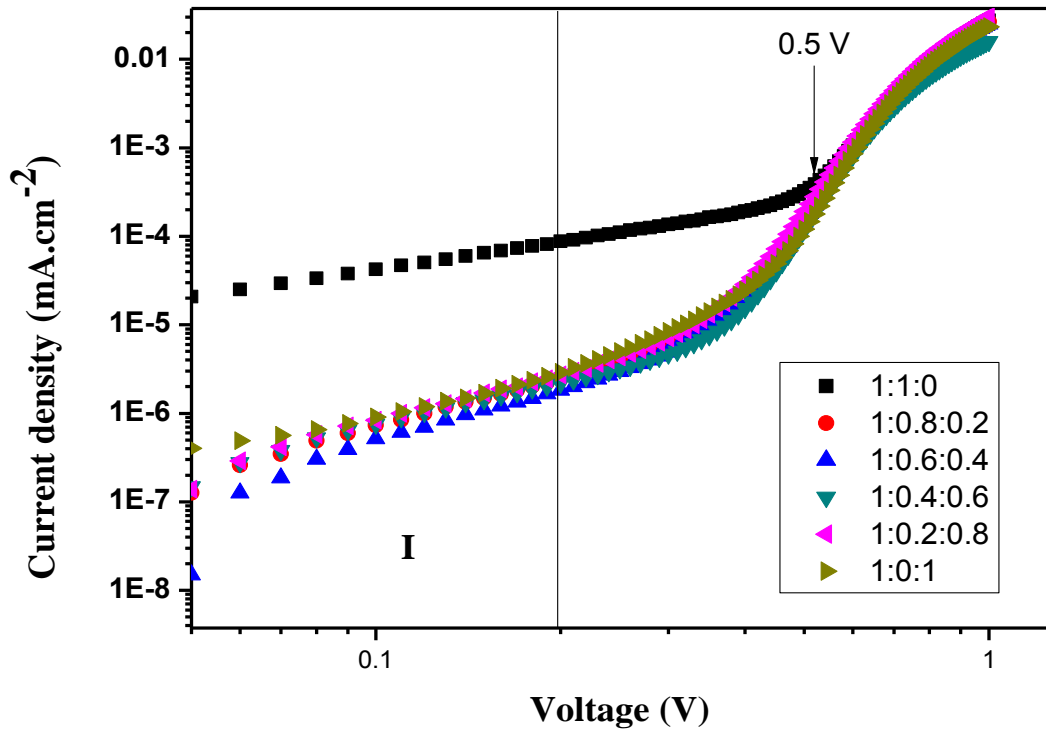


Figure 5.10: $J - V$ characteristics in the dark in log-log scale for varying donor:acceptor1:acceptor2 ratios in the photoactive layer of ITO/PEDOT:PSS/P3HT:PC₆₁BM:PC₇₁BM/Al devices.

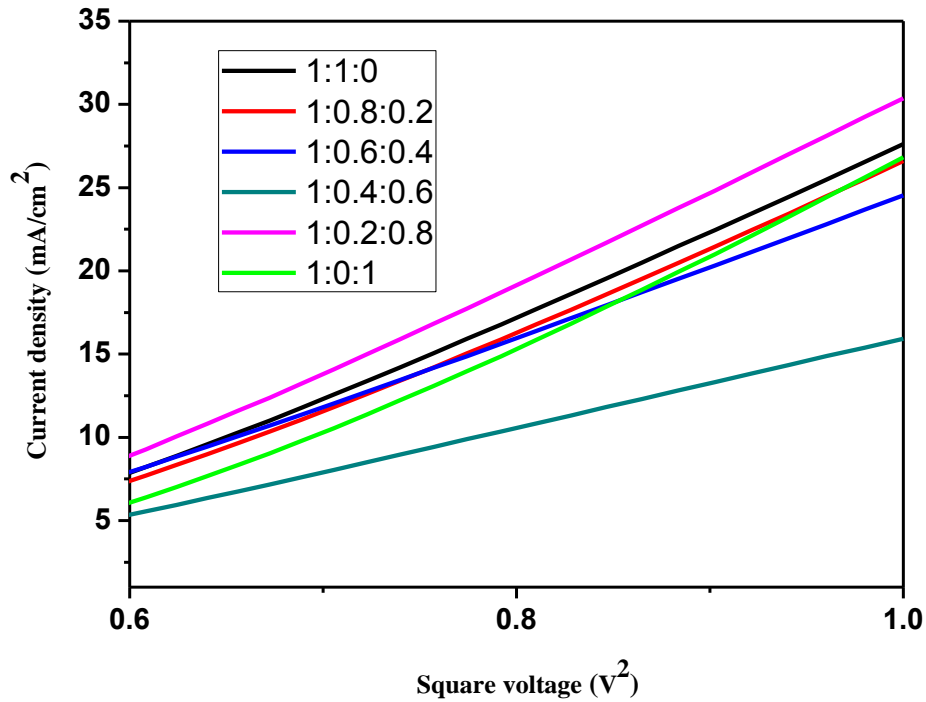


Figure 5.11: Linear fits of J_{sc} vs V^2 based on the Mott-Gurney law for charge mobility extraction.

5.3.4 Variations of OPV parameters with incident light intensity

Figures 5.12 (a) and (b) help us to establish the type or types of recombination mechanisms that affect the operation and hence the efficiency of the OPV devices. In Figure 5.12 (a), we use the fact that at V_{oc} conditions, all photogenerated charge carriers recombine within their diffusion lengths inside the bulk material, to probe dominant recombination mechanisms. Recombination mechanisms can then be extracted by studying V_{oc} as a function of input light intensity, P_{light} . For bimolecular recombination to be dominant, the slope of the plot of V_{oc} versus the natural logarithm of the input light intensity is expected to be $nk_B T/q$ with $n = 1$. The n being the ideality factor under illumination. At values of $n > 1$, then monomolecular or trap-assisted (SRH-type) recombination processes are prevalent in the active layer of the PV device. On the other hand, values of $n < 1$ would corroborate the Auger type recombination of charge carriers. Additionally, where $n = 2$, the

Shockley-Read-Hall recombination process predominates over all possible recombination processes. Ideality factors greater than 2 have been observed and ascribed to possible non-ohmic metal-semiconductor contacts, accompanied by relatively high resistances [21].

The calculation of ideality factors under illumination is meant to avoid the strong influences of shunt and series resistances and space charge effects at higher voltages on $J - V$ characteristics that are typical in the dark [22].

All ideality factors are directly related to the slopes of the curves and as can be seen in Table 5.3 with calculated values are greater than 1 indicating that bimolecular or non-geminate recombination is not the only recombination mechanism in effect. The device 1:0:1 shows a strong dependence of the current on monomolecular or trap-assisted recombination with an enhanced dependence of the open circuit on the input light intensity i.e. slope = $2k_B T/q$ [23 – 25].

The power law dependence of J_{sc} on input light intensity P_{light} in organic photovoltaics is shown in the log-log plot in Figure 5.12(b). That is, $J_{sc} \propto (P_{light})^\alpha$. Strong dependence of the J_{sc} on geminate or monomolecular recombination (weak bimolecular recombination) will be seen from the linear dependence of the J_{sc} on P_{light} when $\alpha = 1$ [23, 24].

Observed from Table 5.3, is that the strongest dependence on geminate recombination at short circuit is in the devices with the highest amount of PC₆₁BM i.e. the P3HT:PC₆₁BM:PC₇₁BM 1:1:0 and the 1:0.8:0.2 devices. Bigger deviations from $\alpha = 1$ are seen in devices with the highest PC₇₁BM content.

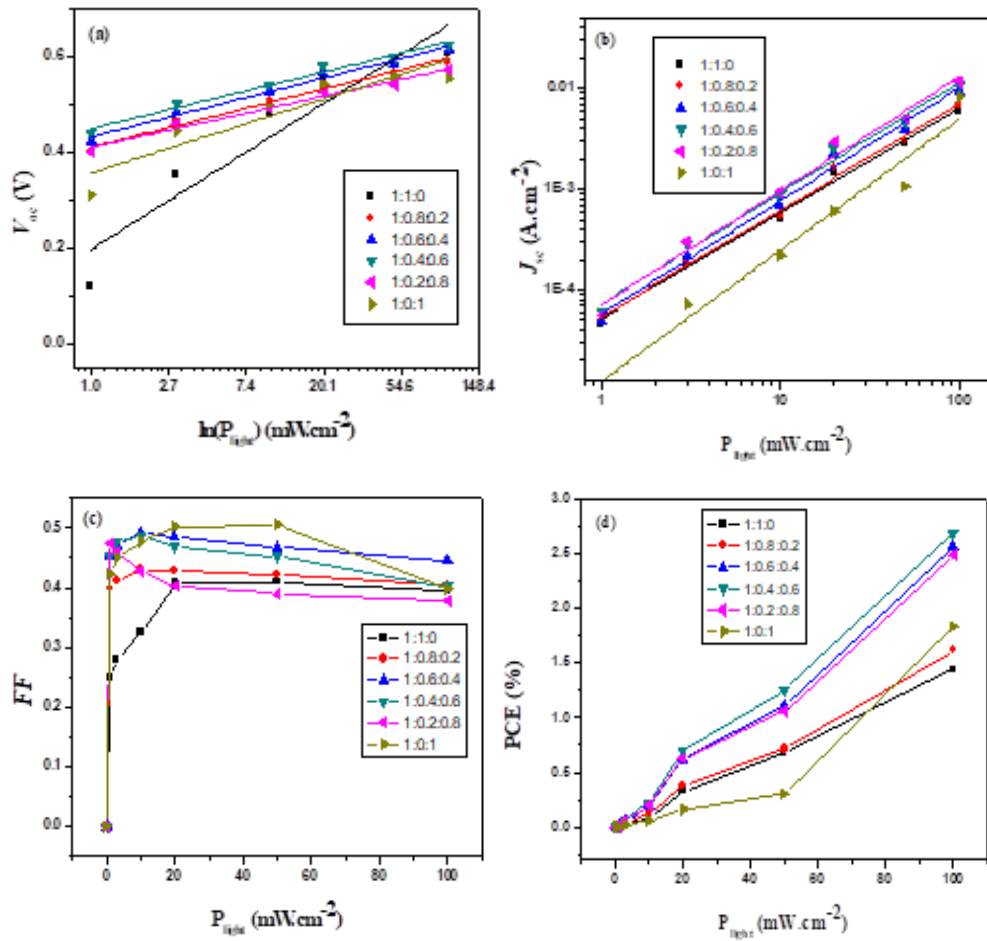


Figure 5.12: Ternary blend variations of (a) open circuit voltage (b) short circuit current density (c) fill factor (d) power conversion efficiency as a function of light intensity (P_{light}).

Figure 5.12 (c) shows the dependence of FF on input light intensity. Higher FF values can be seen at lower light intensities and the lower values at high illumination intensities are an indication of recombination losses. The biggest drop in FF i.e. from low illumination to high illumination is in the device with the strongest trap-assisted recombination dependence at open circuit and the strongest dependence on bimolecular dependence at short circuit conditions. The device 1:0:1 had slope $= 2k_B T/q$ in the V_{oc} vs P_{light} plot and $\alpha = 1.30$ in J_{sc} vs P_{light} log-log plot. The dependence of the PCE on illumination intensity reveals the often observed increased in PCE with an increase in light intensity as can be seen in Figure 5.12 (d).

Table 5.3: Average values for charge carrier mobilities and recombination parameters of ternary blends.

Device	n ± 0.13	μ $\pm 0.006 \times 10^{-6}$ (cm ² /Vs)	α ± 0.18
1:1:0	3.94	1.418	1.04
1:0.8:0.2	1.57	1.405	1.06
1:0.6:0.4	1.59	1.364	1.12
1:0.4:0.6	1.52	0.900	1.10
1:0.2:0.8	1.37	1.640	1.13
1:0:1	2.00	1.335	1.30

To further understand the effect of the ternary blending of the photoactive layer on the performance of fabricated devices, we studied the behaviour of the photocurrent density (J_{ph}) as a function of the effective voltage (V_{eff}). The measured relationships, which enable the determination of the saturation current density J_{sat} , the maximum exciton generation G_{max} and the exciton dissociation probability P(E,T), are shown in Figure 5.13.

As described in Chapter 4, J_{ph} is found as $J_{ph} = J_L - J_D$, where J_L is the photocurrent density under illumination by one sun and J_D in the current density measured in the dark. V_{eff} is determined as $V_{eff} = V_0 - V_a$, where V_0 is the voltage at which $J_{ph} = 0$ and V_a is the applied bias voltage. It is generally assumed that the J_{sat} is directly proportional to G_{max} such that $J_{sat} = qG_{max}L$ as in Equation (4.4).

The plots in Figure 5.13 indicate that J_{ph} saturates for $V_{eff} > 0.8$ V, however an even greater field dependence is still in evidence beyond this point particularly for the 1:0:1 device. The observed trend for this device is out of kilter with the rest of the devices. Bearing this observation in mind, we assumed saturation beyond 0.8 V and proceeded to calculate J_{sat} at 0.9 V for all devices with the aim of establishing possible $J_{ph} - V_{eff}$ behavioural patterns.

For the ternary blends, it was seen in Figure 5.3 that an increase in the mass ratio of PC₇₁BM in the P3HT:PC₆₁BM:PC₇₁BM blend led to an enhancement in optical absorption. The optical absorption qualities of each blend can be linked to the maximum exciton generation rate and hence the saturated current density. Under ideal conditions, the saturation current density is the same as the short circuit current density. Despite non-ideal conditions in our case, we can see the J_{sat} pattern of an

increase in PC₇₁BM replicated in the increase in J_{sc} , following the same pattern. This can be seen in J_{sat} values in Table 5.4 and J_{sc} values in Table 5.2.

Table 5.4: Saturation current densities and maximum exciton generation rates for ternary blends.

Device	J_{sat} (mA.cm ⁻²)	G_{max} (x10 ²⁷) (m ⁻³ s ⁻¹)
1:1:0	6.84	3.28
1:0.8:0.2	7.88	3.78
1:0.6:0.4	10.48	5.03
1:0.4:0.6	11.88	5.70
1:0.2:0.8	14.01	6.73
1:0:1	9.67	4.64

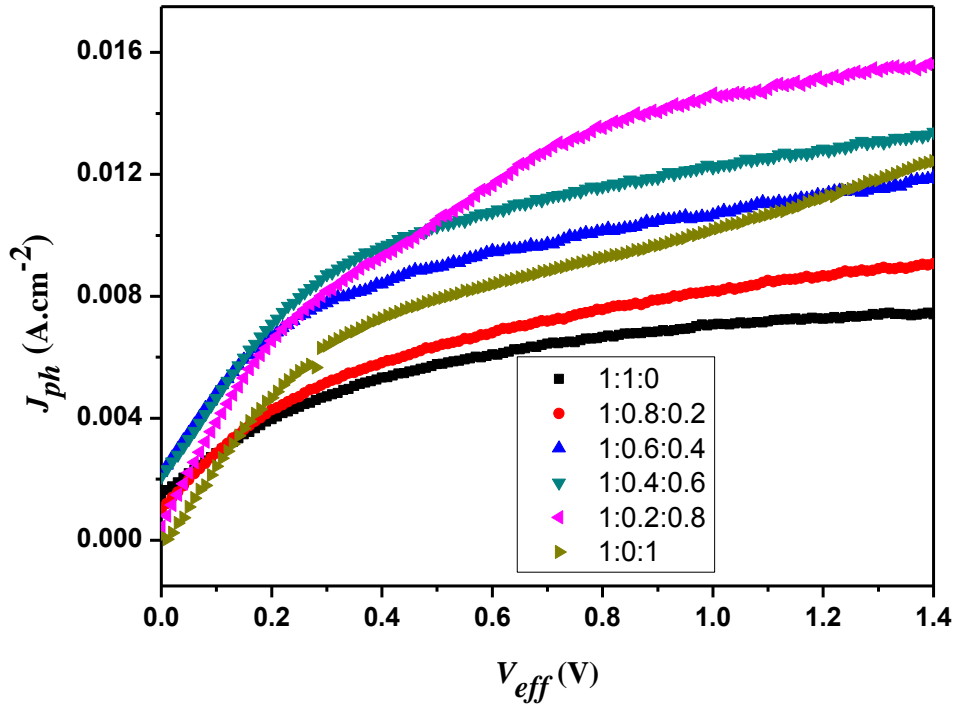


Figure 5.13: J_{ph} vs V_{eff} for ternary blends showing the attainment of saturation currents at high effective voltages.

5.4 Conclusion

We have demonstrated that ternary BHJ OPV devices can easily be fabricated by using electron acceptor materials that are chemically and electronically similar. These mixtures of PC₆₁BM and PC₇₁BM fullerene derivatives formed a semiconducting alloy in the photoactive layer. Though the P3HT:PC₆₁BM:PC₇₁BM (1:0.8:0.2) devices showed the largest short circuit current densities, it was the (1:0.4:0.6) devices that gave the best power conversion efficiencies of about 2.69%. To have a better understanding of the performance of fabricated devices, as a function of C60 fullerene derivative ratio in the photoactive blend, we measured the strengths of recombination characteristics both at open circuit voltage and at short circuit current, the exciton generation rates, charge carrier mobilities and optical absorption properties. The strongest correlations were found between a relative increase in the PC₇₁BM content of the photoactive layer with an increase in optical absorption and photogenerated currents.

5.5 References

- [1] Jørgensen, M., Norrman, K., Gevorgyan, S.A., Tromholt, T., Andreasen, B. and Krebs, F.C. (2012). *Advanced Materials* **24** (5) 580.
- [2] Li, W., Hendriks, K.H., Roelofs, W.S.C., Kim, Y., Wienk, M.M. and Janssen, R.A.J. (2013). *Advanced Materials* **25** (23), 3182.
- [3] Hu, Z., Tang, S., Ahlvers, A., Khondaker, S.I. and Gesquiere, A.J. (2012). *Applied Physics Letters* **101** (5), 053308.
- [4] Zhang, M., Zhang, F., An, Q., Sun, Q., Wang, J., Li, L., Wangand, W. and Zhang, J. (2015). *Solar Energy Materials and Solar Cells* **141**, 154.
- [5] Lessard, B.H., Dang, J.D., Grant, T.M., Gao, D., Seferosand, D.S. and Bender, T.P. (2014). *ACS Applied Materials and Interfaces* **6** (17), 15040.
- [6] Mandoc, M.M., Kooistra, F.B., Hummelen, J.C., de Boer, B. and Blom, P.W.M. (2007). *Applied Physics Letters* **91** (26), 263505.
- [7] Zhen, Y.G., Tanaka, H., Harano, K., Okada, S., Matsuo, Y. and Nakamura, E. (2015). *Journal of the American Chemical Society* **137** (6), 2247.
- [8] Chen, C.-H., Hsieh, C.-H., Dubosc, M., Cheng, Y.-J. and Hsu, C.-S. (2010). *Macromolecules* **43** (2), 697.
- [9] Itskos, G., Othonos, A., Rauch, T., Tedde, S.F., Hayden, O., Kovalenko, M.V., Heiss, W. and Choulis, S.A. (2011). *Advanced Energy Materials* **1** (5), 802.
- [10] Ameri, T., Min, J., Li, N., Machui, F., Baram, D., Forster, M., Schottler, K.J., Dolfen, D., Scherf, U. and Brabec, C.J. (2012). *Advanced Energy Materials* **2** (10), 1198.
- [11] Yang, L., Zhou, H., Price, S. C. and You, W. (2012). *Journal of the American Chemical Society* **134** (12), 5432.

- [12] Khlyabich, P.P., Burkhart, B. and Thompson, B.C. (2011). *Journal of the American Chemical Society* **133** (37), 14534.
- [13] Khlyabich, P.P., Burkhart, B. and Thompson, B.C. (2012). *Journal of the American Chemical Society* **134** (22), 9074.
- [14] Street, R.A., Davies, D., Khlyabich, P.P., Burkhart, B. and Thompson, B.C. (2013). *Journal of the American Chemical Society* **135** (3), 986.
- [15] Khlyabich, P.P., Rudenko, A.E., Thompson, B.C. and Loo, Y.-L. (2015). *Advanced Functional Materials* **25** (34), 5557.
- [16] Khlyabich, P.P., Rudenko, A.E., Street, R.A. and Thompson, B.C. (2014). *ACS Applied Materials and Interfaces* **6** (13), 9913.
- [17] Ko, S.-J., Lee, W., Choi, H., Walker, B., Yum, S., Kim, S., Shin, T.J., Woo, H.Y. and Kim J.Y. (2015). *Advanced Energy Materials* **5** (5), 1401687.
- [18] Santo, Y., Jeon, I., Yeo, K.S., Nakagawa, T. and Matsuo, Y. (2013). *Applied Physics Letters* **103** (7), 073306.
- [19] Chiguvare, Z. (2005). *Electrical and Optical Characterization of Bulk Heterojunction Polymer- Fullerene Solar Cells*. PhD thesis, Oldenburg University, Germany.
- [20] Campbell, A.J., Weaver, M.S., Lidzey, D.G. and Bradley, D.D.C. (1998). *Journal of Applied Physics* **84** (12), 6736.
- [21] Zekry, A., Abdel-Naby, M., Ragaie, H.F. and El Akkad, F.E. (1993). *IEEE Transactions on Electron Devices* **40** (2), 259.
- [22] Kirchatz, T., Deledalle, F., Tuladhar, P.S., Durrant, J.R. and Nelson, J. (2013). *Journal of Physical Chemistry Letters* **4** (14), 2371.

- [23] Riedel, I., Parisi, J., Dyakonov, V., Vanderzande, D. and Hummelen, J.C. (2004). *Advanced Functional Materials* **14** (1), 38.
- [24] Cowan, S.R., Roy, A. and Heeger, A.J. (2010). *Physical Review B* **82** (24), 245207.
- [25] Koster, L.J.A., Mihailetschi, V.D., Ramaker, R. and Blom, P.W.M. (2005). *Applied Physics Letters* **86** (12), 123509.

Chapter 6

Photovoltaic investigation of N-MWCNT incorporated BHJ OPV devices

6.1 Introduction

Efforts aimed at seeing widespread usage of renewable energy sources have led to significant research interest in organic photovoltaics (OPVs). One of the most desirable characteristics of OPVs is the possibility of low cost processing of large area devices on flexible substrates [1]. In as far as being the source for the generation of clean renewable energy is concerned, OPVs have an additional advantage of having high optical absorption coefficients that lead to light absorption within very thin layers thereby requiring reduced quantities of photo-active materials for fabrication [2]. OPVs can also be fabricated with shorter energy pay-back times on the basis of the roll-to-roll printing technology with high throughputs at low production temperatures [3 - 4].

The bulk heterojunction (BHJ) device architecture has been widely employed in order to maximise the donor-acceptor interface in OPV devices. The BHJ concept is based on the solution processing approach that blends electron donor and acceptor materials that make up the photoactive layer of the OPV device. The blending of the active layer materials enables an efficient charge separation at the donor-acceptor (D – A) interface and a higher charge collection efficiency from the inter-penetrating network of the (D – A) blend [5]. Recently, particularly in the last decade, the power conversion efficiency (PCE) of OPVs has seen a remarkable improvement even though the highest values are still around 10 – 16% [6 – 10]. It has to be noted though that some of the approaches in these improvements involved using higher priced low bandgap polymers as donor materials and the adoption of tandem morphologies in the fabrication of OPV devices. These improvements in power conversion efficiencies (PCEs) have not led to large scale mass production

of OPVs for commercialisation owing to low efficiencies and poor lifetime stabilities as compared to conventional inorganic solar cells [11]. The (D – A) binary blend of the photoactive layer still suffers from the following shortcomings that inhibit enhanced device performances: a narrow and weak optical absorption spectrum (< 650 nm and requiring a thicker photoactive layer); poor charge transfer efficiencies and energy losses from the HOMO – LUMO that is much greater than the required 0.3 eV minimum; inferior charge transport pathways as a result of disordered (D - A) interface that also hinders charge extraction and the Schottky barriers between the photoactive layer energy levels and the workfunction of the electrodes [5].

The performance of OPV devices has been evaluated subsequent to the incorporation, into the photoactive layer, of a variety of materials such as carbon nanotubes (CNTs), graphene, metallic nanoparticles, quantum dots, etc. CNTs hold the promise of being exciton dissociation centres and also providing conductive conduits for high charge carrier mobilities [12, 13]. Additionally, CNTs can also improve mechanical stability of polymer-based solar cells [14].

Nitrogen doped multiwalled CNTs (N-MWCNTs) have been found to be largely metallic with electrical conductivities greater than those of pure CNTs [15, 16]. In the study by Lau *et al.* [17], they reported an improvement of 30% in the PCE of P3HT:PCBM devices when short MWCNTs were included in the photoactive layer. The bulk heterojunction PTB7:PC₇₁BM study that incorporated 1.5 % nitrogen doped CNTs by Lu *et al.* [18] reported an 18% increase in the PCE. However, it should be noted that the role played by CNTs in the performance of BHJ OPVs is still open to varying interpretations. The inclusion of CNTs in the photoactive layer of OPVs has also been found to be counter-productive with device performance declining with the addition of CNTs [19].

In keeping with the ever present promise associated with OPVs i.e. of low fabrication costs and simple device fabrication processes we have stuck to the well-studied poly (3-hexylthiophene) (P3HT) and [6,6]-phenyl-C₆₁ butyric acid methyl ester (PC₆₁BM) as donor and acceptor active layer materials respectively, for this study into optical and electrical effects of incorporating N-MWCNTs. Different mass loadings of nitrogen doped multiwalled CNTs (N-MWCNTs) were introduced

into the photoactive layer of fabricated OPV devices and the effects of these loadings on the PCE were studied. The desired outcomes of incorporating CNTs into OPV devices have already been mentioned but we can further mention that nitrogen-doped MWCNTs bring excess electrons, relative to the carbon atom, leading to the shifting of the workfunction of the MWCNTs closer to the LUMO level of the PCBM thereby aiding in electron transport. Furthermore, MWCNTs are relatively less cumbersome to synthesise, thus characterised by simpler and cost effective processes. The synthesis and characterisation of N-MWCNTs is briefly discussed and PCEs of fabricated BHJ OPVs devices as a function of N-MWCNT mass loadings are evaluated by analysing their optical and electrical characteristics. A further analysis of the effects of including N-MWCNTs into the P3HT:PC₆₁BM devices was carried out by fabricating devices without the fullerene component. That is, P3HT:N-MWCNT devices, with similar mass loading of carbon nanotubes, were fabricated and characterised in virtually the same way for comparative purposes.

A detailed description of the synthesis and characterisation of N-MWCNTs that were used in this study can be found in the doctoral thesis of I.B. Usman [20].

6.2 Experimental details

6.2.1 Synthesis and functionalisation of N-MWCNTs

Nitrogen-doping of multiwalled carbon nanotubes (N-CNT) was done by the decomposition of acetylene (C₂H₂) (Afrox) over a 5% Fe-Co bimetallic catalysts supported on CaCO₃ [21] at 850°C for 45 mins. In a typical procedure 250 mg of catalyst (Fe-Co/CaCO₃) in a quartz boat (120 mm × 15 mm) was placed in the centre of a quartz tube (51 cm × 1.9 cm) in a horizontal programmable furnace. The furnace can be electronically controlled to provide accurately the desired heating rates ($\pm 1^\circ\text{C}$), reaction temperature and gas flow rates. The catalyst was spread to form a thin layer in the quartz boat. The furnace was then heated at 10 °C min⁻¹ under a continuous flow of nitrogen gas (N₂) (Afrox) (240mLmin⁻¹). Once the desired temperature was reached (850 °C), the N₂ (240 mL min⁻¹) and C₂H₂ (90 mL

min⁻¹) were simultaneously bubbled through acetonitrile (CH₃CN) at room temperature into the furnace for nitrogen doping to take place [22]. The reaction was allowed to take place for 45 minutes. After this, the bubbling of the gases through CH₃CN was stopped and the system was left to cool down to room temperature under N₂ (240 mL min⁻¹). The quartz boat was then removed from the reactor for the weighing of the carbon deposit along with the catalyst.

The weighed samples were purified using 55 % HNO₃ under reflux in an oil bath held at 110 °C for 6 hours to remove the residual catalyst and to introduce oxygen surface groups on the CNT surface. The acid-treated carbon materials were then filtered and washed several times with distilled water until the pH of the filtrate was neutral. The nitrogen-containing materials were dried at 120 °C for 12 hours. The CaCO₃ support as well as catalyst particles (Fe-Co) were removed without affecting the CNT wall structures. Some residual material (~3 %) appears to be left behind after the washing. The purified samples were then denoted as N-CNT.

6.2.2 Preparation of P3HT:PC₆₁BM:N-MWCNT active layer solutions

Photoactive layers were prepared by initially weighing 10 mg each of P3HT and PC₆₁BM and then adding 0.13 mg, 0.25 mg and 0.50 mg of functionalised N-MWCNTs to the three vials containing P3HT. The P3HT, P3HT plus the N-MWCNTs and the PC₆₁BM samples were each dissolved in 0.5 ml of chlorobenzene by stirring them for 3 hours. Photoactive layer blends comprising of the control blend of P3HT:PC₆₁BM in a 1:1 ratio (sample R), carbon nanotube incorporated sample R1, P3HT:PC₆₁BM:N-MWCNTs in the ratio 1:1:0.13, sample R2 of P3HT:PC₆₁BM:N-MWCNTs with ratio 1:1:0.25 and finally sample R3 having P3HT:PC₆₁BM:N-MWCNTs in the ratio 1:1:0.50, making 20 mg/ml, 20.13 mg/ml, 20.25 mg/ml and 20.50 mg/ml solutions in chlorobenzene, were stirred for a further 2 hours to agitate a thorough mixing of the materials.

6.2.3 Fabrication of BHJ OPV devices

The general fabrication process of OPV devices was outlined in Chapter 3. Device fabrication details related to this study will be highlighted with careful effort to minimize repetition. A series of BHJ OPV devices with N-MWCNT loadings ranging from 0 to 0.50 mg were fabricated under ambient conditions, on ITO coated glass substrates. The patterning of the ITO substrates involved ITO etching by using zinc paste and a 2M hydrochloric acid solution. Etched substrates were cleaned via a sonication process that took them through a detergent solution, distilled water, acetone and ethanol for the achievement of blemish free foundations on which the stacking of materials could be made in the building of OPV devices. The cleaning process was done in a fume cupboard with controlled bursts of nitrogen gas being used to dry cleaned ITO substrates.

6.3 Results and discussion

6.3.1 Spectroscopic characteristics

6.3.1.1 Optical absorption

Figure 6.1 shows the effect of different mass loadings of N-MWCNTs on the optical absorption spectra of the photoactive layer. The characteristic P3HT absorption profile with an intense peak at 515 nm and the PC₆₁BM peak at 335 nm can be clearly identified. Optical absorbance is seen to vary as the mass of incorporated N-MWCNTs is increased from 0 mg to 0.5 mg. All mass loadings show some form of an enhancement in absorption intensities. However, as opposed to observations made by Singh et.al. [23], where a red shift with an increase in MWCNT concentration was observed in their study, the P3HT maximum absorption peak shows no noticeable shift with the addition of N-MWCNTs into the photoactive layer of fabricated devices. Also observed in Figure 6.1 is the broadening of the spectrum which could suggest an effect on the morphology of thin films due to the incorporation of the carbon nanotubes into the photoactive layer. However, this could not readily be established.

Interestingly, it has been mentioned that optical absorption measurements of MWCNTs can be difficult, with a possibility of being inconclusive, so one has to be very cautious when reading information from related absorption spectra [24].

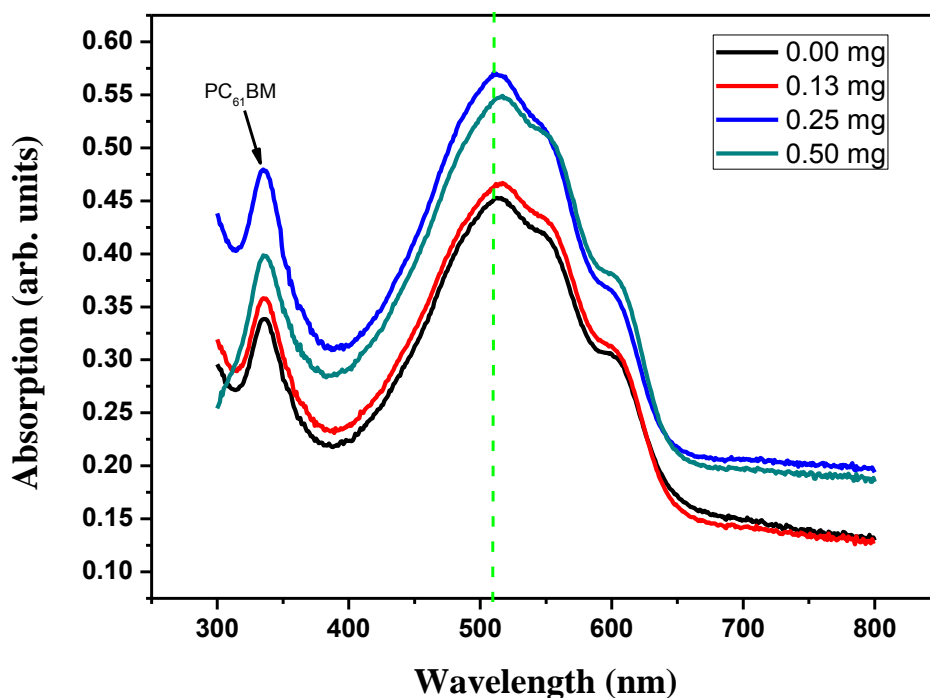


Figure 6.1: UV-Vis spectra comparing N-MWCNTs mass loadings in the P3HT:PC₆₁BM active layer.

6.3.1.2 Raman spectra characterisations

The Raman spectra for fabricated devices with different N-MWCNT loadings is shown in Figure 6.2. The Raman spectra of all devices are also dominated by the P3HT component just like in binary P3HT:PC₇₁BM systems we encountered in Chapter 4. A more detailed description of a Raman spectrum for the polymer P3HT was given in Table 4.5. A brief identification of a few characteristic modes is given for ease of reference:- bands associated with symmetric C = C stretching mode (1450 cm^{-1}), the inter-ring C - C stretch mode that is sensitive to π - electron delocalisation (1379 cm^{-1}), the inter-ring stretching (1180 cm^{-1}), C - H bending (1092 cm^{-1}) and C-S-C deformation mode (723 cm^{-1}). No peak shifts or new peaks

were observed as a result of incorporating N-MWCNTs into the photoactive layer. For example, the most intense peaks was at 1453 cm^{-1} for all the devices and had an average FWHM value of $32.61 \pm 0.05\text{ cm}^{-1}$. Hence, we could rule out any formation of chemical bonds between the CNTs and the photoactive layer materials. In short, the structural order of the photoactive blend was not impacted by the incorporation of the CNTs.

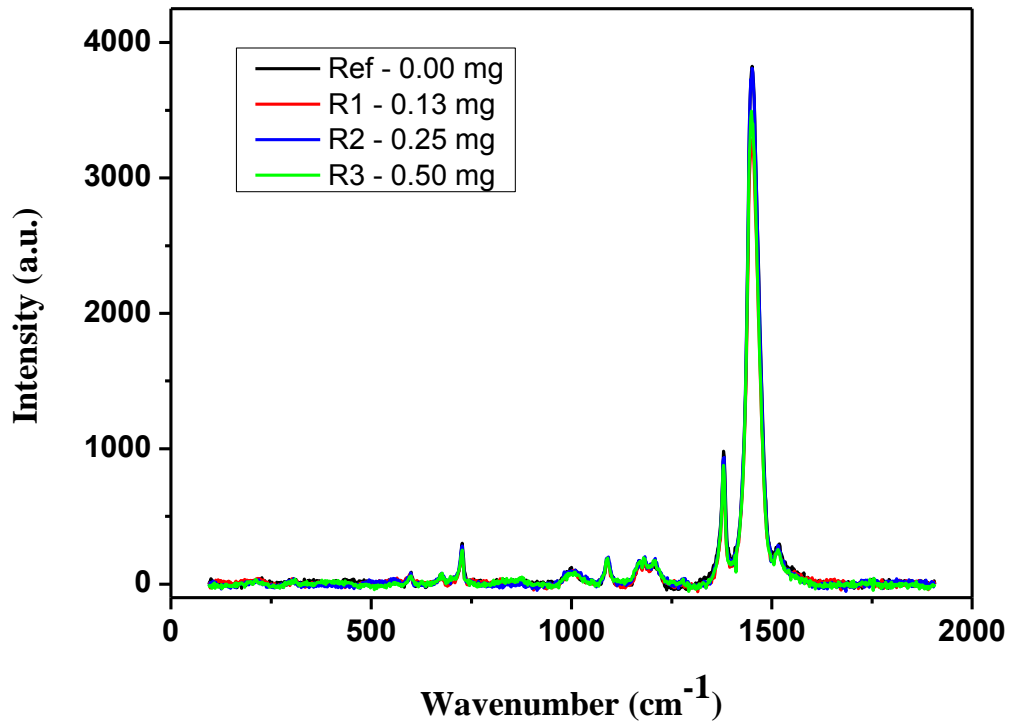


Figure 6.2: Raman spectra of P3HT:PC₆₁BM devices with varying N-MWCNT mass loadings.

6.3.2 Electrical characteristics

Figures 6.3 and 6.4 show, in linear and semi-log scales, $J - V$ characteristics of fabricated devices with different concentrations of N-MWCNTs both in the dark and under AM1.5 illumination at 100 mW/cm^2 . All devices displayed rectification for solar cell application. The extent of each device's rectifying behaviour can be determined by computing their respective dark current rectification ratios (RR) as shown in Table 6.1. The addition of N-MWCNTs into active layers of fabricated

devices leads to a deterioration in diode behaviour. This unfavourable rectification means that potential barriers formed at active layer/Al interfaces will have a lesser capability of preventing back electron transfer.

Table 6.1: Rectification ratios for N-MWCNT loadings into the P3HT:PC₆₁BM active layer blend.

Device	RR
Ref - 0.00 mg	32.00
R1 - 0.13 mg	6.15
R2 - 0.25 mg	6.22
R3 - 0.50 mg	2.74

The summary of $J - V$ measurements in Table 6.2 indicates that the overall performance of devices with N-MWCNT loadings did not improve. Device R, the control device, had a V_{oc} of 0.60 V, a J_{sc} of 6.29 mA/cm² and a PCE of 1.40%. The loading of N-MWCNTs into the photoactive layer resulted in at least a 50% drop in current density accompanied by a minimum 30% reduction in the value of the V_{oc} . Reductions in V_{oc} values could be caused by a mismatch of energy bands. It has been mentioned previously that the V_{oc} in polymer:fullerene photovoltaics is primarily determined from difference between the HOMO of the polymer and the LUMO of the fullerene. Furthermore, these big drops in key device parameters could be emanating from a high recombination of charge carriers. The effect of recombination in these devices will be discussed later in the chapter when light intensity dependencies are analysed.

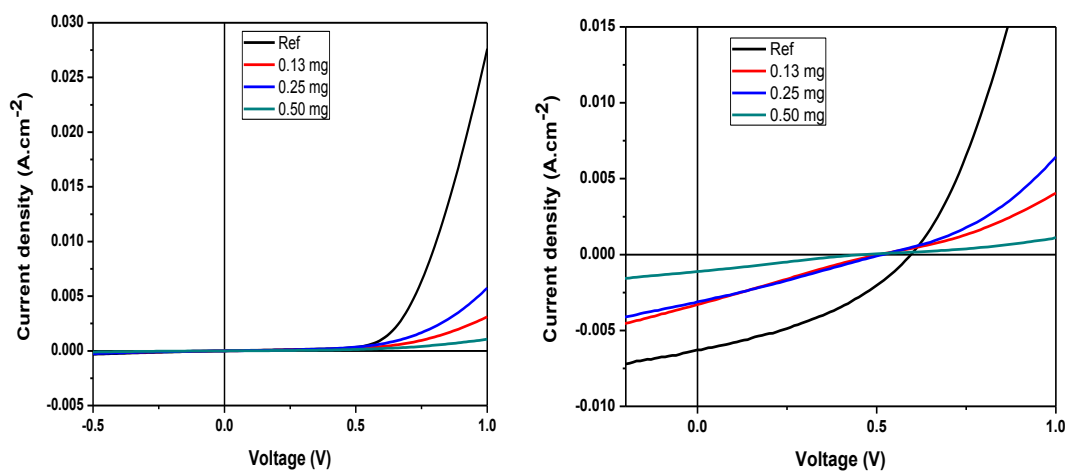


Figure 6.3: Dark (left) and 100 mW.cm⁻² (AM1.5) illumination (right) current-voltage plots.

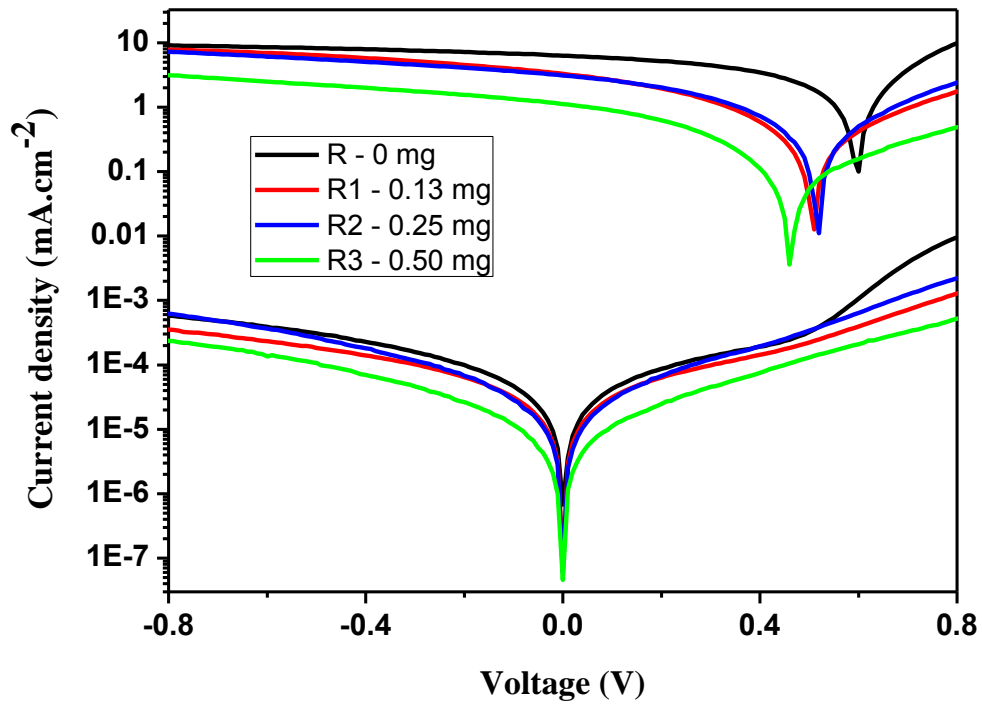


Figure 6.4: Dark and illuminated semi-log plots of $J - V$ characteristics.

Table 6.2.: Summary of the performance of fabricated OPV devices with varying N-MWCNT concentrations with the masses, in mg, of loaded N-MWCNTs shown next to the device label.

Device	J_{sc} (mA/cm ²)	V_{oc} (V)	FF (%)	PCE (%)	R_{sh} (Ω cm ²)	R_s (Ω cm ²)	$1 + R_s/R_{sh}$
Ref - 0.00	6.29	0.60	37.5	1.40	262.5	36.6	1+0.14
R1 - 0.13	3.29	0.51	24.1	0.40	154.9	207.2	1+1.34
R2 - 0.25	3.11	0.52	26.4	0.43	171.4	174.6	1+1.02
R3 - 0.50	1.11	0.46	24.3	0.13	451.4	642.1	1+1.42

6.3.3 Charge transport properties

6.3.3.1 Injection limited behaviour

If the current is dominated by Fowler-Nordheim tunnelling a plot of $\ln(J/V^2)$ vs $(1/V)$ will yield a straight line with a negative slope. The flow of charge carriers through a potential barrier is thus governed by quantum mechanical tunnelling. The FN plots shown in Figure 6.5 exhibit this characteristic behaviour at high applied electric fields i.e. low $(1/V)$ values. It is therefore concluded that charge carriers are going through the potential barriers at the metal/active layer interfaces of fabricated device by FN quantum tunnelling mechanism. Linear fits on the slopes of the FN indicated a mass loading dependence. The device with no N-MWCNTs had the steepest slope and the steepness was found to decrease with an increase in N-MWCNT mass loading. As seen in Chapter 2, the steepness of the straight line slopes in FN plots is directly proportional to the barrier height. The expectation, which does not necessarily imply better photovoltaic performance of fabricated devices, was that the introduction of the CNTs would lower the potential barrier height of the metal-active layer interface(s) [13]. This was in evidence, from the slopes of the straight line fits and their related potential barrier heights as obtained from Figure 6.5. These can then be arranged as follows: $m_{\text{Ref}} > m_{\text{R1}} > m_{\text{R2}} > m_{\text{R3}}$ for the slopes and $\phi_{B(\text{Ref})} > \phi_{B(\text{R1})} > \phi_{B(\text{R2})} > \phi_{B(\text{R3})}$ for the potential barriers.

The non-linear behaviour of the plots at lower applied electric fields i.e. high $(1/V)$ values is indicative of charge injection by Richardson-Schottky (RS) thermionic emission mechanism. This illustrates the contributions of both direct tunnelling and thermionic emission mechanisms towards the transport dynamics of charge carriers at metal/active layer interfaces.

In the RS plots of $\ln J$ vs \sqrt{V} in Figure 6.6 linear fits at low applied bias voltages yield positive slopes which is indicative of charge injection by thermionic emission through the metal/polymer interface. The non-linear behaviour at higher voltages suggest that a transition has taken place towards quantum mechanical tunnelling.

The minima of the curves in Figure 6.6 indicate transition points where charge transport through a barrier changes from RS dominated thermionic emission to FN dominated field emission. A slight variation in the dependence of the transition field on N-MWCNT mass loading was observed. An average electric for this transition was found to be $3.00 \times 10^6 \text{ V.m}^{-1}$. The upper and lower limits of applied fields in this set of devices can be found from the V_{oc} of the reference device and that with the 0.50 mg N-MWCNT mass loading, respectively. Their magnitudes are $4.62 \times 10^6 \text{ V.m}^{-1}$ and $3.54 \times 10^6 \text{ V.m}^{-1}$.

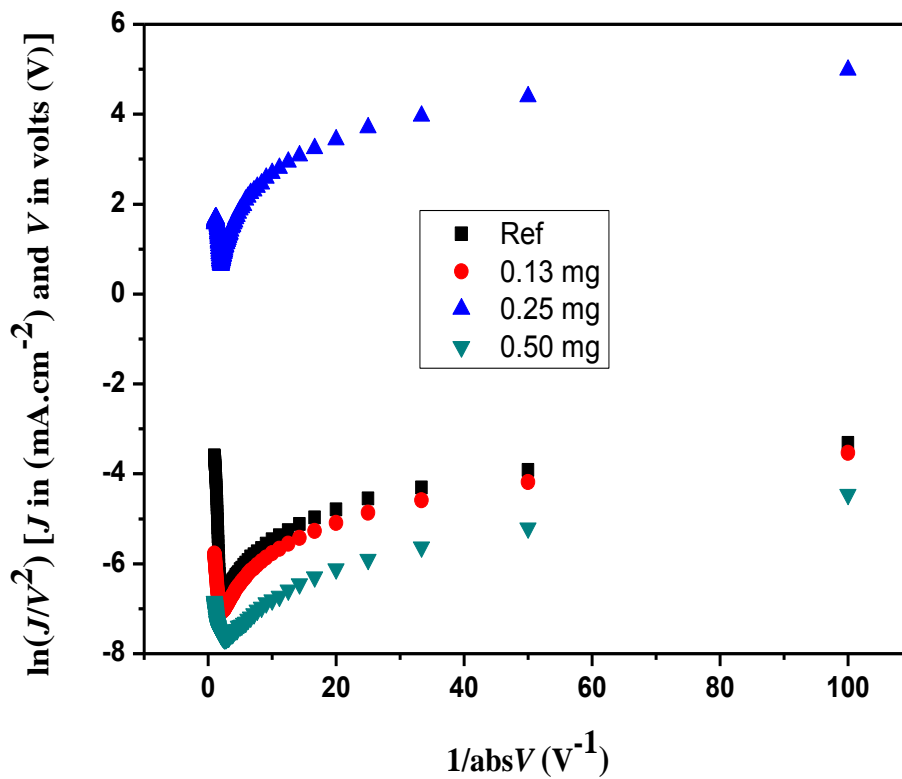


Figure 6.5: FN plots for increased N-MWCNT loadings into P3HT:PC₆₁BM photoactive layer blends.

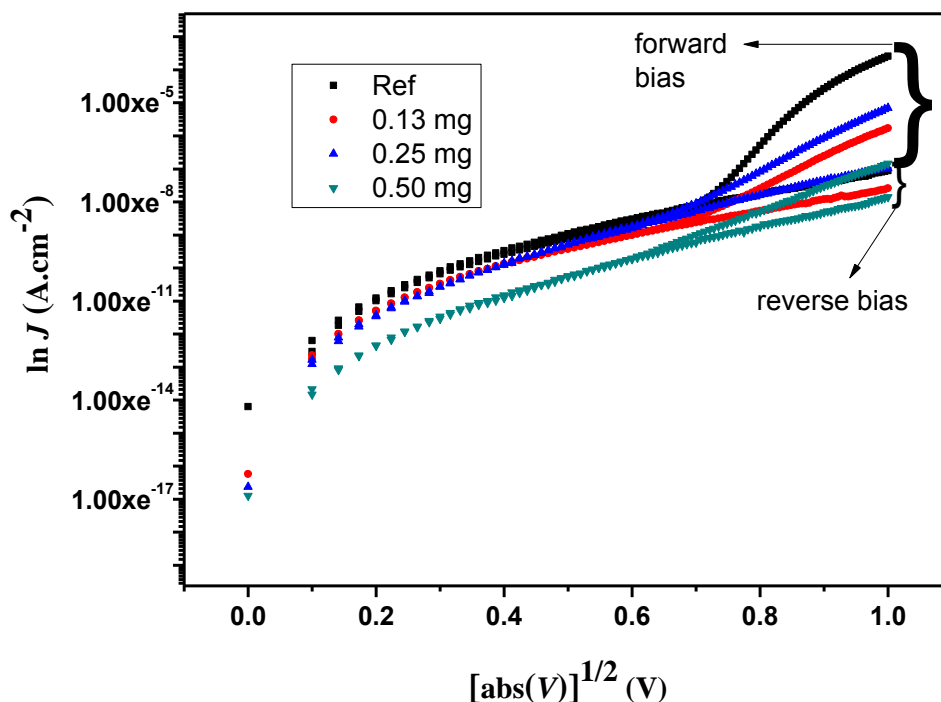


Figure 6.6: RS plots under reverse and forward bias for devices with an increasing content of N-MWCNT in the P3HT:PC₆₁BM photoactive layer blends.

6.3.3.2 Bulk limited behaviour

In Figure 6.7 we plotted log-log forward bias $J - V$ characteristics in the dark in order to study bulk charge transport mechanisms of fabricated devices. The curves were found to obey the power law $J \propto V^m$, such that from $\log J = m \log V + \log \beta$, m is the bias dependent slope and $\log \beta$ is the constant. Following the discussion on bulk charge transport mechanisms in Chapter 2, we proceeded to identify regions of interest in Figure 6.7 to enable a precise description of bulk charge transport behaviour in our devices.

Region I is the low voltage region, $V < 0.15$ V, where the slopes of the $J - V$ curves had values close to 1 signifying Ohmic behaviour. The average value of the slope in this region was found to be $m = 1.01 \pm 0.02$.

The average slope of the linear fit in Region 2 was approximately 2, $m = 1.9 \pm 0.1$. This region where $0.15 < V < 0.65$, was identified as dominated by SCLC.

Finally, region 3 gave slopes greater than 3 indicating the filling of traps where transport is dominated by trap free space charge limited current (TFSCLC). The differences in the slopes of the curves in the TFSCLC region for all the devices suggests trap density and trap depths vary with N-MWCNT mass loadings.

With the space charge limited conduction identified, we used the Mott-Gurney law to determine the N-MWCNTs dependent mobilities of charge carriers. From the linear fits in the plots of J vs V^2 in Figure 6.8, we get the slopes that are directly proportional to the charge carrier mobilities. Visually, it can be seen that the addition of N-MWCNTs into the P3HT:PC₆₁BM active layer, decreases the mobility of charge carriers.

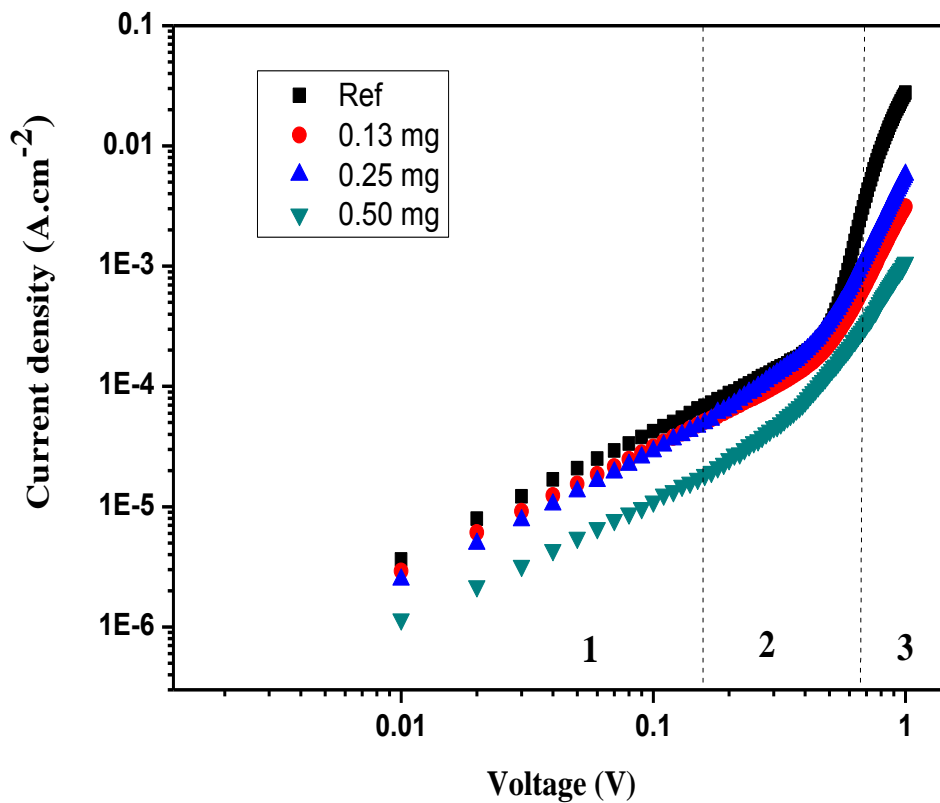


Figure 6.7: Dark current $J - V$ characteristics in double log scale under forward bias.

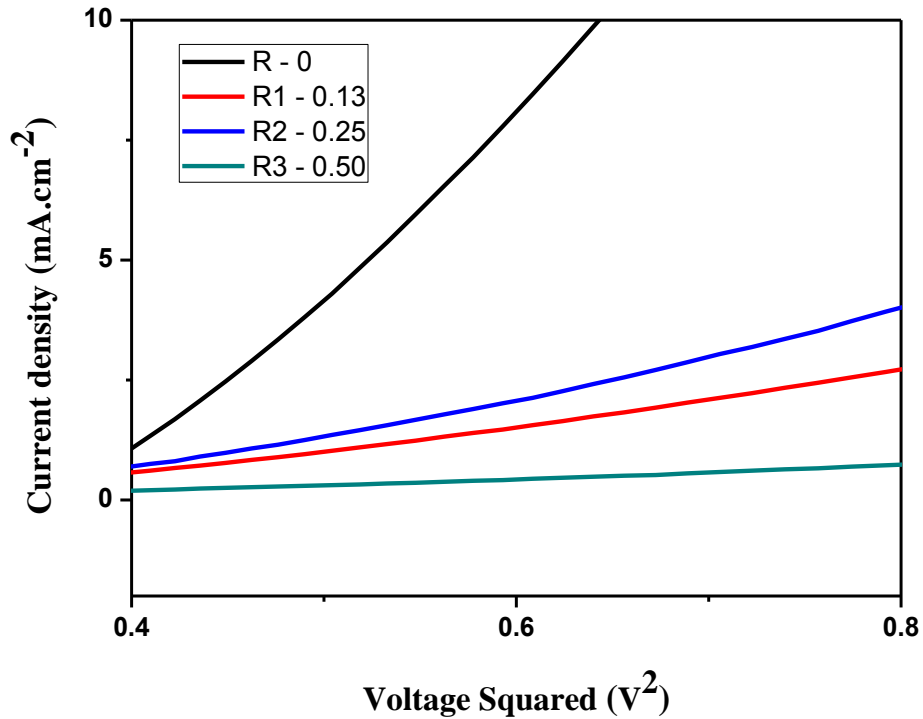


Figure 6.8: Linear fit curves of the Mott-Gurney law for the determination of charge carrier mobilities as a function of N-MWCNT loading on the photoactive blend.

6.3.4 Key parameter variations with light intensity

It has now been seen that our findings show a decrease in the PCE with the addition of N-MWCNTs into the P3HT:PC₆₁BM active layer of fabricated devices. Though other researchers have found similar effects, as explained in the Introduction, the causes of such degradations in performance require further analysis. To this end, we undertook recombination studies in these devices to gain more insight into their electrical characteristics. Recombination dynamics were then probed via light intensity dependence of V_{oc} and J_{sc} .

Linear fits of semi-log V_{oc} vs light intensity (P_{light}) plots in Figure 6.9 (a) give slopes that are equal to $nk_B T/q$. Where n is the ideality factor and other symbols have their normal meanings. As seen in Chapter 4, strong bimolecular recombination is dominant when $n = 1$, whilst an ideality factor of 2 (or more) is interpreted as SRH-

type trap-assisted type recombination. All values of n in these N-MWCNTs loaded devices were greater than 3 indicating trap-assisted recombination mechanisms to be dominating open circuit conditions. Ideality factors are shown in Table 6.3 do not follow a set trend except that the zero loaded device had the highest value. The occurrence of trap assisted recombination could, amongst other factors, be due to non-ideal device morphologies particularly in the photoactive layer.

Table 6.3: Recombination parameters at open and short circuit condition with a charge mobility trend.

Device	n ± 0.12	μ $\pm 0.002 \times 10^{-6}$ (cm^2/Vs)	α ± 0.05
Ref - 0.00 mg	3.88	2.093	1.05
R1 – 0.13 mg	3.29	0.128	0.96
R2 – 0.25 mg	3.70	0.356	1.05
R3 – 0.50 mg	3.62	0.019	1.06

Figure 6.9 (b) shows the log-log plot of J_{sc} vs light intensity that is based on the relation $J_{sc} \propto (P_{\text{light}})^{\alpha}$. This plot is used in the determination of the dominant recombination mechanism at short circuit conditions. From this power law dependence, it is concluded that weak bimolecular recombination will be indicated by the condition that will see the exponential factor α being equal to 1. Extracted α values, seen in Table 6.3, are close to unity and indicate weak bimolecular recombination. The similarity in values shows negligible effect of N-MWCNT mass loadings towards bimolecular recombination at short circuit conditions.

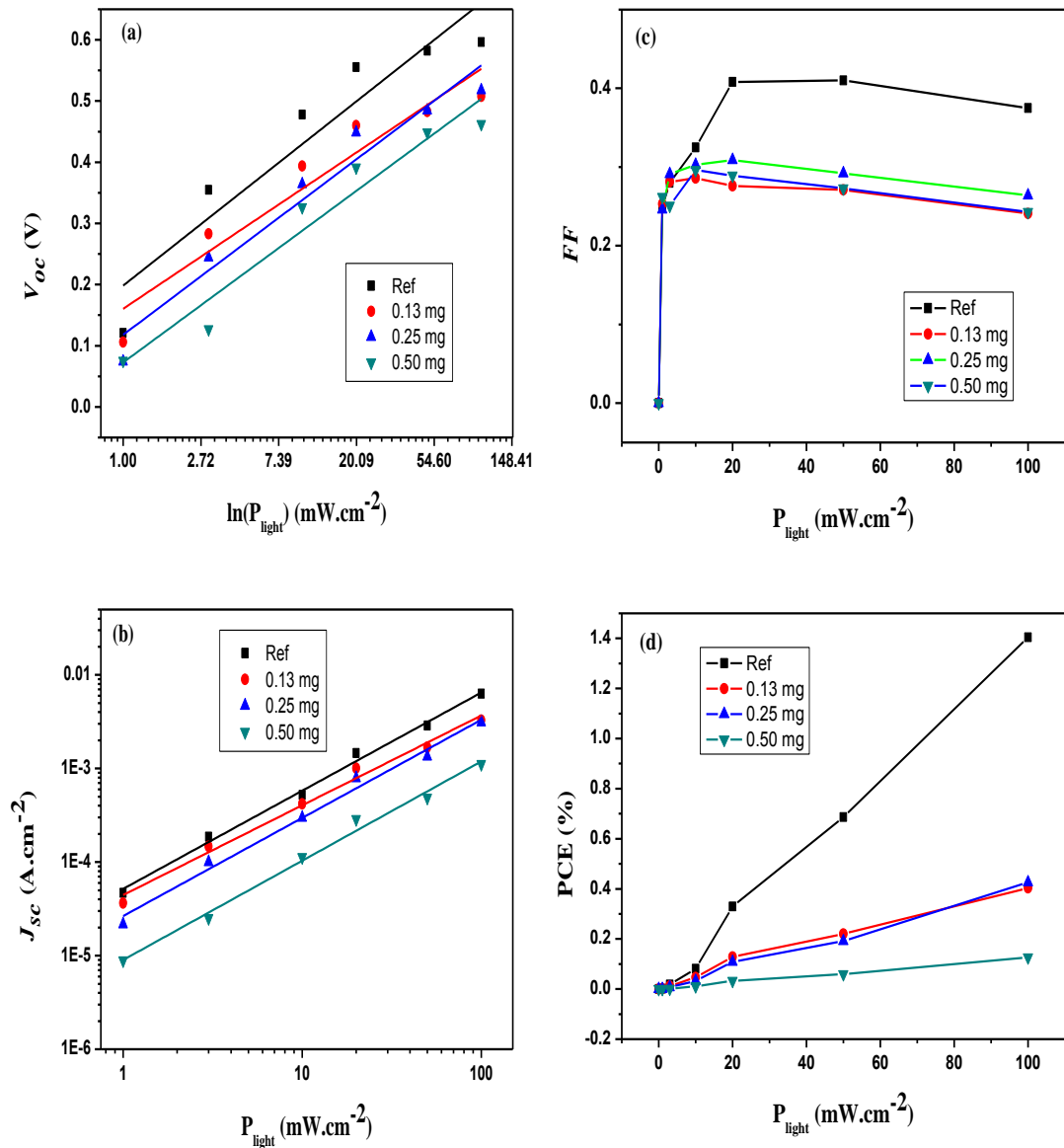


Figure 6.9: N-MWCNT based variations of (a) open circuit voltage (b) short circuit current density (c) fill factor (d) power conversion efficiency as a function of light intensity.

The fill factor FF increases peaking at light intensities lower than $20 mW.cm^{-2}$ before decreasing slightly with an increase in (Figure 6.9 (c)). The decrease could be due to the influence of parasitic resistances. In Chapter 2 we came across the effect of the factor $(1 + R_s/R_{sh})$ on the measured current in an OPV device. As seen

in Table 6.3 this factor also has an effect on the fill factor within a reasonable spread of values. The effects on the PCE of increasing the mass loadings of N-MWCNT in the active layer are shown in Figure 6.9 (d). Though all devices show an increase in PCE with increasing light intensity, the inclusion of N-MWCNTs led to much lower PCEs at all light intensities.

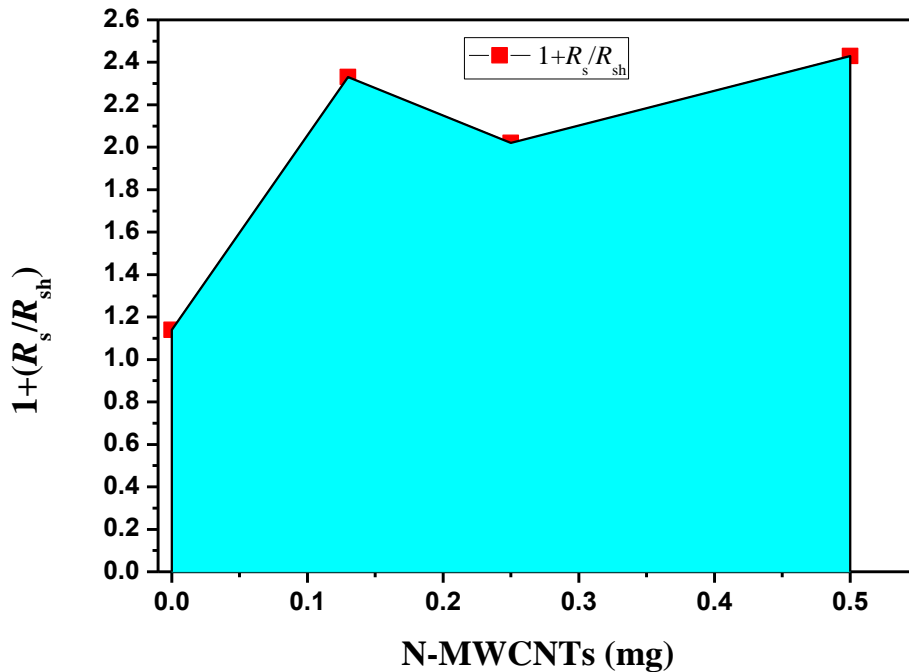


Figure 6.10: The graph of $(1+R_s/R_{sh})$ for different N-MWCNT mass loadings indicating the degree of the diminishing of the current density.

Figure 6.10 shows $(1+R_s/R_{sh})$ which can give an idea about the extent of recombination as a function of different N-MWCNT mass loadings. All devices with CNTs incorporated into their photoactive layer show a high extent of recombination. Amongst the three devices, the one containing 0.25 mg of N-MWCNTs shows the least extent of recombination. This device exhibited a higher PCE when compared to the other two. It has been reported that should there be a presence of metallic CNTs in the photoactive layer, a recombination of charges will in all likelihood take place [25].

Our study of electrical characteristics of N-MWCNT loaded P3HT:PC₆₁BM extended into studying the relation between effective voltage (V_{eff}) and generated photocurrent (J_{ph}). The photocurrent is directly related to absorbed photons and hence as shown in Chapter 4, it is the difference between 1 sun illuminated current (AM1.5) and dark current. The dissociation of excitons, and hence the generated photocurrent, is a voltage dependent process [26, 27]. The photocurrent, as seen in Figure 6.11, increases with the increasing effective field until a point where all generated charges are extracted i.e. saturation.

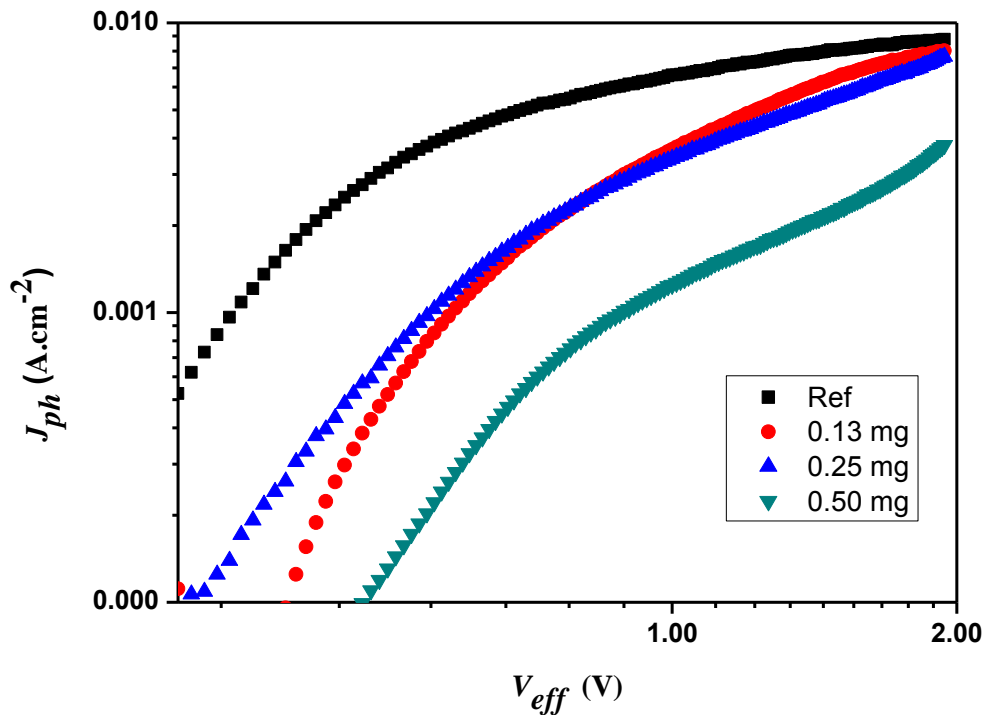


Figure 6.11: J_{ph} vs V_{eff} curves for different N-MWCNT loadings in the 130 nm thick photoactive layer showing the degree of current saturation with respect to the effective field.

In Figure 6.11 we see a clearer picture of the effect of biasing by the much more pronounced field dependence of the photocurrent. Devices with N-MWCNTs are seen not to have reached saturation at higher effective fields as opposed to the reference device with zero mass loading which saturates at about 1.0 V. The linear increase of J_{ph} at lower V_{eff} happens at comparatively higher effective voltages for N-MWCNTs loaded devices. A quantitative comparison of saturated current and

maximum exciton generation rates cannot be made in this case as most curves do not show saturation within measured voltage scales.

6.4 P3HT:N-MWCNT

Having seen the loading of the N-MWCNTs into the photoactive layer not producing the expected outcome of PV performance enhancement, we decided to test polymer:N-MWCNT devices under similar conditions. Synthesised N-MWCNTs were expected to complement the PC₆₁BM as acceptor materials leading to improved device performances. Fabricating devices with these CNTs and P3HT will then reveal their diode properties and hence the suitability of these CNTs in the fabrication of OPV devices.

6.4.1 Fabrication of OPV devices

Substrates were prepared by following the methods explained in Chapter 3. P3HT:N-MWCNT solutions were prepared by directly mixing 10 mg of P3HT with x mg of N-MWCNTs where x = 0.13 mg, 0.25 mg and 0.50 mg. To prepare active layer blends, the mixtures were then dispersed in 0.5 ml of chlorobenzene via magnetic stirring for 5 hours. Four categories of samples identified by their N-MWCNT mass loading as Ref – 0.00 mg, P1 – 0.13 mg, P2 – 0.25 and P3 – 0.50 mg were thus prepared. OPV devices were then fabricated by spin coating the hole blocking layer (PEDOT:PSS) on cleaned patterned substrates. Subsequently, active layer blends were spin coated on top of the PEDOT:PSS after thermal annealing on a hot plate as previously described. All spin coating was done at 2000rpm for 60 seconds. Cathodes in the form of aluminium (~100 nm thick) were metalised in a thermal evaporator at very high vacuums of about 1.5×10^{-6} mbar to complete the devices.

Devices with structures GLASS/ITO/PEDOT:PSS/P3HT:N-MWCNT/Al were thus prepared for measurements.

As stated previously, current–voltage (I – V) characteristics were acquired using the solar simulator (150 W Xe lamp) with 1.5 Air Mass filters and a source/Measure unit (HP 4141B DC) unit under 100 mW/cm² illumination. Optical absorption

measurements of fabricated devices were made using the Cary 500 UV – VIS - NIR spectrometer. The Raman characteristics and the structural order of all fabricated devices were examined using a Jobin Yvon T64000 Raman spectrometer equipped with an Ar ion laser (514.5 nm).

All measurements were carried out in air at room temperature.

6.4.2 Spectroscopic characteristics

6.4.2.1 UV-Vis characterisation

The UV-Vis spectra in Figure 6.12 show the expected $\pi - \pi^*$ based P3HT absorption profile given its mass ratio in the photoactive blend. The details of the P3HT optical absorption profile have been given in Chapters 4 and 5. What is observed in this case is that the absorption profile is influenced by the N-MWCNT loadings with the neat P3HT showing lowest absorbance. However, there is no pattern of absorption that can be directly linked with mass loadings. For example, the 0.50 mg device has a lower intensity when compared to the 0.25 mg device. With an increase in the N-MWNT content, there is a slight broadening of the spectrum which is more noticeable for the 0.25 mg device. Any suggestion of changes in the morphology of spin coated films was probed with Raman spectroscopy.

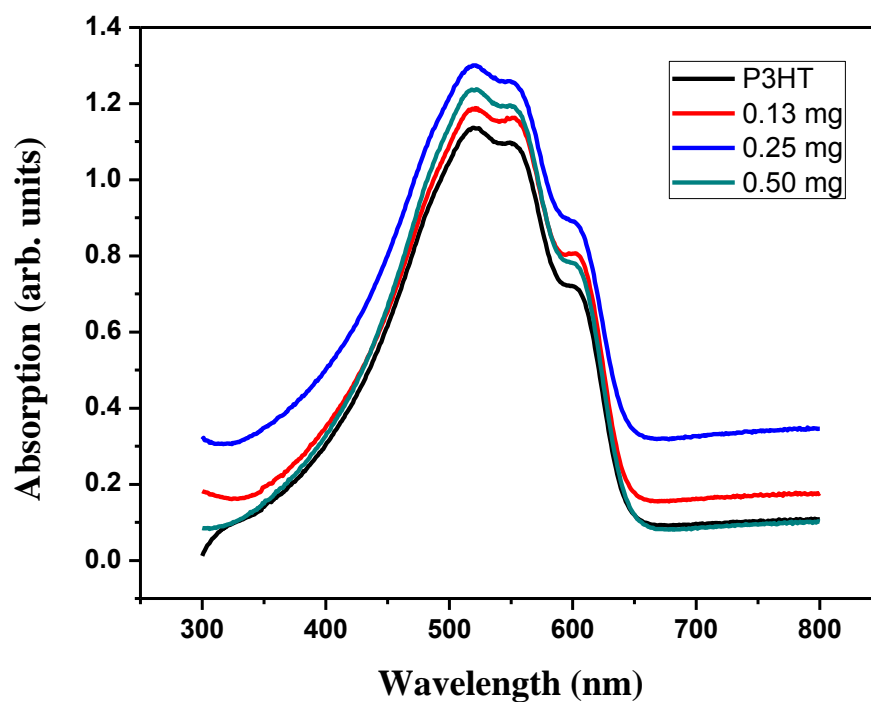


Figure 6.12: Optical absorption spectra of devices with P3HT:N-MWCNT photoactive layer materials.

6.4.2.2 Raman characteristics

Raman measurements as shown in Figure 6.13 were virtually a carbon copy for all devices. The P3HT spectrum, which was explained in detail in Chapter 4, remained unchanged with the addition of N-MWCNTs. No effect on its structural order was noticeable.

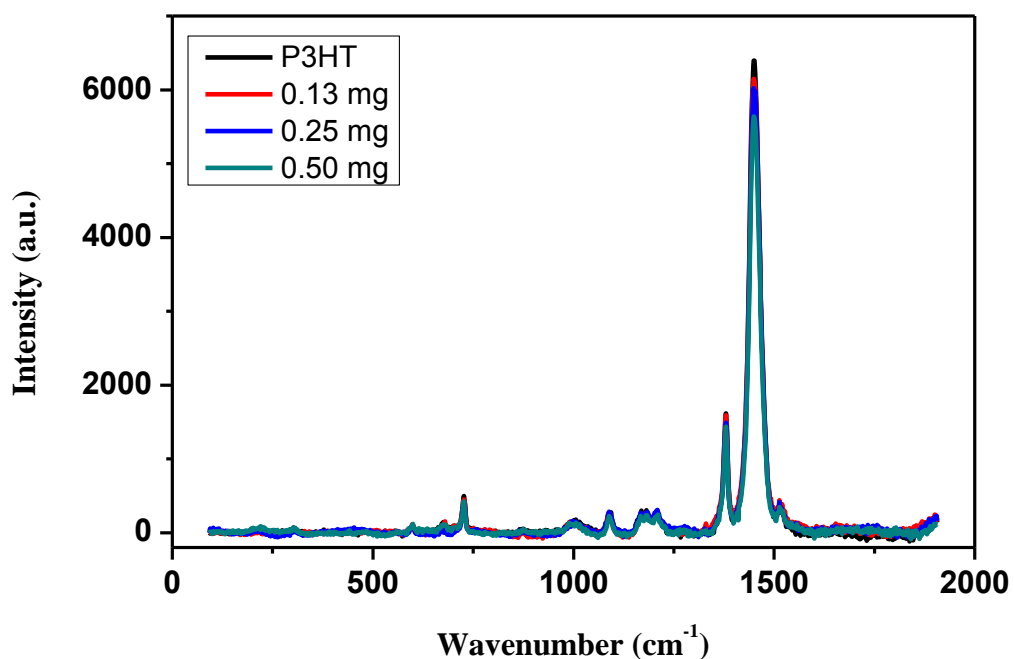


Figure 6.13: Raman spectra of P3HT:N-MWCNT photoactive layers showing unchanged profiles for varying mass content of N-MWCNTs.

6.4.3 $J - V$ characteristics

The $J - V$ measurements on Figure 6.14 (a) show the expected profile from the P3HT sample as it showed an Ohmic behaviour. Dark current characteristics in Figures 6.14 (b) and (c) in linear and semi-log scales respectively, were used to assess the diode behaviour or lack thereof, by calculating rectification ratios of the rest of the devices. The 0.25 mg device showed the best rectification behaviour (Table 6.4) and it was then expected that it should exhibit the best PV behaviour.

Table 6.4: Rectification ratios for P3HT:N-MWCNT devices.

Device	RR
Ref - 0.00 mg	1.00
R1 - 0.13 mg	0.84
R2 - 0.25 mg	8.44
R3 - 0.50 mg	5.28

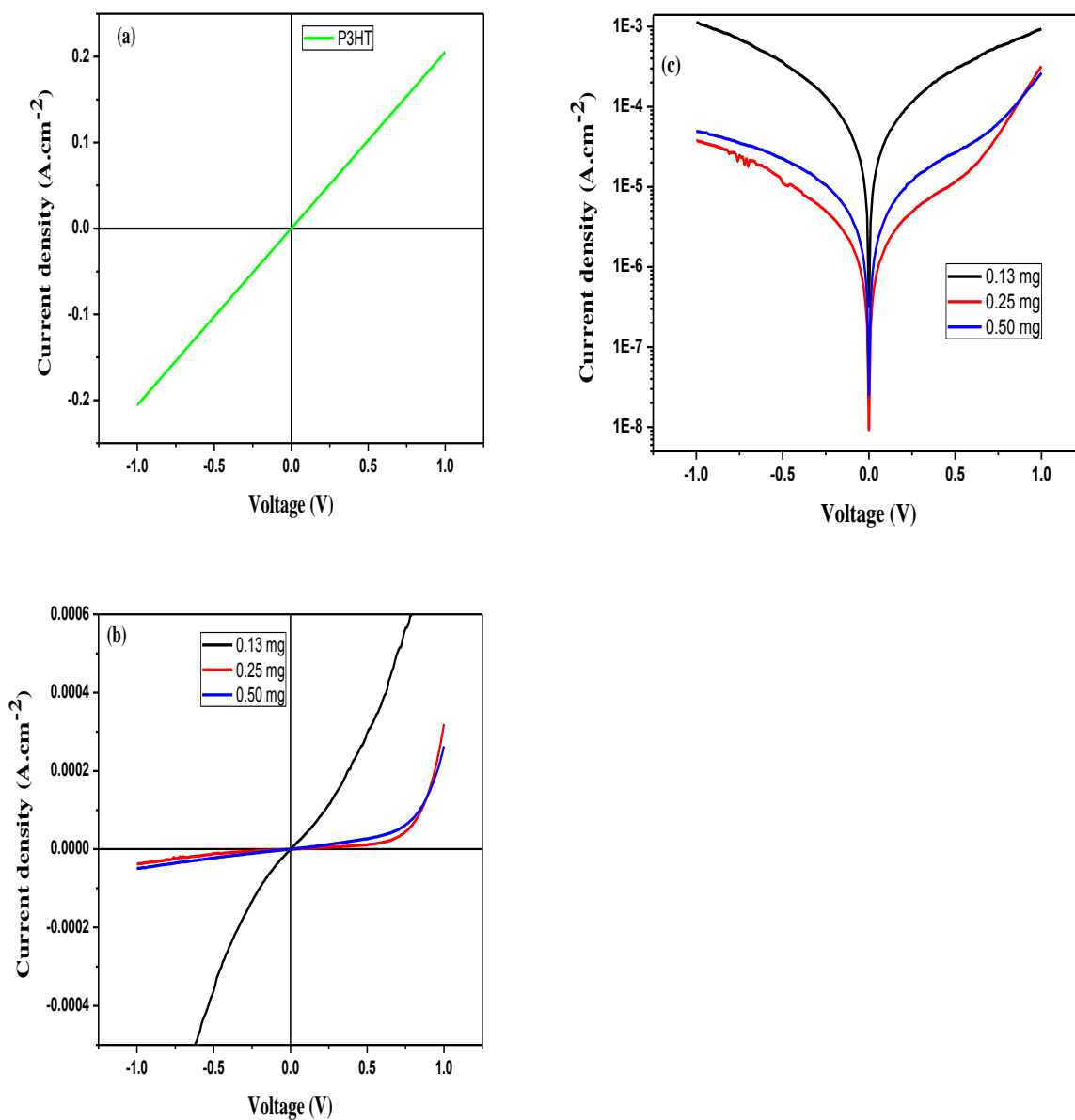


Figure 6.14: Dark current $J - V$ plots (a) P3HT only (b) P3HT:N-MWCNT linear scale (c) P3HT:N-MWCNT linear scale semi-log scale.

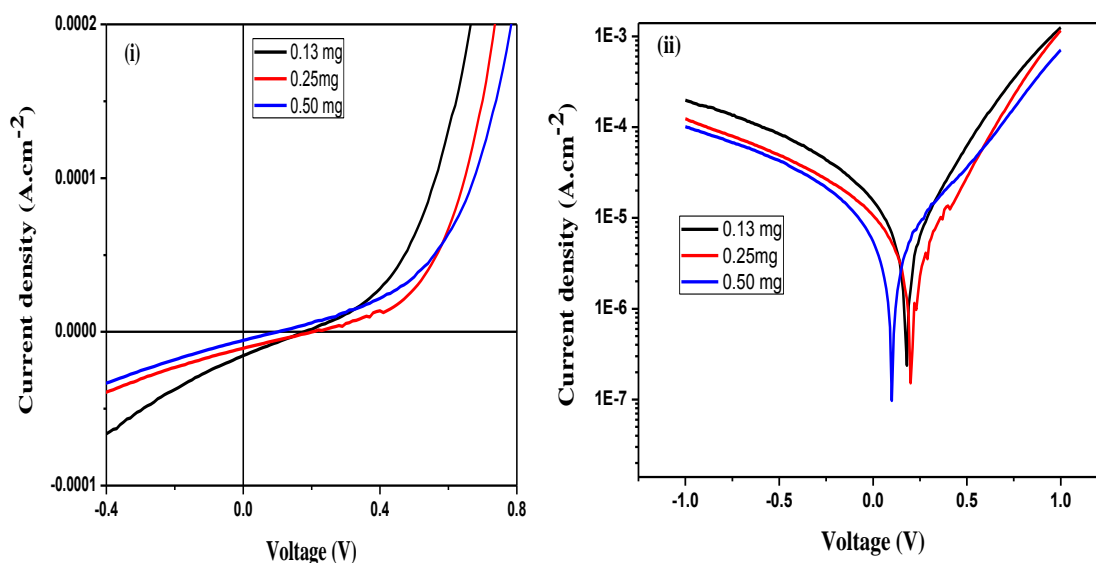


Figure 6.15: $J - V$ characteristics of P3HT:N-MWCNTs at 100 mW/cm^2 (AM1.5) in (a) linear and (b) semi-log scale.

The current – voltage measurements captured in Figure 6.15 are summarised in Table 6.5. In evidence is the fact that usage of synthesised N-MWCNTs as acceptor materials in fabricated OPV devices needs further refinements. Compared to P3HT:PC₆₁BM active layer blends P3HT:N-MWCNT blends have very poor key performance parameters despite the highlighted superior opto-electrical properties. The parasitic resistances are seen to be increasing with an increase in N-MWCNT loading. The effect that is always desired is to have a decreasing resistance and an increasing shunt resistance. The 0.25 mg device showed the best performance of the three in as far the PCE is concerned.

Table 6.5: Summary of $J - V$ performance characteristics of P3HT:N-MWCNT devices.

Device x mg	J_{sc} (mA/cm ²)	V_{oc} (V)	FF (%)	PCE (%)	R_{sh} (k Ω cm ²)	R_s (k Ω cm ²)	$1+R_s/R_{sh}$
0.13	14.8 μ A	0.04	24.2	12.7x10 ⁻⁵	2.35	2.44	1+1.038
0.25	10.7 μ A	0.20	24.7	53.5x10 ⁻⁵	16.2	16.4	1+1.012
0.50	5.5 μ A	0.10	24.1	6.83x10 ⁻⁵	17.3	18.1	1+1.046

6.4.4 Charge transport properties

6.4.4.1 Injection limited

An assessment of the devices' transport properties is begun by looking at dynamics at interfaces. It has been reported that the $J - V$ characteristics nanotubes can be described by the Fowler–Nordheim model with an acceptable accuracy [28]. Figure 6.16 depicts FN plots with characteristic negative slopes at high electric fields indicating charge injection through a potential barrier by tunnelling. Tunnelling is mass loading dependent as the linear fits of this part of the FN plot yielded slopes such that the slope of the 0.25 mg device is greater than that of the 0.50 mg device. With the slopes directly proportional to the barrier heights, it follows that the 0.25 mg device has a greater potential barrier height at the metal/active layer interface. Interestingly, the 0.13 mg device shown so direct tunnelling properties. This device has least amount of N-MWCNT which could be having very little impact. The non-linear fits of the turning points of the curves give electric fields where transition from thermionic to quantum mechanical tunnelling takes place. The 0.50 mg device requires a greater electric field for the transition to take place. Having no variation in temperature we however, assess thermionic contributions to tunnelling by using the RS plot in Figure 6.17. The plot of $\ln J$ vs \sqrt{V} is indicating positive slopes of straight line fit in the low electric field regions which is indicative of charge injection by thermionic emission through the metal/active layer interface. There has been experimental evidence that has shown that CNTs, metallic or semiconducting, exhibit good emission properties that can be approximated along the Fowler – Nordheim behaviour [29, 30].

What we see here is that both tunnelling mechanism are present at the meal/active layer interface in varying degrees, with the thermionic emission behaviour seemingly very pronounced. However, this is not the case for the 0.13 mg device.

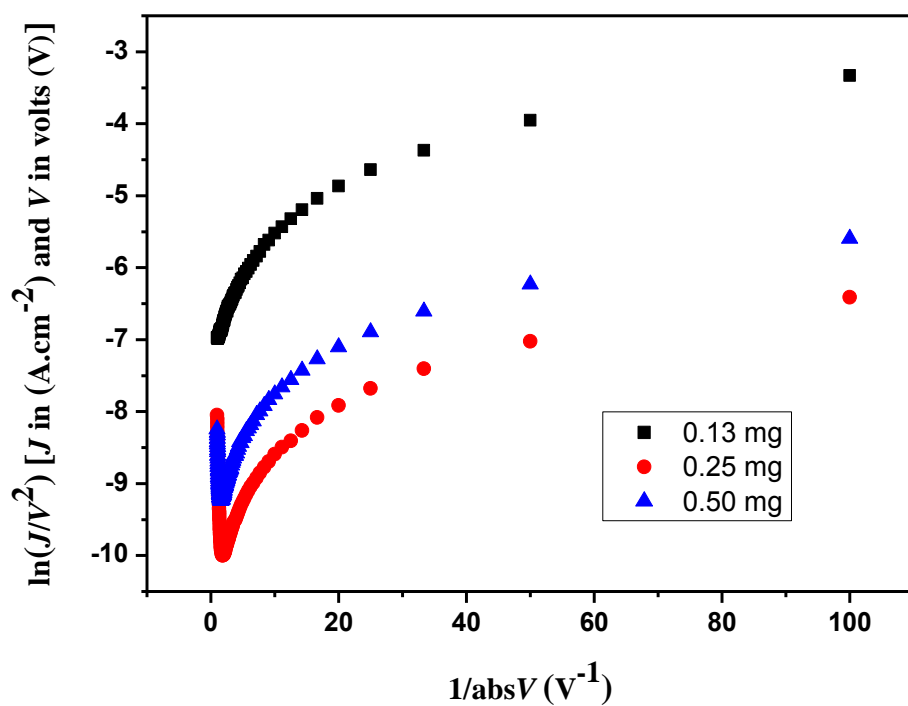


Figure 6.16: FN plots for P3HT:N-MWCNTs as the photoactive layer in fabricated devices showing the prominence of thermionic emission.

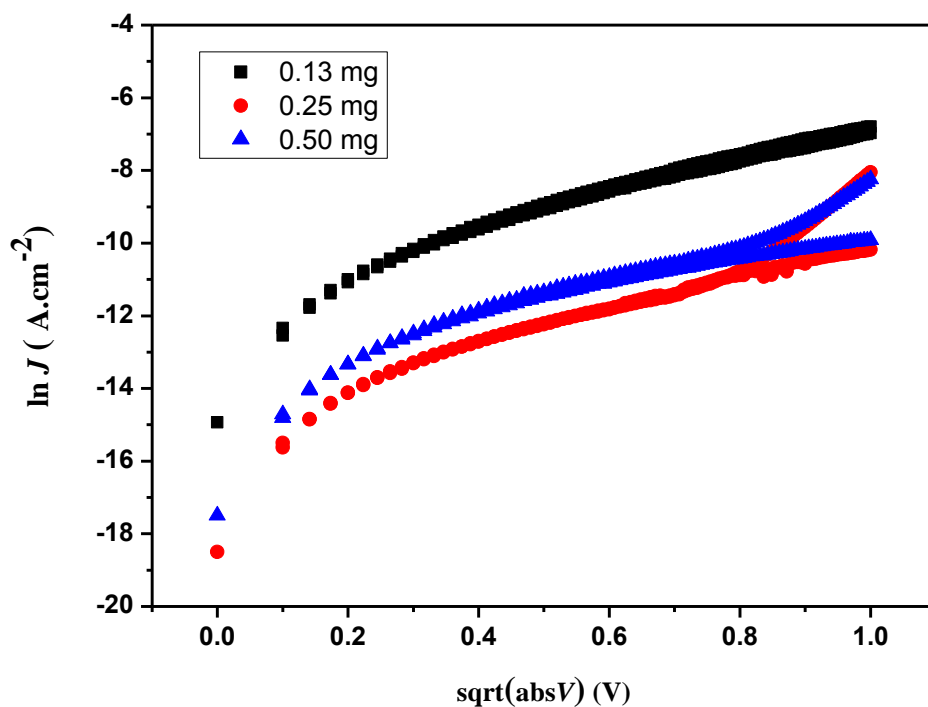


Figure 6.17: RS plots for P3HT:N-MWCNTs showing characteristic thermionic emission profiles.

6.4.4.2 Bulk limited

Bulk transport properties were studied by analysing SCLC mechanisms through the usage of log-log $J - V$ plots shown in Figure 6.18. The linear fit of the curve for the 0.13 mg device gave a slope of about 1 indicating Ohmic conduction. This was the case even at high bias voltages. On the other hand the 0.25 mg device exhibited an Ohmic behaviour for voltages up to 0.55 V. In the region 0.55 V to 0.75 V the fitted curve gave a slope of about 1.9 ± 0.1 indicating the SCLC regime. Between 0.75 V and 1.00 V the slope of the linear fit was about 3.5 ± 0.2 showing the filling of exponentially distributed traps with the transport mechanism being by TFSCLC. The 0.50 mg device showed Ohmic conduction up to 0.85 V. The trap free, meaning the filling of exponentially distributed traps was observed from 0.85 V to 1.00 V where the slope of the fitted curve was about 2.81 ± 0.1 . Furthermore, the 0.50 mg device indicated a higher transition voltage from Ohmic conduction meaning that this device had a higher charge carrier trap density.

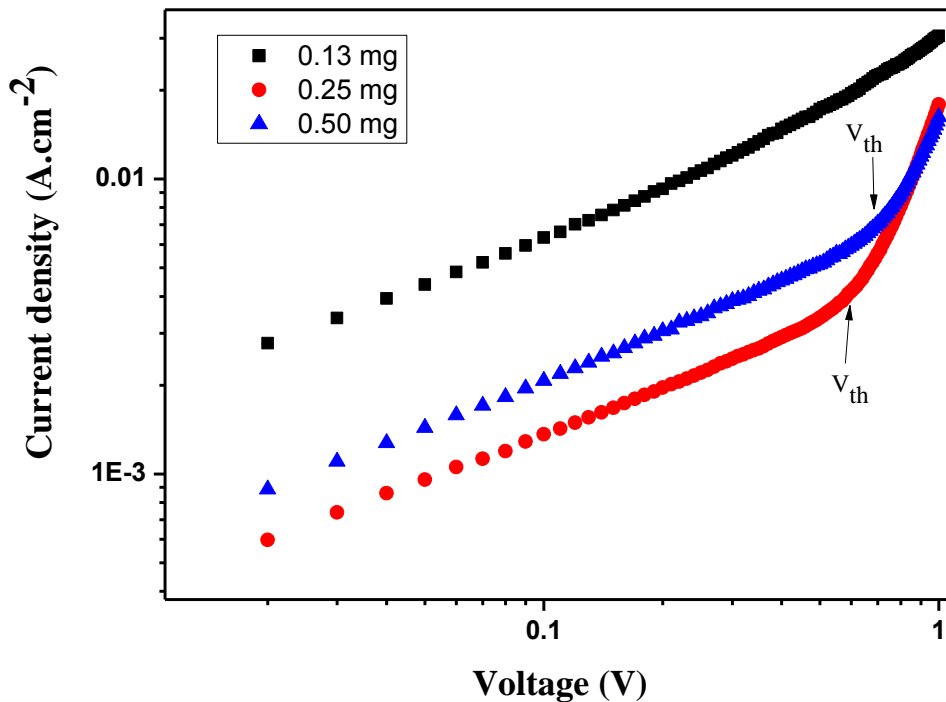


Figure 6.18: Log-log plots of $J - V$ characteristics of P3HT:N-MWCNTs indicating a higher Ohmic to SCLC threshold voltage for the 0.50 mg N-MWCNT.

Having identified the SCLC and TFSCLC dominated regions we proceeded to apply the Mott-Gurney law to describe and quantify bulk transport behaviour. It should be noted that the contact barrier and built in fields are negligible when TFSCLC is achieved, hence charge carrier mobility will only depend on the properties of the bulk [31].

Figure 6.19 is the Mott-Gurney plot that shows the charge carrier mobilities of the 0.25 mg and the 0.50 mg devices. With the slope proportional to the mobility, it can be seen from the linear fits that higher charge carrier mobilities are associated with the 0.25 mg device.

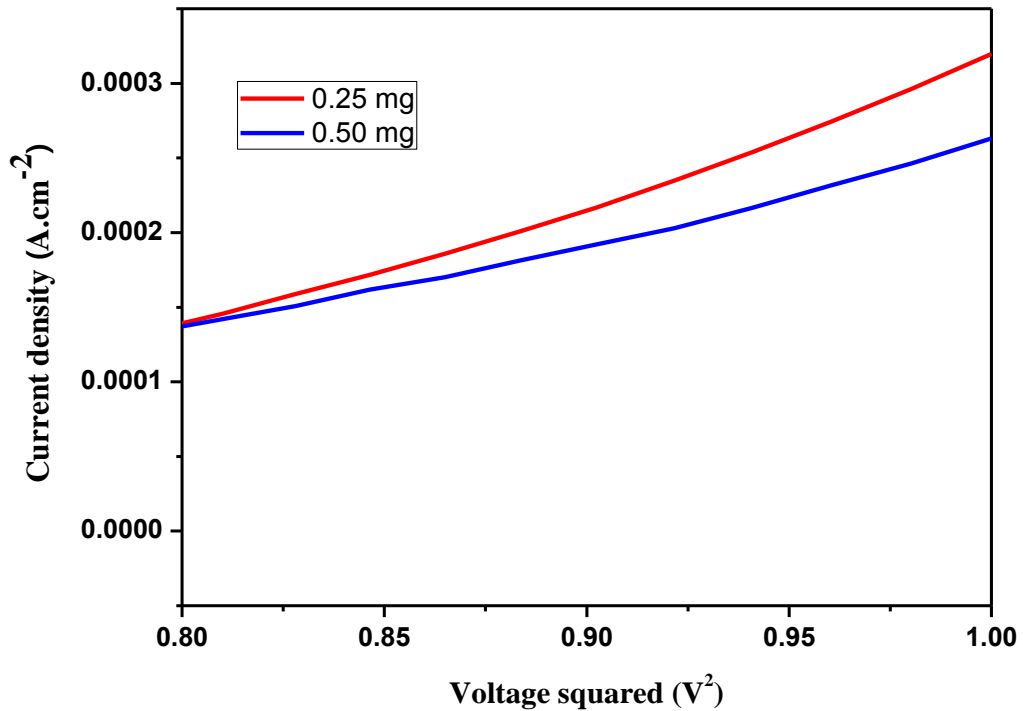


Figure 6.19: Linear fit of J_{sc} vs V^2 for P3HT:N-MWCNTs based on the Mott-Gurney law.

6.4.5 Variations of OPV parameters with light intensity

Recombination mechanisms at short circuit and open circuit conditions are explained using the linear fits in Figure 6.20. The ideality factors obtained from the linear fits of the semi-log V_{oc} vs light intensity plot (Figure 6.20 (a)) are shown in Table 6.6. With $n = 0.64$, the 0.13 mg device is seen to be affected by Auger type

recombination mechanisms [32]. The 0.25 mg and 0.50 mg have ideality factors greater than 1, showing the domination of trap assisted SRH type recombination at open circuit.

At short circuit conditions, a lack of or an insignificant bimolecular recombination is indicated by a linear dependence of current density with light intensity i.e. the slope (α) of the log-log J_{sc} vs light plot is about 1. On the other hand charge transport limited by Langevin type bimolecular recombination for slopes that are less than 1. As stated in Chapter 4, values of α that are not equal to 1 could arise from unbalanced charge carrier mobility in the system. All the slopes in Figure 6.20 (b) are less than 1 as can be seen in Table 6.6.

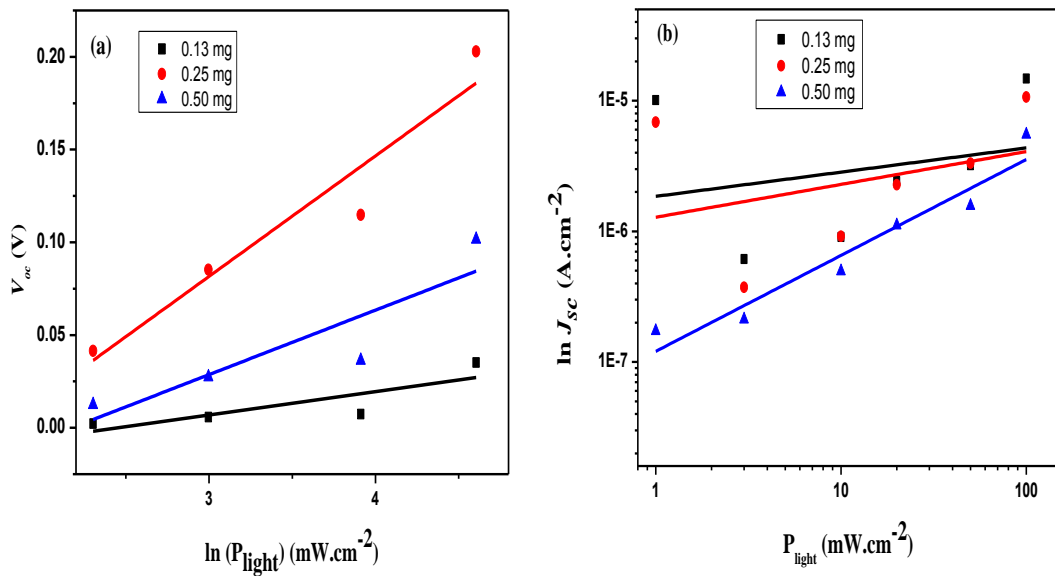


Figure 6.20: Variation of (a) V_{oc} and (b) J_{sc} with light intensity to determine recombination parameters.

Table 6.6: Recombination parameters for light intensity measurements together with mobilities

Sample	n ± 0.24	μ $\pm 0.002 \times 10^{-6} \text{ (cm}^2/\text{Vs)}$	α ± 0.02
0.13 mg	0.64	N/A	0.19
0.25 mg	4.43	1.462	0.25
0.50 mg	2.02	1.002	0.73

Though this study did not focus on morphological properties and their effects on photovoltaic performances, we wanted to have a sense of how well dispersed or not the N-MWCNTs were in the polymer:fullerene matrix. Figure 6.21 is showing a progressive degree of clump formation with the increase of N-MWCNTs in the photoactive layer. The dark spots are the loaded carbon nanotubes. This highlights the disadvantage of the direct mixing method. Subsequently, how well the carbon nanotubes are dispersed in the active layer becomes a statistical question.

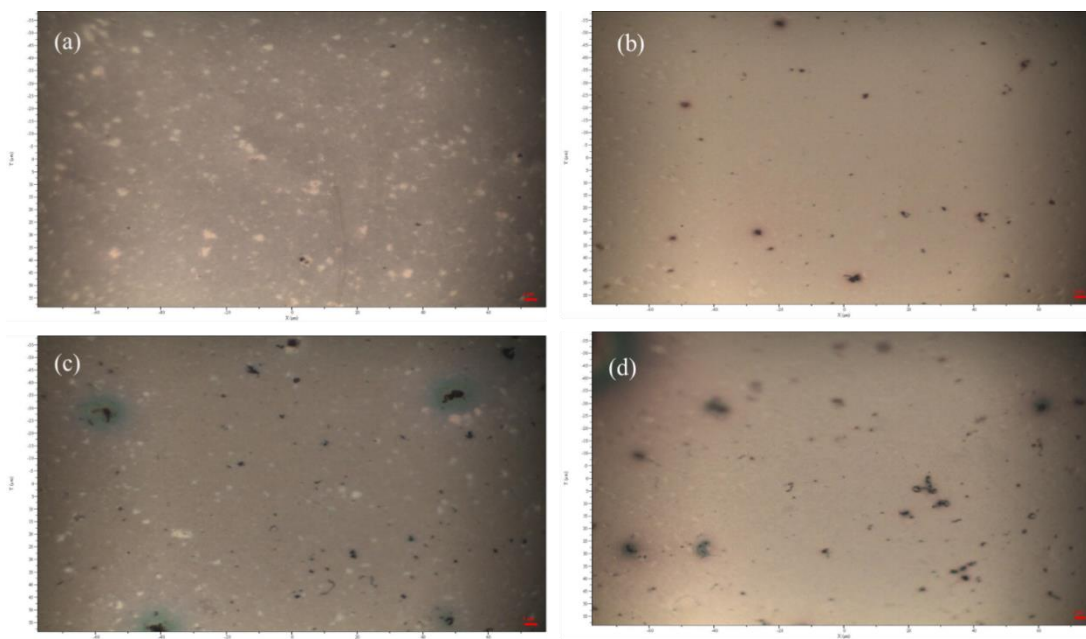


Figure 6.21: Optical micrographs of (a) P3HT:PC₆₁BM (b) P3HT:PC₆₁BM:N-MWCNT (0.13 mg) (c) P3HT:PC₆₁BM:N-MWCNT (0.25 mg) (d) P3HT:PC₆₁BM:N-MWCNT (0.50 mg).

6.5 Conclusion

Functionalised nitrogen doped CNTs were successfully synthesised and incorporated into the photoactive layer of fabricated BHJ OPV devices by a direct mixing method. A small increase in the intensity of the optical absorption spectra was observed with the addition of N-MWCNTs in the photoactive layer. A reduction in key performance parameters such as V_{oc} , J_{sc} and FF resulted in low PCEs for all devices fabricated with CNTs in the photoactive blend. Charge carrier recombination was found to be a major contributor for a reduction in the PCEs of devices with CNTs in the photoactive layer. In as far as the incorporation of CNTs into the photoactive layer is concerned, the solution based fabrication process did not afford any control of the orientation and distribution of the CNTs therein. This meant that the random orientation and the clumping of carbon nanotubes within the overall device architecture presented some of the main challenges with regards to device optimisation for improved power conversion efficiencies.

6.6 References

- [1] Günes, S., Neugebauer, H. and Sariciftci, N.S. (2007). *Chemical Reviews* **107** (4), 1324.
- [2] Zhokhavets, U., Erb, T., Gobsch, G., Al-Ibrahim, M. and Ambacher, O. (2006). *Chemical Physics Letters* **418** (4-6), 347.
- [3] Shaheen, S.E., Radspinner, R., Peyghambarian, N. and Jabbour, G.E. (2001). *Applied Physics Letters* **79** (18), 2996.
- [4] Gustafsson, G., Cao, Y., Treacy, G.M., Klavetter, F., Colaneri, N. and Heeger, A.J. (1992). *Nature* **357**, 477.
- [5] Cheng, P. and Zhan, X. (2015). *Materials Horizons* **2** (5), 462.
- [6] Etxebarria, I., Ajuria, J. and Pacios, R. (2015). *Journal of Photonics for Energy* **5**, (1), 057214.
- [7] Chen, J.-D., Cui, C., Li, Y.-Q., Zhou, L., Ou, Q.-D., Li, C., Li, Y. and Tang, J.-X. (2015). *Advanced Materials* **27** (6), 1035.
- [8] Yusoff, A.R.B.M., Kim, D., Kim, H.P., Shneider, F.K., Da Silva, W.J. and Jang, J. (2015). *Energy and Environmental Science* **8** (1), 303.
- [9] Yang, Y., Zhang, Z., Bin, H., Chen, S., Gao, L., Xue, L., Yang, C. and Li, Y. (2016). *Journal of the American Chemical Society* **138**, (45), 15011.
- [10] Bin, H., Gao, L., Zhang, Z.G., Yang, Y., Zhang, Y., Zhang, C., Chen, S., Xue, L., Yang, C., Xiao, M. and Li, Y. (2016). *Nature Communications* **7**, 13651.
- [11] Jørgensen, M., Norrman, K., Gevorgyan, S.A., Tromholt, T., Andreasen, B. and Krebs, F.C. (2012). *Advanced Materials* **24** (5) 580.
- [12] Nismy, N.A., Jayawardena, K.D.G.I., Adikaari, A.A.D.T. and Silva, S.R.P. (2011). *Advanced Materials* **23** (33), 3796.

- [13] AbdulBaki, M.K., Tangonan, A., Advincula, R.C., Lee, T.R. and Krishnamoorti, T. (2012). *Journal of Polymer Science Part B: Polymer Physics* **50** (4), 272.
- [14] Lee, H.S., Park, J.S., Lim, B.K., Mo, C.B., Lee, W.J., Lee, J.M., Hong, S.H. and Kim, S.O. (2009). *Soft Matter* **5** (12), 2343.
- [15] Sen, K., Satishkumar, B.C., Govindaraj, A., Harikumar, K.R., Raina, G., Zhang, J.-P., Cheetham, A.K. and Rao, C.N.R. (1998). *Chemical Physics Letters* **287** (5-6), 671.
- [16] Panchakarla, L.S., Govindaraj, A. and Rao, C.N.R. (2010). *Inorganica Chimica Acta* **363** (15), 4163.
- [17] Lau, X.C., Wu, Z. and Mitra, S. (2014). *ACS Applied Materials and Interfaces* **6** (3), 1640 (2014).
- [18] Lu, L., Xu, T., Chen, W., Lee, J.M., Luo, Z., Jung, I.H., Park, H.I., Kim, S.O. and Yu, L. (2013). *Nano Letters* **13** (6), 2365.
- [19] Alley, N.J., Liao, K.S., Andreoli, E., Dias, S., Dillon, E.P., Orbaek, A.W., Barron, A.R., Byrne, H.J. and Curran, S.A. (2012). *Synthetic Metals* **162** (1), 95.
- [20] Usman, I.B. (2018). *Synthesis and characterization of nitrogen-doped CNTs and carbon-doped GaN nanostructures for sensor and solar cell applications*, PhD thesis, University of the Witwatersrand, Johannesburg.
- [21] Mhlanga, S.D., Mondal, K.C., Carter, R., Witcomb, M.J. and Coville, N.J. (2009). *South African Journal of Chemistry* **62** (1), 67.
- [22] Tetana, Z., Mhlanga, S., Bepete, G., Krause, R. and Coville, N.J. (2012). *South African Journal Chemistry* **65** (1), 39.
- [23] Singh, V., Arora, S., Arora, M., Sharma, V. and Tandon, R.P. (2014). *Physics Letters A* **378** (41), 3046.

- [24] Raffaella, R.P., Landi, B.J., Harris, J.D., Bailey, S.G. and Hepp, A.F. (2005). *Materials Science and Engineering B* **116** (3), 233.
- [25] Derbal-Habak, H., Bergeret, C., Cousseau, J. and Nunzi, J.M. (2011). *Solar Energy Materials and Solar Cells* **95** (supplement 1), S53.
- [26] Gregg, B.A. and Hanna, M.C. (2003). *Journal of Applied Physics* **93** (6), 3605.
- [27] Koster, L.J.A., Smits, E.C.P., Mihailetschi, V.D. and Blom, P.W.M. (2005). *Physical Review B* **72** (8), 085205.
- [28] Gomer, R. (1993). *Field Emission and Field Ionization* 2nd edition, (AIP Press), New York, USA.
- [29] Bonard, J.-M., Salvétat, J.-P., Stöckli, T., Forró, L.A. Châtelain, A. (1999). *Applied Physics A* **69** (3), 245.
- [30] Tang, H., Liang, S.-D., Deng, S.Z. and Xu, N.S. (2006). *Journal of Physics D: Applied Physics* **39** (24), 5280.
- [31] Chiguvare, Z. (2005). *Electrical and Optical Characterization of Bulk Heterojunction Polymer- Fullerene Solar Cells*. PhD thesis, Oldenburg University, Germany.
- [32] Hall, R.N. (1981). *Solid-State Electronics* **24** (7) (1981) 595.

Chapter 7

Conclusions and outlook

7.1 Conclusions

This thesis set out to elucidate, enhance and deepen our understanding and knowledge related to the fabrication of bulk heterojunction OPVs under ambient conditions and the characterisation of their opto-electrical properties. This entailed UV-Vis measurements for the quantification and characterisation of respective optical absorbances, Raman measurements to characterise the structural order of fabricated thin films and the ($I - V$) or ($J - V$) measurements for the evaluation of photovoltaic characteristics. To this end, three different device architectures were fabricated and characterised. These are summarised as follows:

In Chapter 4, devices with an architecture ITO/PEDOT:PSS/P3HT:PC₇₁BM/Al were fabricated with a variation in the relative mass ratio of P3HT:PC₇₁BM in the active layer. The goal was to identify an optimum ratio for further analysis. The key photovoltaic performance indicator, the PCE, was used to identify the optimum active layer polymer:fullerene blend mass as 1:0.8, with the PCE peaking at 2.86%. Devices with the 1:0.8 optimum blend ratio were then fabricated for kinetic and energetic studies. In the kinetics measurements an optimum PCE of 1.78% was found for the device with a J_{sc} of 7.49 mA/cm², a FF of 35.5 % and a V_{oc} of 0.67 V. This device was annealed at 50 °C for 10 minutes. Energetics measurements also led to the best performing device with a PCE of 2.35 % that was annealed at 50 °C with a V_{oc} of 0.64 V, a J_{sc} of 8.24 mA/cm² and a FF of 44.2 %.

Chapter 5 reported on the experiments done on ternary blend bulk heterojunction devices using one donor (P3HT) and two acceptors with similar chemical and electronic properties namely i.e. (PC₆₁BM) and (PC₇₁BM). Whilst keeping the P3HT content constant, several devices were fabricated where the relative ratios of the two acceptors were changed in order to identify the best performing mixture. The P3HT: PC₆₁BM:PC₇₁BM (1:0.4:0.6) blend was found to be the best performing

blend, on the basis of the measured PCE of 2.69 % in comparison to devices with binary photoactive layer blends.

The viability of harnessing much reported opto-electrical characteristics of CNTs that could enhance the photovoltaic performance of polymer:fullerene OPVs was investigated in Chapter 6. Different concentrations of Nitrogen-doped MWCNTs (N-MWCNTs) were incorporated into the photoactive layer of 1:1 (P3HT:PC₆₁BM) OPV devices. The fabrication capability was clearly demonstrated by producing numerous devices for characterisation. The importance of an appropriate preparation of CNTs for inclusion into OPV devices was demonstrated by the observed deterioration in the photovoltaic performance of fabricated devices. An increase in the mass content of N-MWCNTs was accompanied by a decrease in the measured PCE. The agglomeration of CNTs, as seen in obtained optical images, was probably one of the factors that led to a deterioration in performance.

Recombination and transport properties in fabricated bulk heterojunction OPV devices were studied by analysing $J - V$ data both under 100 mW/cm² illumination (AM1.5G) and in the dark. In the three mentioned OPV device architectures, bimolecular recombination was found to be the dominant recombination mechanism at open circuit conditions on the basis of extracted ideality factors from the V_{oc} vs light intensity plots. Weak bimolecular recombination was observed at short circuit conditions where the dependence of J_{sc} on light intensity was analysed on the basis of the power law relation $J_{sc} \propto (P_{light})^\alpha$, with $\alpha = 1$ indicating weak bimolecular recombination. Studying charge transport properties of fabricated devices showed contributions from thermionic emission and quantum tunnelling currents for injection limited currents based on the FN and the RS models. The Mott-Gurney law was applied beyond the trap filling voltages to rank the charge carrier mobility of different device architectures.

7.2 Outlook

- A better understanding of the OPV performance of fabricated devices will be aided by detailed morphological studies of fabricated devices. For example, a better understanding of intermolecular packing structure and

domain size correlations in active layer materials can be probed by 2D-GIXRD/GIWAXS measurements, which can be compared with obtained UV-Vis spectra.

- Neutron reflectivity can be explored as a technique to characterise the depth profile of devices. The phase segregation brought about by thermal annealing can be probed to gain insight into device morphologies thereby leading to a better understanding of charge carrier pathways between electrodes.
 - Recombination loss mechanism can be further probed and characterised via a thickness dependence transient photoconductive study of the polymer:fullerene film.
 - Further studies on annealing effects on the BHJ photoactive layer as well as at interfaces with electrodes should be refined for a better understanding so that desirable fabrication conditions and protocols can be established.
- 2D time resolved fluorescence measurements needed to extract dual Forster Resonance Energy Transfer (FRET) effects from exciton lifetimes of the ternary blend and thus determine the dynamics of energy transfer.

The optimisation of donor and acceptor materials, of the best performing device architecture and morphology, of the ideal device fabrication conditions and protocols and the refinement of theoretical models to explain the physics of organic solar cells all point to need for further research and development in making OPVs a key player in the photovoltaic space and the energy mix as whole.

Publications and Presentations

Papers in preparation for publication submissions

1. L.M. Kotane, I.B. Usman, D. Wamwangi and R.M. Erasmus, **Photovoltaic investigation of N-MWCNT incorporated BHJ OPV devices**
2. L.M. Kotane, D. Wamwangi and R.M. Erasmus, **Power conversion efficiency assessment of bulk heterojunction donor: acceptor: acceptor ternary organic photovoltaic devices.** *Journal of Power Sources*. Under Review.
3. L.M. Kotane, D. Wamwangi and R.M. Erasmus, **Optical and electrical mass ratio studies of P3HT:PC₇₁BM BHJ OPV devices**

Presentations

1. NECSA-Wits workshop on Radiation, Material Sciences and High Energy Physics, 10-11 September 2015, oral presentation on **Fabrication and characterisation of high efficiency carbon nanotube based organic solar cells.**
2. South African Institute of Physics, 05 July 2016, oral presentation on **Application of Ag nanocubes for efficiency enhancement in organic photovoltaic (OPV) devices.**
3. MPRI seminar – School of Physics, Wits University, 01 June 2017, oral presentation on **Assessment of performance enhancement strategies of bulk heterojunction organic photovoltaic devices.**
4. Carbon solar cells and sensors meeting – School of Chemistry, Wits University, 19 October 2018, oral presentation on **J-V characteristics of fabricated polymer:fullerene BHJ OPV devices with a direct integration of N-MWCNTs in the photoactive layer.**
5. International School of Materials for Sustainable Development & Energy - 1st Course. Erice (Italy), July 7th – 12th 2018. Materials for Energy and Sustainability VII (ISMES VII). Many topics covered materials science and technology applied to the generation, storage, and use of green energy sources for sustainable development. **Group presentation on the creation of an ‘Energy Positive’ cruise ship.**